SDC-91-158

SDC
SOLENOIDAL DETECTOR NOTES

HYBRID CENTRAL TRACKING CHAMBER COLLABORATION PROGRESS REPORT FOR FY1991

September 1991

Hybrid Central Tracking Chamber Collaboration

Progress Report for FY1991

Submitted to

Physics Research Division
SSC Laboratory
2550 Beckleymeade Avenue
Dallas, TX 75237-3946

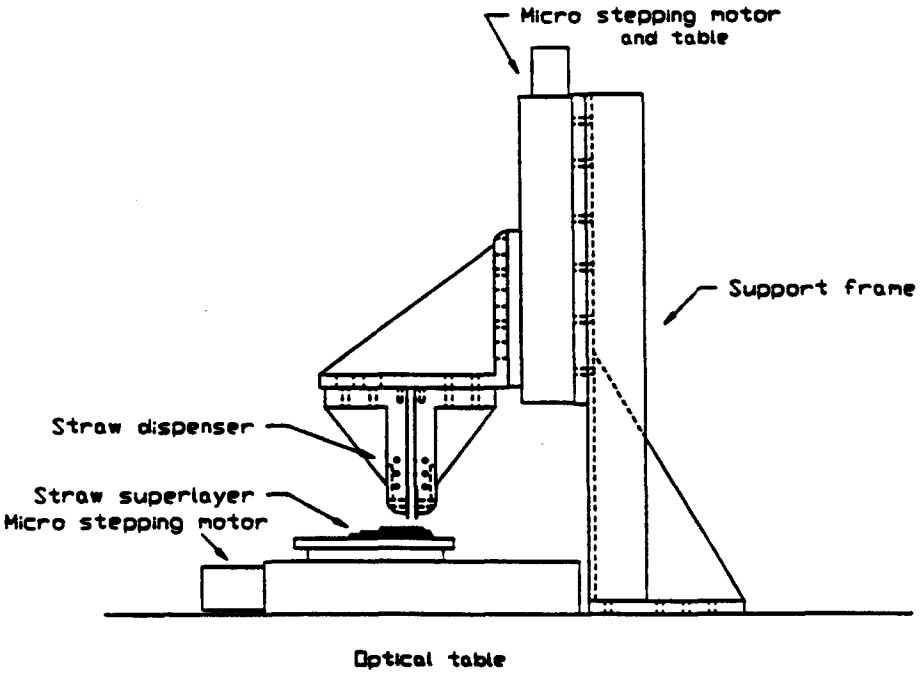

Prepared by

Continuous Electron Beam
Accelerator Facility
Duke University
EG&G, Canada
Florida State University
KEK
North Carolina State University
Northeastern University
Oak Ridge National Laboratory
Quantum Research Services
Supercomputer Computations
Research Institute
TRIUMF
University of Pennsylvania

September 1991

Collaboration Members

Continuous Electron Beam Accelerator Facility	**Dr. Stan Majewski**	
	Mr. B. Kross	Mr. R. Wojcik
	Dr. Carl Zorn	
Duke University	**Dr. Alfred T. Goshaw** (Co-spokesman)	
	Dr. Seog Oh	Dr. William Robertson
	Mr. Joseph D. Simpkins	Mr. Malie Yin
EG&G, Canada	**Dr. Robert McIntyre**	
	Dr. Henri Dautet	
Florida State University	**Dr. Vaskan Hagopian**	
	Mr. E. Hernandez	Mr. K. Hu
	Dr. Kurtis Johnson	
KEK	**Dr. Hirokazu Ikeda**	
	Dr. Yasuo Arai	
North Carolina State University	**Dr. John Paulos**	
	Mr. Steve Blake	Dr. Thomas S. Elleman
Northeastern University	**Dr. Stephen Reucroft** (Co-spokesman)	
	Dr. George Alverson	Mr. Addison Grimes
	Dr. Mike Glaubman	Dr. Ian Leedom
	Dr. T. Yasuda	
Oak Ridge National Laboratory	**Dr. Tony Gabriel**	
	Mr. Gary Alley	Mr. Hugh Brashear
	Mr. Charles L. Britton, Jr.	Mr. Michael Emory
	Dr. Charles Glover	Mr. Ted Ryan
	Mr. David Vandergriff	
Quantum Research Services, Inc.	**Dr. William L. Dunn**	
	Dr. Fearghus O'Foghludha	Dr. A.M. Yacout
Supercomputer Computation Research Institute	**Dr. Martyn Corden**	
	Dr. Mike Mermikides	Dr. D. Xiao
TRIUMF	**Dr. Martin Solomon**	
	Dr. Robert Henderson	Dr. Wayne Fraszer
	Mr. Robert Openshaw	
University of Pennsylvania	**Dr. Rick van Berg**	

Primary Contact Person:

Dr. Alfred T. Goshaw
Physics Department
Duke University
Durham, NC 27706
(919) 684-8134
GOSHAW @ FNAL

Hybrid Central Tracking Chamber Collaboration

Abstract

This Progress Report for FY1991 is submitted to the SSC Laboratory in partial fulfillment of the terms of the Memorandum of Understanding (MOU) between the Hybrid Central Tracking Chamber (HCTC) Collaboration and the SSC Laboratory for FY90. The report for FY1991 provides a comprehensive account of the research and development carried out under the MOU during the current fiscal year. Since most of the HCTC collaboration members are also members of the Solenoidal Detector Collaboration (SDC) and since our research is in direct support of the SDC detector, no funding request for FY1992 is included here; rather funds will be sought directly through SDC to continue the research and development efforts in future years. The HCTC collaboration has the same 12 member institutions as last year, with the cosmetic change that the group formerly from General Electric Canada, Inc. was acquired by EG&G. The Executive Summary presents a brief overview of the HCTC design and the major accomplishments of FY1991. The remainder of this report consists of mini-reports from the member groups providing detailed information on their activities during the year. During FY1991, we have made considerable progress toward our goal of developing a large volume tracking detector for the SSC that borrows desirable features of two promising technologies, straw tubes and plastic scintillating fibers (PSF). Our research confirms our prior position that the hybrid straw-tube/PSF approach offers significant advantages in performance without compromising cost, permits straightforward and inexpensive upgrade to accommodate higher luminosity, and is a flexible option for central tracking in the large general-purpose SDC detector.

Hybrid Central Tracking Chamber Collaboration

Progress Report for FY1991

Table of Contents

Section		Page
	Collaboration Members	ii
	Abstract	iii
	Table of Contents	iv
1.0	Executive Summary	1
2.0	Individual Group Reports	8
2.1	CEBAF – Results of a Low Dose Rate Irradiation of Selected Plastic Scintillating Fibers	
2.2	Duke University – Straw Tube and Straw Tube Superlayer Studies	
2.3	EG&G – Avalanche Photodiode Studies	
2.4	Florida State University – Performance and Radiation Hardness of 1 mm Fibers for Use in Tracking for the SSC	
2.5	KEK – Conceptual Design of Straw Tube Readout with TMC	
2.6	North Carolina State University – Front-End Electronics for the HCTC	
2.7	Northeastern University – Studies of Plastic Scintillating Fibers with Avalanche Photodiode Readout	
2.8	Oak Ridge National Laboratory – Straw Tube Electronics	
2.9	Oak Ridge National Laboratory – Mechanical Engineering and Integration	
2.10	Quantum Research Services and North Carolina State University – Radiation Damage Assessment Activities	
2.11	Supercomputer Computations Research Institute – Central Tracking Chamber Simulation	
2.12	TRIUMF – Straw Tube Radiation Damage Studies	
2.13	Univeristy of Pennsylvania – Straw Electronics	
3.0	Appendices	

1.0 Executive Summary

1.1 Introduction

This progress report presents results from the second year of activity of the Hybrid Central Tracking Chamber (HCTC) Collaboration. Taking into account our R&D work over the past two years, plus the results of other workers, we now believe that we have the knowledge and expertise to design a central tracking system containing an optimized arrangement of both straw tubes and scintillating fibers for a major SSC detector.

Over the past year the HCTC Collaboration has in particular focused its attention on the design of the outer barrel tracker for the Solenoidal Detector Collaboration, and nine of the 12 HCTC institutions are now members of SDC. We are participating in the development of the FY1992 R&D plan for SDC and expect to continue our tracking chamber research as part of this collaboration. Although the barrel tracker technology to be used by SDC has not been chosen as of this date, it appears certain that aspects of the straw tube and/or scintillating fiber research done by the HCTC will be used in the SDC tracking detector.

The SDC tracking system is composed of an inner silicon detector (strips plus possibly pixels) covering the pseudorapidity range $|\eta| < 2.5$ and extends to an outer radius of 46 cm. The HCTC collaboration has been designing a detector to cover the central region outside the silicon detector. It covers the radial region 60 to 170 cm and $|\eta| < 1.6$. This barrel tracker uses the basic principles proposed by the HCTC collaboration but has been modified to take advantage of the complimentary information provided by the silicon tracker and reduced in scope to conform to budget constraints imposed upon the SDC detector. Figure 1.1 shows the currently proposed radial structure of the hybrid barrel tracker. As described elsewhere in this report (see the report from SCRI in section 2) our simulation studies indicate that this tracking configuration looks very attractive for the SDC detector.

This hybrid central tracking chamber takes advantage of the natural strengths of the alternate tracking technologies. Straw tubes yield excellent single track resolution while plastic scintillating fiber of the appropriate diameter yields good two track

Fig. 1.1 Radial structure of the hybrid design of the SDC barrel tracker. All superlayers are supported on cylindrical stable-base supports which span the full length of the detector.

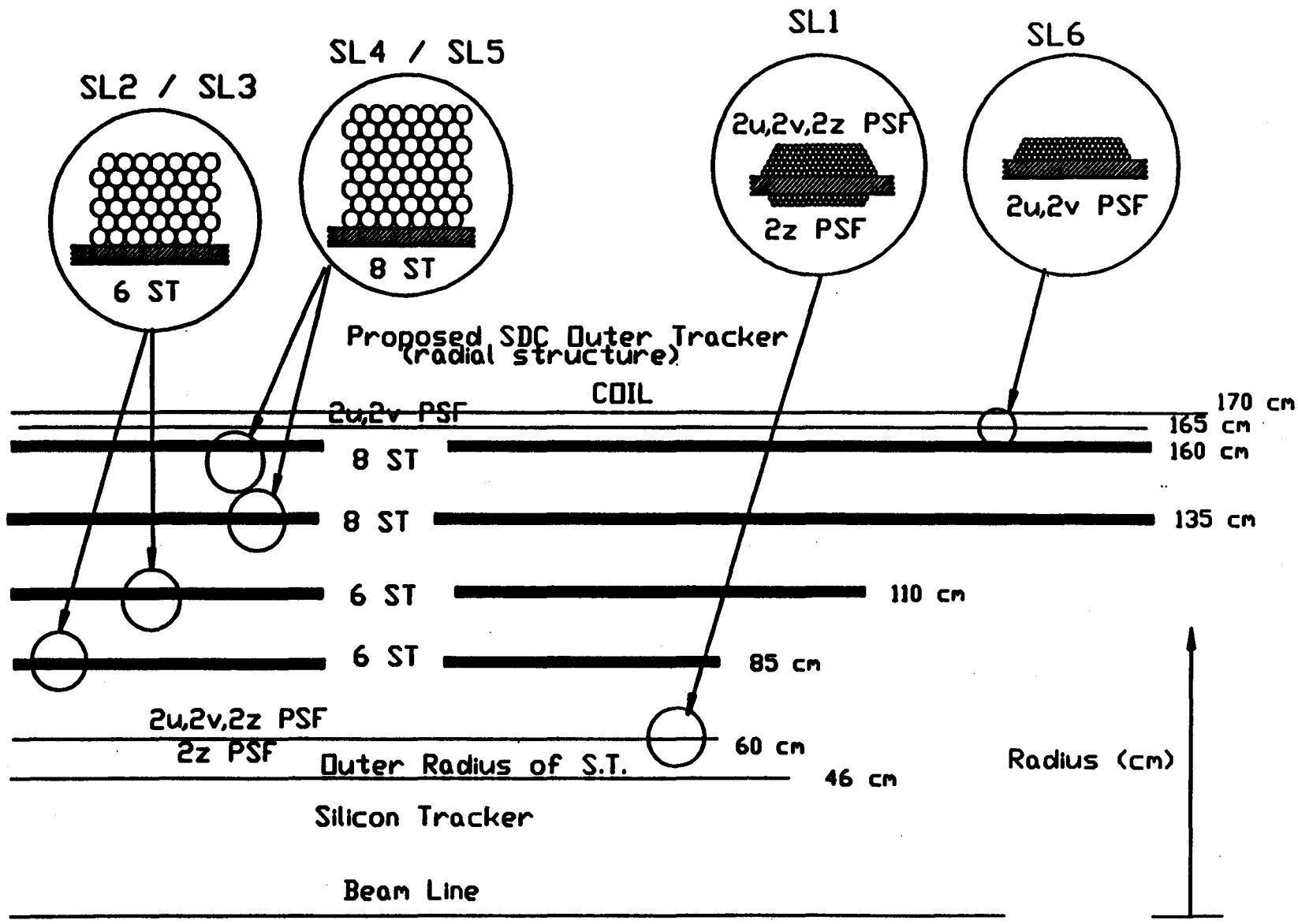

resolution. A straw tube system has fewer channels than a comparable fiber system. Straw tubes can be readily used parallel to the beam line to give high precision azimuthal track measurements but with some difficulty to give stereo information. Fibers on the other hand are natural stereo detectors but require a prohibitive number of channels in order to attain the azimuthal precision and pattern recognition capabilities of straw tubes. At a given radius, fibers have lower occupancy than straw tubes.

The cost of such a "mixed" system would be comparable to the cost of an all straw system with similar performance characteristics and much less than that of an all fiber system of similar performance. R&D costs over the next few years would be less for the mixed system because the optimized matching of the straw tube and fiber techniques means that neither technique would need to be stretched beyond our current knowledge of its performance limitations. Also, the hybrid system lends itself naturally and efficiently to upgrades that would be required if machine luminosity were increased.

The remainder of this report reviews the specific R&D results obtained by the HCTC Collaboration during FY1991. An overview is given in section 1.2 below and the details are presented in Section 2.0.

1.2 Overview of Major R&D Results from FY1991.

Some of the major R&D results obtained by the 12 institutions in the HCTC Collaboration are summarized below. These are grouped into four tasks.

Task 1: straw tube drift chambers

Duke: straw tube drift cell and straw tube superlayer construction and testing.
KEK, NCSU, ORNL, and Penn: straw tube electronics
TRIUMF and QRS: gas aging and radiation hardness of materials

<u>Construction and testing of a 2.7 m straw tube superlayer</u>

- For the past 18 months we have had in operation an 8-deep straw tube superlayer constructed of 4 mm diameter straw tubes. This has been used to study construction techniques, to determine measurement resolution ($\sigma < 120\ \mu m$) and to study other straw tube performance characteristics ($\lambda \approx 500$ cm). To our knowledge, this is the only long (~3 m), small cell (4 mm diameter) straw tube superlayer in operation.

Construction and testing of 7 m straw tube drift cells

- Recently, we have brought into operation 7 m long straw tube drift cells (4 mm diameter) using 25 μm sense wires and 1500 Å copper cathodes. These include a mid-tube insulating break in the sense wire which will allow readout from each end of two electrically isolated half cells.

Semi-automatic straw tube placement machine

- A computer-controlled straw tube laying machine has been designed and all the components have been ordered. This will be the first attempt to automate the construction of straw tube superlayers. The prototype is designed to lay 3 meter long straw tubes to an accuracy of better than 100 μm.

Sense wire position measurement

- A technique has been developed to measure *in situ* the positions of straw tube sense wires to an accuracy of about 50 μm.

Radiation hardness studies

- We have studied the radiation hardness of materials used to construct straw tubes. The aging of straw tube anodes and cathodes has been measured using CF4-isobutane (80:20). The only problems observed were connected with the deterioration of poorly constructed aluminum cathodes. Tubes with copper cathodes are presently being evaluated.

Evaluation of straw tube readout electronics

- The 2.7 m straw tube superlayer is being used to evaluate readout electronics as they become available from Penn and KEK. In particular, we report the first evaluation of the KEK designed Time Memory Cell using real straw tube signals. A detailed computer simulation of the response of readout electronics to straw tube signals has been made.

Task 2: scintillating fiber tracking

EG&G and NU: properties of plastic scintillating fibers and ribbons; avalanche photodiode development

CEBAF, FSU, NCSU, and QRS: radiation hardness of fibers and electronics

APD's

- Progress was made in developing fabrication techniques for large (0.5 mm) 'Slik' APD's and in optically coupling large (~1 mm) fibers to 0.5 mm APD's using high-index ball lenses.

- Improvements in passive quenching were obtained (dead times on the order of 300 ns), but investigations of active quench circuits have not yet been successful.
- Preliminary indications exist that in sub-geiger mode dead times of 15 ns can be achieved with no afterpulsing and linear count rates up to 10^7 s^{-1}.

Fibers

- Fibers from Bicron, Kuraray, and Optectron were tested. The Bicron H fiber gives the best efficiencies at 0.5 mm diameter.
- Promising results for 1 mm fibers were obtained for Bicron G2, Kuraray SCSF 81, and Kuraray SCSF 3HF fibers.

Radiation Damage

- A systematic investigation of low-dose-rate effects on fibers was conducted. Early results indicate that, generally, fibers irradiated slowly in an oxygen-containing environment (air) suffer more damage than fibers irradiated slowly in an oxygen-free environment (argon). Further, and significantly, fibers irradiated at low dose rates (whether in air or in argon) suffer more damage than those irradiated at high dose rates.
- Neutron irradiations of APD's show that damage is due to fast neutrons and the threshold for neutron damage occurs at relatively low fast-neutron fluences – of the order of 10^6 cm^{-2} for APD's operated in the geiger mode. Interestingly, a slow recovery, initially of about 10-20% reduction in dark count rate per month, occurs if the APD's are stored at room temperature with no further irradiation.
- Mixed neutron-photon irradiations of three types of fibers indicated no residual damage one day after exposure to $2x10^{12}$ cm^{-2} fast fluence, 10^{13} cm^{-2} thermal fluence, and ~3 krad gamma-ray dose. Similarly, no appreciable difference in light output or light attenuation between irradiated and unirradiated fibers was measured one month after exposure of five fiber types (Bicron and Kuraray) to $4x10^{13}$ cm^{-2} fast fluence ($2x10^{14}$ cm^{-2}, thermal) and about 6-9 krad gamma dose.
- Various types of fibers, including some with a new cladding material, were exposed to 3-MeV electrons. Fibers with the new cladding exhibit almost 50% increased light yield but 30% reduced attenuation length. The fibers recover fairly quickly but not fully over four weeks. The attenuation length of long (3-4 meters) fibers increases by about 80% toward the end of the fibers.

Ribbons

- Fiber ribbons were obtained from two manufacturers (Bicron and Kuraray). The average center to center spacing of the fibers was measured and found to

be, for the Bicron ribbon, 1.1025±0.0015 mm over a one m length and, for the Kuraray ribbon, 1.072±0.20 mm. We conclude that fiber suppliers have developed sufficient expertise to manufacture ribbons of high enough quality for central tracking purposes.

Task 3: mechanical engineering

Duke and ORNL: support structure, integration and construction schedule for the hybrid tracker; general mechanical design of straw tube placement machine

Superlayer Support Structure

- The HCTC collaboration has proposed a superlayer support structure (for straw tubes and fibers) based upon large cylinders fabricated from carbon fiber sheets with foam spacers (thickness on the order of 0.25% of a radiation length). In FY1991 further studies of this support structure have shown that affordable stable-base cylinders of the required precision (10 mil total radial run out) can be constructed. These have been adopted by SDC as the preferred primary superlayer support structure. Details of the overall hybrid support structures and interfaces are under study.

HCTC Design, Cost, and Schedule

- Various HCTC designs have been evaluated and cost estimates made based upon level-five work breakdown structures. These have shown that the hybrid barrel tracker required for the Solenoidal Detector would cost on the order of $30 M. The integration of the HCTC design into the Solenoidal Detector has resulted in a Resource Requirement Report and an extensive Gantt chart/network diagram which describes complete interface relationships as they progress through fabrication and installation.

Task 4: Monte Carlo simulation studies

QRS and SCRI: simulation of hybrid detectors response to SSC events and backgrounds; pattern recognition

Incorporation of HCTC simulation into the SDC software environment

- Simulation of the HCTC detector has been incorporated into the full SDC tracking detector. This allows us to evaluate the performance of the entire tracking system and make more informed judgements about the HCTC architecture. It is essential to simulate the entire SDC tracker in order to optimize the performance and overall cost.

Momentum resolution

- A detector consisting of 8 silicon, 5 straw, and one fiber superlayers has been simulated. The momentum resolution for 200 GeV/c muons is measured to be $\sigma/p = 17\%$.

Pattern recognition efficiency

- A descoped version of the SDC tracker with 8 silicon layers, 4 axial straw layers and a single stereo fiber layer was simulated. The track finding efficiency for 200 GeV/c muons in an SSC environment with luminosity up to 2×10^{33} cm^{-2}-s^{-1} has been measured to be approximately 99%. Higher luminosity studies are in progress.

CAD-to-GEANT Interface

- With funding under the Small Business Innovation Research program, one of the Collaboration members has developed the rudiments of a robust interface between Computer Aided Design (CAD) packages and the GEANT simulation code. The work successfully demonstrated the conversion of CAD output files containing collections of shapes (in either multiple 2-D views or single 3-D representations) into the appropriate FORTRAN coding to effect input into GEANT.

2.0 Individual Group Reports

Toward the end of August 1991, we asked each of the HCTC collaborating institutions to provide us with a short written progress report of FY1991 activities. Rather than reformat them, we simply collect all these individual group reports together in this section.

Hybrid Subsystem Progress Report for FY1991

Results of a Low Dose Rate Irradiation of Selected Plastic Scintillating Fibers

CEBAF, Physics Division
12,000 Jefferson Avenue
Newport News, VA 23606

Brian Kross, Stan Majewski, Randy Wojcik, and Carl Zorn†

† contact person

ABSTRACT

We report on the initial results from the analysis of data from a low dose rate (< 10 Gy/hr) irradiation of a wide variety of plastic scintillating fiber formulations. The results are striking and seem to be the following: (1) those fibers irradiated slowly in air (i.e., oxygenated) suffer the greatest amount of damage, (2) fibers irradiated rapidly in air and then allowed to recover in air, suffer the least amount of damage, and (3) those fibers irradiated slowly in argon (an oxygen-free atmosphere) suffer an intermediate level of damage somewhere between the levels seen in (1) and (2). We note a particular exception: a green-emitting fiber known as SCSF-Y8 which does not display any differences in damages levels. The data analysis continues on such matters as loss in intrinsic light output (as compared to transmission losses), and quantifying the overall losses among the fibers.

Introduction

To our knowledge, this is the first report of a systematic investigation of possible low dose rate effects in plastic scintillating fiber. Current and past investigations of radiation damage effects have used relatively high rates (100 to 10,000 Gy/hr where 1 Gy (Grey) = 100 rad) to achieve the target doses (1 kGy to > 100 kGy) within a realistic time frame. We will briefly summarize the chief characteristic results of such an irradiation [1].

Under high rate conditions, color centers are formed which absorb heavily in the UV and blue, but also in the green and red to some some extent. The concentration of these color centers is proportional to the dose and may saturate at extremely high doses. After completion of the irradiation, an annealing phenomenon is observed. That is, the concentration of color centers decreases with passage of time. This annealing takes place most rapidly in the presence of oxygen which bleaches the scintillator as it diffuses into the plastic (see figure 1). The rate of annealing is consistent with the rate of diffusion of oxygen into the material, and this rate will decrease somwhat with increasing accumulated dose. Annealing can also take place in the absence of oxygen, but at a much smaller rate. An increase of the ambient temperature can increase the rate significantly. After annealing is completed, there is a residual level of damage remaining which is proportional to the accumulated dose. To appreciate the effect of these color centers upon the performance of the scintillator, we proceed to briefly describe the energy transfer mechanisms within the scintillator.

The most popular scintillators consist of a weakly fluorescent plastic solvent (polystyrene) doped with a high concentration of a primary fluor plus a much lower

concentration of secondary fluor. Excited states in the solvent primarily transfer their energy to the primary via a non-radiative dipole-dipole interaction. Subsequently, the fluorescent emission of the primary is absorbed and re-emitted by the secondary at a suitably longer wavelength (> 400 nm).

The residual color centers absorb most strongly in the UV where the primary radiatively transfers energy to the secondary. Hence these color centers compete with the secondary with a resulting decrease in light output being observed. There is also some level of increased absorption at longer wavelengths so that attenuation of the secondary emission also increases. Figure 2 displays the effect of decreased light output and transmission upon a scintillating fiber.

A key concern that has arisen is whether the residual level of damage observed after a high rate irradiation will be the same if the irradiation is performed at a more realistic rate. There is plenty of evidence from studies of *mechanical* damage to polymers that indicates that oxygen diffusion **during** the irradiation can lead to increased levels of residual damage. At high rates, the oxygen does not have time to diffuse into the plastic and participate in deleterious reactions. In fact, extraneous *optical* damage has recently been observed in undoped polystyrene samples [2] in a high rate Co-60 gamma irradiation (0.5 kGy/hr). By using large samples (1 in^3) and a high dose (160 kGy), the researchers were able to observe a thin layer (about 2 mm in thickness) after annealing that had increased color absorption. The thickness of this layer is consistent with the extent to which oxygen would diffuse into the sample during the irradiation.

The Experimental Procedure

In our experiment, we have selected a wide variety of blue and green-emitting fibers (listed in figures 8(a) through 8(t)). The fibers labelled as SCSF-38C, -81C, and -Y8C are special formulations of the fibers SCSF-38, -81, and -Y8 that use a new low refractive index cladding resulting in higher light collection efficiency. There were a total of ten fiber types with 12 samples of each fiber. All fibers were 150 cm long and 1 mm in diameter. The latter is typical for fibers and the length was sufficient for measuring attenuation changes. All fibers were shipped in straight lengths as curled samples would produce a wider variation in attenuation behavior. One end of each fiber was hand-polished and a 3 cm long strip of flat-black paint applied to that end to eliminate any contributions from light

propagating in the cladding (as this light is a known source of noise). The other end was blackened to eliminate reflections.

The attenuation characteristics (and relative brightness) of the fibers were measured on a scanning device shown in figure 3. A continuous x-ray source from X-Tech was used as the excitation source. This device generated 8 keV x-rays which could penetrate the 1 mm diameter fiber. The generated light was detected by a bialkali phototube set in DC mode, and the current measured with a Keithley picoammeter. The scan is controlled via a personal computer. By using the DC mode, the many necessary measurements could be made fairly quickly. A bialkali tube was used for several reasons: (1) it was readily available, (2) although the goal is to use highly efficient green and red-sensitive photodetectors, they are still a research curiosity at present, (3) most of the fibers are blue-emitting in any case, (4) bialkali tubes may still be used in calorimeter applications, and (5) the use of optical filters can qualitatively simulate the effect of green-sensitive photodetectors, and most importantly (6) any low dose rate effects will not qualitatively change by use of an improved photodetector.

In terms of what dose and dose rate one should use, one can use the recent study by Groom for guidance [3]. The central tracking chamber is envisioned to cover the radial region from about 0.6 to 1.6 meters. At the design luminosity of 10^{33} $cm^{-2}s^{-1}$, one can estimate doses of 15 (outer radius) to 110 Gy (inner radius) per year. At the high luminosity option of 10^{34} $cm^{-2}s^{-1}$ for ten years, this becomes 1.5 to 11 kGy which is not a negligible dose. Since it seems likely that a fairly appreciable dose is required to create significant changes in attenuation, it was decided to choose somewhat extreme doses so as to clearly see a low dose rate effect, namely 5 and 20 kGy. With such doses, the information obtained could also be useful to calorimeter researchers who will be dealing with such doses (and worse) in the forward region. In choosing a dose rate, we wanted something low enough that oxygen would have time to permeate the fibers during the irradiations. Other researchers [4] found that for dose rates below 45 Gy/hr, oxygen would permeate their 2.6 mm thick sheets of polystyrene-based scintillator (SCSN-38). Hence we aimed for a dose rate below 10 Gy/hr.

Figure 4 is a schematic of the irradiation setup at the Nuclear Reactor Facility of the University of Virginia. A set of depleted Co-60 line sources was used to create the low rate radiation field. The fiber sets were divided into 4 subsets (3 fibers of each type per subset for statistics), and placed in four stainless steel tubes sealed with gas-tight enclosures. Besides splitting them into the two dose subsets, one tube from each dose subset was tied

into the same gas circulation system: two with dry argon gas, and two with dry air. The two subsets closest to the line source experienced a dose rate of 6.7 Gy/hr. These were taken to 20 kGy. The outer ones were irradiated to 5 kGy at a rate of 5.5 Gy/hr. Note that the first 30 cm of the fiber samples were shielded with a lead annulus with sufficient thickness to give a factor of 200 less in accumulated dose. This was done so that one can obtain a measure of intrinsic light output loss by looking for a "step" beyond 30 cm in the attenuation curve after the irradiations.

In addition to the low dose rate irradiations, another two subsets of fibers were irradiated at a typical high rate at the 3 MeV electron beam facility of Florida State University. One subset was irradiated to 5 kGy and the other to 20 kGy. From past experience with irradiating such fibers at a high rate, one week of recovery in air was allowed before measurements were made. (For the low rate data, the fibers were also re-measured 2-3 weeks later to see if any recovery effects were present. None were found.)

Finally, some measurements (for the 5 kGy low rate) were made with a set of optical filters. These filters had several purposes: (1) for green-emitting fibers, an appropriate filter can qualitatively simulate the use of a green-sensitive photodetector (this was verified by using a multialkali green and red-sensitive phototube), (2) the extent of damage as a function of wavelength can be ascertained, and (3) the use of an optical filter can qualitatively simulate the effect of natural optical filtration by long lengths of undoped readout fiber. Figure 5 displays the transmission characteristics of the filters. As a point of reference, the blue fibers emit in the range of 400 to 440 nm. The green-emitting 3HF fiber emits at 530 nm and the SCSF-Y8 fiber emits at 500 nm.

The Preliminary Results

Figure 6 displays the relative light outputs of the fibers as measured with the bialkali phototube. BCF-10 was used as the reference. The second set of columns displays the light output after 1.5 meters of attenuation is allowed to take place. Again BCF-10 (at 1.5 meters) is used as the reference. Figure 7 displays typical attenuation data. Fits to the double exponential function $y = A_1 * \exp(-x/\lambda_1) + A_2 * \exp(-x/\lambda_2)$ were used to quantitatively describe the attenuation behavior.

Figures 8(a) through 8(t) display the results of the low and high rate irradiations. The upper graphs are the results for the 5 kGy irradiations and the lower for 20 kGy for

each fiber type. Only changes in attenuation are shown as changes in the intrinsic light output are currently under investigation. Finally, figure 9(a) through 9(o) display the effects of using an optical filter for the low rate 5 kGy data. (Note that all the light outputs in figures 8 and 9 were normalized to the same value at 0 cm (0.5) in order to best display the attenuation changes. Figure 6 is a guide to how the actual light output would change when using a bialkali phototube.)

We see two primary effects. For the low dose data, we see that in fact oxygen does introduce an increased level of damage. Furthermore, there seems to be an additional low dose rate effect independent of the presence of oxygen. The high rate data shows considerably less damage for many of the fibers than for those irradiated slowly in argon. The one exception is SCSF-Y8 and -Y8C which do not display this hierarchy. We are currently investigating the possibility of some systematic effect creating the difference between the fibers irradiated slowly in argon and those irradiated quickly. However, as of this point in time, we see no reason to disbelieve the results as shown.

Closing Remarks

The analysis of the data is continuing, particularly in the area of ascertaining any loss in intrinsic light output, and in quantifying the overal light output losses (transmission and intrinsic) over the length of the fiber. In particular, we wish to compare the performance of the PMMA-clad Kuraray fibers with the new versions clad in lower refractive index material.

As to the implication of the results as they stand at present, it seems clear that high dose rate experiments may seriously underestimate the levels of damage to be expected with scintillating fibers. It will be interesting to compare the results reported here for fibers with those of an ongoing experiment on low dose rate effects upon *plate* scintillator [5].

REFERENCES:

[1] For details (including a complete bibliography), the interested reader is referred to a new review *Fast Scintillators for High Radiation Areas* by Stan Majewski and Carl Zorn. It will be published as a chapter in an upcoming book *Instrumentation in High Energy Physics* edited by Fabio Sauli and will be published by World Scientific. Copies of the preprint version of the review may be obtained from either of the authors.

[2] J.S. Wallace, Sandia National Laboratories, private communication.

[3] D.E. Groom, "Ionizing Radiation Environment in SSC Detectors," *Proceedings of the Workshop on Radiation Hardness of Plastic Scintillator*, ed. K.F. Johnson (March 19-21, 1990, Tallahassee, Florida) pp. 69-75.

[4] B. Bicken et al., *IEEE Trans. Nucl. Sc.* 38 (1991) 188.

[5] N.D. Giokaris, Fermilab, private communication.

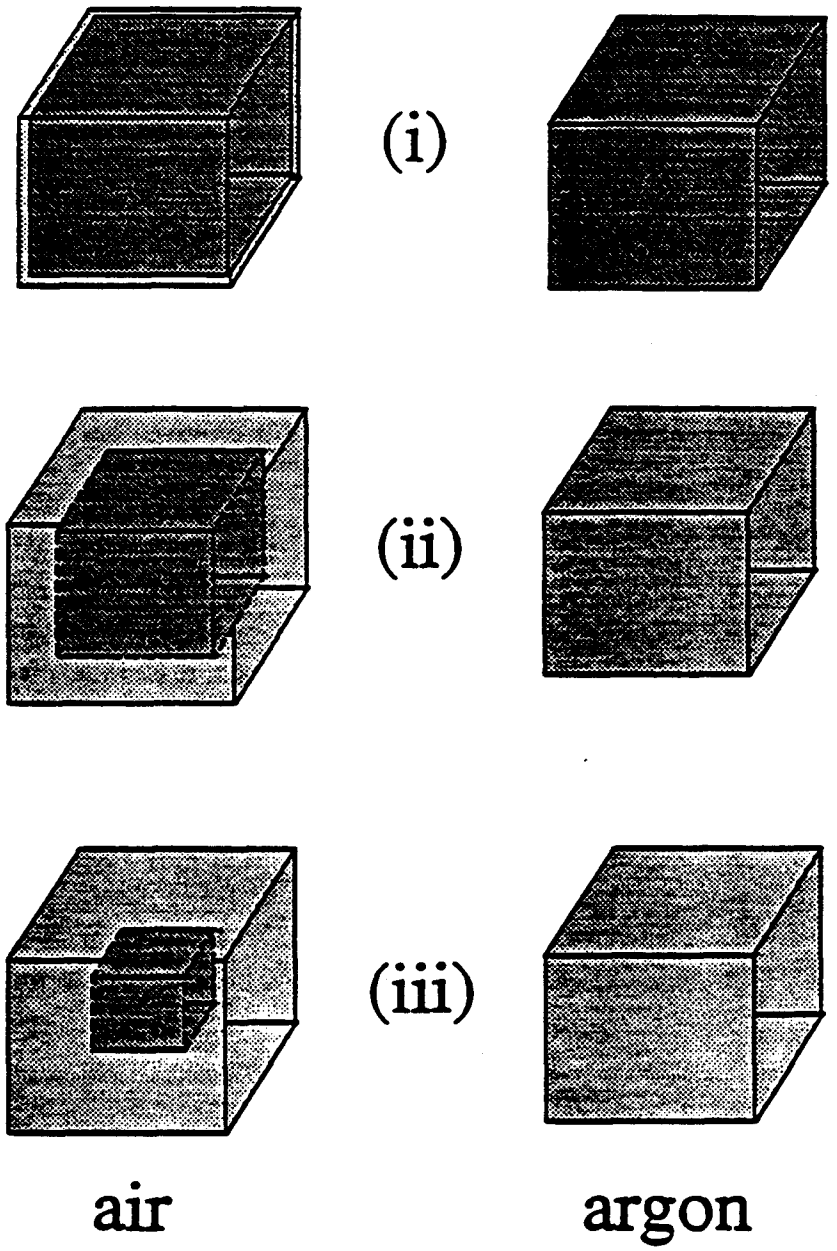

FIGURE 1: A pictorial representation of post-irradiation annealing in polystyrene cubes after a high dose rate irradiation. In air, oxygen diffusion drives the bleaching process at a rapid rate while in an oxygen-free atmosphere (e.g., argon), color center relaxation takes place slowly throughout the volume of the material. In air, the time scale from (i) to (iii) can be a matter of days while in argon the relevant time scale can be several months.

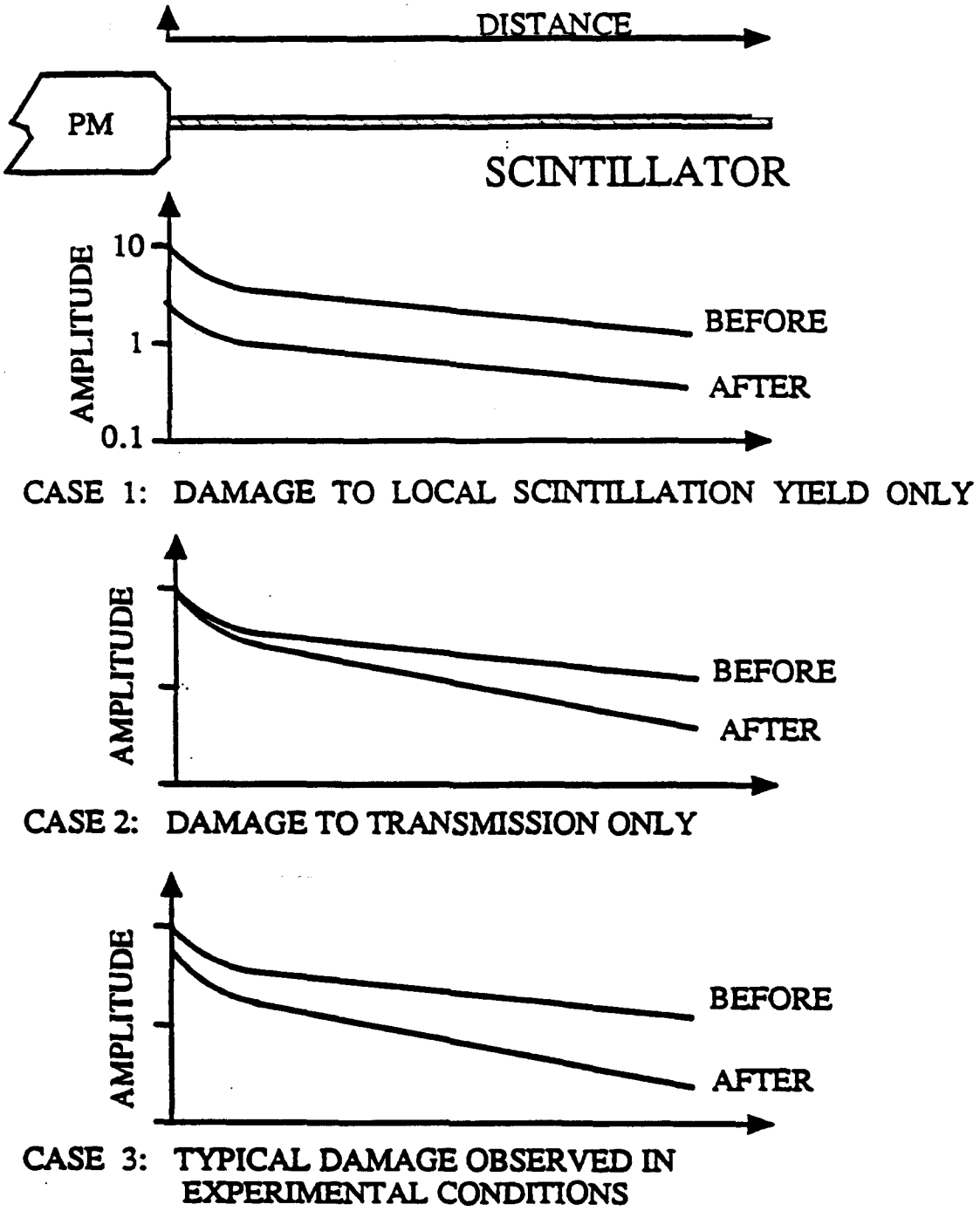

FIGURE 2: Effect of radiation damage upon optical performance of scintillators.

SCINTILLATING FIBER SCANNER

(4 meter scan)

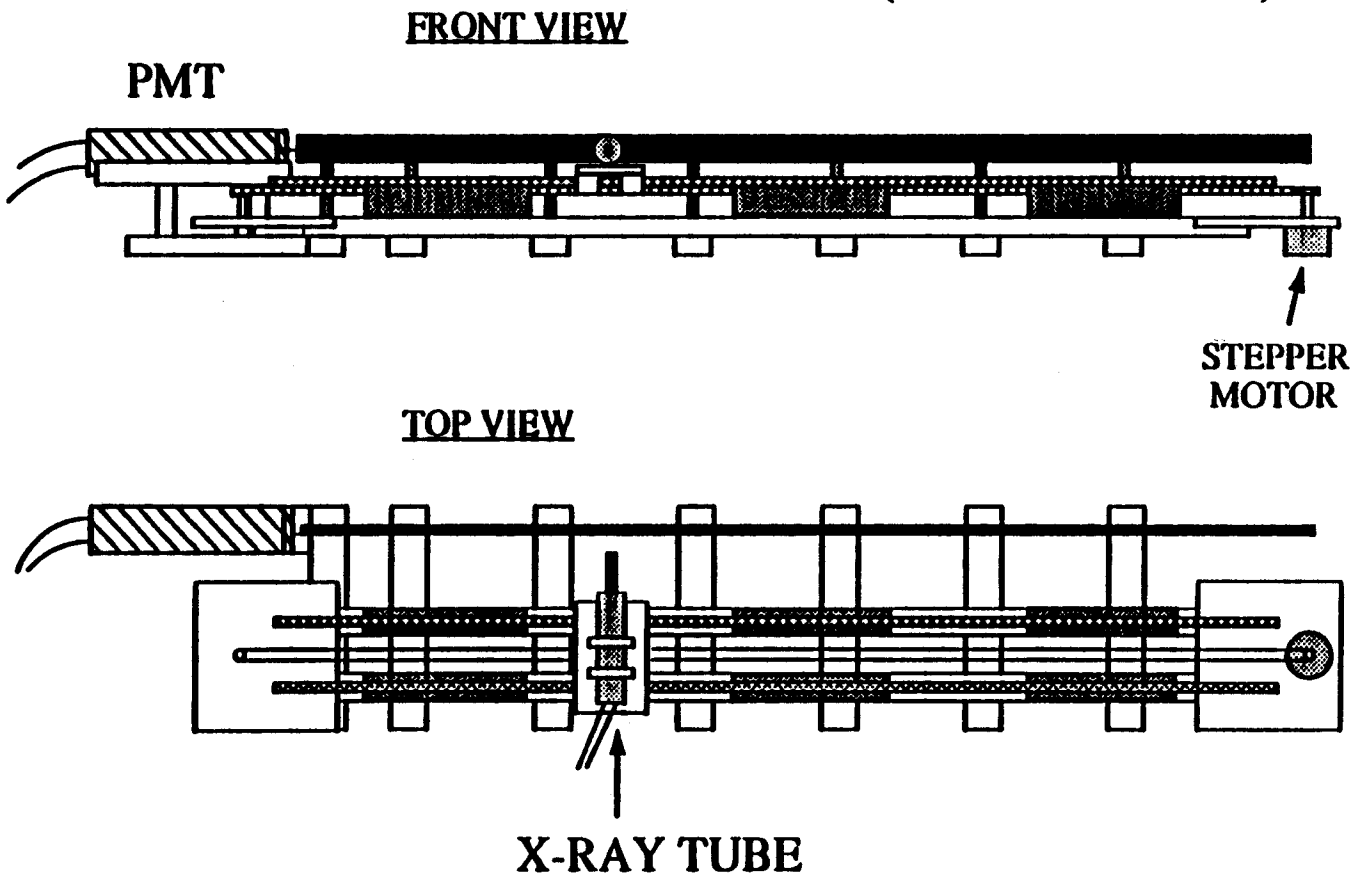

Figure 3: Schematic of the PC-controlled scanner used in measuring the attenuation curves for the fiber sample set.

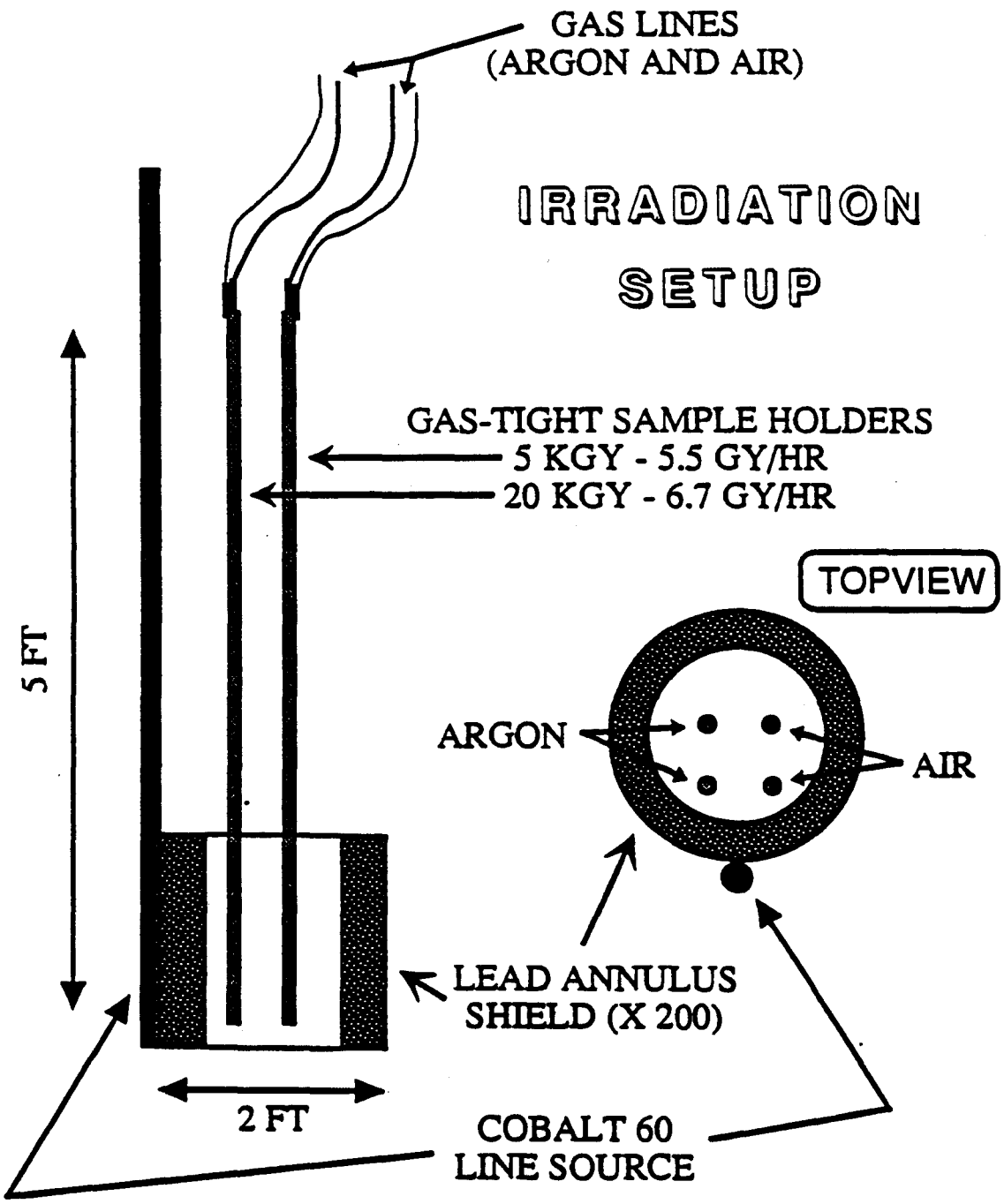

Figure 4: Schematic of the irradiation setup for the low dose rate irradiation.

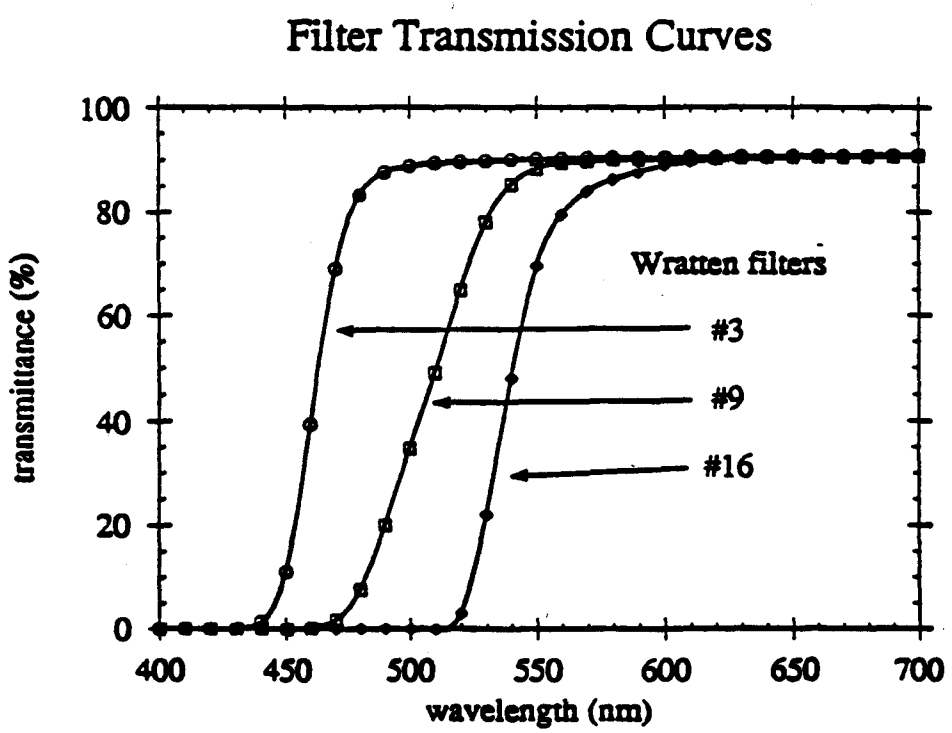

Figure 5: Transmission spectra for optical filters. Wratten #3 was used for the blue-emitting fibers while #9 and #16 were for the green-emitting fibers SCSF-Y8, -Y8C and 3HF.

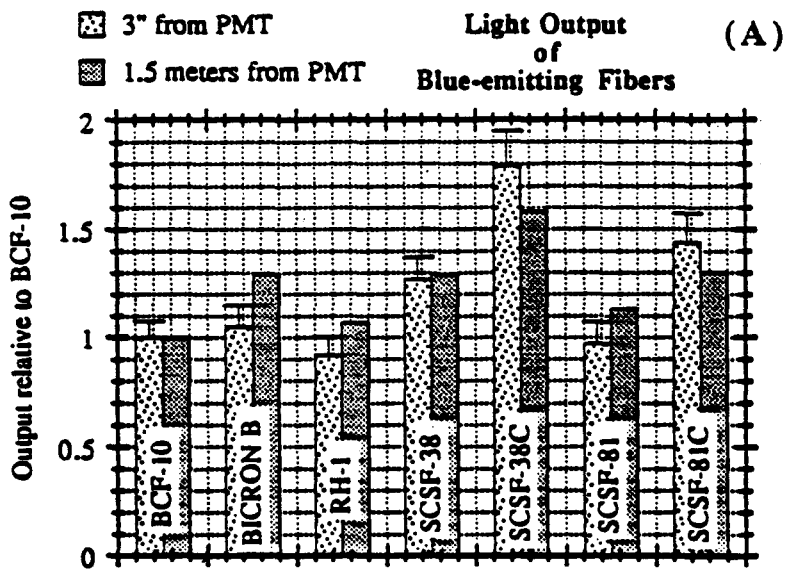

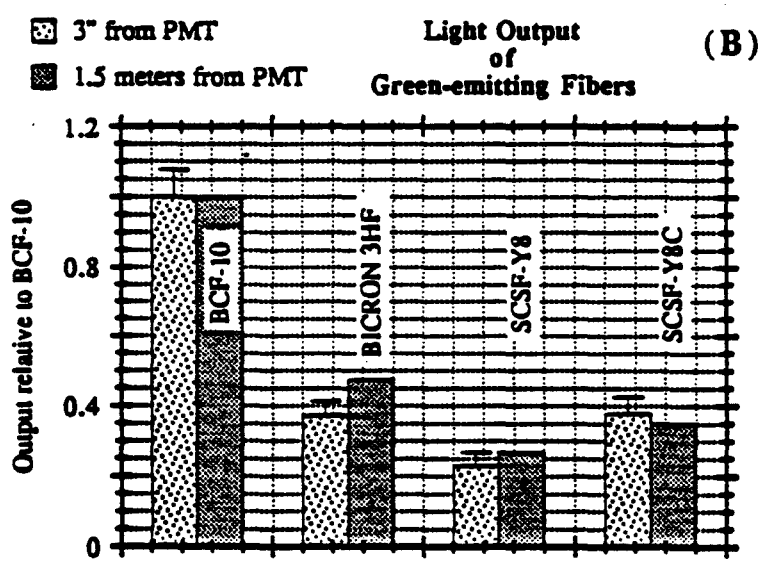

Figure 6: Relative light output of fibers as measured with a bialkali phototube. BCF-10 is used as the standard. The second set of columns show the light output after 1.5 m of attenuation with BCF-10 at 1.5 m used as the reference output.

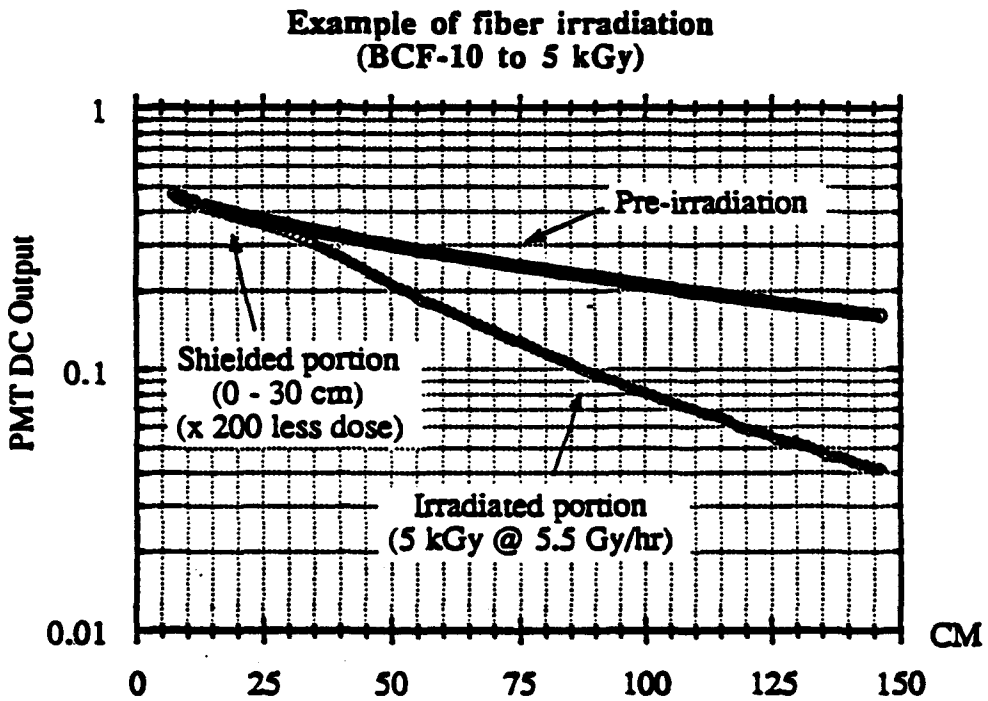

Figure 7: Example of typical data from the low dose rate irradiation experiment. Functional fits were made to function $y = a_1 * \exp(-x/\lambda_1) + a_2 * \exp(-x/\lambda_2)$ to quantitatively describe the data.-

Figure 8(a): BCF-10 5 kGy

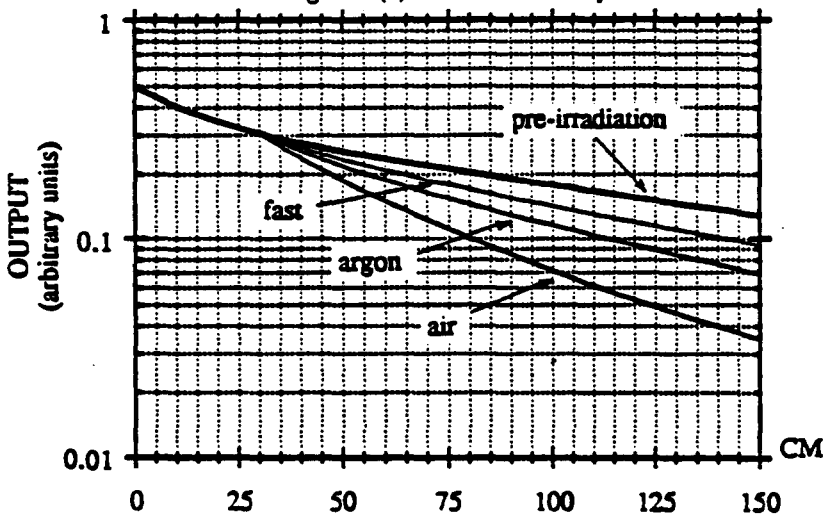

Figure 8(b): BCF-10 20 kGy

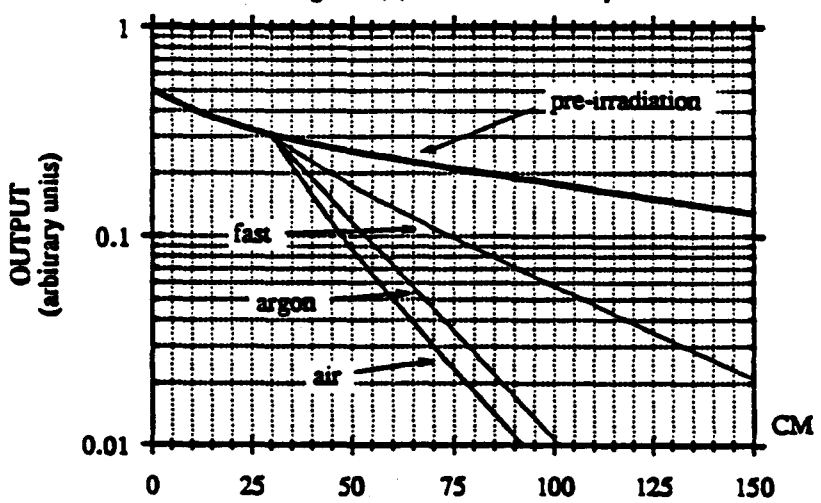

Figure 8(c): Bicron B 5 kGy

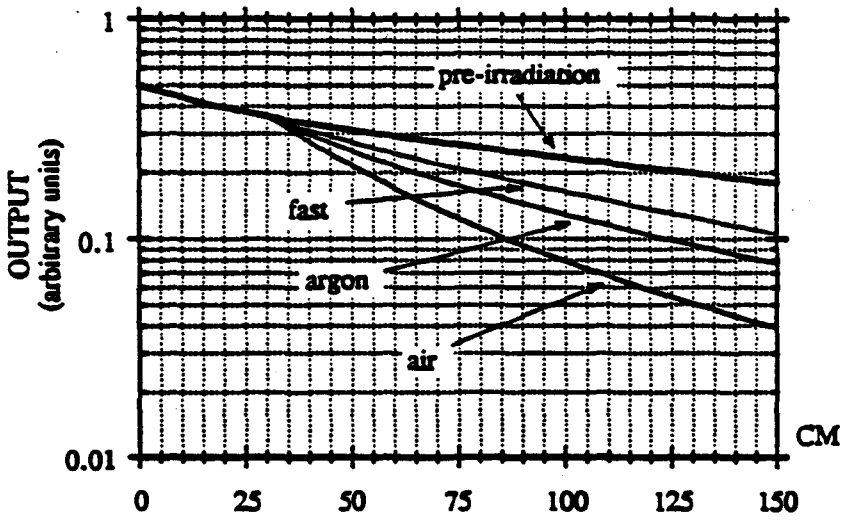

Figure 8(d): Bicron B 20 kGy

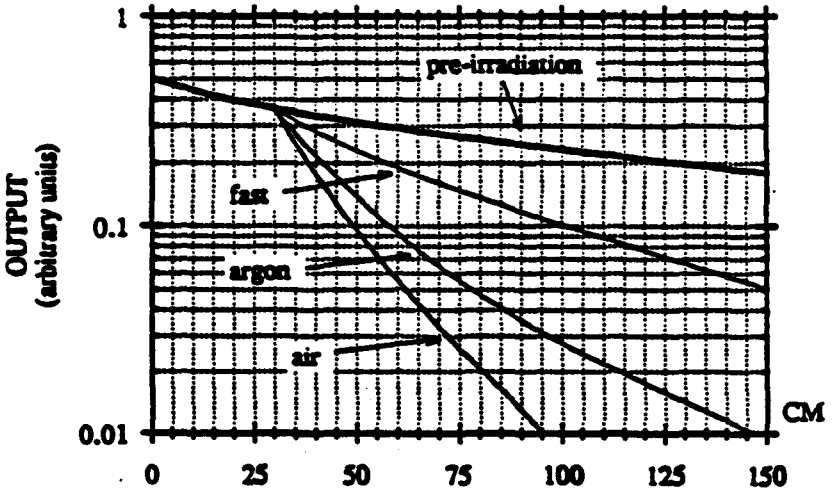

Figure 8(e): Bicron RH-1 5 kGy

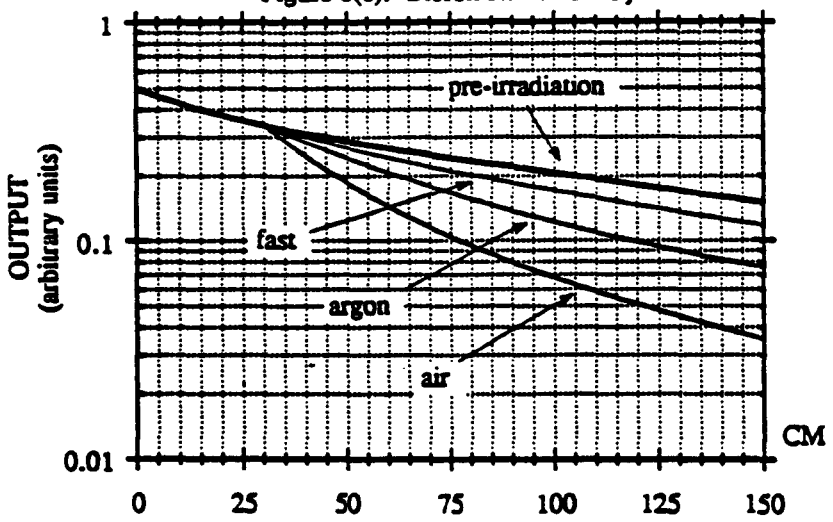

Figure 8(f): Bicron RH-1 20 kGy

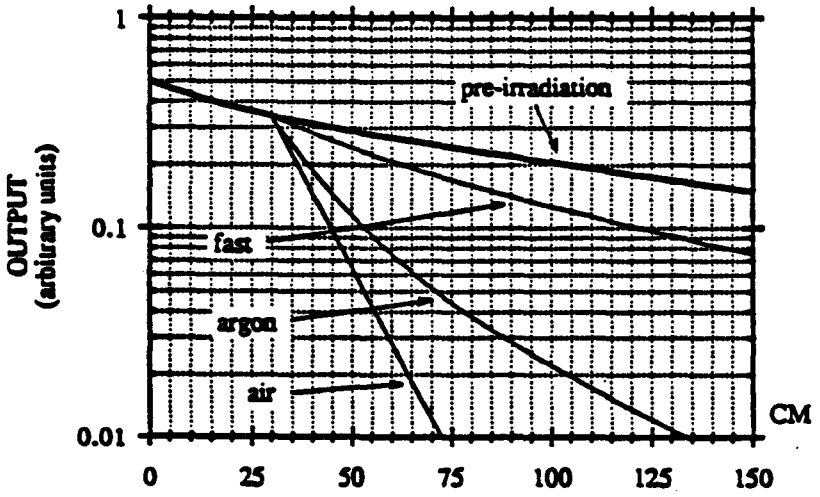

Figure 8(g): SCSF-38 5 kGy

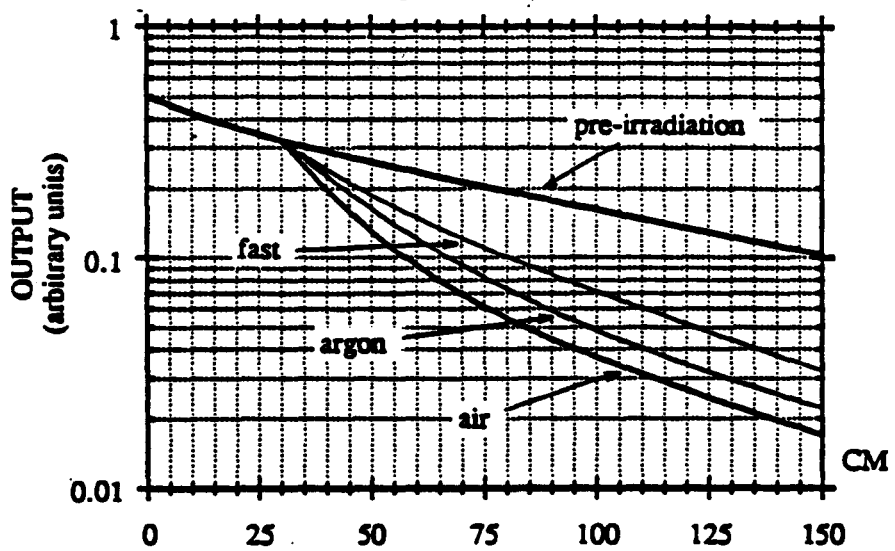

Figure 8(h): SCSF-38 20 kGy

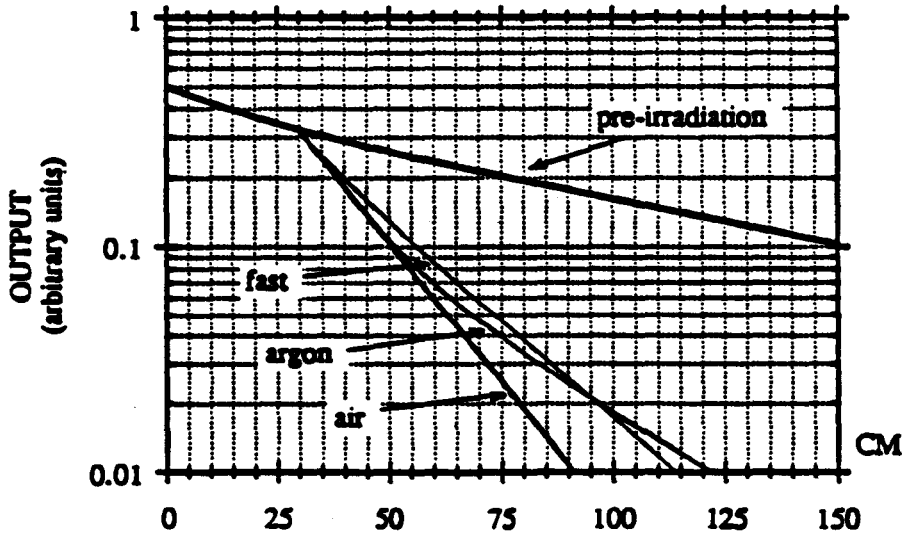

Figure 8(i): SCSF-81 5 kGy

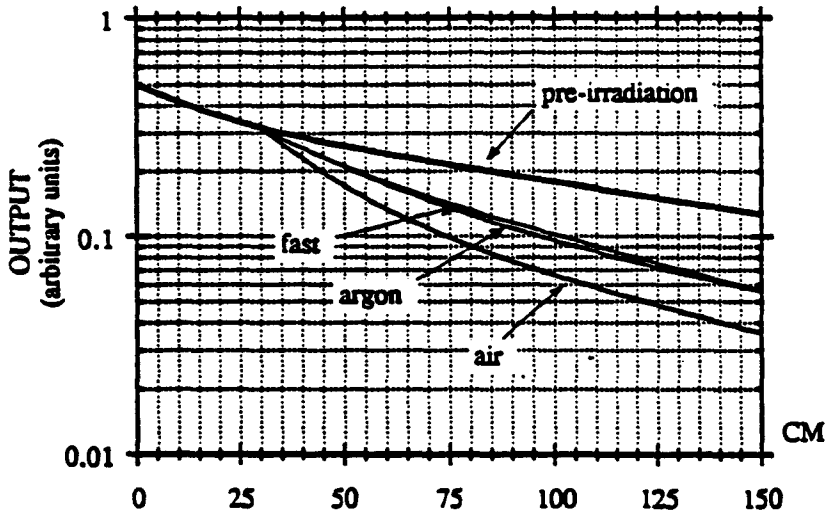

Figure 8(j): SCSF-81 20 kGy

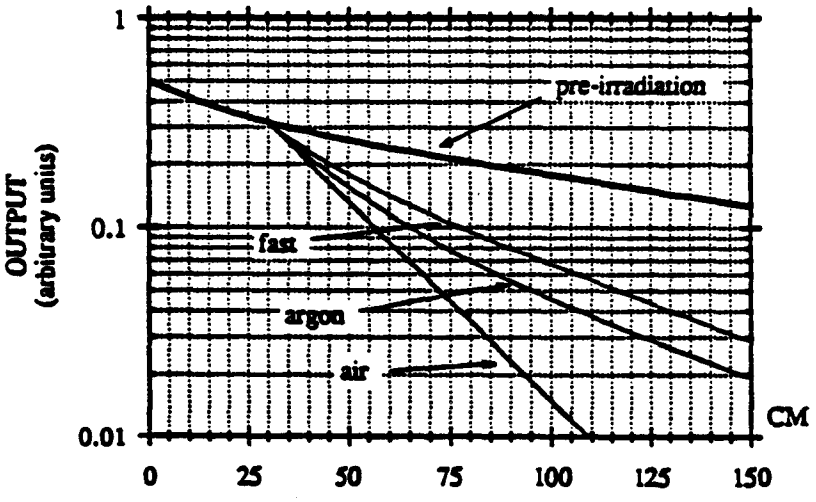

Figure 8(k): SCSF-38C 5 kGy

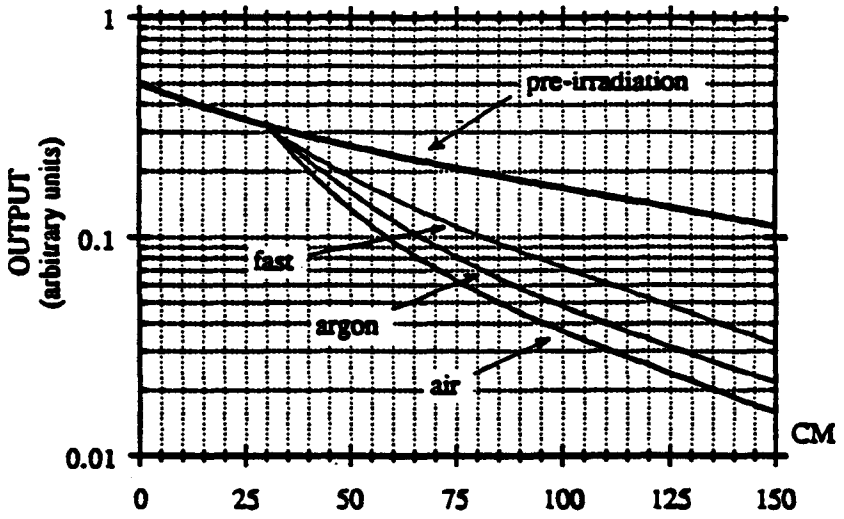

Figure 8(l): SCSF-38C 20 kGy

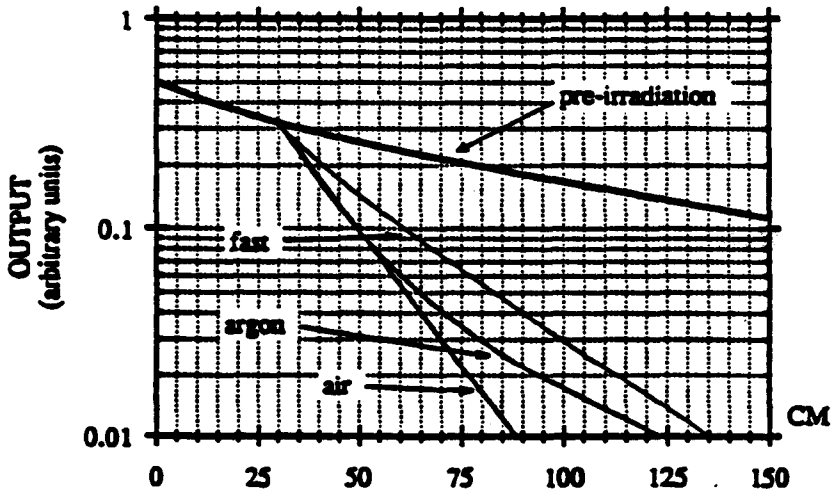

Figure 8(m): SCSF-81C 5 kGy

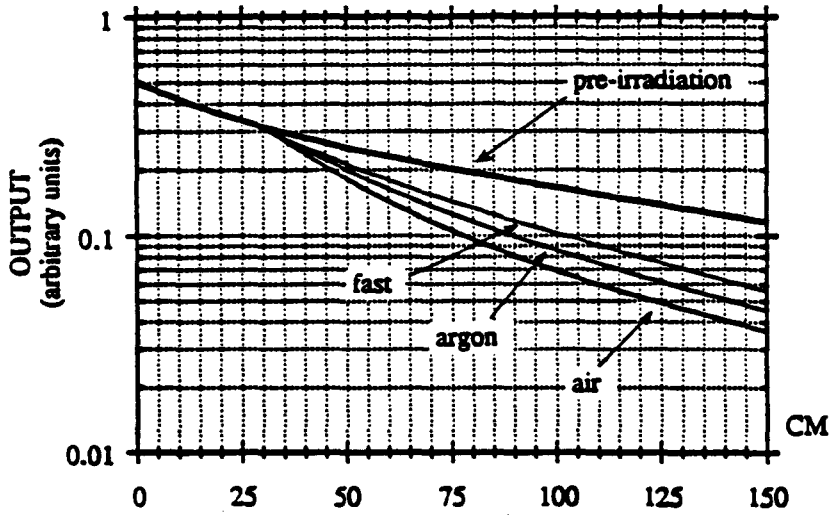

Figure 8(n): SCSF-81C 20 kGy

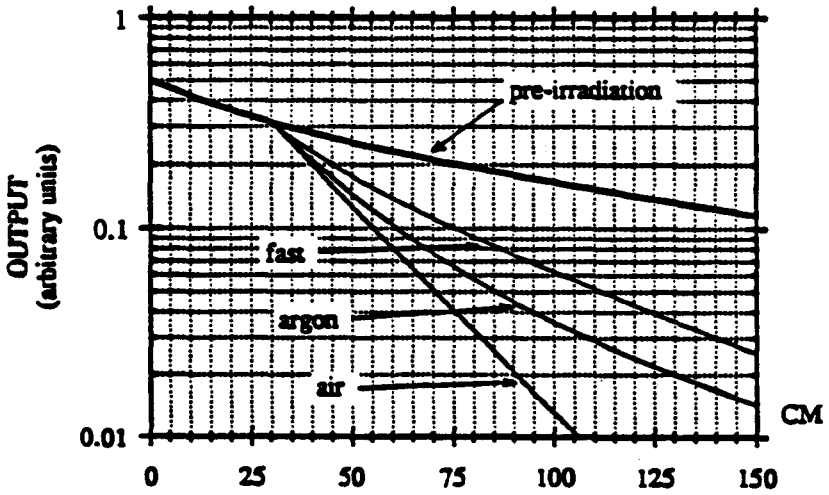

Figure 8(o): Bicron 3HF 5 kGy

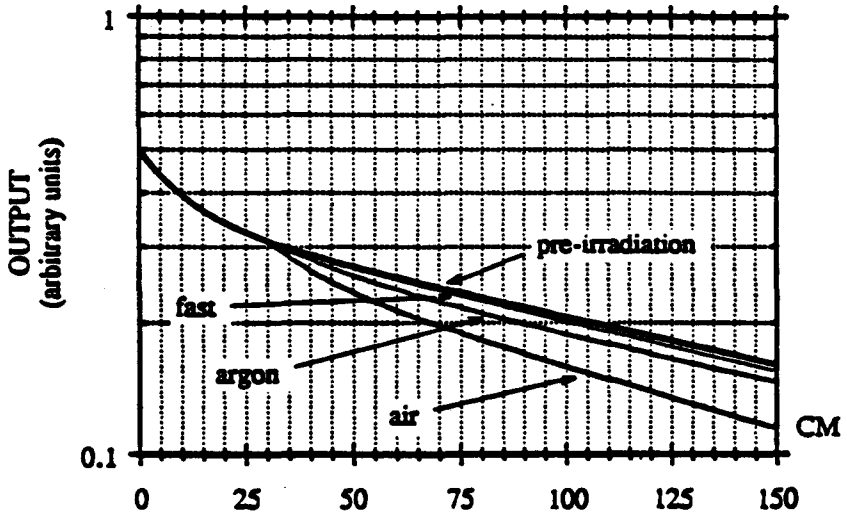

Figure 8(p): Bicron 3HF 20 kGy

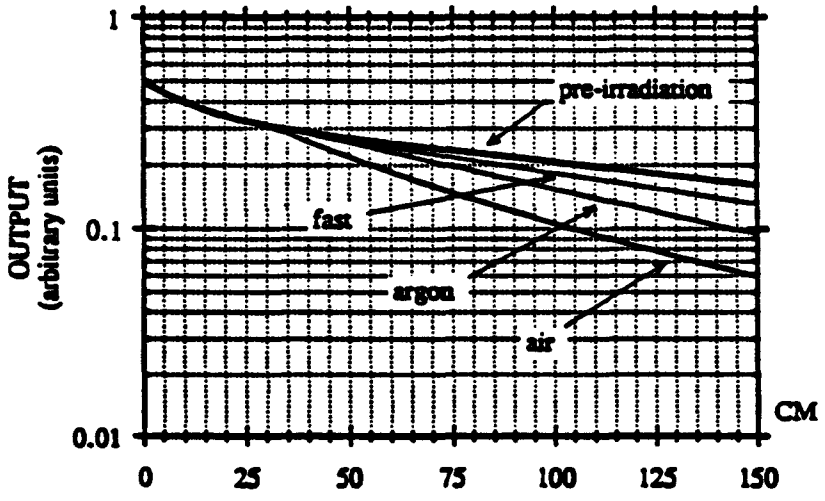

Figure 8(q): SCSF-Y8 5 kGy

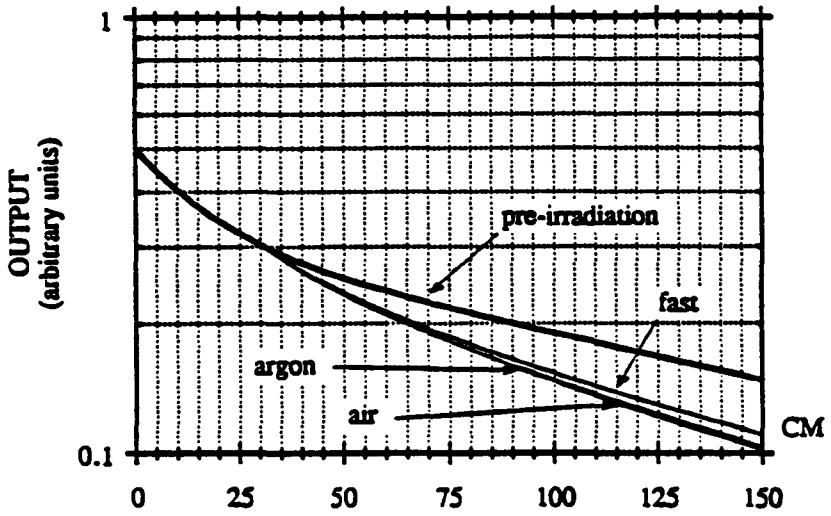

Figure 8(r): SCSF-Y8 20 kGy

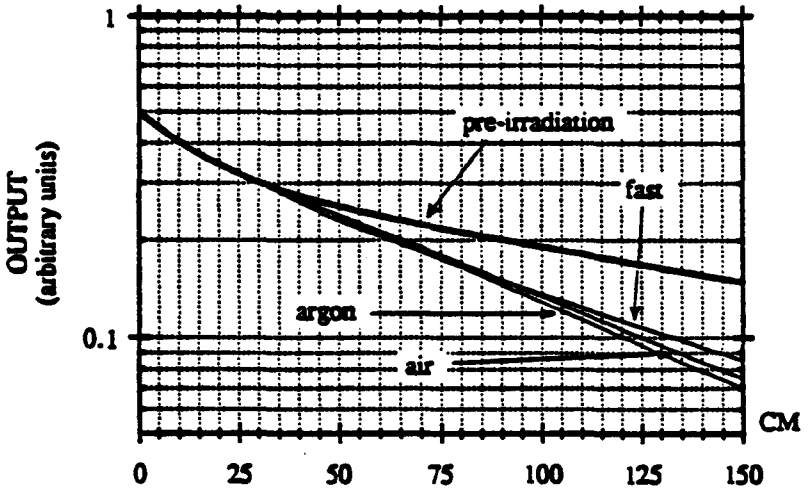

Figure 8(s): SCSF-Y8C 5 kGy

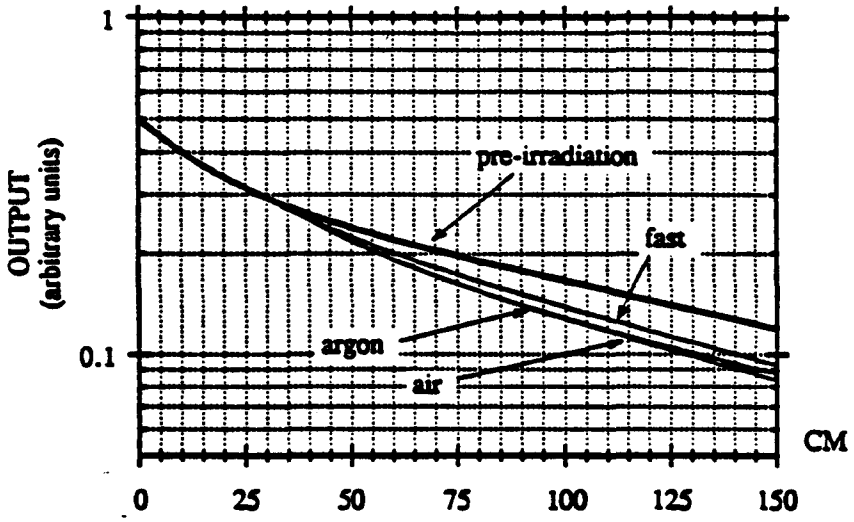

Figure 8(t): SCSF-Y8C 20 kGy

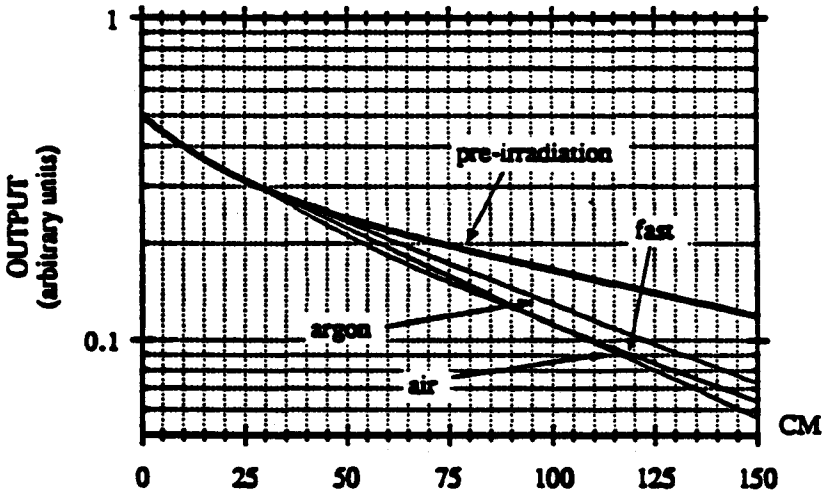

Figure 9(a)
BCF-10 5 kGy Wratten #3

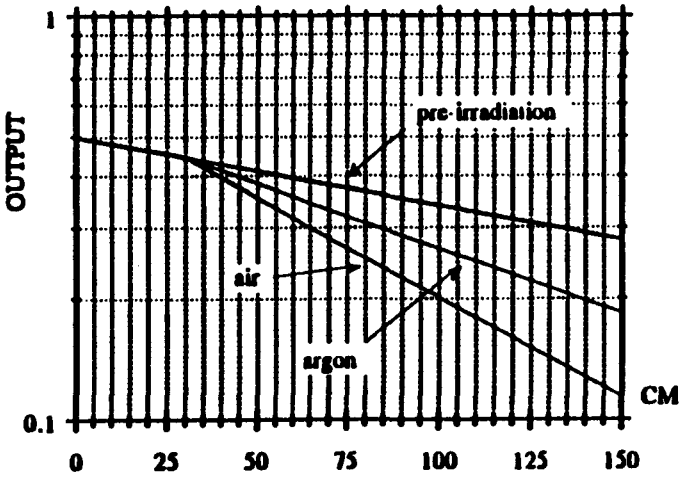

Figure 9(b)
Bicron B 5 kGy Wratten #3

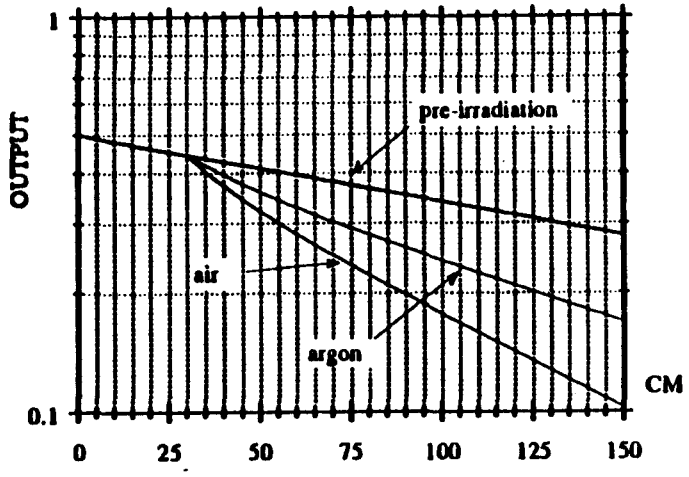

Figure 9(c)
Bicron RH-1 5 kGy Wratten #3

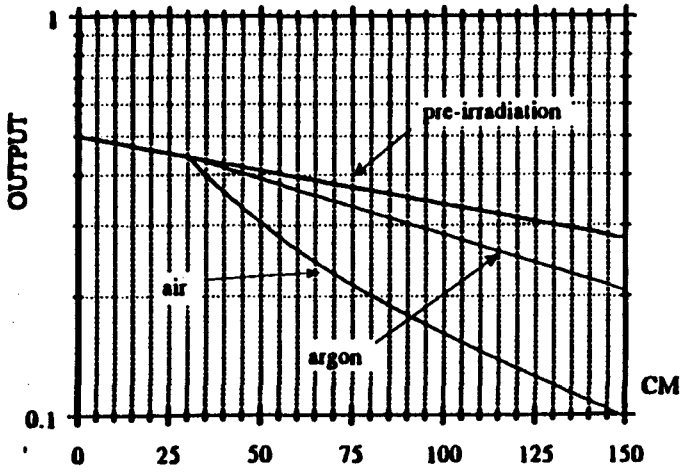

Figure 9(d)
SCSF-38 5 kGy Wratten #3

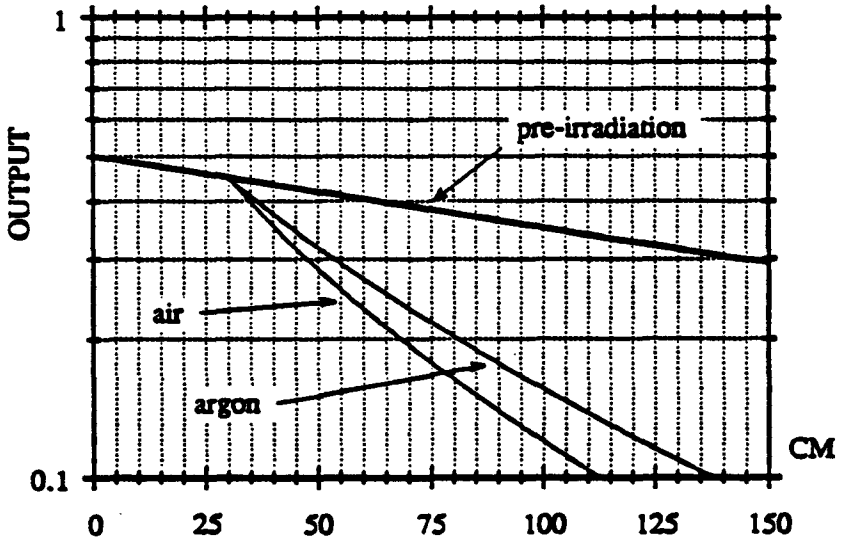

Figure 9(e)
SCSF-81 5 kGy Wratten #3

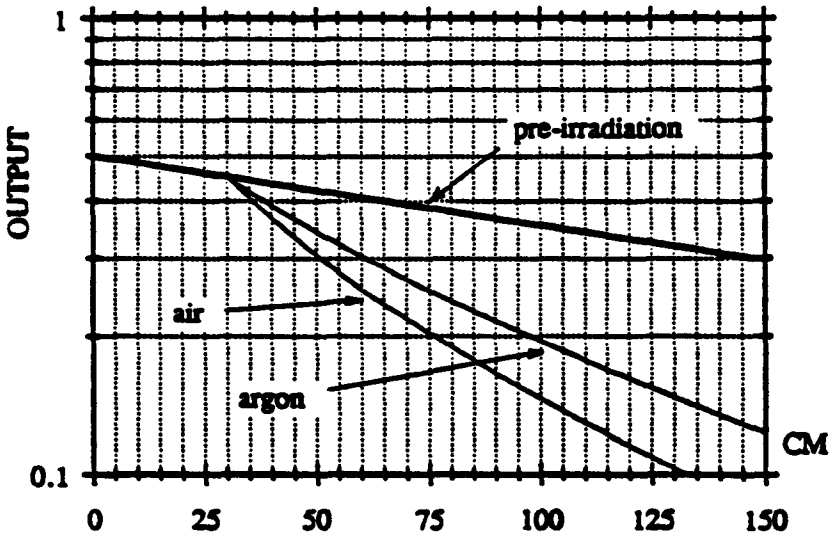

Figure 9(f)
SCSF-38C 5 kGy Wratten #3

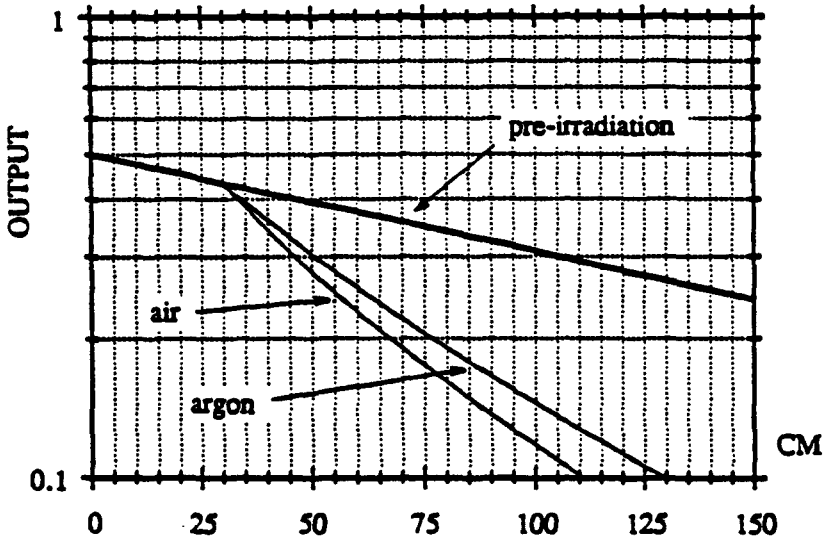

Figure 9(g)
SCSF-81C 5 kGy Wratten #3

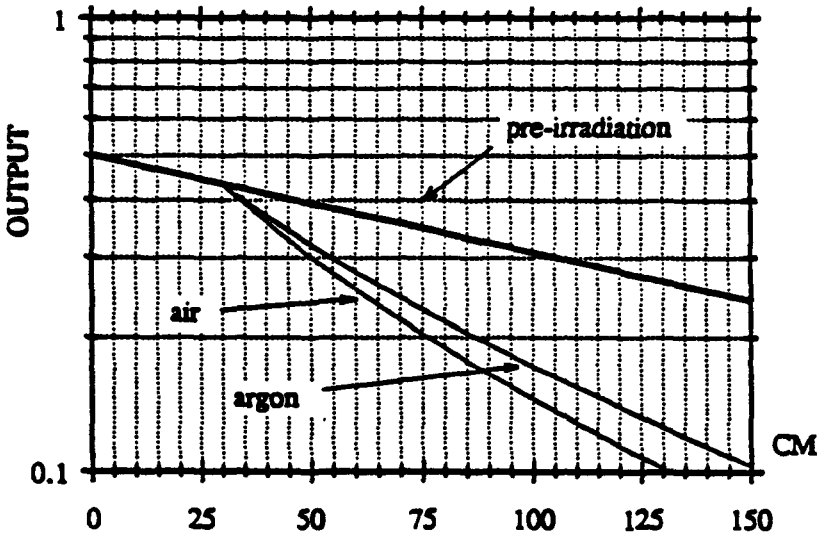

Figure 9(h)
Bicron 3HF 5 kGy Wratten #9

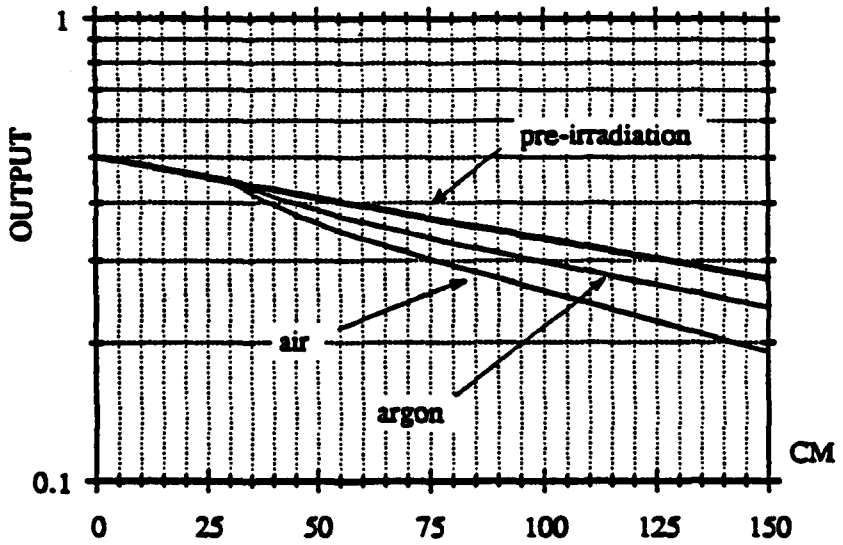

Figure 9(i)
Bicron 3HF 5 kGy Wratten #16

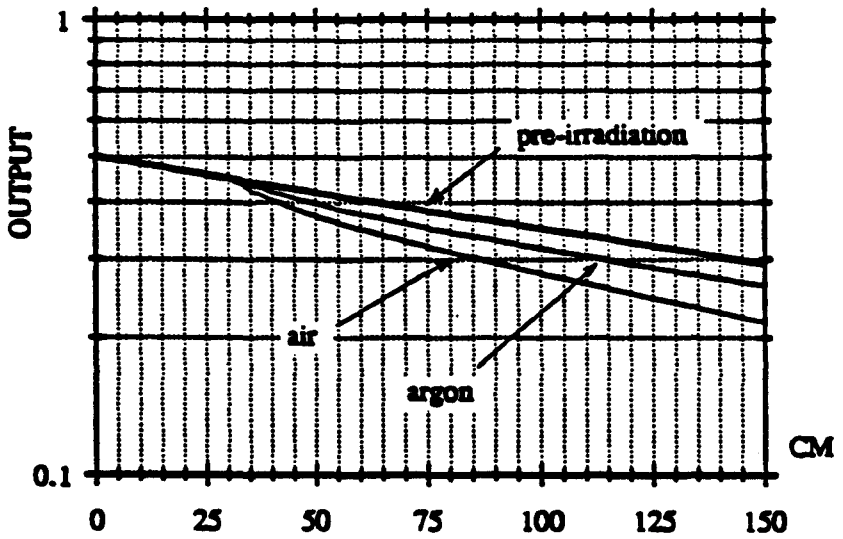

Figure 9(j)
SCSF-Y8 5 kGy Wratten #9

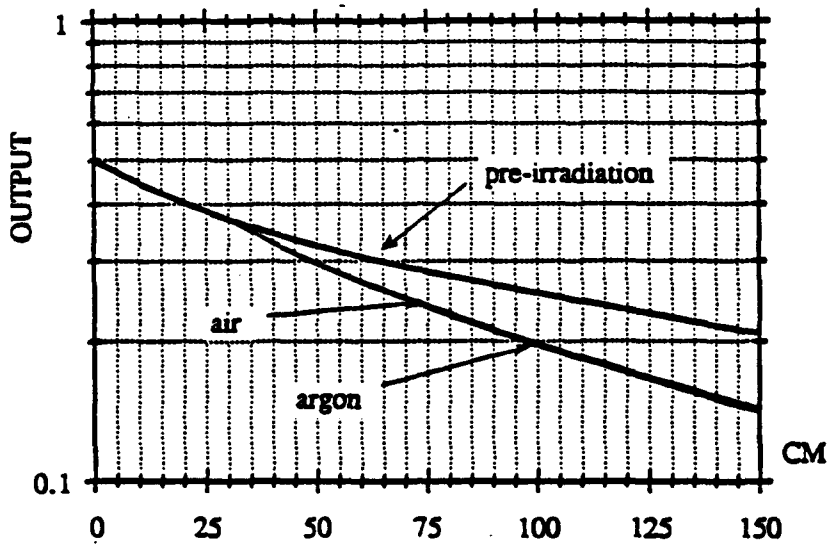

Figure 9(k)
SCSF-Y8 5 kGy Wratten #16

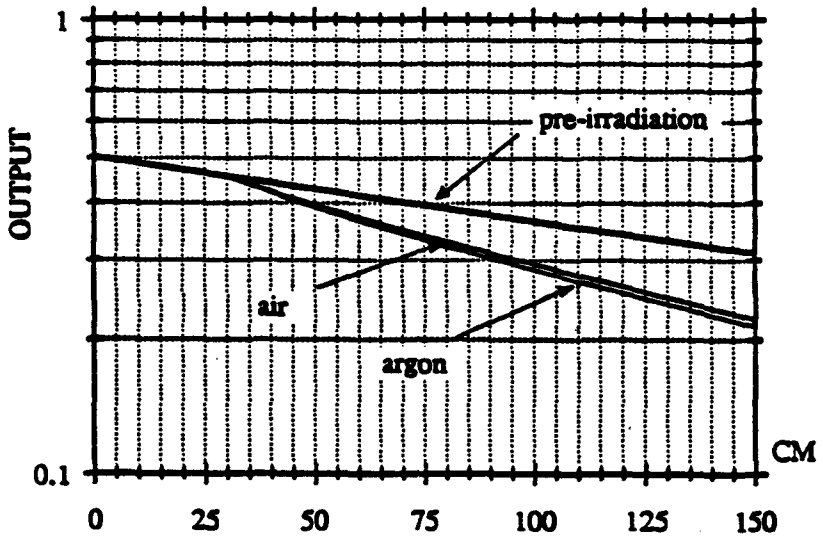

Figure 9(l)
SCSF-Y8C 5 kGy Wratten #9

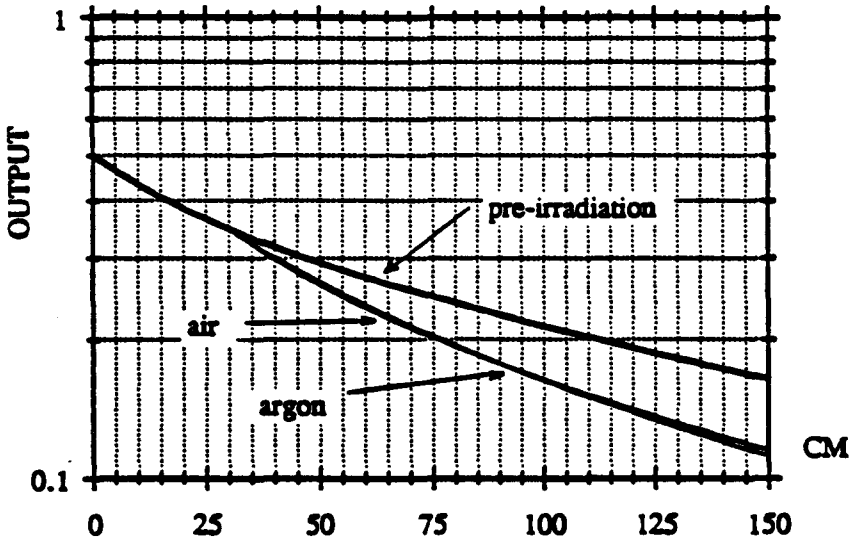

Figure 9(m)
SCSF-Y8C 5 kGy Wratten #16

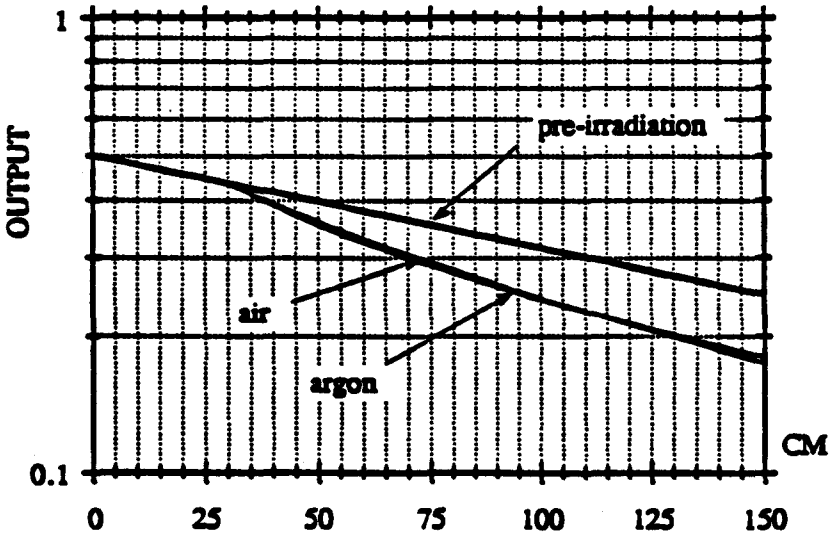

Hybrid Subsystem Progress Report for FY1991

Straw Tube and Straw Tube Superlayer Studies

Duke University
A.T. Goshaw
S. H. Oh
J.D. Simpkins
W.J. Robertson
M. Yin

September 1991

1.0 Research and Development of Straw Tube Drift Chambers

During FY90 we constructed a 2.7 meter long straw tube superlayer consisting of 60 channels of straw tube drift cells. The straw tubes have a 2 mm radius and are stacked in a pyramid with 8 tube layers. There are two wire supports inside each tube for electrostatic stability. During FY91, 28 tubes out of 60 in the superlayer have been instrumented with electronics for measurement of resolution, gas gain, and attenuation length. There have been two publications in Nuclear Instruments and Methods related to this work. The publications are included at the end of this progress report.

This 2.7m prototype has been used for a variety of studies. First, it was used to demonstrate that long tubes can be placed on a surface to an accuracy of better than 100 microns. Second, we have shown that the sense wire can be supported with proper wire supports inside a long straw tube. Our earlier studies have shown that for 50 gram tension in the wire, a wire support is required about every meter. Third, we have verified that a sense wire can be threaded through a straw tube with wire supports in place. Fourth, we have demonstrated that a chamber with a large number of straws can be made operational without difficulty.

The detailed method used to construct the chamber is presented in the NIM articles enclosed so it will not be repeated here. During the construction many original ideas were implemented, such as a wire-support design, an end-plate design, and a mid-termination design. Mid-termination is necessary if wires are to be read out from both ends as in our present outer tracker design for SDC.

Presently we are constructing a straw tube module. This module is different from the one being developed at the University of Indiana and Colorado. Unlike their module, ours does not require an outer shell. By not having a shell, the material in the chambers is reduced by over 35%, and cost is less because an expensive outer shell is not required. Also an outer shell could have structural changes over a long period, which might result in sense wire mislocation. Another advantage of the shell-less module is the flexibility of the module. Since a module is flexible, it can be aligned to a great accuracy when the module is placed on the cylindrical base. The detailed method of construction of the shell-less module is given in Section 1.5.2.

Another area of study at Duke is construction and operation of 7 meter long straw tube drift cells. A 7 meter long cell is necessary if we want to construct the SDC barrel chamber using one of our schemes which calls for laying single straws on a cylindrical base. Presently we have several working 7 meter long cells under high voltage. Preliminary tests of these cells are presented in Section 1.6.

1.1 Attenuation Length Measurement (2.7 meter long straw tubes)

The attenuation length is measured using an Fe55 source. Because of the gain variation near the straw tube joints, the peak of the signal is measured from both ends of the chamber. From the ratio of the two peaks as a function of distance from one end, the attenuation shown in Figure 1.1 is calculated. An attenuation length of about 500 cm is measured.

1.2 Resolution Measurement

Twenty eight channels of the 2.7m straw tube superlayer have been instrumented for a resolution measurement. The sense wires are connected to Lecroy 2735 amplifier-discriminators. The discriminated output is connected to a Lecroy TDC's (2282). Using cosmic rays, the resolution of the chamber is measured. In Figure 1.2, the residuals are plotted. The residuals are calculated using tracks with six or more hits. By fitting the curve with a gaussian, a resolution of 120-130 microns is obtained. A 50-50 mixture of CF4 and ethane is used for the chamber gas. The average electron drift velocity in the gas is about 90 microns/ns.

The intrinsic resolution of the chamber should be much less than the 120-130 microns, since the resolution includes the timing uncertainty in the amplifier-discriminator and in the electronics. The resolution is also measured as a function of the high voltage and shown in Figure 1.3. There is little change in the resolution after the high voltage reaches about 2100 volts.

1.3 Test of the 2.7m Prototype in a Simulated SSC Environment

Using five 10 milicurie Sr90 radioactive sources, the SSC environment can be simulated. The sources are placed in front of the chamber such that the count rate from each cell is between 1 to 2 MHz and the current draw is about 5 micro-amp per cell. Under these conditions, the resolution of the chamber is obtained using cosmic

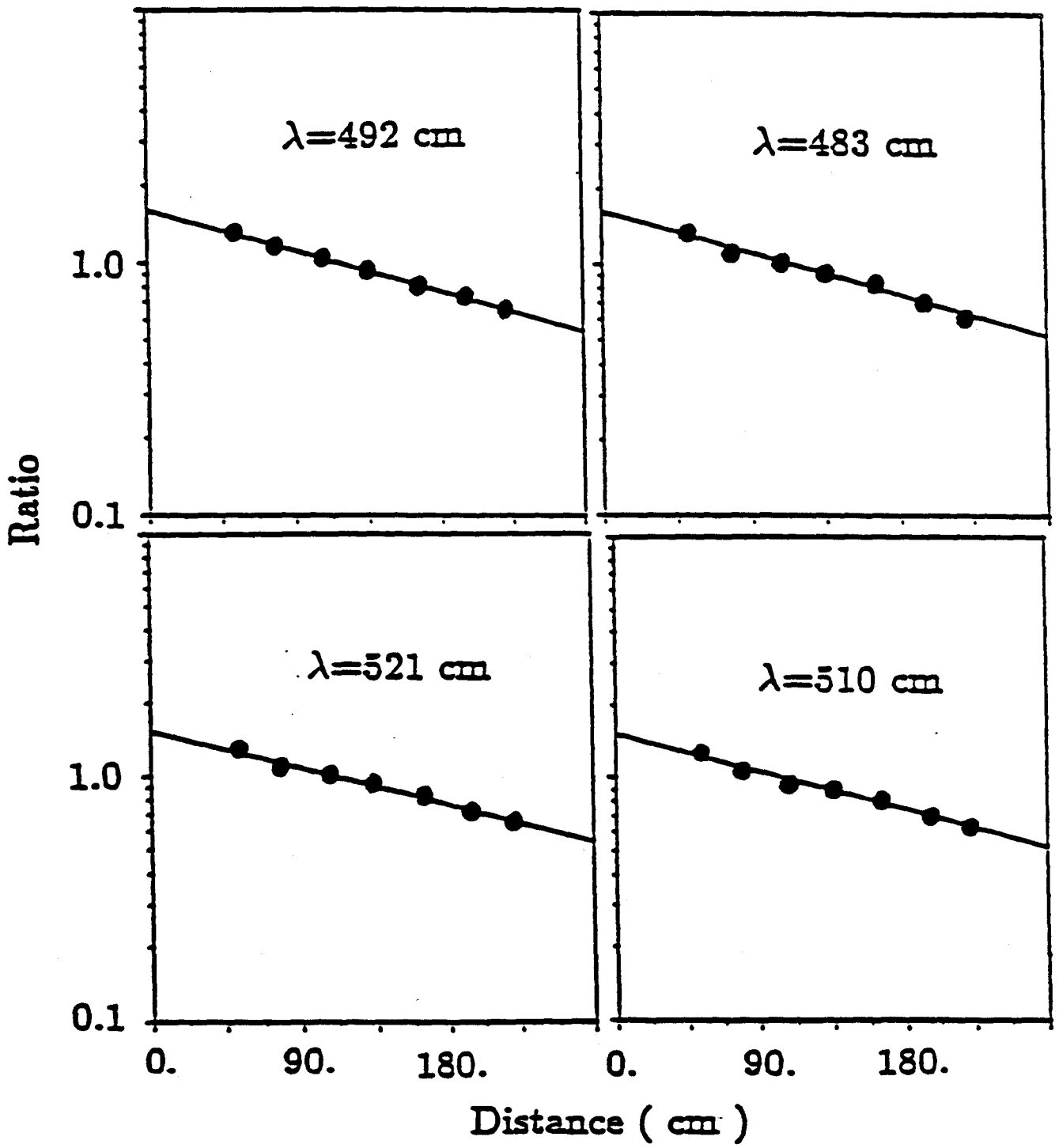

Fig. 1.1 Measurement of signal attenuation in 4 typical straw tubes with 4mm diameter.

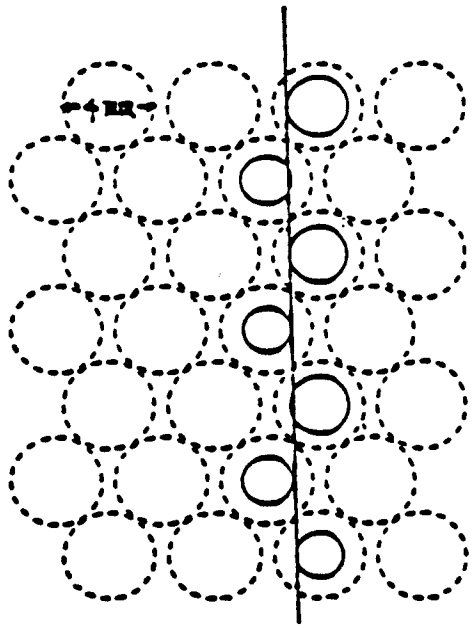

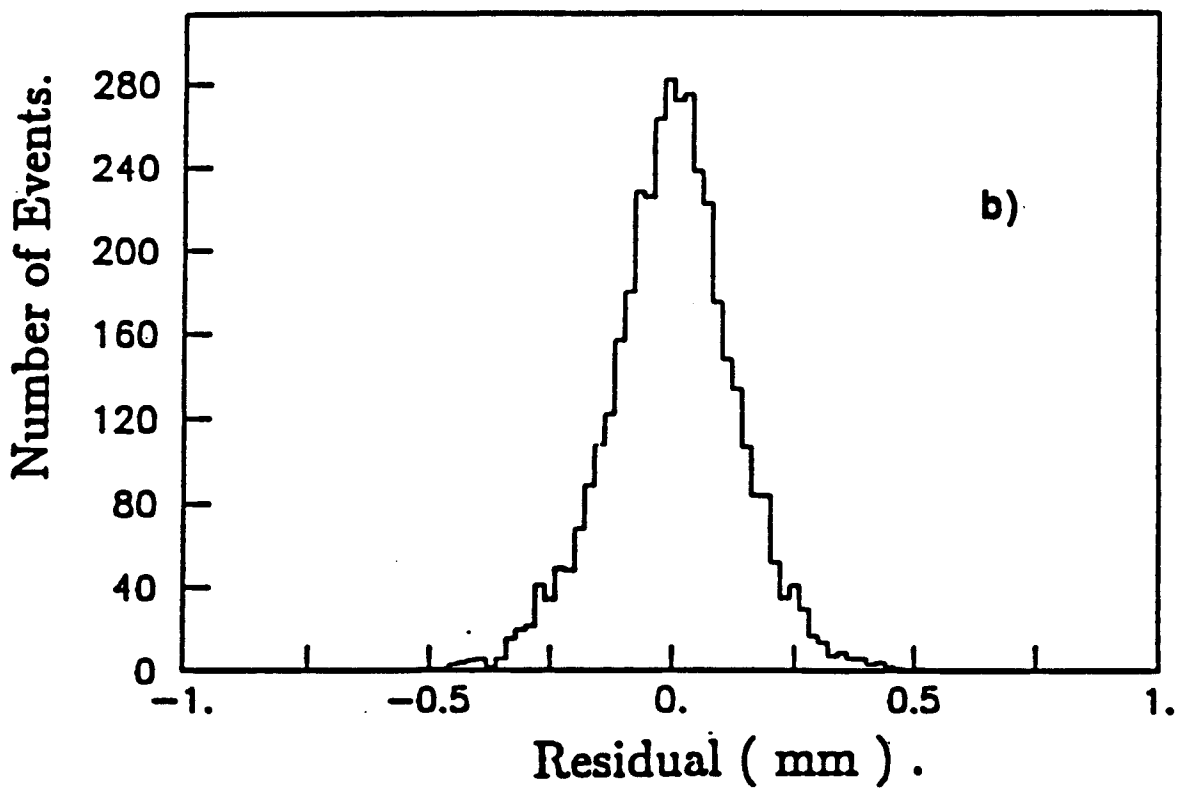

Fig. 1.2 a) A triggered cosmic ray track traversing the superlayer.
b) Resolution measured from cosmic ray track residuals.

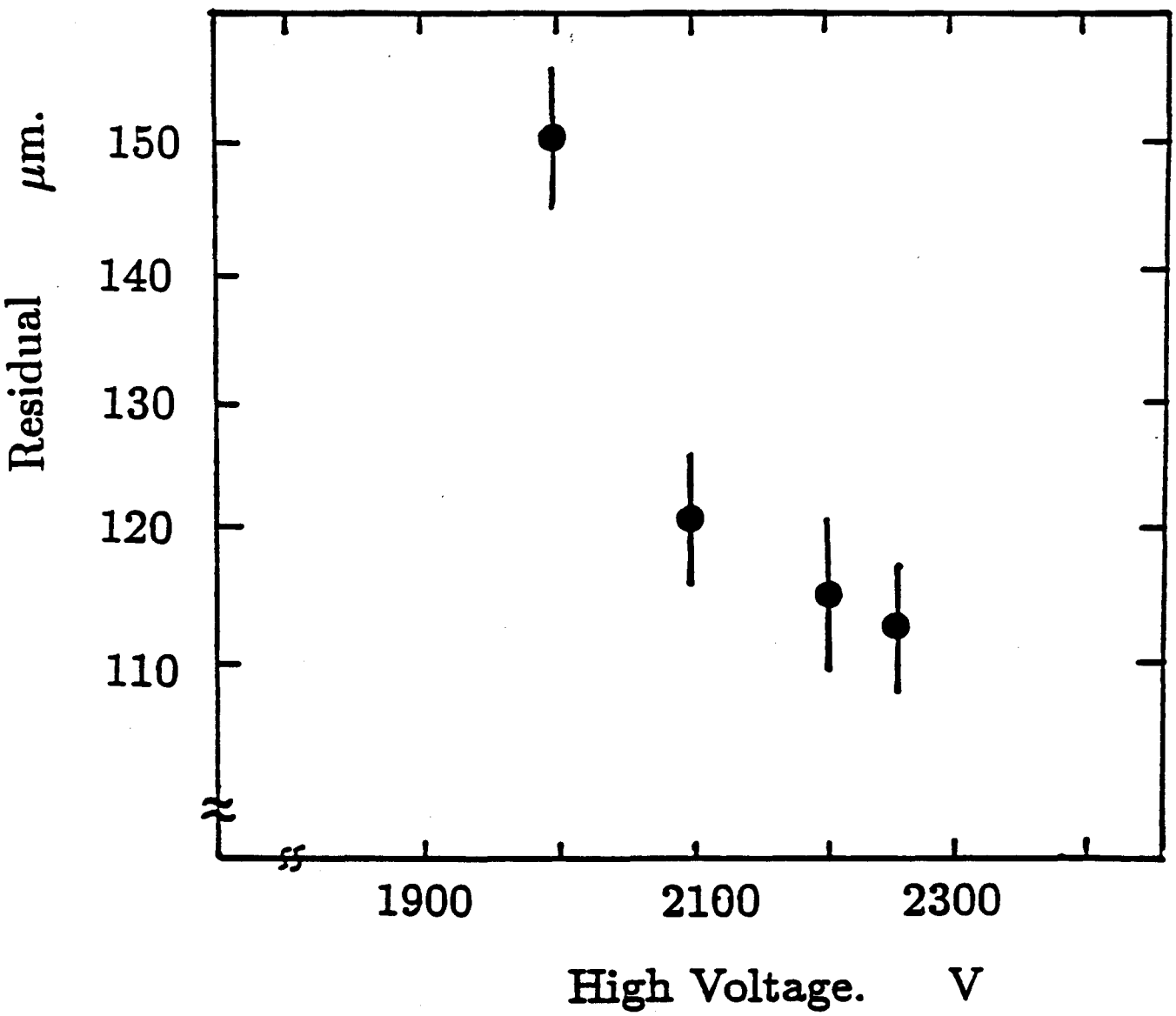

Fig. 1.3 Straw tube resolution versus high voltage.

tracks The results are shown in Figure 1.4. Compared to the measurement without the sources (Figure 1.2) there is almost no change in the resolution of the chamber.

1.4 KEK Time Memory Chip Test

The 2.7m chamber has been also used to test TDC's developed at KEK for the SDC straw tube tracker. The TDC based on the time memory chip (TMC) is replaced by the LeCroy TDC's and the resolution is remeasured. In Figure 1.5, the residual plots using LeCroy TDC's (with 100 ps least count) and KEK TMC's (with 1 ns least count) are shown. The difference between the resolutions can be explained by the difference in the least count of the two TDC's.

In the near future, the LeCroy amplifier-discriminators will be replaced with a prototype amplifier-discriminator for the SSC developed at the University of Pennsylvania. Presently a gas gain of close to 10**5 is necessary to obtain a good efficiency and resolution. This is because the gain of the LeCroy amplifier-discriminator is not high enough. Using the new amplifier-discriminator, we hope to operate the chamber with a gas gain less than 2*10**4.

1.5 Prototype SDC Cylindrical Barrel Tracker Construction

According to the SDC construction schedule, a full size prototype superlayer must be constructed in 1992. Presently there are several schemes for construction of the straw part of the tracking chamber. In one scheme the tension of the sense wires is taken up by the cylindrical support base while in the other they are not. In the first scheme, each straw is layered on the cylindrical base and glued to it. Straws are tested with sense wire loaded before placing them on the base (see Section 1.5.1 below).

There are two variations in the second scheme. One of them uses a shell (trapezoid shape) to make a self-sustaining module consisting of about two hundred 4 meter long straws. The shell is necessary because the wires are under tension. A variation of this scheme being developed at Duke does not use the outer shell. Like the module with the shell, about 200 straws are glued in a shape of a trapezoid. In this scheme, sense wires are strung and tensioned for test. For this test, modules are placed on a jig with the sense wires under tension. After the test the tension in the wire is relieved. The tension in the wire has to be relieved since the shell-less module cannot sustain the wire tension. The wire is re-tensioned after the module is

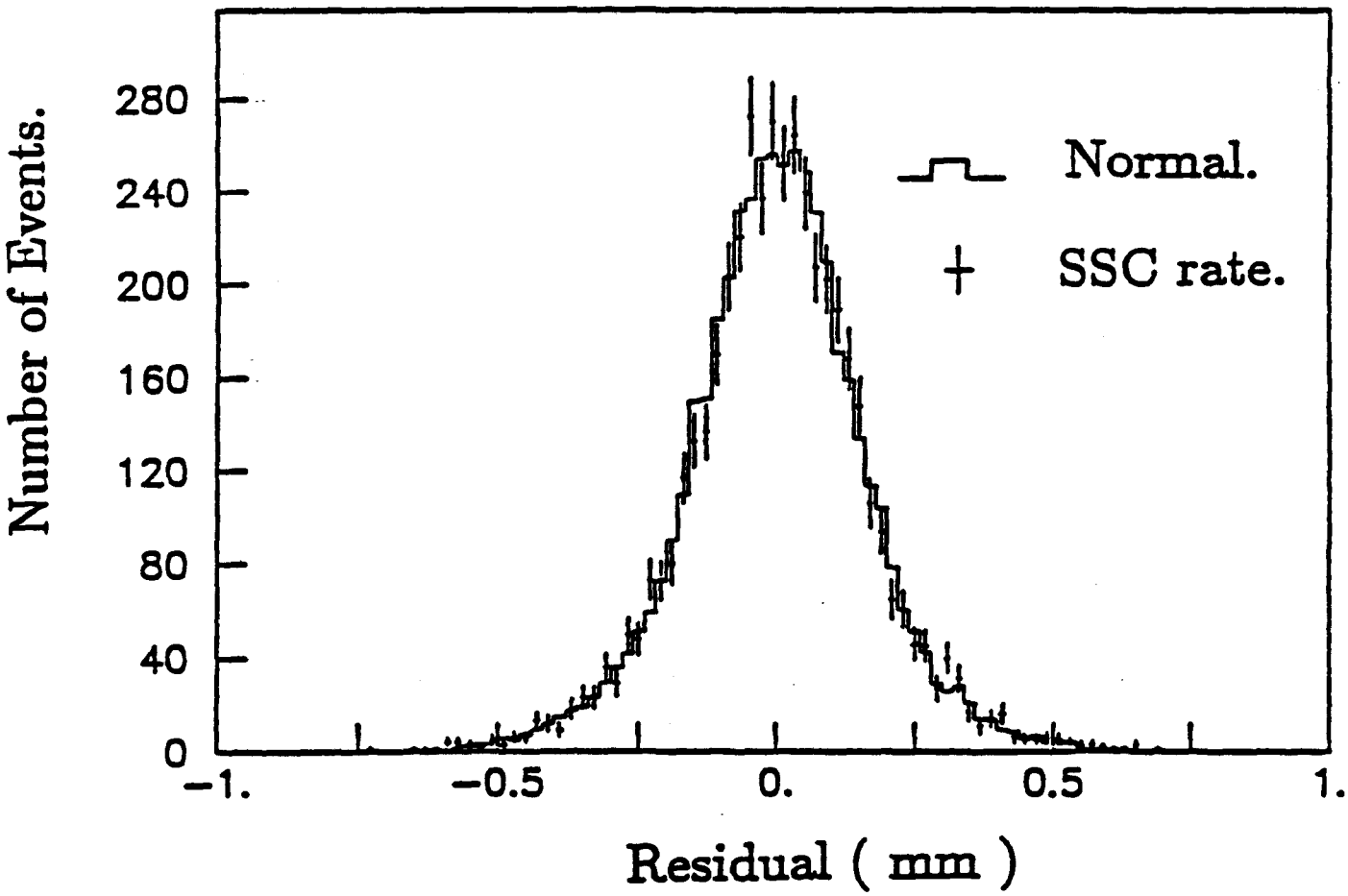

Fig. 1.4 Resolution of a straw tube superlayer under simulated SSC counting rates.

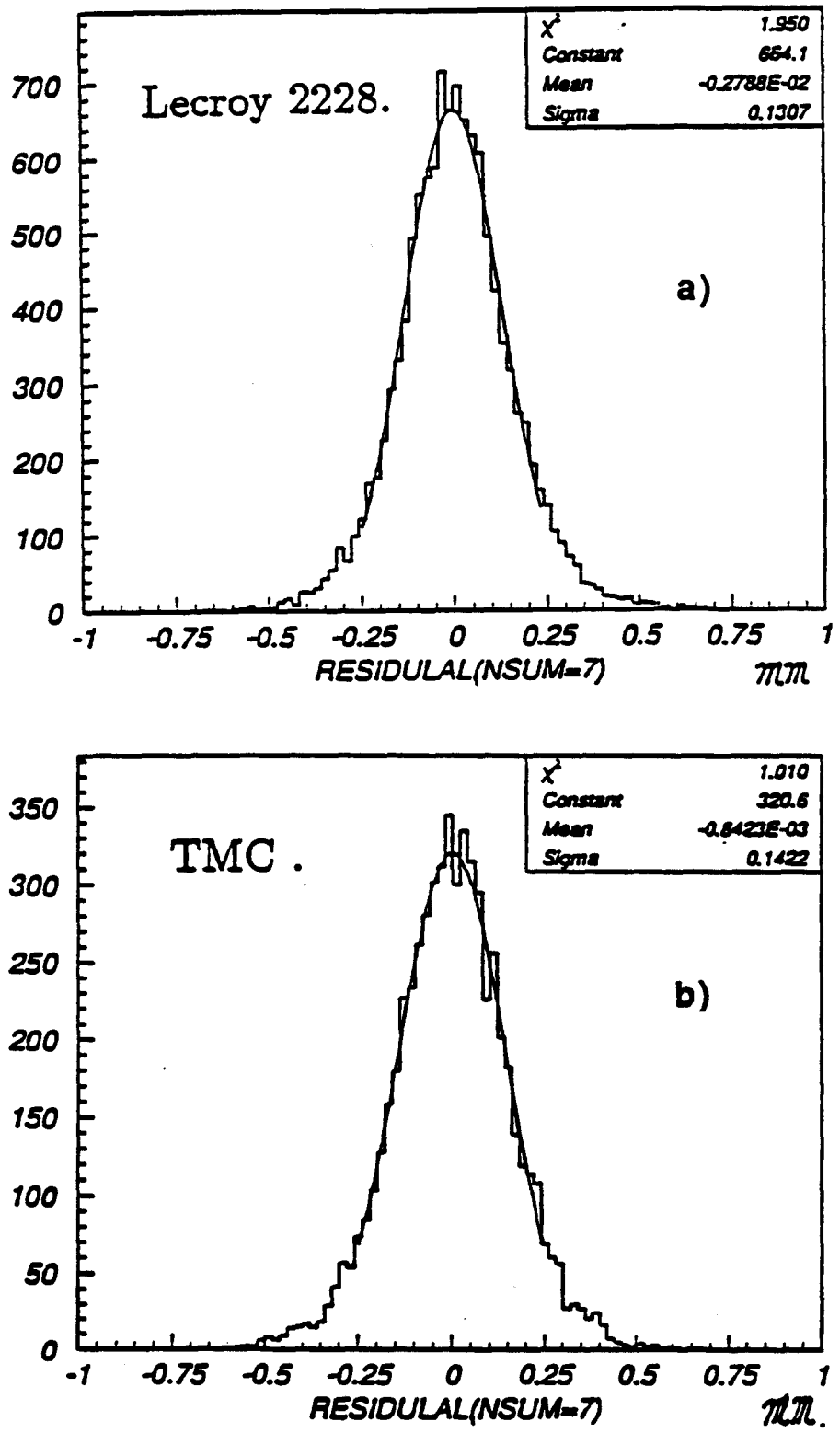

Fig 1.5 Tests of straw tube resolution using different TDC's. a) LeCroy 2228 TDC. b) TDC developed at KEK using a time memory chip (TMC).

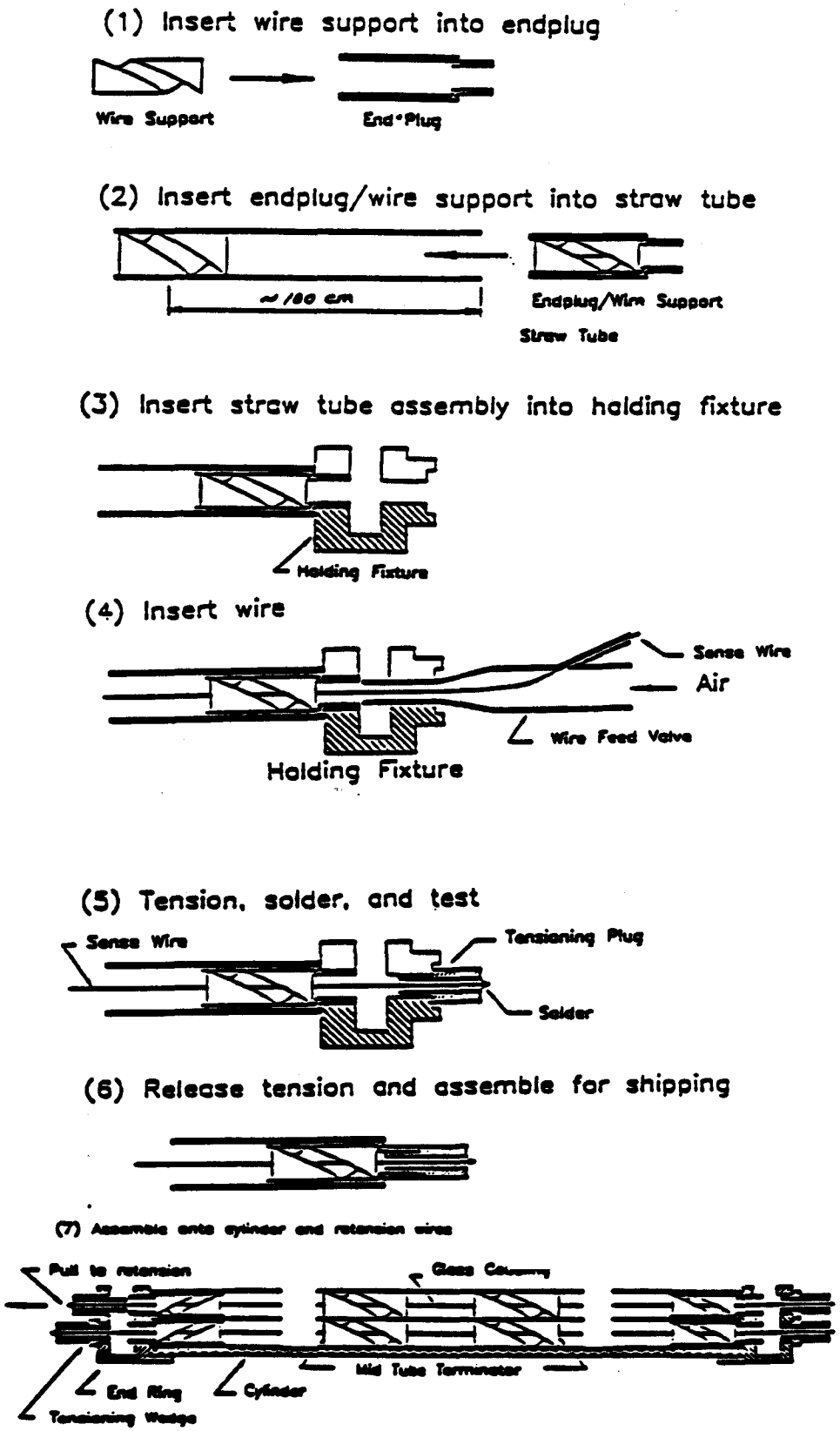

Fig. 1.6 Procedure for assembling and testing individual straw tube drift cells (steps 1 to 6). Step 7 illustrates the subsequent placement of the drift cells on the support cylinder.

placed on the cylinder (see Section 1.5.2 below). As mentioned earlier, this scheme is advantageous since there is less material, less cost and reduced structural complications from an outer shell.

1.5.1 Single Straw Superlayer Construction Scheme

One way to construct the SCD straw chamber is to place straws directly on the cylindrical surface. A procedure for testing straws under tension and relieving the tension in the wire after the test for subsequent steps has been developed at Duke. This procedure is necessary to expedite parallel construction and to reduce the repairs due to defective tubes.

In this approach, tubes with all the necessary components (like wire supports, end-plugs, and mid-terminator) are assembled first. The assembled tubes are placed on a jig to straighten them. There are holding fixtures at both ends to hold the tubes and feed-throughs (Figure 1.6). The wire is blown through, tensioned and soldered (clamped). After the sense wire is strung gas will be introduced into the tube for gas leak, high voltage and source testing.

After selecting good cells, the tension in the wire is relieved by removing the feed-through from the holding fixture and putting it into the end-plug. This is possible since 25 micron diameter tungsten wire stretches about 2.8 mm per meter under 50 grams of tension.

The completely tested straw tube drift cells are placed directly onto the support base cylinder. After they are placed on the cylinder, the wire is re-tensioned by simply moving the feed-through to the end-plate.

This scheme calls for straws as long as the chamber itself (up to 8 meters) and eliminates end-plates in the middle to reduce the material at 90 degrees. To reduce the occupancy, sense wires have to be cut and joined at the middle with an insulating connection. By doing so, signals can be read out from both ends thus reducing the signals rate by half.

Figure 1.7 shows the scheme developed at Duke. The sense wire is cut and joined by a very thin glass tube. Each sense wire is terminated to ground to reduce reflection. Without the terminator the dead time of each cell may be increased. As

shown in Figure 1.8 , the terminator consists of a wire support made of a conductive plastic (about 300 ohm) and a 50 micron mylar tube (forming a capacitor with about 50 pf capacitance). We are in the process of testing this scheme using 7 meter long straw cells.

1.5.2 Shell-less Module

The first step to construct a shell-less module is to make straw ribbons.Ten to twenty straws are lain on an L shaped jig. The length of the jig does not have to span the whole tube length. We found that about a 30 cm length was sufficient. The tubes are pushed slightly against the wall of the jig from one end by a plate as shown in Figure 1.9. The distance between the plate and the wall is set using a traveling microscope to set a gap calculated from the size of the tubes. Once the plate is positioned, the tubes are glued together. Tubes are glued about every 20 cm (half of the gluing is done on the opposite side of the ribbon).

Once enough ribbons are made, they are stacked on top of each other forming a trapezoid as shown in Figure 1.10a. After they are stacked, trapezoidally shaped bands (Figure 1.10b) are inserted and positioned every 20 cm. The length of a band depends on its location. The bands at the end of a module are about 7 cm long and those near the wire supports are about 5 cm. The remaining bands are 1cm long.

The most important function of the bands is to keep the tubes and wire supports in place by compressing them slightly. Once straw tube ribbons are stacked, the vertical dimension of the module is slightly larger than what it should be. This is because the tubes are not perfectly straight when manufactured. A slight compression keeps them in place. The compression at the wire support locations is especially important since the wire supports determine the accuracy of the sense wire position. We have not measured the position of the sense wires yet. This will be done in the near future.

Since these modules are not stiff (unlike modules with an outer shell), each module can be aligned with a good accuracy when it is installed on the cylindrical base. This is another advantage of the shell-less module. The alignment is done at the band locations.

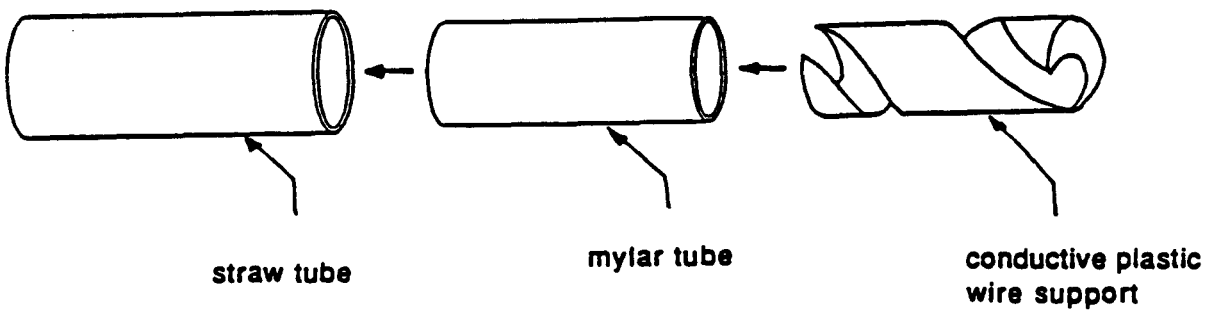

Fig. 1.8 Mid-tube terminator design.

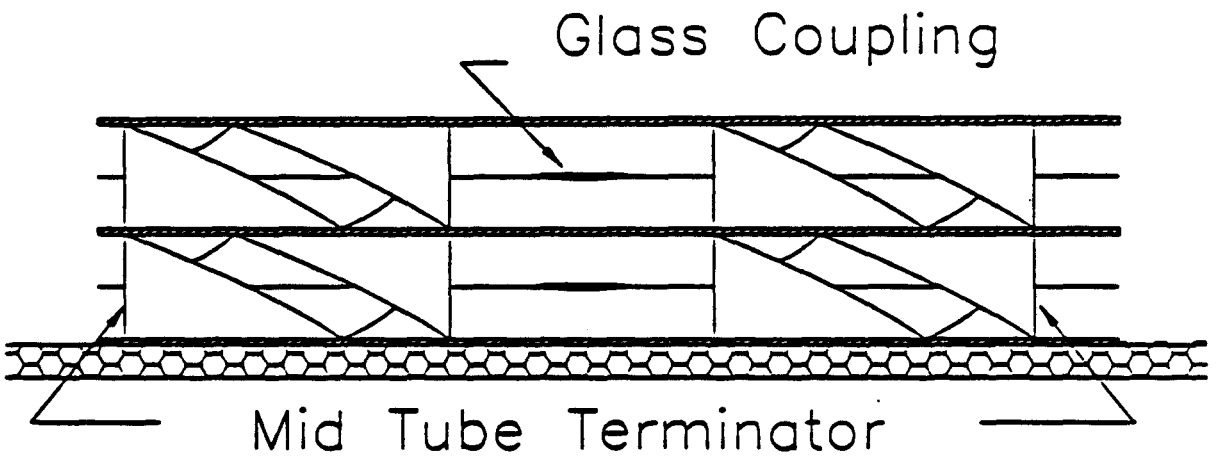

Fig. 1.7 Mid-tube electrical termination scheme developed at Duke.

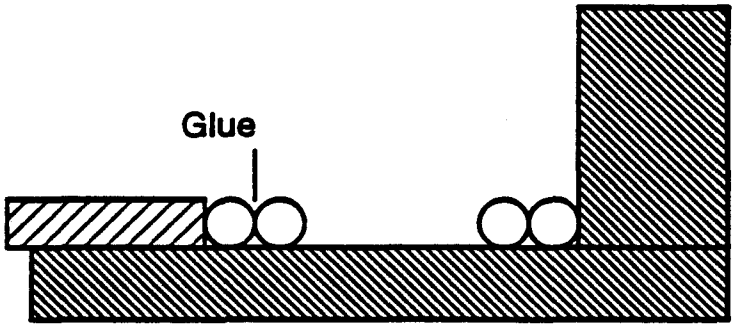

Straw Ribbon Assembly.

Fig. 1.9 Jig used to construct straw tube ribbons.

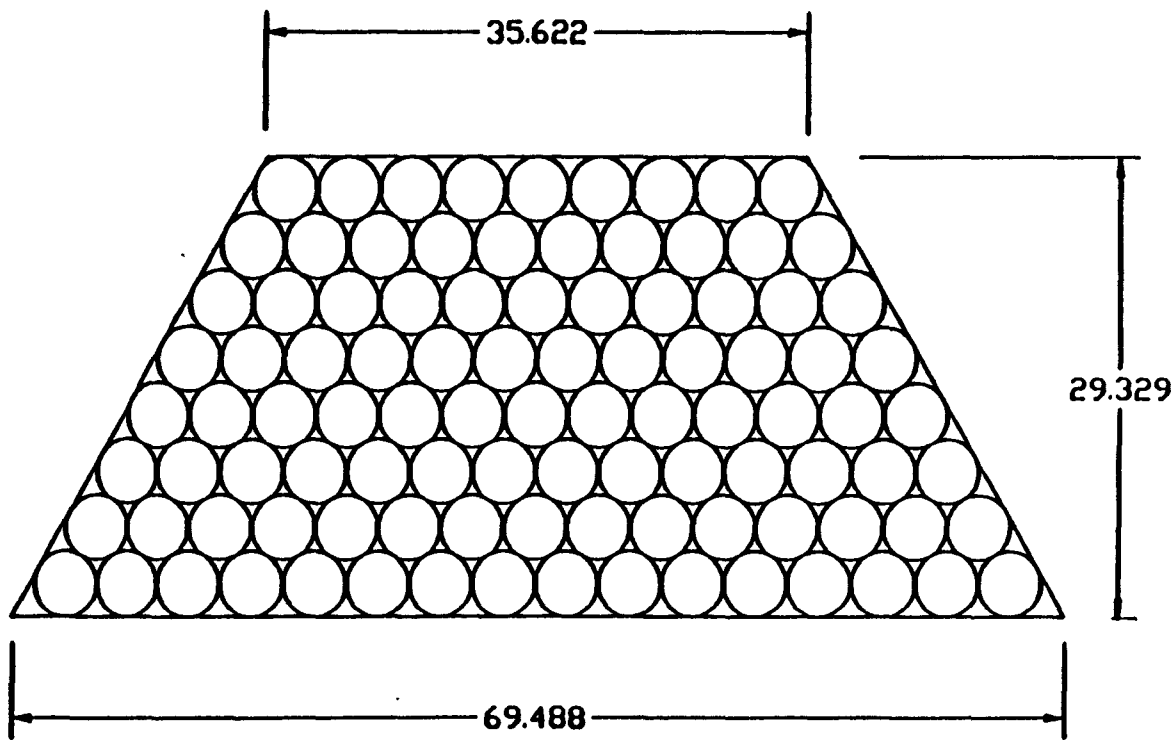

Fig. 1.10a Trapezoidal straw tube module.

Duke

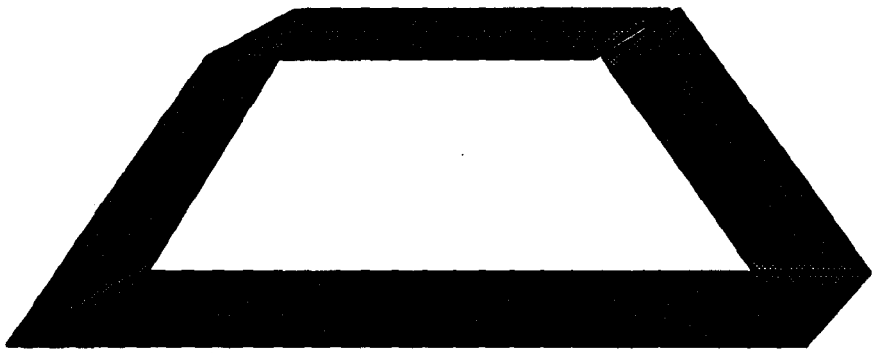

Fig. 1.10b Trapozoid shape band around tube stack

Once a module is completed, it is placed on a flat surface for sense wire stringing. The surface should be stiff enough to take up the wire tension. After all wires are strung, the module is tested for gas leaks, high voltage, and detection sensitivity. After it passes these tests, then the tension in the wire is relieved for storage of the module. The tension in the wire is relieved by simply removing a stopper (Figure 1.11). This procedure is reversed when the modules are installed on the stable base cylinders.

The module being constructed at Duke is expected to be completed within a few months. We plan to instrument it with electronics from Penn and/or KEK when the electronics becomes available.

1.6 Test of 7 Meter Long Straw Cells

We have placed six 7 meter long straw tubes on an optical table. Each tube has 8 of the wire supports designed at Duke. Presently a sense wire is strung in two of the tubes. In one, the sense wire is cut and joined in the middle with a 1mm (0.1mm) outer (inner) diameter glass tube. In both straw tubes, we were able to raise the high voltage to about 2700 volts. We believe that this is the first operational 7 meter long straw tube drift cell.

One of the studies made was designed to understand the efficiency near the wire support and the wire joint. For this study, a Sr90 source was collimated by a 1 mm slit and placed on the top of a tube and moved in steps of about 2 mm. In Figure 1.12, the singles counting rate is plotted as a function of slit position around a wire support. As expected, the region of the wire within the wire support is not sensitive at all. The sharpness of the curve at the ends of the wire support shows that the chamber is useful even very near the wire support.

In Figure 1.13, the scan near the wire joint is shown. The collimated source is moved as in the previous study. Again there is a sharp drop of singles count at the wire joint. Once the source has passed the wire joint, the count rate drops close to zero, which shows there is no problem with cross talk between two separated wire halves.

In the near future, the mid-terminator described earlier will be placed in the middle of a tube to study its effect on the signal. One important study is to determine

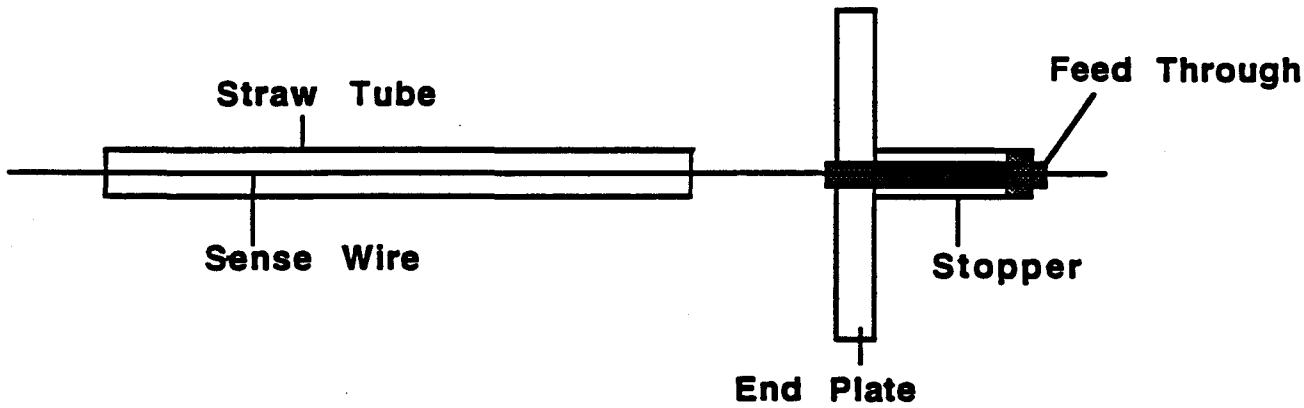

Tension in the Wire.

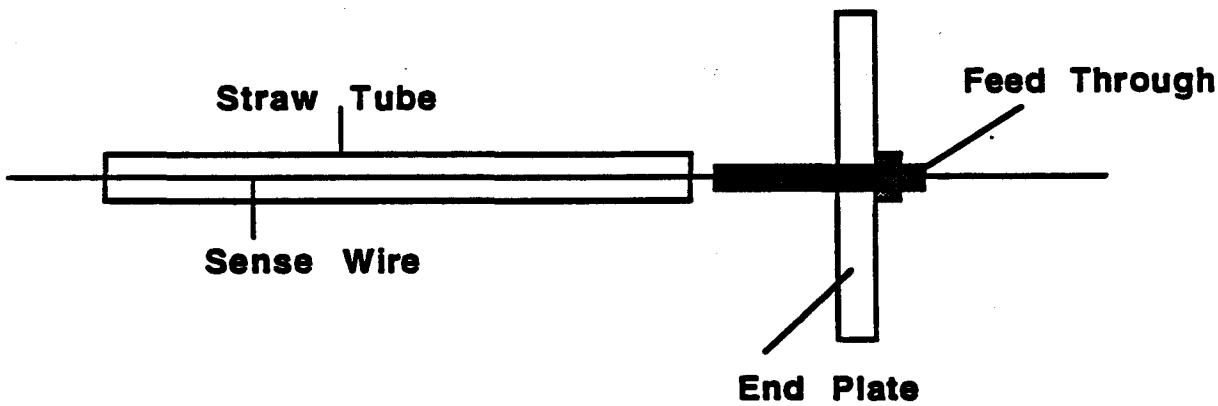

Tension is relieved.

Fig. 1.11 Method for relieving sense wire tension.

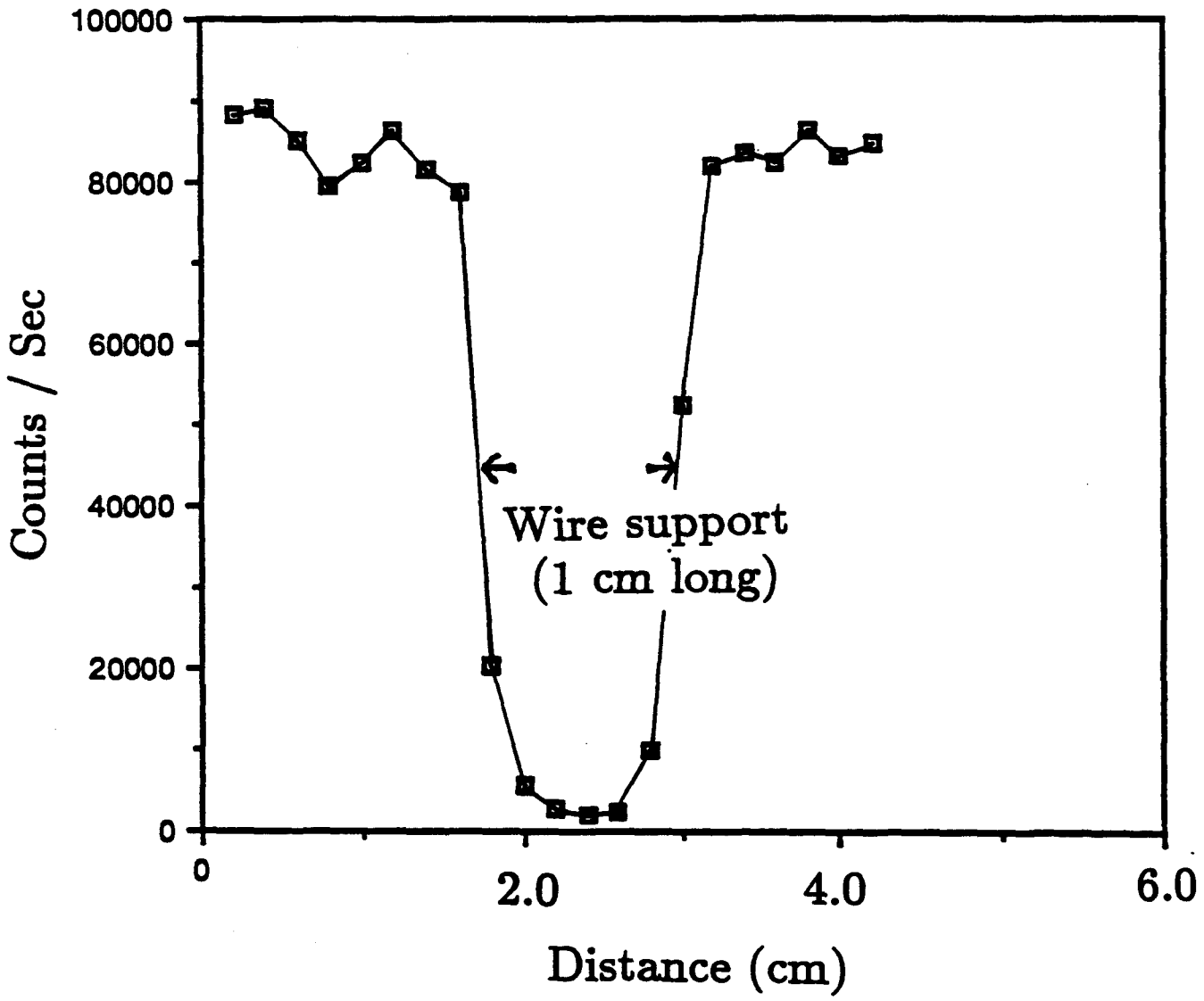

Fig. 1.12 Straw tube detection efficiency near the wire support.

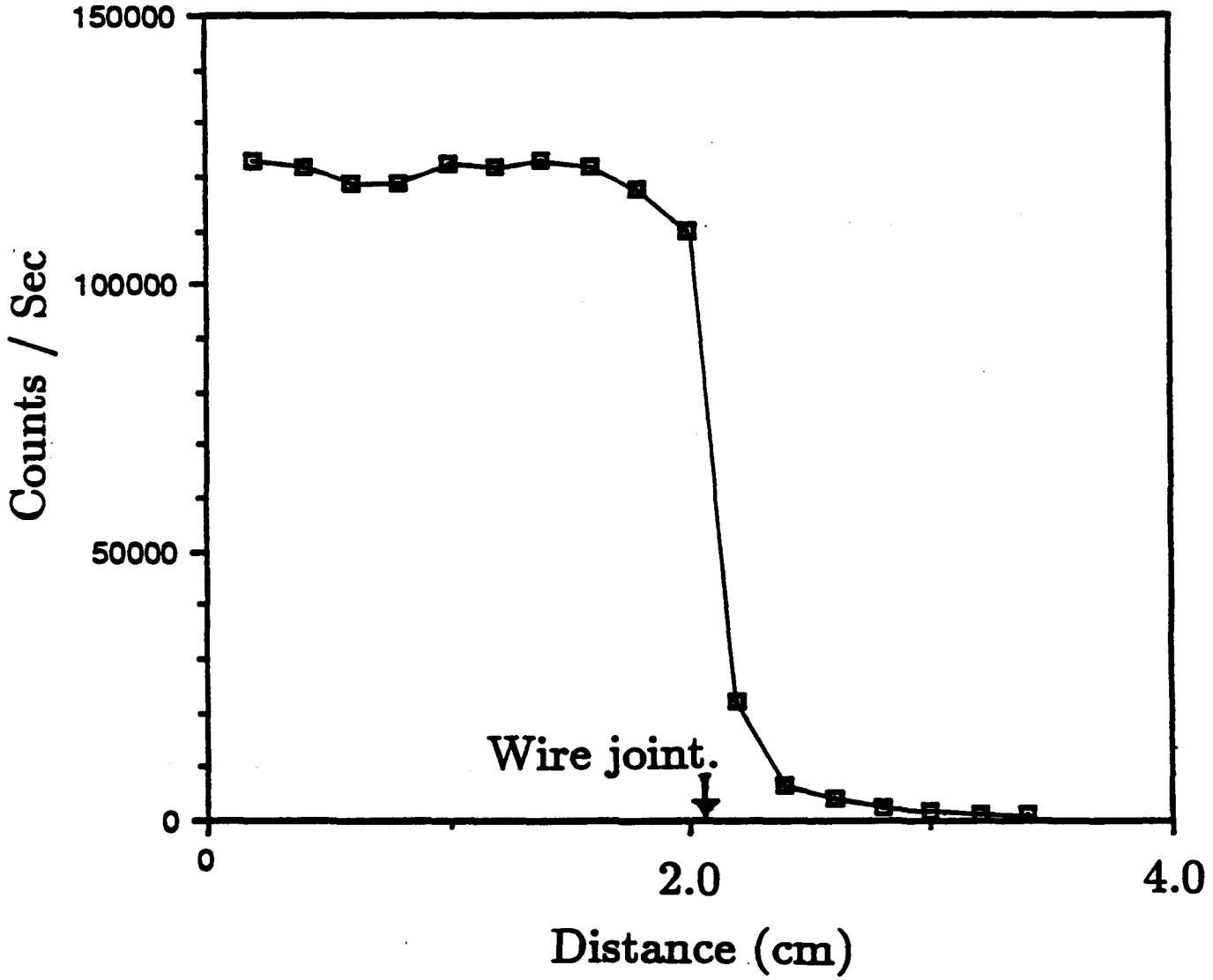

Fig. 1.13 Straw tube detection efficiency near the wire break.

if the terminators are necessary. Not using terminators inside the straw tubes would simplify the chamber construction and reduce the amount of material.

In Figure 1.14, the result of an attenuation length measurement using the 7 meter tubes is shown. In Figure 1.1, we showed the same measurement using our 2.7 meter long chamber. The cathode material for the 7 meter long tubes is different from the material used in the 2.7 meter prototype. The new cathodes are made of 1500 angstrom copper rather than 1/3 mil thick aluminum. By fitting the data points, we obtain 510 $\pm$ 20 cm for the attenuation length, which is compatible with the earlier measurement.

1.7 Wire Position Measurement

To obtain a detector resolution of 150 microns, the sense wire location has to be known to better than 100 microns (the intrinsic drift cell resolution is about 100 microns). Although the position of sense wires can be calibrated using tracks from interactions, it is desirable to be able to measure the wire location before installation.

We have devised a technique for measuring the wire position using a collimated Sr90 source. Preliminary studies show that the wire position can be measured to an accuracy of about 50 microns.

In this technique, a chamber is sandwiched between two slits as shown in Figure 1.15. A Sr90 source is placed behind one slit and a scintillator is placed behind the other slit. A signal from the scintillator is used to start a TDC and a signal from a tube is used to stop the TDC. As the slits move across a tube, the drift time is measured as a function of the slit position. Figure 1.16 shows a typical time measurement as a function of the slit position. The sense wire position is calculated by fitting the data to the form T(x)=a(x-x0)+b(x-x0)**2+c(x-x0)**3 where x0 is the sense wire location.

The accuracy of this technique was tested using a 4 tube chamber with known wire positions. A small hole was made in each tube to measure the wire location using a traveling microscope. The chamber was then placed between the slits as shown in Figure 1.15 and scanned. Figure 1.17 show the results of the scan of the chamber. From a fit to the data, we obtain 4280, 4350 and 4390 microns for the distance between wires. These distances are in good agreement with the measured sense wire positions: 4270, 4320 and 4410 microns.

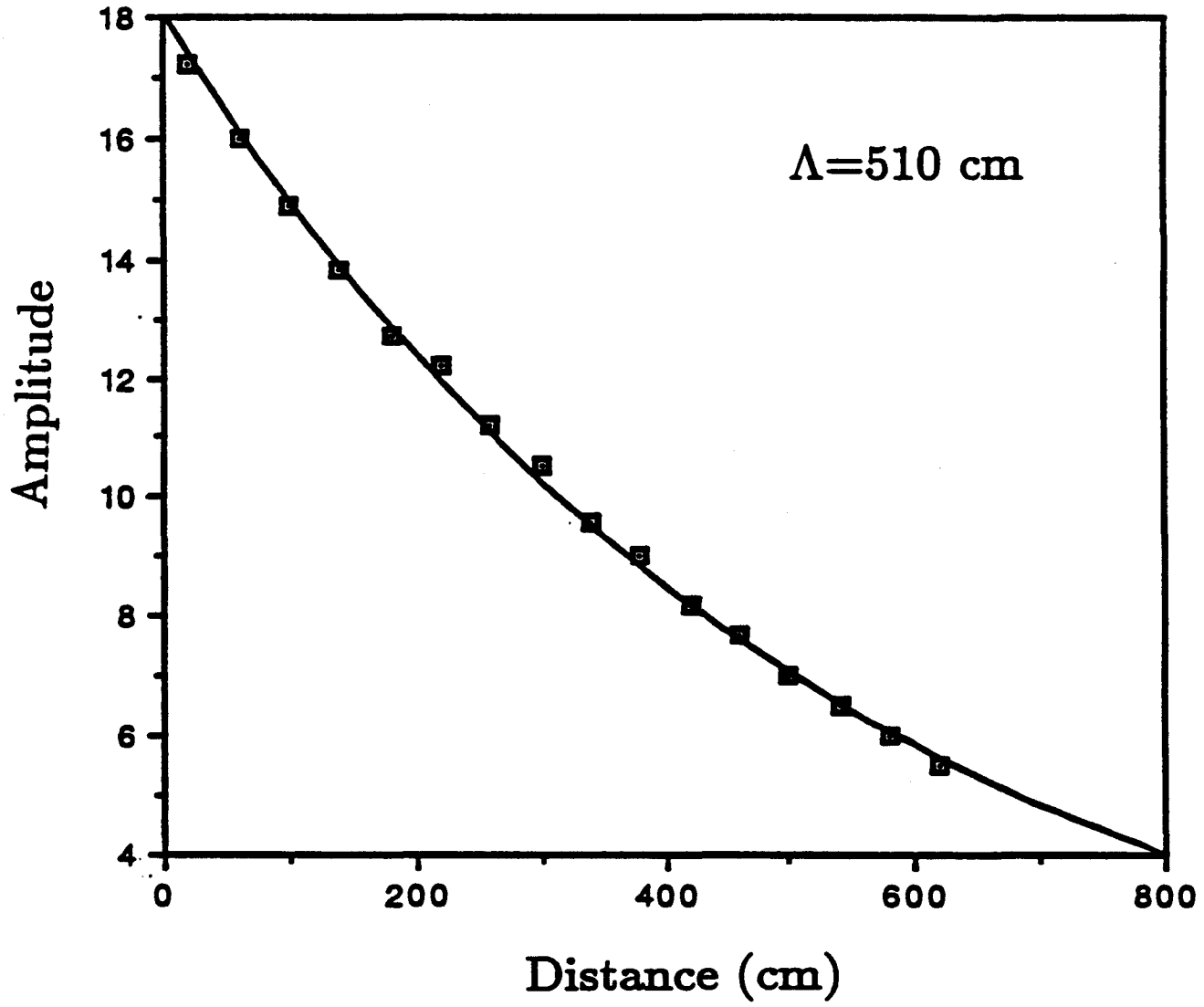

Fig. 1.14 Straw tube attenuation length measurement (7 m straw tubes).

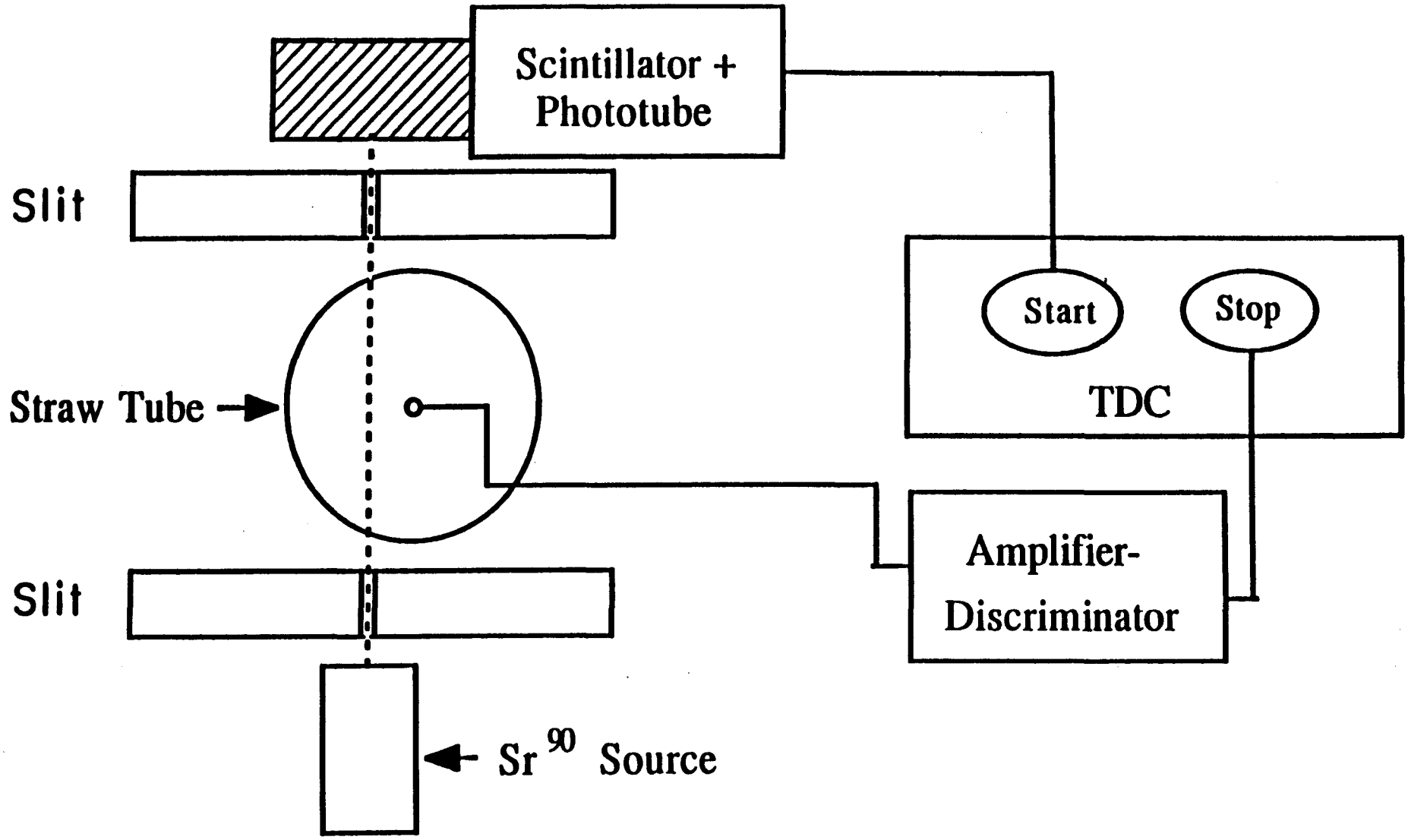

Fig.1.15 Setup for measurement of straw tube sense wire position using a collimated Sr90 source.

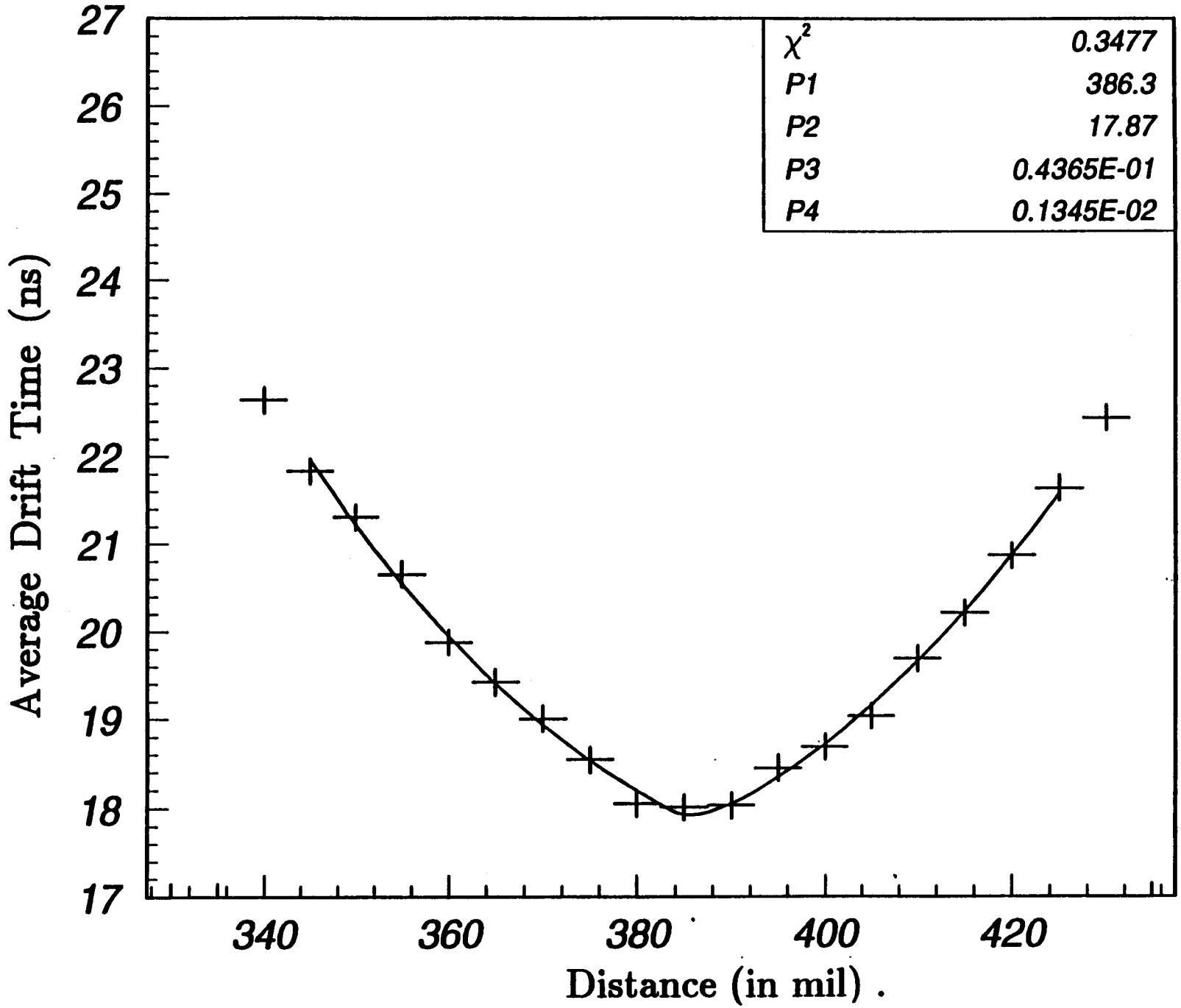

Fig. 1.16 Time measurement as a function of Sr90 slit position.

Duke

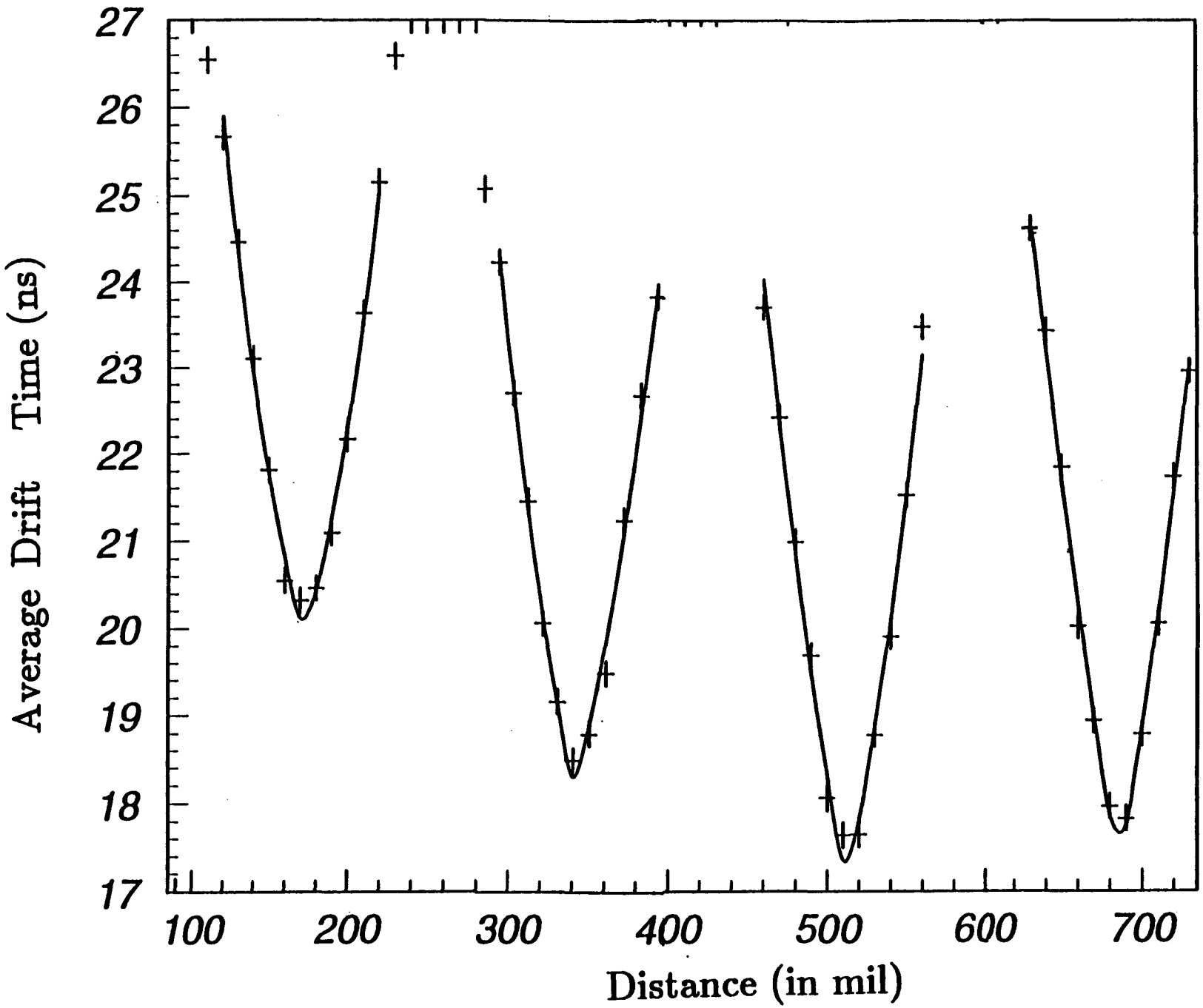

Fig. 1.17 Wire position measurement from Sr90 source scan.

Another way to test this scanning technique is to move the chamber by a known amount after the wire positions are measured. The wire positions are remeasured after the chamber is moved. By comparing the wire positions to the distance the chamber is moved, one can estimate the accuracy of this technique. For this test, the chamber is positioned as shown in Figure 1.18. In Figure 1.19 the two sets of data are shown from one of four wires. One set is before the chamber is moved, and the other set is after the chamber is moved by 160 microns vertically. The measured change in the wire positions are 160, 158, 168, and 180 microns.

There is a limitation of this technique. Since the energy of electrons from Sr90 is about 3 MeV, more material in the path of the electrons means worse accuracy in the wire position determination. We have tested the technique with up to 8 tubes in a row and found the the accuracy is still better than 100 microns in good agreement with the known translation of 160 micron.

1.8 Chamber Stability

Using the setup discussed in Section 1.8, the chamber stability (in drift time) is studied. For this study, the slit position is fixed and the drift time is measured as a function of time. In Figure 1.20, the drift time is plotted over a period of one day. As can be seen in the figure, there is little variation of the drift time.

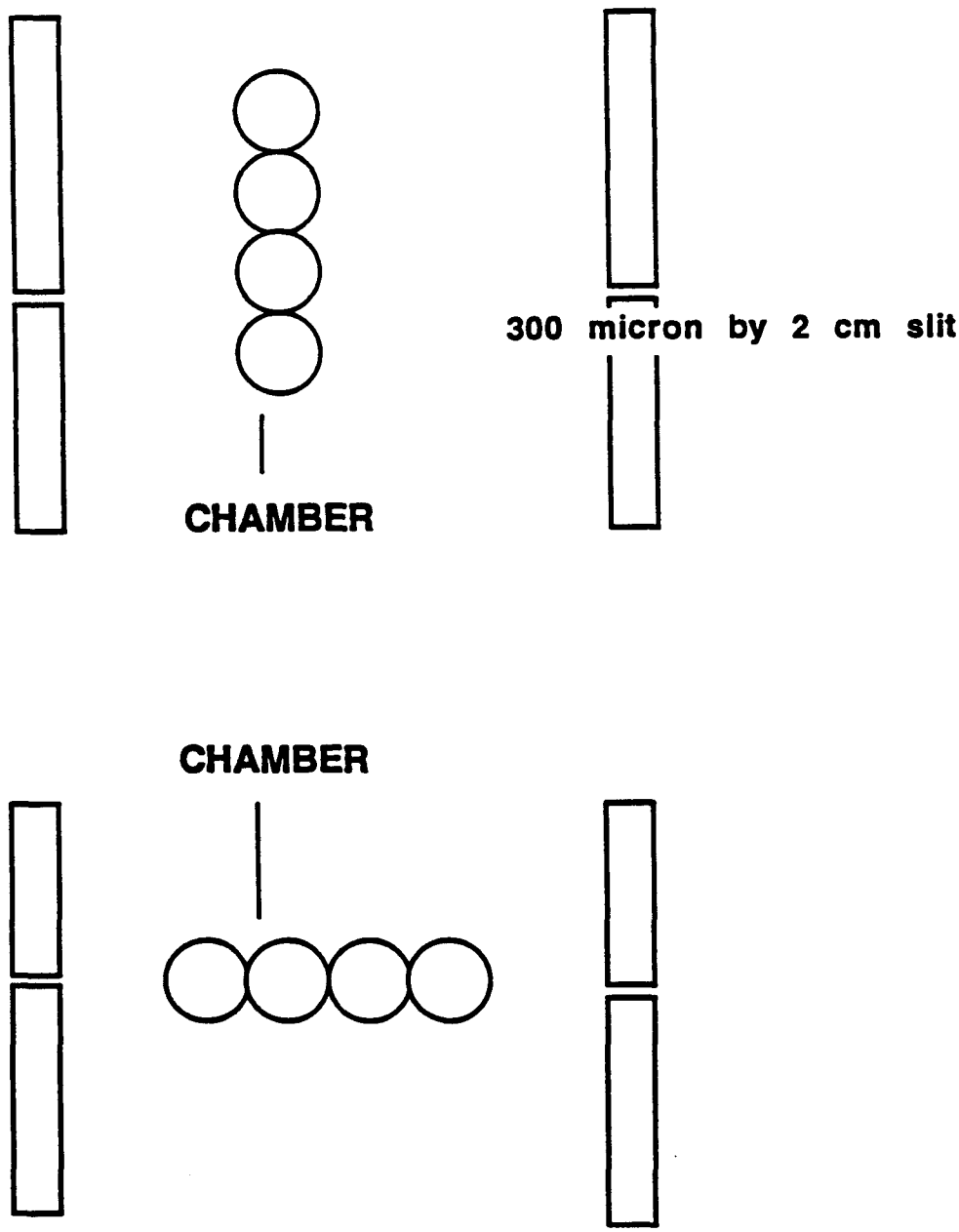

Fig. 1.18 Position of the chamber for wire position measurement.

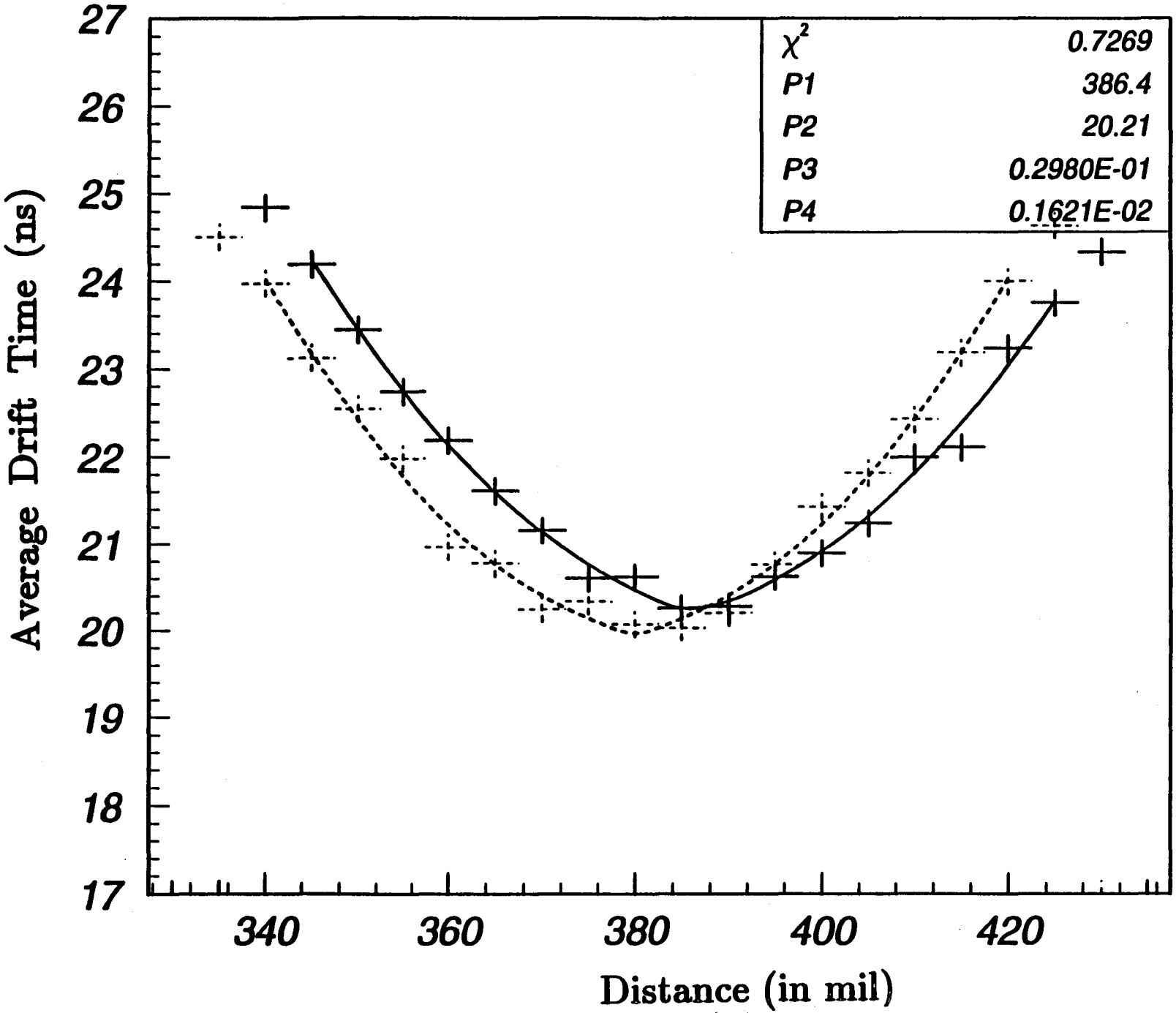

Fig. 1.19 Average drift time as a fu n of slit position.

Duke

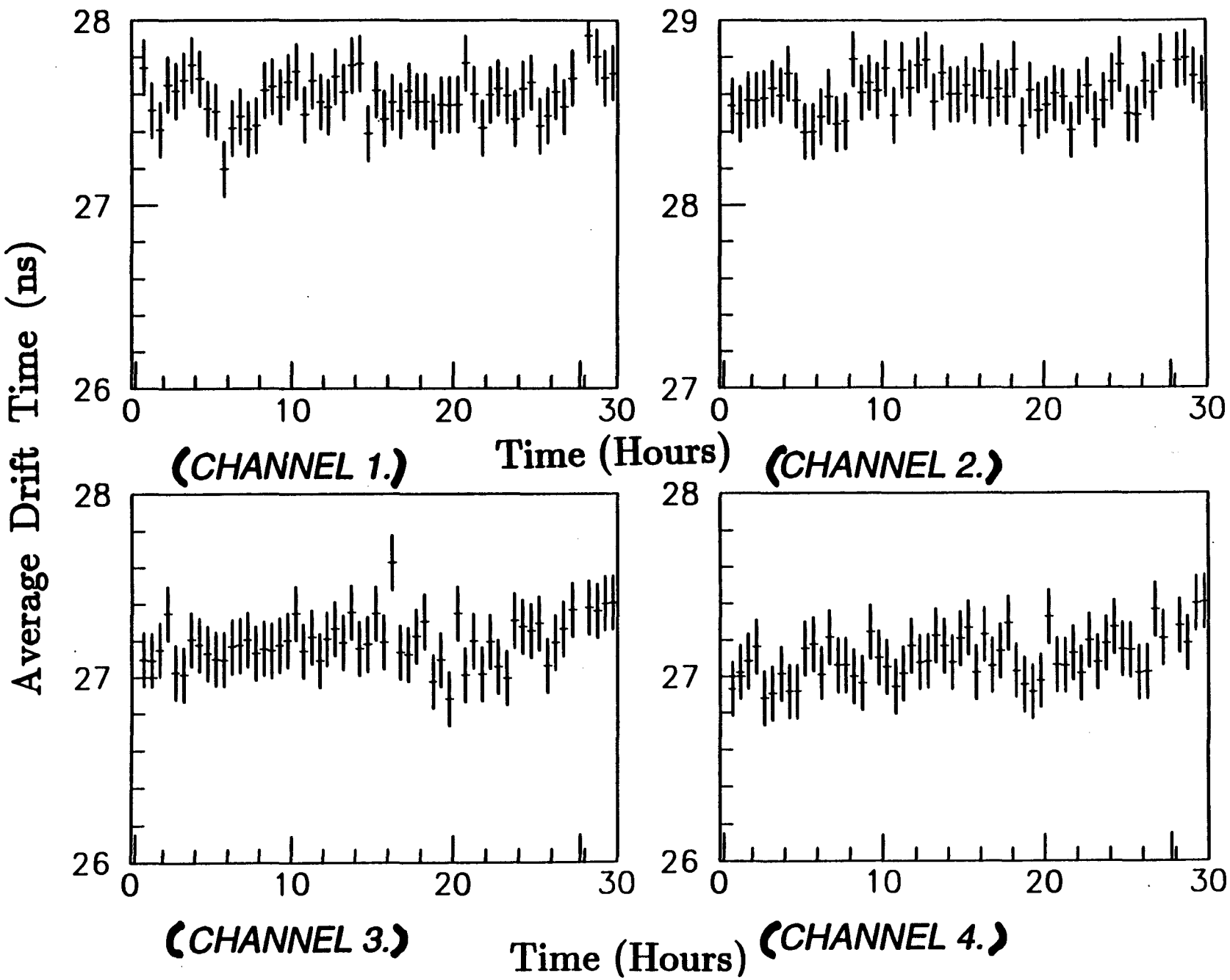

Fig. 1.20 Average time measurement as a function of time. The data is obtained over a period of 30 hours.

2.0 Design of a Semi-automatic Straw Tube Placement Machine

2.1 Overview

Our proposal for the construction of straw tube superlayers for the SDC tracking detector involves the precision placement of on the order of 100K straw tubes on large stable-base cylinders. Over the past six months, Duke, in collaboration with Oak Ridge National Laboratory, has designed the first prototype of a machine which will semi-automatically lay three meter long straw tubes. The construction and testing of this three meter prototype is necessary for the proof of principle required before a full scale straw placement machine is designed. This R&D work is a high priority task for Duke within the Hybrid Subsystem collaboration and has been identified as a critical R&D issue by the overall straw tube group within SDC.

An end view of the straw placement machine is shown in Fig. 2.1. The straw tube guide is formed from two 10 foot long precision ground steel beams having an L shaped cross section (3 in. by 5 in.). Precision spacers are used to separate the steel beams, leaving a slot with a width approximately 4 mm (the straw tube diameter) and length 10 feet. To achieve the required flatness and straightness, the steel beams will be manufactured using the following sequence of steps:

1) rough machined
2) heat treated
3) precision machined
4) heat treated
5) precision ground

We have placed an order for the precision steel beams from H & H Machine Tool Company Inc. (Dayton, Ohio) and expect delivery by early October. The manufacturer has guaranteed that the beams will be flat to 0.001 inch (total run out over 10 feet).

For this test, the straw tube superlayer will be constructed on a horizontal flat surface mounted on a precision roller bearing slide table (see Fig. 2.1). The straw dispenser will not move horizontally, but can be raised and lowered vertically with a lead screw drive controlled by micro-stepping motors. The straws are picked up into

Fig. 2.1 Transverse cross section of the straw tube placement machine.

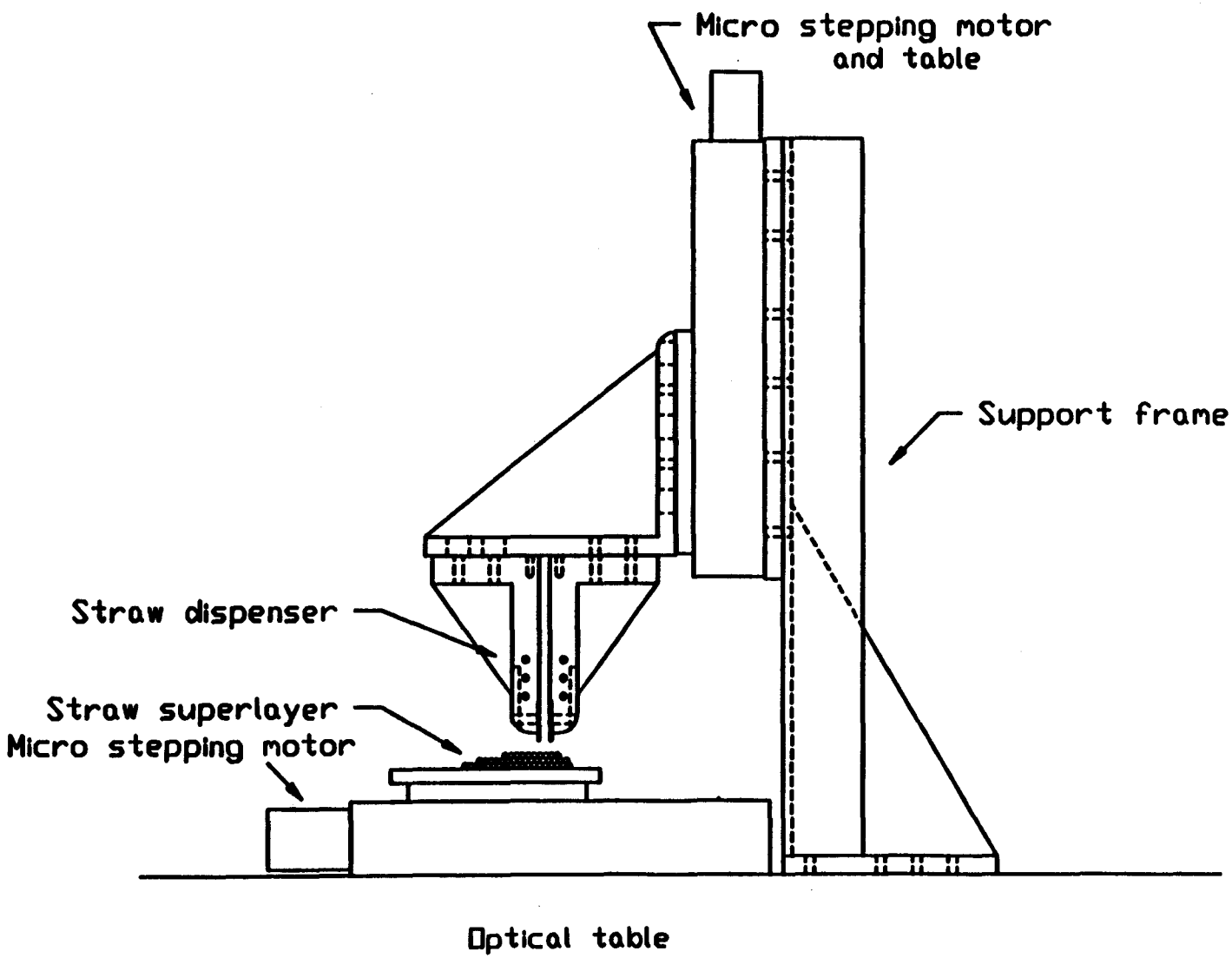

and dispensed from the 10 foot long slot by means of a computer controlled vacuum pickup and over pressure ejection.

Using this basic concept, we have designed a semiautomatic procedure for constructing a 3 meter long straw tube superlayer on a flat surface. A PC based control system implemented by a menu driven software is being written specifically for this straw placement task. The general procedure for the construction of a superlayer consists of the following steps:

1) The superlayer base plate is indexed to the proper horizontal location for the placement of a straw tube.
2) The straw dispenser is raised vertically and a straw is loaded into the straw slot and pulled into position using a low vacuum.
3) The straw guide is then lowered until the dispenser edge is 2 mm above the top of the present straw tube layer.
4) After the straw dispenser is stationary, the straw is ejected by a slight overpressure in the guide slot. The straw is held in position by two razor thin (4 mil) guides attached to the lower of straw dispenser.
5) The straw is then glued to the superlayer with an automatic hypodermic glue injection system.
6) The straw dispenser is raised and steps 1) to 5) repeated for the next straw.

Details of the straw placement machine and alignment concepts are given below.

2.2 Straw Tube Superlayer Surface

In this prototype, the superlayer surface consists of a flat plate mounted on two precision slides. The slides are driven by a micro stepping motor and ball screw mechanism. This precision indexing is critical to construction of the superlayer since the motion of the surface will determine the horizontal spacing between adjacent straws. The absolute position of the surface will be determined by an encoder attached to the indexing motor.

2.3 Position Control

All motions of the superlayer surface and the straw machine will be controlled using a UNIDEX 14 four axis controller made by AeroTech, interfaced to a PC. All feedbacks for positioning and sensing will be controlled from the PC using an A/D

interface board. A schematic of the system control architecture is shown in Fig. 2.2. The UNIDEX controller allows the micro-stepping motors to be synchronized in pairs by running off the same clock. If slight alignment adjustments are necessary, the motors can be operate independently.

2.4 Software Interface

Software for the PC control system is being written in the program language C. The interface with the user is a menu driven interface to allow users with limited familiarity with the control system to operate the straw placement controls. The software consists of a set of routines that allow the user to look at input parameters, setup system defaults, calibrate and monitor the alignment system, move the straw superlayer surface plate, move the straw placement dispenser and record data. Figure 2.3 illustrates the design of a typical terminal menu option with its sub-menus.

Fig. 2.2 System control architecture for the straw tube placement machine.

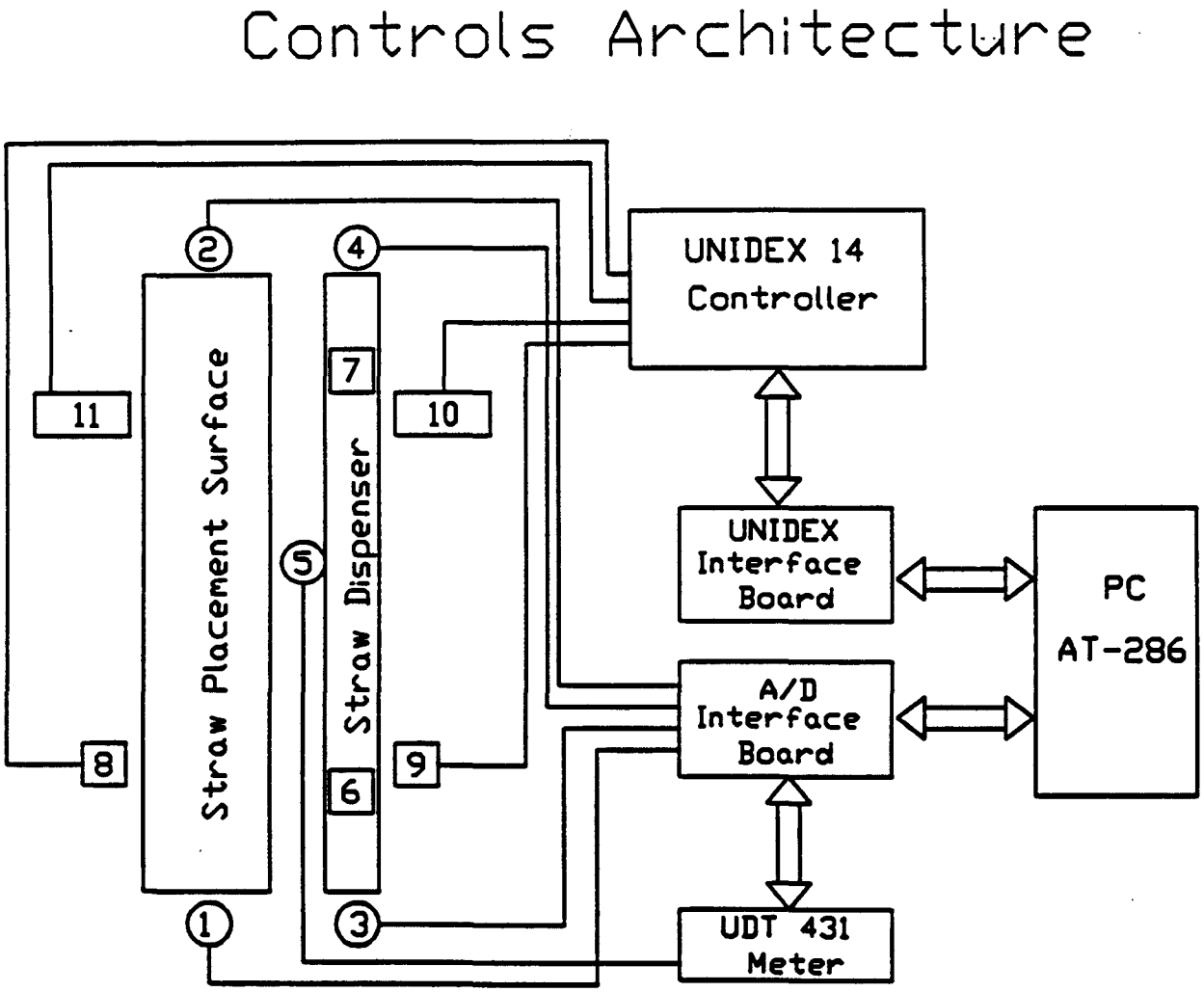

① Linear Variable Displacement Transducer

② Linear Variable Displacement Transducer

③ Linear Variable Displacement Transducer

④ Linear Variable Displacement Transducer

⑤ UDT Lateral Effect Detector

6 Air valve

7 Air valve

8 Microstepping motor

9 Microstepping motor

10 Microstepping motor/Absolute encoder

11 Microstepping motor/Absolute encoder

Fig. 2.3 Example of terminal menu options for straw placement alignment control.

```
MAIN          INPUTS        UDT METER
CONTROLS      UDT METER     MONITOR
INPUTS        LVDT 1        SETUP
EXIT          LVDT 2        DEFAULTS
              LVDT 3
              LVDT 4
              ENCODER 1
              ENCODER 2

                Working Area
CHAN 1    GAIN +/- 10V      Size 900

X dist from center = 20 microns
Y dist from center = 350 microns

Time Remaining 00:28:34                Sigma 3.4
                Help
Strike any key to terminate monitoring UDT

                Menu Description
Monitor X,Y voltage converted to microns
```

3.0 Alignment and Measurement System

An important part of any straw placement device is the alignment procedure. We will use a laser based measurement system made by United Detector Technologies (UDT, Orlando, Florida) to assist in alignment of the detector during construction and to check alignment of the superlayer as it is being fabricated. The UDT system has the ability to measure the centroid of a laser beam to a precision of 6 microns. This system has been thoroughly tested for resolution and reliability in measuring transverse displacements from a laser beam over a distance of 3 meters along the beam. A HeNe laser is filtered and collimated to establish the straight-line reference. The 2 cm by 2 cm lateral effect photodiode is then monitored using instrumentation provided by UDT (model 431 X-Y axis monitor). The lateral effect detector is a photodiode array made up of individual light sensitive photodiodes that transduce incident light into charge which is proportional to the light intensity. A narrow bandpass filter is used to insure that only the 633 nm HeNe light reaches the detector. The 431 monitor uses an LCD to display the X and Y offsets of the beam on the photodiode. The monitor also provides X and Y access ports to allow direct interface with the PC using an A/D board.

An overview of the laser alignment system is shown in Fig. 3.1.

3.1 Alignment System Calibration

The UDT system was carefully calibrated to obtain the results discussed in the next section. A 1 mW HeNe laser was mounted to an optical table using a gimble mount. The laser beam was roughly leveled with the optical table. The detector was then mounted on a 1 micron resolution stage with 20 micron divisions which was mounted to another stage fixed to a magnetic base. The detector was placed a distance (x) from the adjustable aperature at the laser. The top stage was set to zero. The lower detector was then moved transverse to the beam line until a near zero voltage indicated the beam spot was near the center of the detector. The top stage was then moved from 0-200 microns at 20 micron increments while the voltage was recorded at each increment. To account for hysteresis, the top stage was moved back to zero from 200 microns at 20 micron increments, recording the voltage at each 20 micron

Fig. 3.1 Overview of laser alignment system.

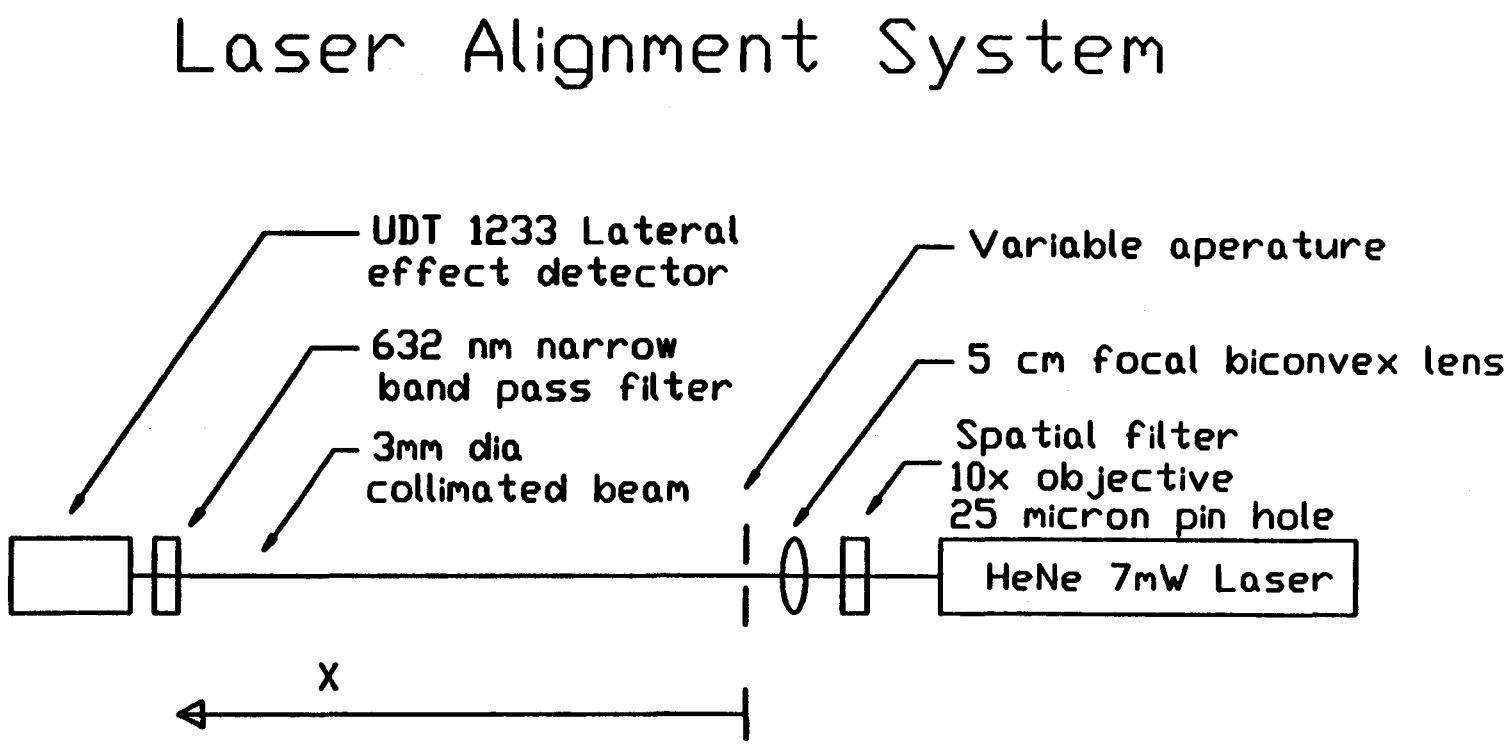

increment. This procedure established the calibration curve for the detector at the given distance, x, from the variable aperature.

3.2 Verifying the UDT Measurements

The measurements taken from the UDT system was verified in three ways after calibration was completed. The first method was to simply move the x translation stage a known amount and compare the calculated (using the calibration curve at x) transverse distance to the known value. The second method was to survey a known surface and compare the results from the UDT to the known profile. This was done at ORNL using a 2 m diagonal on a granite table known to be flat within +/- 0.0005 in. The results from this measurement are shown in Fig. 3.2. A third method was to survey along a line on an optical table and then place a known thickness of shim at the survey points and resurvey the line and compare the results with the original results.

The best measurement resolutions were obtained using the UDT system with a collimated beam having a spot size diameter of approximately 3mm. Test results indicate that a measurement resolution of 9.0 microns (sigma) can be obtained at up to 4 m from the beam source. This is well below the alignment precision required for our straw tube placement.

3.3 Future Tests on Alignment System

Tests on the UDT system will continue to better understand the capabilities of the system. Software is currently being written to allow the system to be monitored over long time intervals to observe any possible drift or changes that may occur in the system over time. Various beam spot sizes and power settings will also be tested to achieve the best possible results.

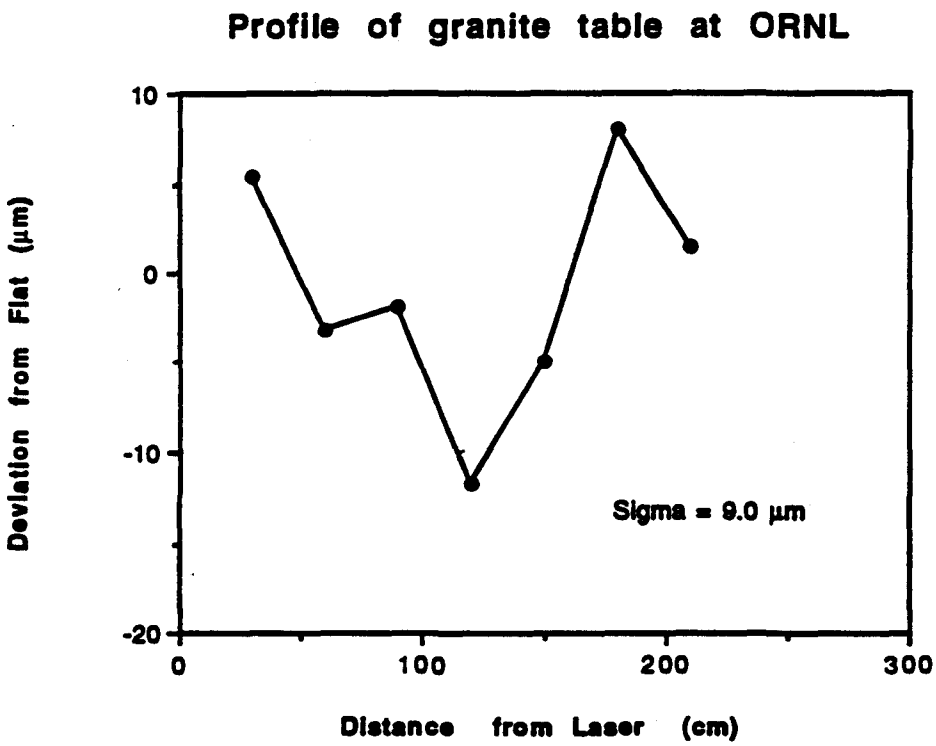

Fig. 3.2 Measurement of the precision of the UDT laser alignment system using a granite optical table for reference

Hybrid Subsystem Progress Report for FY1991

Avalanche Photodiode Studies

EG&G Electro-Optics
Vaudreuil
Canada
Henri Dautet and Bob McIntyre

September 1991

APD Readout R&D Progress During FY1991

Work had concentrated in the following areas:

1. APD development; 0.5 mm 'Slik' detectors
2. Faster Quench circuits
   a. passive quench
   b. active quench
3. Fiber-detector coupling
   a. ball lens
   b. non-imaging concentrators (NIC's)
4. Device modeling
5. Sub-geiger operation

1. 0.5 mm 'Slik' APD

This device is desirable for its higher detection efficiency in both the geiger and sub-geiger modes, and its lower noise in the linear mode. 'Large' devices are difficult to fabricate, however, because of their extreme sensitivity to thickness variations. A procedure has been developed to avoid the necessity of etching wells; this, however, resulted initially in poor blue-green response. This problem has now (we believe) been cured, but the final results are not yet in. Dark count rates will be higher than C30902S, so that cooling may be required.

2. Faster Quench Circuits

a. Passive Quench: A new passive quench circuit has been developed which is an improvement on the simple RC circuit. The RC circuit gives exponential recovery, requiring several RC time-constants to recover to initial photon detection efficiency. New circuit uses an FET to replace R; result is a linear recovery: dead time reduced from ~500 ns to about 300 ns or less, depending on V. Usable recovery slope limited by trapping, and avoidance of latching. Count rates (~2 MHz) limited by diode heating.

b. Active Quench Circuit: Chris Moir's circuit was tried and found not to work. C. Moir has also had difficulty reproducing it. Initial reported results either a fluke or incorrect.

Other fast quench circuits tried, but none found fast enough to prevent a considerable portion of the charge going through the diode. Problem seems to be that one needs a sensitive trigger so that quench pulse is initiated in the first ns. We will abandon this work for now until we investigate sensitive frond ends.

3. Fiber-to-Detector Coupling

Fibers are likely to be in the 0.8 to 1.5 mm range; detectors should be 0.5 mm or less to reduce their capacitances, dark count rates, and cost. Problem: how to collect the light.

We have demonstrated, both by computer modeling and experiment, that a 1.5 mm diameter high index (1.82) ball lens will concentrate 90% of the light which emerges from a fiber with angles within ±20° of the axis onto the detector provided the fiber lens spacing is small and the lens is coupled directly to the detector. This approach has been designed into prototype packages using 'standard' (k=.02) and low-k (.006) devices (C#0902E(S)BL; C30607E(S)BL, respectively. The 'S' designation implies a lower dark count rate and better device uniformity, and is required for Geiger or sub-geiger operation).

An experiment is in progress to measure the angular distribution of light from a scintillating fiber as a function of source-to-detector distance.

We have also begun an investigation of now-imaging-concentrators (NIC's) as a possible alternate to the ball lens [see *Scientific American*, March 1991]. These are moldable shaped light-guides based on off-axis parabolas which are supposed to be quite efficient and possibly of lower cost than ball lens. No results yet.

4. Device Modeling

Efforts are continuing to try to understand in detail the mechanism by which the Geiger pulse develops and spreads. We are working on this in cooperation with Ripamonti, et al., at University of Milan. Nothing definite to report yet.

5. Sub-geiger Operation

This work was delayed because of work on fast quench and ball-lens approach and limited effort. However, a paper sent to RJM for review reports dead times of 15 ns[1], virtually no after-pulsing, and linear count rates up to at least 10^7/sec. Preamp used was

[1] 15 ns dead time was determined primarily by the recovery time of the comparator used.

an overkill: a noisy one with a 200 MHz bandwidth; this resulted in a detection efficiency of only 5%. With a better amplifier and a low-k or slik detector, single photon detection efficiencies of 30-40% should be possible.

Hybrid Subsystem Progress Report for FY1991

Performance and Radiation Hardness of 1 mm Fibers for Use in Tracking for the SSC

High Energy Physics Group
Department of Physics, B-159
Florida State University
Tallahassee, Florida 32306

E. Bartosz
M. Bertoldi
V. Hagopian
E. Hernandez
K. Hu
C. Immer
K.F. Johnson
J. Thomaston
H. Whitaker

September 1991

1.0 Introduction

For a SSC detector, fibers in conjunction with straw tubes make a powerful tracking system, where performance exceeds both straws alone or fibers alone. Even though this effort was performed under the auspices of HCTC, the results are also applicable to an all fiber system as well as shower maximum in the calorimeter. In tracking of the barrel region, even at luminosities of 10^{34} for 10 years, the radiation levels will be only about 400 Krad. Essentially all fibers that we have tested show little damage at this level of irradiation. We have studied a large number of 1.2 meter long fibers and two samples which were 4 meters long. A sample of the results are discussed under Section 2.0 of this report. The critical value is not what the attenuation length is at the end of the fiber, but how many photons are lost by the full length of the fiber. During the past year we have tested several hundred samples and our opinion is that if APD's or VLPC's can be made to work economically, then we do have working fibers.

For the intermediate section of tracking, the situation is not the same, as radiation levels are considerably higher. In the very forward direction present day fibers will have marginal number of photons.

We have also irradiated straw tube subassemblies to 10 Mrad and find no damage.

The FSU group has now been working on various radiation damage studies for many components of SSC detectors. Our effort on this project is about 20% of our total effort. The rest is mostly calorimetry. The HCTC funds received in 1991 for this project totaled $15,000.

2. Results

Fibers were irradiated by 3 MeV electrons and recovered for 1 month. Most recovery occurred in one week, but after 4 weeks recovery was still continuing. Measurements were by Hamamatsu R329 biakali photomultiplier tubes. The relative quantum efficiencies of the R329 at various wavelengths are given in Table 1. Results of various fiber tests are given in Table 2.

Fibers employing a new cladding material are identified by the designator -N in Table 2. It is seen that the new cladding reduces attenuation length by about 30% ± 5%, and increases light yield by about 47% ± 16%.

For a fiber with 200 cm attenuation length and 140 cm new cladding attenuation length the new cladding fiber has 1.47 times the light yield. The cross over point is 180 cm, i.e., after 180 cm the new cladding fiber will have less light output.

Attenuation length increases toward the end of long fibers. Between 3 and 4 meter RH1 fiber attenuation length increased 80%, BCF-E (3HF) increased also by 80%. Both fibers tested are manufactured by Bicron.

Note: After 1 Mrad radiation and recovery, the ratio of attenuation lengths between old cladding and new cladding is smaller, i.e., 13% ± 8% instead of 30% ± 5%.

Table 3 presents some reults of fiber irradiation to 10 Mrad. 3HF attenuation length is now much lower than before, also light output is lower. The 3HF got damaged by being under fluorescent lights in the lab.

Table 1. Hamamatsu R329 Relative Quantum Efficiencies for Various Fibers

Fiber	Spectrum Peak (nm)	Rel. Quantum Eff. of R329
Kuraray SCF38	430	1.0
Kuraray SCSF81	430	1.0
Kuraray SCSF81Y7	490	0.70
Kuraray SCSF81Y8	515	0.63
Kuraray SCSF81Y9	485	0.74
Kuraray SCSF3HF	525	0.41
Bicron 02 B	430	1.0
Bicron 07 RH-1	425	1.0
Bicron 18 G-1	472	0.73
Bicron 23 G-2	492	0.66

Table 2. Representative Fiber Tests Results

Fiber	Attn. Length (cm)	Light Yield		Irradiation 1.2 Mrad		
		Measured	Corrected	Attn. (cm)	Yield Loss (%)	Yield 80 cm (%)
SCSF38	166 ± 4	1.3	1.3	49	4.6 ± 1	18
SCSF38-N	144 ± 2	1.6	1.6	52	4.5	20
SCSF81	177 ± 3	1.0	1.0	84	3.5	43
SCSF81-N	126 ± 2	1.4	1.4	71	3.1	43
SCSF81Y7	170 ± 16	0.29	0.41	116	3.8	73
SCSF81Y7-N	123 ± 3	0.44	0.63	111	3.6	81
SCSF81Y8	201 ± 12	0.20	0.32	142	4.3	82
SCSF81Y8-N	153 ± 5	0.28	0.44	128	3.9	79
SCSF81Y9	160 ± 5	0.33	0.45	69	4.2	39
SCSF81Y9-N	115 ± 6	0.48	0.65	55	3.9	35
SCSF3HF	216 ± 5	0.33	0.81	118	2.1	70
SCSF3HF-N	159 ± 4	0.53	1.3	106	1.5	67
02 B	215 ± 5	1.2	1.2	95	2.9	47
07 RH-1	195 ± 10	1.0	1.0	112	3.1	62
18 G-1	160 ± 9	0.69	0.95	104	10	67
23 G-2	141 ± 4	0.47	0.71	81	19	43

Table 3 Results of 10-Mrad Irradiation on 10 April 1991

Fiber	Attn. Length (cm)	Light Yield		Irradiation to 10 Mrad		
		Measured	Corrected	Attn. (cm)	Yield Loss (%)	Yield 80 cm (%)
SCSF81	134 ± 10	1.0	1.0	44	23 ± 3	7
SCSF81-N	111 ± 3	1.4	1.4	40	23	9
SCSF81Y7	161 ± 10	0.29	0.41	64	22	25
SCSF81Y7-N	111 ± 3	0.44	0.63	54	24	24
SCSF81Y8	171 ± 12	0.20	0.32	83	23	40
SCSF81Y8-N	147 ± 5	0.28	0.44	70	26	33
SCSF3HF	90 ± 5	0.33	0.81	52	13	32
SCSF3HF-N	90 ± 4	0.53	1.3	52	13	32
02 B	203 ± 5	1.2	1.2	46	27	5
07 RH-1	186 ± 10	1.0	1.0	44	23	6

Hybrid Subsystem Progress Report for FY1991

Conceptual Design of Straw Tube Readout with TMC

KEK National Lab. for High Energy Physics
Japan
Yasuo Arai
Hirokazu Ikeda
Yoshiyuki Watase

September 1991

Conceptual Design of Straw Tube Readout with TMC

The electronics group at KEK received no funding from the Hybrid Subsystem grant. However, KEK (Y. Arai, H. Ikeda and Y. Watase) and Duke (S. Oh) have collaborated on testing the Time Memory Cell (TMC) developed at KEK as a time digitizer for signals from a straw tube array constructed at Duke. The results of these tests are discussed in Sections 1.4 of Duke's contribution to this progress report. The TMC development was not part of the Hybrid System work and will not be described here. A recent article describing the conceptual design of the TMC is available from Y. Arai, et al., at KEK.

Hybrid Subsystem Progress Report for FY1991

Front-End Electronics for the HCTC

Department of Electrical and Computering Engineering
North Carolina State University
Raleigh, NC 27695-7909
Steven L. Blake and John J. Paulos

September 1991

Front-End Electronics for the HCTC: Summary Report

Steven L. Blake and John J. Paulos

Department of Electrical and Computer Engineering
North Carolina State University
Raleigh, NC 27695-7911

Abstract

An investigation of the signal characteristics of ionization pulses generated in HCTC straw tubes was performed. The most relevant characteristic of these signals is their rise time and their tail. The behavior of the proposed straw tube design was examined for attenuation and reflections. The large tail response of the ionization pulses will impede double-hit timing resolution for the straw unless the tail can be filtered out. A suitable filter for this application is proposed. Timing studies for the tail cancellation filter and for the Univ. of Penn. device are performed for varying track radii and for varying hit positions. Timing performance for various fixed and proportional thresholds is compared. The feasibility of using long straw tube detectors depends on the impact of signal reflections resulting from the improper termination of the straw tube. Timing studies are performed to ascertain the impact of these reflections on double-hit timing resolution.

1 Straw Tube Physical and Electrical Parameters

The proposed wire chamber elements for the Hybrid Central Tracking Chamber (HCTC) consist of 4 mm diameter mylar straws that have been coated on the inside wall with a $\sim 8\ \mu m$ layer of aluminum. Through the middle of each straw a 25 μm diameter gold-plated tungsten wire is strung under tension. Under operation the tube will be pressurized with an ionization gas (possibly Ar/CH_4 or CF_4) with $\geq 1500\ V$ potential between the center

(anode) wire and the straw tube wall. An ionization track will be formed in the gas when a collider generated particle intersects the tube. The ionization charges will generate avalanche currents as they collect on the anode wire; these avalanche currents will form a current pulse that will propagate down the straw tube to the front-end electronics. The behavior of the straw tube as a transmission line must be understood to ensure accurate timing recovery at the front-end. Table 1 lists the RLC parameters for the straw tube transmission line.

TABLE 1

Passive equivalent parameters for HCTC straw tube.

Parameter	Value
R_0	113.0 Ω/m
R_{GND}	0.270 Ω/m
C_0	10.96 pF/m
L_0	1.015 $\mu H/m$

The characteristic impedance of the straw tube is given by (1) [1].

$$Z_0 = \sqrt{\frac{R_0 + j\omega L_0}{j\omega C_0}}. \tag{1}$$

The conductance of the gas medium and R_{GND} are negligible and are thus ignored. Note that this impedance is complex. At high frequencies the characteristic impedance Z_0 can be approximated by

$$Z_0 \simeq R_0 + \frac{1}{j\omega C_{eq}} \tag{2}$$

where C_{eq} is given by

$$C_{eq} = \frac{2\sqrt{L_0 C_0}}{R_0}. \tag{3}$$

For the particular straw tube parameters given the characteristic impedance approximation is given by

$$Z_T = 305\ \Omega + \frac{1}{j\omega 59\ pF}.$$

This is the desired impedance for use at the termination and at the front-end of the straw tube. A capacitance at the termination and at the front-end is required in any event to block the high DC voltage of the anode wire. Using Z_T as the terminating impedance at each end of the straw tube, the derived reflection coefficient ρ is given by

$$\rho = 0.00644$$

at 50 MHz [1]. The reflection coefficient is non-zero due to the approximate matching of the terminating impedance to the characteristic impedance. The derived propagation delay per unit length t_d is given by

$$t_d = 3.384 \ ns/m$$

at 50 MHz [1]. The propagation delay matches the delay observed in simulations.

In the SPICE simulations of the straw tube a lumped-parameter RLC model is used. Forty RLC sections are used per meter (see Figure 1). The simulated attenuation length of 6.15 m appears to match experimental results obtained at Duke University.

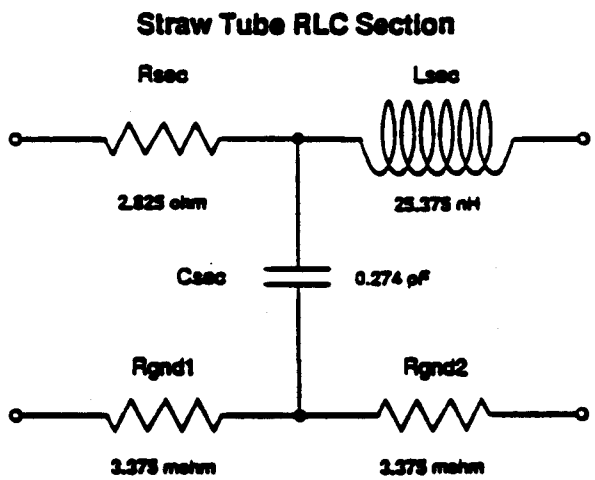

Figure 1: Lumped RLC section for straw tube transmission line model. Forty sections per meter of tube used.

2 Ionization Avalanche Response and Straw Tube Reflection Behavior

Ionization electrons produced by a collider particle track will drift towards the anode wire and will cause a charge avalanche due to the high field region at the wire [2]. The determination of the appropriate avalanche current for the straw tube simulations was based on the following assumptions [3]:

- The avalanche occurs at the surface of the anode wire with constant gas gain = 75000.

- The mobility of the positive ions μ^+ is 1.9 $cm^2/s/V$.
- The anode voltage is 1750 V.
- The tube radius b is 2 mm. The wire radius a is 12.5 μm.

The avalanche current $i_{av}(t)$ is given by (4) where Q is the total charge collected on the wire

$$i_{av}(t) = \frac{Q}{2\ln(b/a)} \cdot \frac{1}{t + t_0} \tag{4}$$

and t_0 is the time scale, given by

$$t_0 = \frac{a^2 \ln(b/a)}{2\mu^+ V_0} \tag{5}$$

and equal to 1.192 ns for these assumptions [3]. Within a scale factor this current exhibits a $t_0/(t + t_0)$ response. Figure 2 is a plot of the avalanche current along with an exponential approximation $h(t)$ used to derive an optimal tail cancellation filter (see Section 4). This response is characterized by a long tail response that remains a substantial fraction of the maximum pulse height tens of nanoseconds after the avalanche occurs. This tail can impede the double-hit resolution of the front-end timing circuitry.

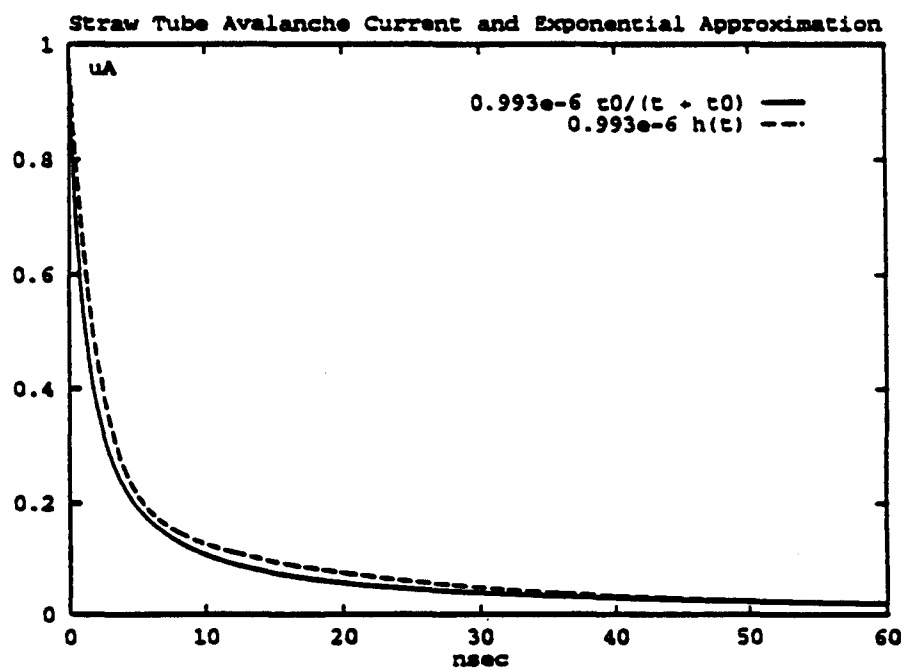

Figure 2: Straw tube avalanche current and exponential approximation (dotted line).

Figure 3 shows the straw tube response for a single avalanche 1 m from the front-end on a 2.75 m tube terminated with the optimal Z_T at each end. Little evidence of reflections can be seen. Figure 4 shows the same avalanche occurring 1 m from the front-end of an 8 m tube. The anode wire of the tube has been broken at the 4 m point to reduce total tube occupancy. The break is modeled as a 0.1 pF capacitor. Figure 5 is a diagram of the straw tube configuration used in this simulation. This break corresponds to an open circuit termination for the half of the tube observed. Notice the pronounced reflection off the line break. In 8 m tube simulations very little crosstalk was observed between the tube sections (< 1%). A single avalanche pulse, with its fast rise time, should have the largest high frequency components of any signal observed. It can be seen that proper termination at both ends of the tube reduces signal reflections.

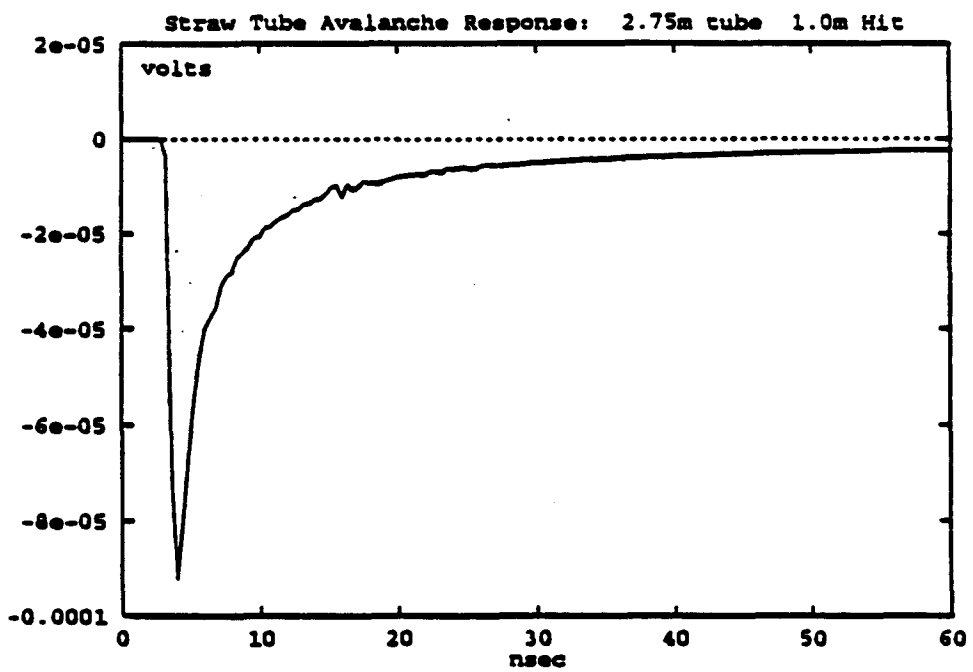

Figure 3: Avalanche response for a 2.75 m straw tube terminated by Z_T at both ends with the avalanche 1.0 m from the front-end.

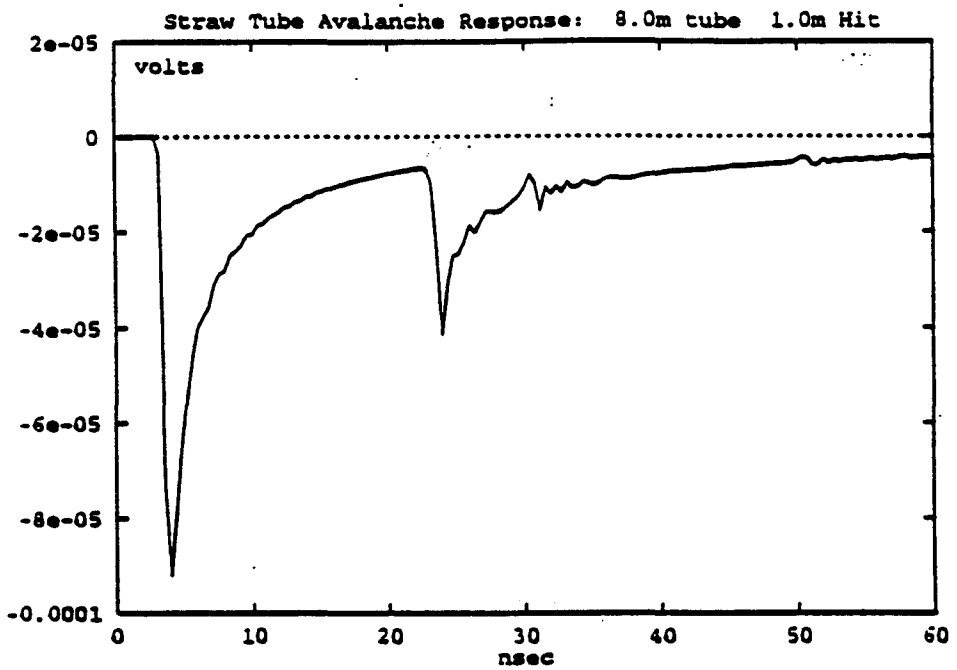

Figure 4: Avalanche response for a 8.0 m straw tube terminated by Z_T at the front-end with an open circuit in the middle with the avalanche 1.0 m from the front-end.

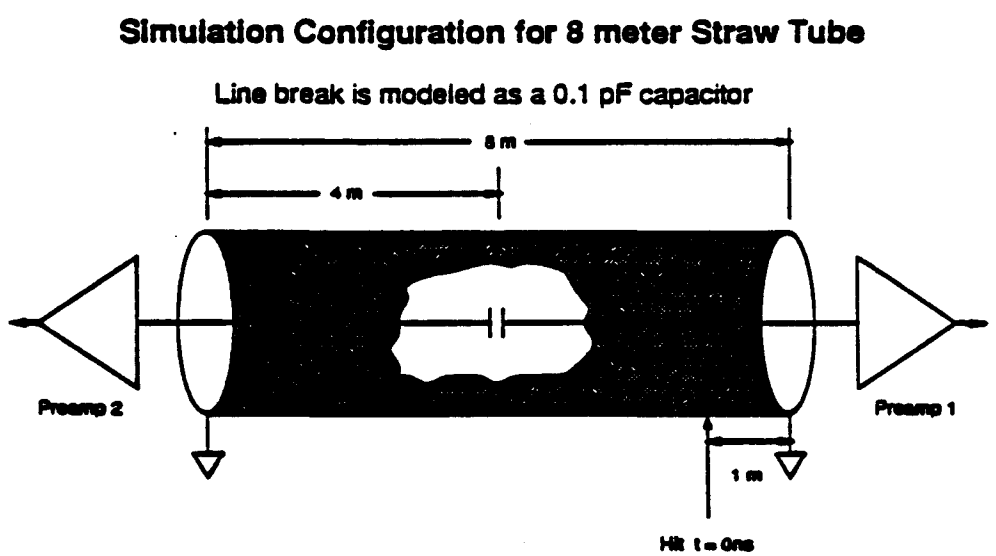

Figure 5: Diagram of the 8 m straw tube configuration used in simulations.

3 Ionization Pulse Currents

The ionization tracks produced by collider particles intersecting a straw tube will in general produce a few tens of free electrons that will drift towards the anode wire at constant velocity [3]. The statistics of the electron distribution on the ionization track are not examined here. Each electron arriving at the anode wire will produce an avalanche current pulse (see Section 2). An intuitive way of viewing this process is as a linear system; the avalanche current is the impulse response of an electron arrival event. The current pulse produced by an ionization track would be the superposition of all the avalanche pulses produced by the arrival of individual electrons, and could be modeled as the convolution of the avalanche pulse response with a series of impulses.

Since the distribution statistics of ionization electrons on the track is neglected, the ionization track can be modeled as a uniformly distributed line of charge, where the total charge on the track is equal to the average observed charge density times the track length. The charge on the ionization track will then appear at the anode wire as a continuous current, which then is convolved with the avalanche response to produce the ionization pulse current [2]. For this analysis it is assumed that tracks pass through the straw perpendicular to the length axis. The arrival current $i_{arr}(t)$ is given by (6) for the listed conditions:

$$i_{arr}(t) = \begin{cases} 0 & t \leq \frac{a}{v_d} \\ 2\rho v_d \frac{v_d t}{\sqrt{(v_d t)^2 - a^2}} & \frac{a}{v_d} < t \leq \frac{r}{v_d} \\ 0 & t > \frac{r}{v_d} \end{cases} \tag{6}$$

- The tube radius $r = 2\ mm$.
- The track radius from the anode wire is a.
- The ionization charge density $\rho = 10\ e/mm$.
- The charge drift velocity $v_d = 100\ \mu m/ns$.

Figure 6 is a plot of the various arrival currents for varying track radii. From (6) it can be seen that the arrival currents will instantaneously decay to zero at $t = 20\ ns$ (the maximum drift time of an ionization charge). For the case where the track intersects the center of the straw, the arrival current is a constant $2\ e/ns$ over the $20\ ns$ drift time. The form of the avalanche current makes the analytical convolution untractable. Ionization pulse currents

were obtained by numerical convolution. Figure 7 is a plot of the corresponding ionization pulse currents for varying track radii. Note that the maximum pulse height for these currents exceeds 6.5 μA in all cases. The track radius that produces 25% of the maximum ionization charge (10 e) is 1.94 mm. This results in a pulse height of 9.228 μA. The height of the ionization pulse does not exhibit a large variance for increasing track radii; however, the rise time of the pulse is reduced for tracks that are near the anode wire. It appears that the pulse height variance should not affect the choice of the timing threshold at the front-end.

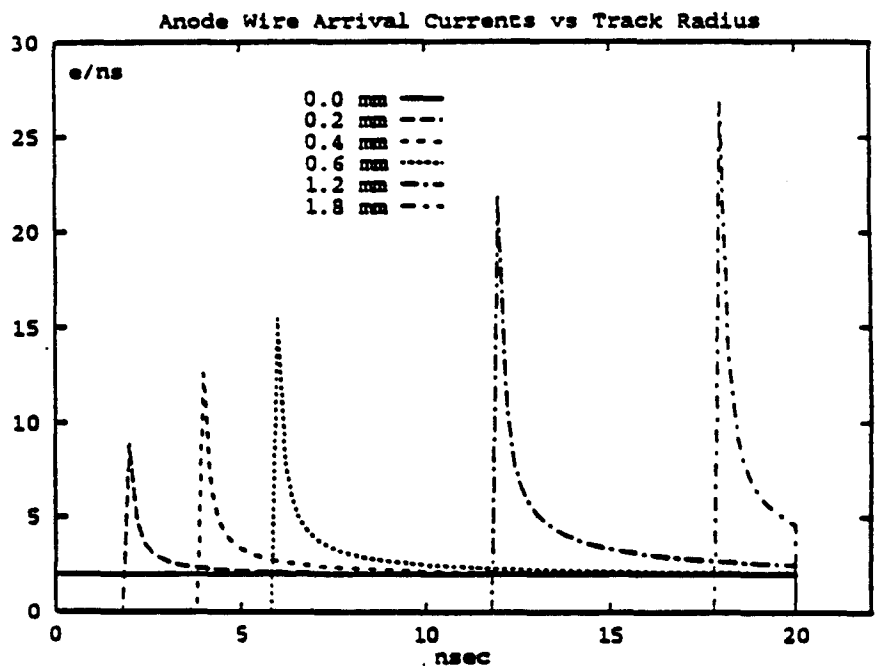

Figure 6: Anode wire arrival currents vs. track radius for the continuous charge ionization track model.

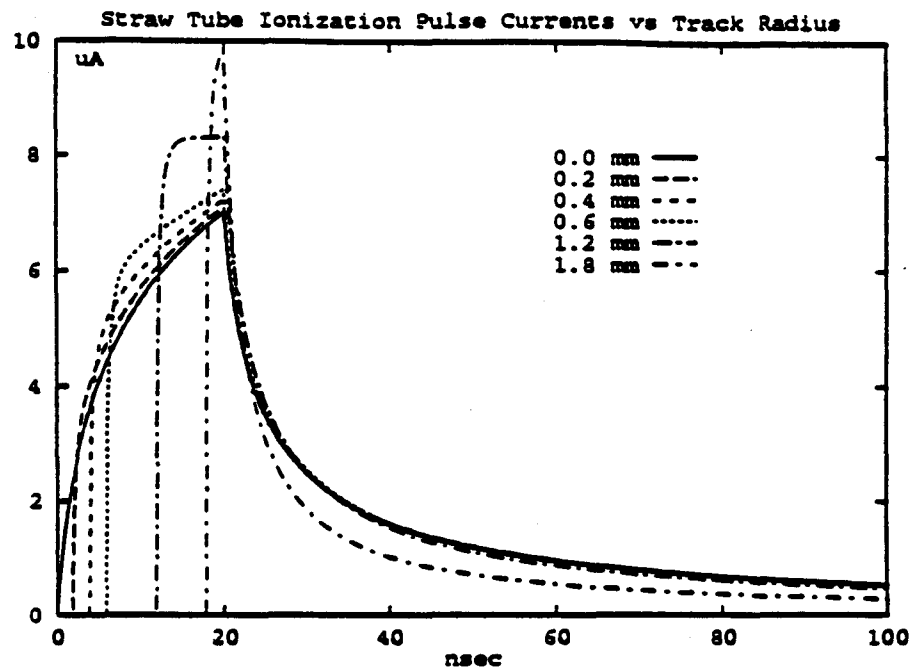

Figure 7: Straw tube ionization pulse currents vs. track radius for the continuous charge ionization track model.

4 Ionization Pulse Tail Cancellation and Preamp Bandwidth

It is clear from Figure 7 that the characteristic tail response for ionization pulses remains a substantial fraction of the maximum pulse height 32 ns (or two collider collision periods) after the onset of the pulse. This may impede the accuracy of double-hit timing for circuits at the front-end that obtain a timing estimate by measuring the time for the ionization signal to cross a threshold, since the baseline of the second arrival is not at zero. A low-threshold detector could be swamped by the pulse tail. Filtering of the ionization pulse to suppress the tail is required to support adequate double-hit resolution on the straw. The choice of preamplifier and filter bandwidth must consider the noise environment the front-end electronics will operate in; bandlimiting must be chosen as low as possible to limit the noise bandwidth of the detector while preserving the rise time of received ionization pulses and the tail cancelling properties of the filter.

From Section 3 it was determined that the ionization pulses could be decomposed into

the convolution of the characteristic avalanche response of the straw tube with a series of impulses representing the arrival of ionization electrons. This signal can be identically modeled as a sum of delayed avalanche pulses. Since the distribution of electron arrivals at the anode wire is variable, the only degree of freedom in the tail cancellation filter design is to shorten the tail of a single avalanche pulse as much as possible. The tail of the summed ionization pulse will consequently be shortened.

In [2] an approximate model of the $t_0/(t+t_0)$ response of the avalanche pulse is given by

$$h(t) \approx Ae^{\frac{-t}{\alpha t_0}} + Be^{\frac{-t}{\beta t_0}} + Ce^{\frac{-t}{\gamma t_0}} \tag{7}$$

where the constants equal

$$A = 0.790;\ \alpha = 1.60;\ B = 0.185;\ \beta = 13.5;\ C = 0.024;\ \gamma = 113.0\ .$$

This model tracks the actual tail decay of the $t_0/(t+t_0)$ response exactly, while diverging slightly in the $t \leq 15\ ns$ region. The approximate model $h(t)$ is shown along with the avalanche pulse in Figure 2. The exponential component with time constant αt_0 decays much faster than the other two components. The tail cancellation filter should preserve the fast exponential component of the avalanche pulse while cancelling the slower components. The spectrum of the approximate model $H(s)$ is given by

$$H(s) = \frac{A}{s+\frac{1}{\alpha t_0}} + \frac{B}{s+\frac{1}{\beta t_0}} + \frac{C}{s+\frac{1}{\gamma t_0}}\ . \tag{8}$$

In [2] it was shown that a filter with the frequency response $F(s)$

$$F(s) = \frac{s+\frac{1}{\beta t_0}}{s+k_1\frac{1}{\beta t_0}} \cdot \frac{s+\frac{1}{\gamma t_0}}{s+k_2\frac{1}{\gamma t_0}} \tag{9}$$

will yield a response $y(t)$ for input $h(t)$

$$y(t) = \mathcal{L}^{-1}[H(s)F(s)] \simeq e^{\frac{-t}{\alpha t_0}} \tag{10}$$

for the given parameter values A, B, C, α, β, γ, and the constants k_1, k_2

$$k_1 = 2.50,\ k_2 = 1.62\ .$$

$F(s)$ is chosen as the frequency response of the tail cancellation filter. For $t_0 = 1.19\ ns$ this results in a zero-pole, zero-pole filter with pole-zero frequencies

$$f_{z_1} = 1.183\ MHz;\ f_{p_1} = 1.916\ MHz;\ f_{z_2} = 9.907\ MHz;\ f_{p_2} = 24.77\ MHz\ .$$

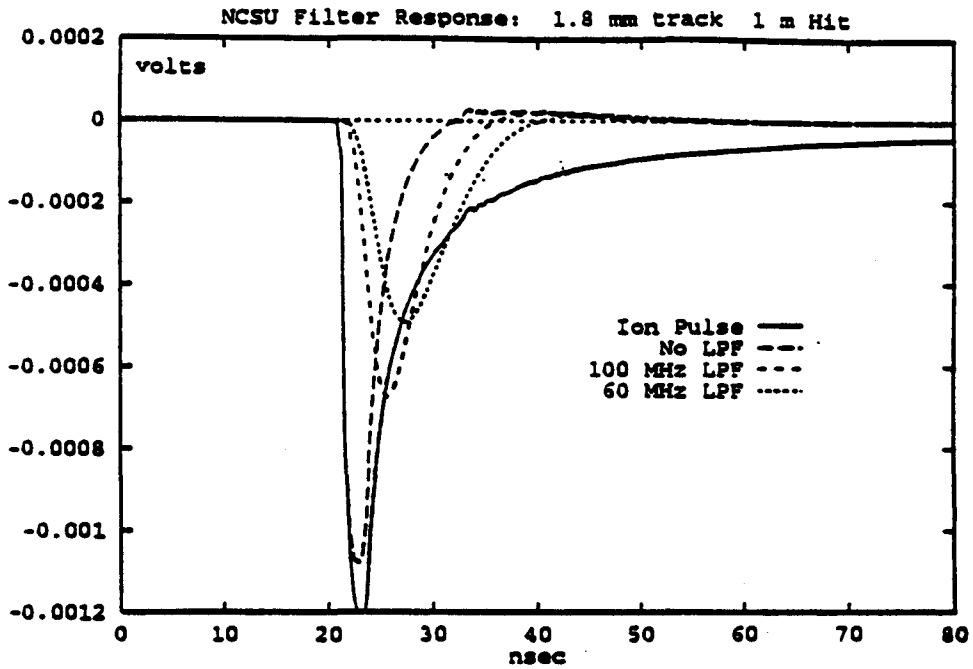

Figure 8: Response of the NCSU filter to an ionization pulse of 1.8 mm track radius at 1 m from the front-end.

This filter is implemented in the SPICE simulations as a buffered series of RC filters. No attempt is made to try to compensate for the frequency response of the straw tube transmission line, the straw tube coupling, or the interconnection parasitics. Figure 8 is a plot of the response of the described tail cancellation filter (NCSU filter) to an ionization pulse with track radius 1.8 mm propagating 1 m down a 2.75 m terminated straw tube. The response of the filter with varying degrees of bandlimiting is also shown. Notice how quickly the filtered pulse returns to the baseline, in comparison to the ionization pulse itself. Figure 9 shows the same ionization signal passed through the University of Pennsylvania (UPenn) preamp/shaper integrated circuit. The UPenn preamp/shaper exhibits gain that is not modeled in the NCSU filter simulations. No attempt was made in the UPenn preamp/shaper design to perform tail cancellation, and it is evident in Figure 9 that the ionization pulse tail is not suppressed. Figure 10 shows the response of the NCSU filter for an ionization pulse with track radius 0.6 mm. Some overshoot in the response is evident. This is likely due to the fact that the avalanche pulse model used in (7) is not exact, as well as the fact that the AC coupling of the straw tube to the front-end (through a 59 pF capacitor) is not taken into account in the NCSU filter design. In any event, this overshoot is well below the ionization pulse tail. Figure 11 is the response of the UPenn preamp/shaper to the same signal.

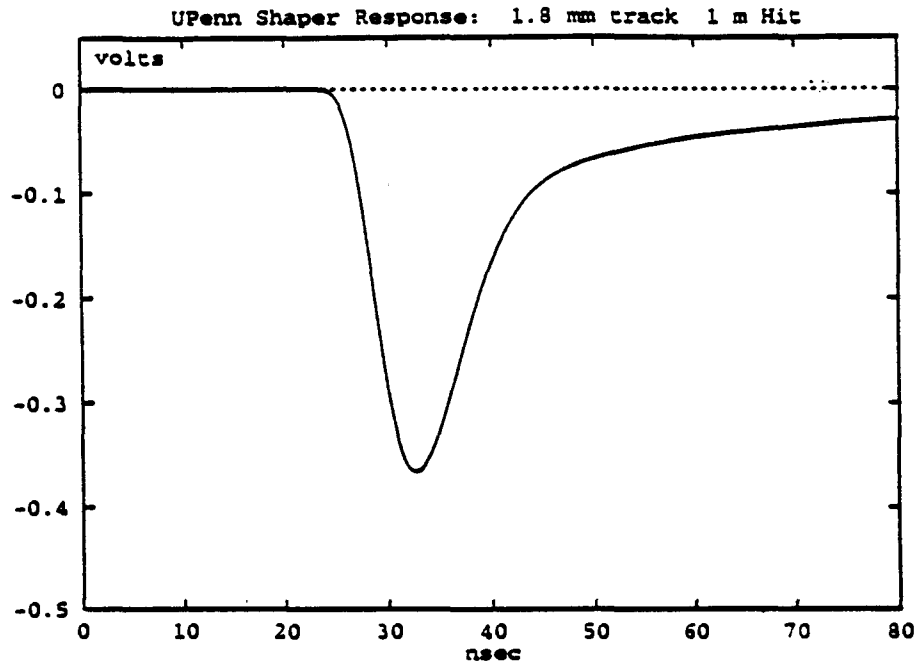

Figure 9: Response of the UPenn shaper to an ionization pulse of 1.8 *mm* track radius at 1 *m* from the front-end.

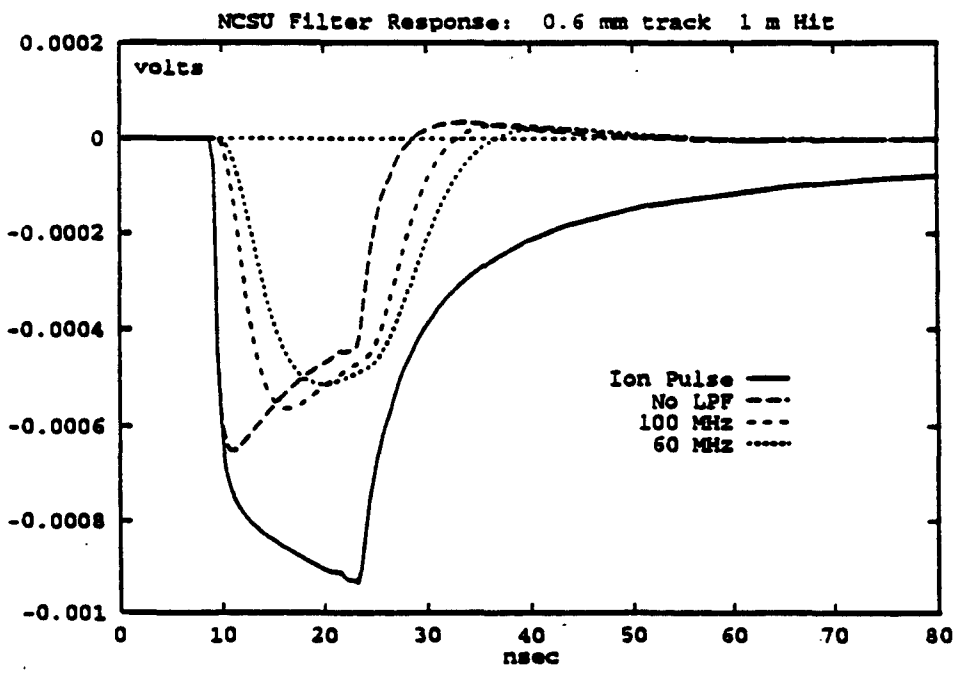

Figure 10: Response of the NCSU filter to an ionization pulse of 0.6 *mm* track radius at 1 *m* from the front-end.

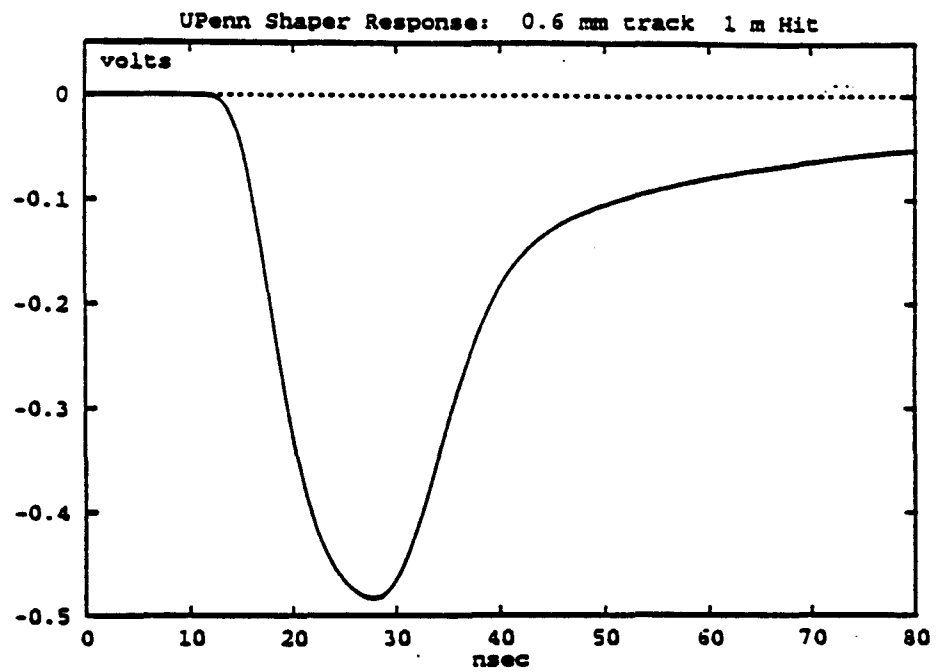

Figure 11: Response of the UPenn shaper to an ionization pulse of 0.6 mm track radius at 1 m from the front-end.

One characteristic of the NCSU filter is its flat gain at arbitrarily large bandwidths. Clearly this cannot be implemented in a real device, nor is it desirable. Some bandlimiting of the filter's frequency response is necessary to reduce the noise bandwidth of the front-end amplifier. The consequence of this bandlimiting is that the rise time of the filtered ionization pulse will be reduced, and the decay time of the pulse may be extended. It is desirable to preserve as much of the rise time of the ionization pulse as possible, since a fast rise time reduces the sensitivity of a time-to-threshold measurement to noise. It is not desirable to smear the filtered pulse by extending its decay time, since double-hit resolution on the tube will be impaired.

Bandlimiting for the NCSU filter is implemented in the SPICE simulations by a series of buffered RC lowpass filters; one filter with a pole at frequency f_b and another filter with two poles at frequency $2f_b$. Values simulated for f_b include 40 MHz, 60 MHz, 80 MHz, and 100 MHz. It was found that bandlimiting at 40 MHz severely reduced the rise time of the ionization pulse and produced smearing. Bandlimiting at 60 MHz and at 100 MHz were found to produce the most interesting results. The results of the bandlimiting can be seen in Figures 8 and 10. Both bandlimiting filters reduce the rise time of the ionization pulse, though the bandlimiting filter with $f_b = 100$ MHz does so less severely. Both bandlimiting

filters cause $\sim 5\ ns$ of smearing of the ionization pulse, with the bandlimiting filter with $f_b = 60\ MHz$ producing more smearing. It is interesting to note that neither bandlimiting filter increases the time at which the filtered ionization pulse returns precisely to the baseline. If an extremely low threshold is chosen for the front-end detector, then the choice of bandlimiting filter will not impact the double-hit resolution *per se*. Figure 12 shows a plot of the NCSU filter frequency response, as well as the frequency response of this filter through both bandlimiting filters. This response is calculated for a fixed amplitude current signal applied directly at the front-end of the straw tube (the amplitude is chosen so that the mid-band voltage at the input of the NCSU filter is at 0 dB). The effects of the straw tube impedance and the front-end coupling can be seen on the filter input signal; roll-off at low frequencies and peaking at high frequencies.

Figure 13 shows the corresponding frequency response for the UPenn preamp/shaper circuit. Notice the fast roll-off of the shaper response, with a 3 dB frequency of 63 MHz. This bandwidth was chosen to reduce the noise bandwidth of the front-end detector, as well as to produce a Gaussian response pulse (the Gaussian response is often used in proportional chambers since the output voltage is proportional to the total charge collected). It is clear from Figures 9 and 11 that the result of this limited bandwidth is a slower rise time for the filtered ionization pulse.

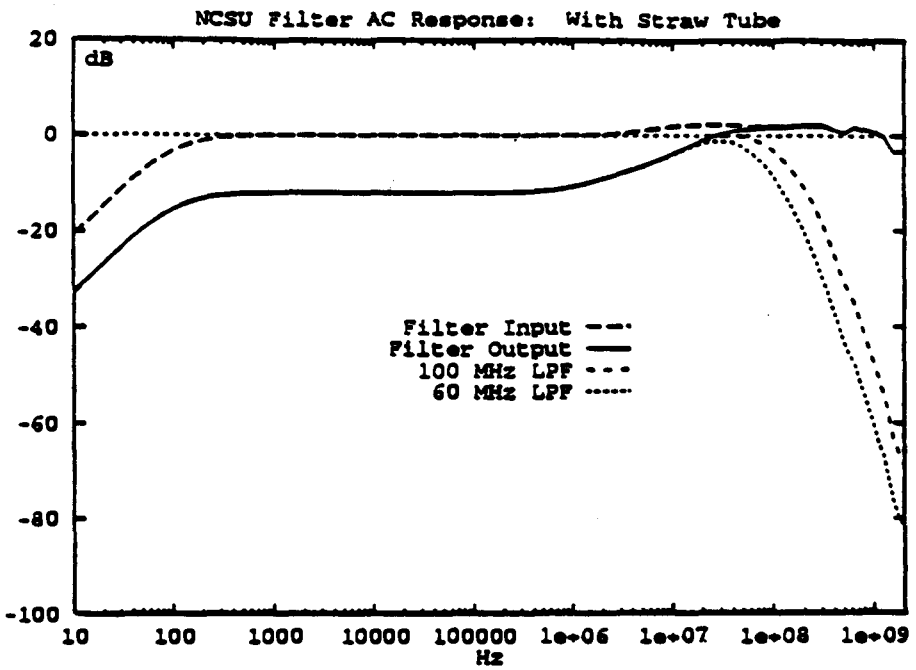

Figure 12: Frequency response of the NCSU filter at the front-end, including the effects of bandlimiting.

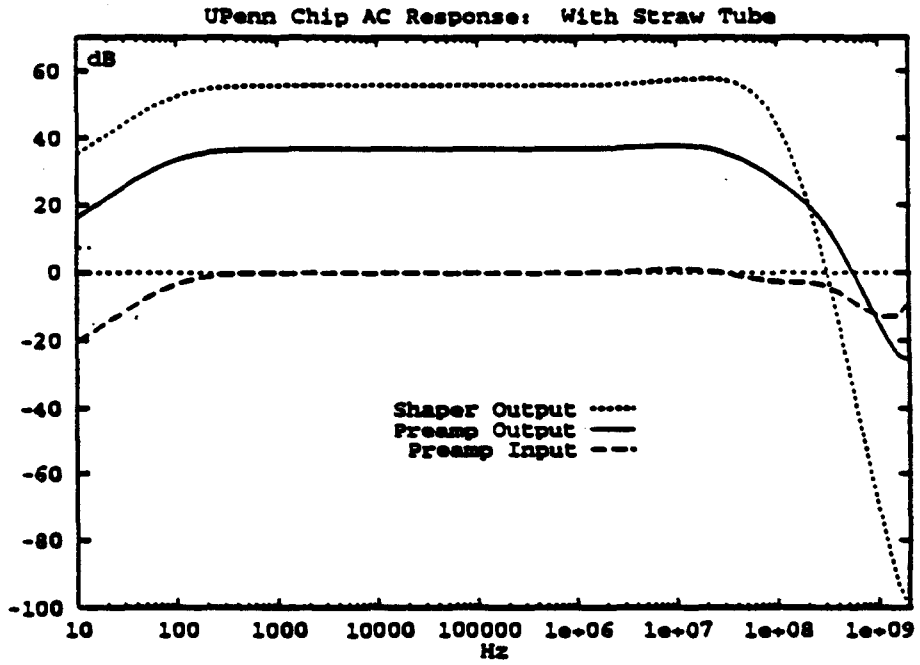

Figure 13: Frequency response of the UPenn shaper at the front-end.

5 Time-to-Threshold versus Track Radius

The design goal for the HCTC straw tube drift chamber is to determine the radius of the ionization track produced by an incident collider generated particle with a positional resolution of $\sim 100\ \mu m$. For a front-end detector that forms its timing estimate by measuring the time-to-threshold of a filtered ionization pulse, a timing resolution $\sim 500\ ps$ is required. An additional requirement is that time-to-threshold measurements on the ionization pulse must be linear with respect to both track radius and hit distance down the straw tube. This has implications for the choice of front-end signal processing and detector threshold selection.

The linearity of time-to-threshold measurements with respect to track radius was examined. SPICE simulations were performed for hits 1 m from the front end of a 2.75 m straw tube for track radii of 0.0 mm, 0.2 mm, 0.4 mm, 0.6 mm, 1.2 mm, and 1.8 mm. The straw tube was terminated at both ends by Z_T. The simulations were performed for the NCSU tail cancellation filter with bandlimiting of both 60 MHz and 100 MHz, and the UPenn preamp/shaper. The variable of comparison within each simulation is the threshold used on the filtered signal by the front-end timing detector. Three thresholds were used for each simulation. The first is an idealized proportional threshold set at half the maximum pulse height. The second is a fixed threshold set at the maximum height of the filter output for a single electron avalanche occurring on the straw tube at 0 m from the front-end (1 e threshold). This threshold level will vary for the NCSU filter for different bandwidths, and will be much larger for the UPenn preamp/shaper due to the circuit's gain. The other threshold is a multiple of the 1 e threshold (5 e). The maximum pulse height of the filter outputs for ionization pulses varies with track radius and hit distance, but usually exceeds the corresponding 10 e threshold. Note that the 1 e threshold for each case may lie below the noise floor of a realizable circuit implementation. It should be noted that the performance of the idealized half-height threshold used in these simulations will probably exceed the performance of a realizable constant-fraction discriminator set at half of the average pulse height. Also, the UPenn preamp/shaper was designed for a front-end timing detector with a low ($\sim$ 25 $mV \simeq$ 1 e) threshold; the 5 e threshold results are included for comparison with the corresponding NCSU filter results.

Figure 14 compares the simulation results for the NCSU filter with 60 MHz bandwidth. For this case the 1 e threshold is $\simeq$ 6 % of the maximum pulse height of a hit with 0.6 mm track radius. The solid line is a plot of the ideal propagation delay of the ionization

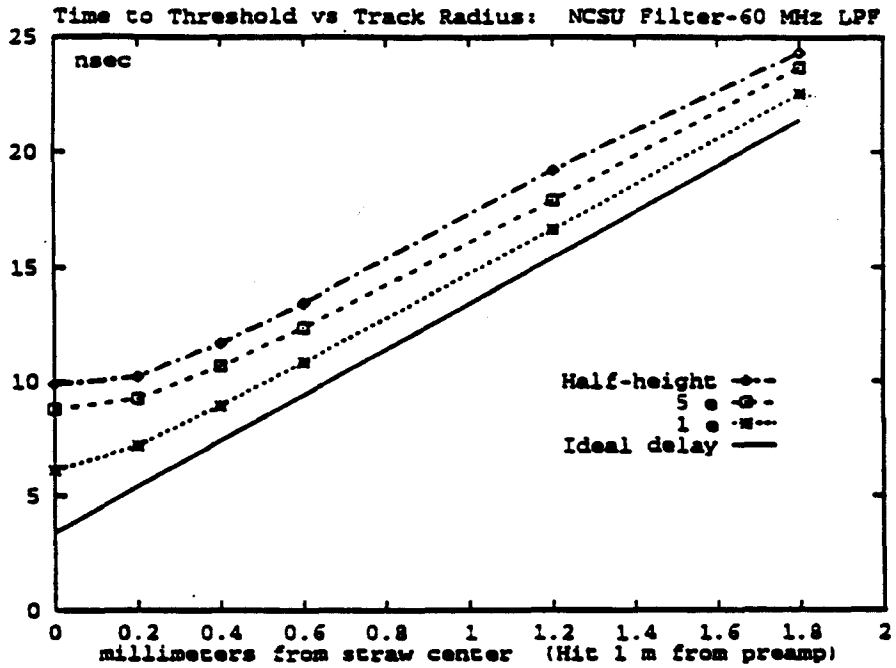

Figure 14: Time-to-Threshold vs Track Radius: NCSU Filter - 60 MHz LPF

pulse, assuming a charge drift velocity of 100 $\mu m/ns$ and a pulse propagation velocity of 3.384 ns/m. The top line shows the results for the half-height threshold, the second line down shows the results for the 5 e threshold, and the third line down shows the results for the 1 e threshold. Lower thresholds give lower time-to-threshold readings since the rise time of the filtered ionization pulse is finite. Ideally, for linear time-to-threshold performance, each line would be parallel to the ideal delay line. Linearity is roughly observed for track radii > 0.4 mm; however, for tracks near the anode wire, the time-to-threshold is larger than a linear response would predict. This is intuitive considering the shape of the ionization pulse for small track radii (see Figure 7). Tracks near the anode wire produce ionization pulses with relatively gentle slopes; the ionization pulses don't exhibit the discontinuous leading edges seen for larger track radii. This skew is most pronounced for the half-height and 5 e thresholds.

Figure 15 shows the comparable results for the NCSU filter with 100 MHz bandwidth. For this case the 1 e threshold is $\simeq$ 8 % of the maximum pulse height of a hit with 0.6 mm track radius. The 1 e threshold for the 100 MHz bandwidth case is larger than the 1 e threshold for the 60 MHz case since from Figures 8 and 10 it can be seen that the 100 MHz bandwidth filter preserves the fast rise time of an ionization pulse better than the 60 MHz

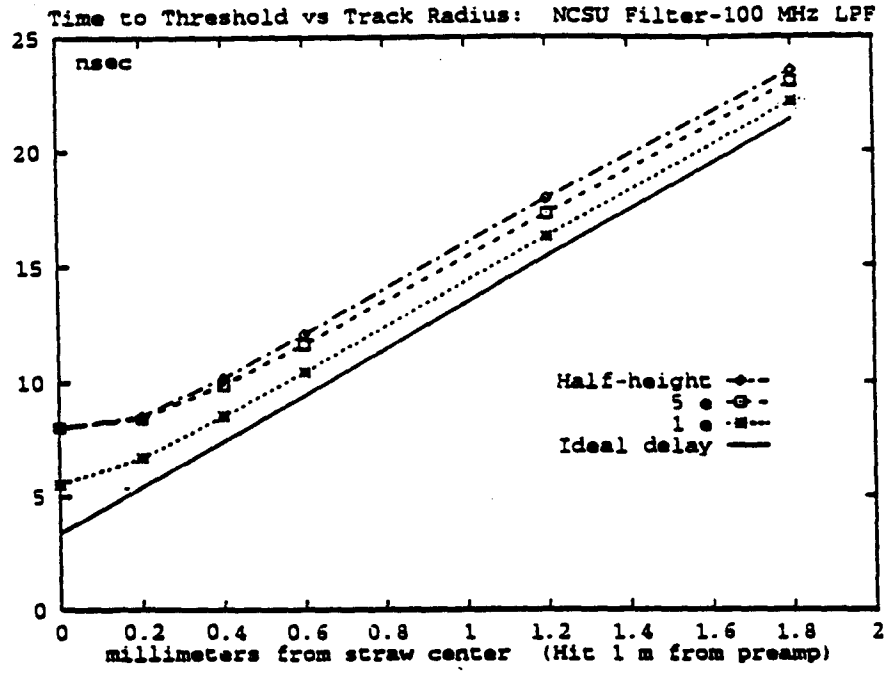

Figure 15: Time-to-Threshold vs Track Radius: NCSU Filter - 100 MHz LPF

bandwidth filter; the fast peak of the avalanche pulse is not as heavilly suppressed. Another result of faster rise time is the tighter packing of the time-to-threshold measurements, as seen in Figure 15. Good linearity is exhibited for all thresholds for all track radii except 0.0 mm. The 1 e threshold appears to exhibit marginally better performance than the 5 e threshold.

Figure 16 shows the results for the UPenn shaper circuit. The results of the UPenn bandlimiting can be seen by the delay between time-to-threshold readings at a fixed radius for different thresholds; the rise time of the ionization pulse is distorted by the UPenn filtering. Some slight skew from linearity can be seen for all track radii, and again linearity is violated for a 0.0 mm radius track. The 1 e and 5 e thresholds appear to exhibit the best linearity.

From Figures 14, 15, and 16 it is apparent that good predictions of ionization charge drift time can be obtained from time-to-threshold measurements at the front-end. The simulations of the NCSU filter for both 60 MHz and 100 MHz bandwidth demonstrate comparable linearity with the UPenn shaper for the 1 e and 5 e thresholds, and slightly better linearity for the half-height threshold, due to the NCSU filters' better preservation of the ionization pulse rise time. The 1 e threshold provides the most linear measurements, although it is only

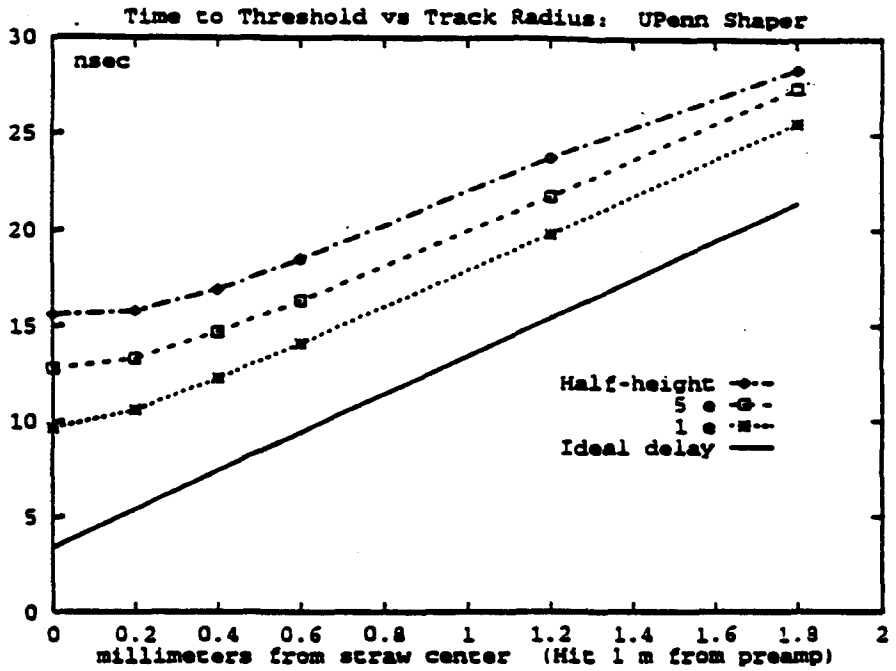

Figure 16: Time-to-Threshold vs Track Radius: UPenn Shaper

marginally better than the 5 e threshold. Performance gain between 60 MHz and 100 MHz bandwidth for the NCSU filter can only be seen for the half-height threshold. The deviation from linearity for short track radii is likely a degenerate case for time-to-threshold detector approaches and not a function of detector threshold or bandwidth. Also, this deviation is probably less significant in real operation, where electrons arrive as discrete charges; the continuum model for electron arrival current used in these simulations will overstate this deviation.

6 Time-to-Threshold versus Hit Distance

Simulations similar to those in Section 5 were performed to determine the linearity of time-to-threshold measurements with respect to hit distance down the straw tube. SPICE simulations were performed at hit distances of 0.25 *m*, 1.00 *m*, 1.75 *m*, and 2.50 *m* for track radii of 0.0 *mm* and 1.8 *mm* using the straw tube from Section 5. The simulations were performed for the UPenn preamp/shaper and the NCSU tail cancellation filter using both 60 *MHz* and 100 *MHz* bandwidth. The variable of comparison within each simulation is again the threshold used by the front-end detector. The set of thresholds used in Section 5 is again used here.

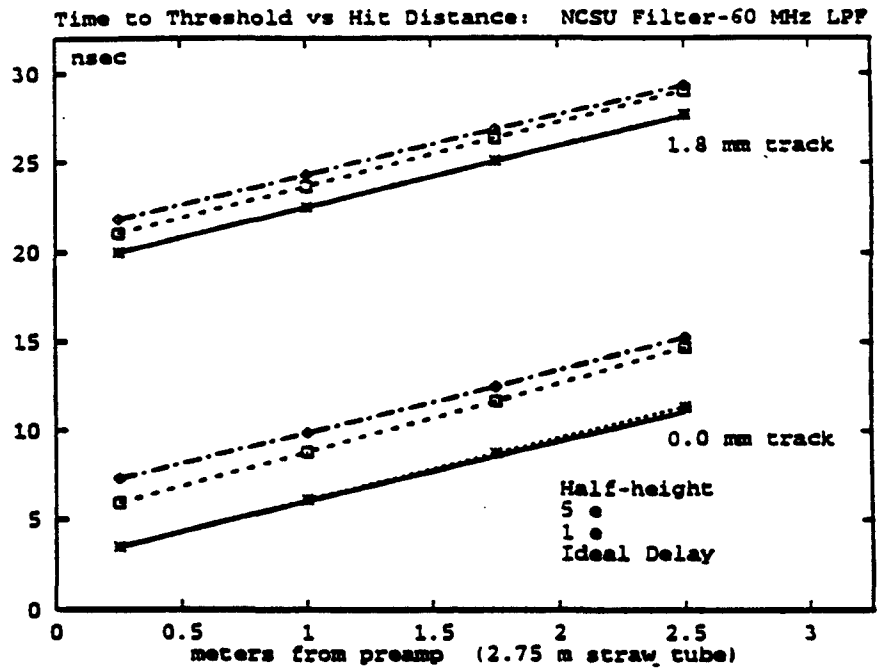

Figure 17: Time-to-Threshold vs Hit Distance: NCSU Filter - 60 *MHz* LPF

Figure 17 compares the simulation results for the NCSU filter with 60 *MHz* bandwidth. Results for the three thresholds are shown for 0.0 *mm* and 1.8 *mm* tracks. The solid line for each cluster of results is a plot of the ideal propagation delay of the ionization pulse, scaled by a constant delay to match the simulation results for each track radius. The top data line for each cluster shows the results for the half-height threshold, the second line down shows the results for the 5 *e* threshold, and the third line down shows the results for the 1 *e* threshold (this line is partially obscured by the ideal delay line). As can be seen, the

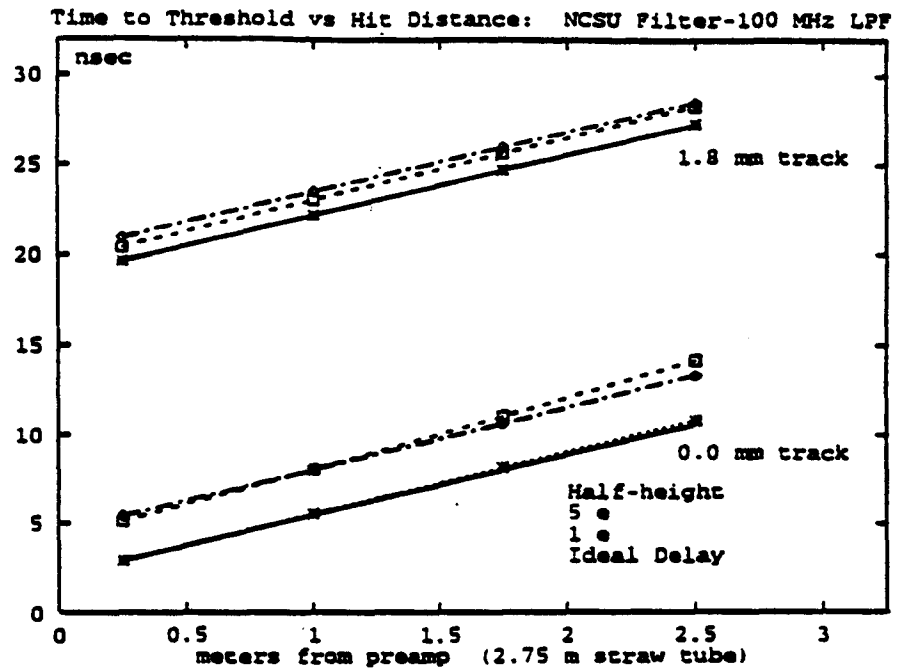

Figure 18: Time-to-Threshold vs Hit Distance: NCSU Filter - 100 *MHz* LPF

half-height threshold gives linear results for the 0.0 *mm* and 1.8 *mm* tracks. This indicates that the attenuation of the straw tube does not significantly affect the shape of the ionization pulse. The 5 *e* threshold shows some skew for the 0.0 *mm* track, but is fairly linear for the 1.8 *mm* track. The deviation from linearity for the 0.0 *mm* track should be related to the lack of a discontinuity in the track's rising edge.

Figure 18 shows the comparable results for the NCSU filter with 100 *MHz* bandwidth. Again excellent linearity is demonstrated for the half-height and 1 *e* thresholds. The 5 *e* threshold again shows skew for the 0.0 *mm* track. Tighter packing of the time-to-threshold measurements is due to the faster rise time of this bandlimiting filter's response.

Figure 19 shows the results for the UPenn shaper circuit. The results for the 5 *e* and 1 *e* thresholds are comparable to the results shown for the NCSU filter with 60 *MHz* bandwidth. The results for the half-height threshold again exhibit good linearity.

Figures 17, 18, and 19 demonstrate that a good prediction of the propagation time along the straw tube for an ionization pulse can be obtained from time-to-threshold measurements at the front-end. The results for the NCSU filter with 100 *MHz* bandwidth for the half-height and 1 *e* thresholds appear to be marginally better than those for the other two filters. Skew

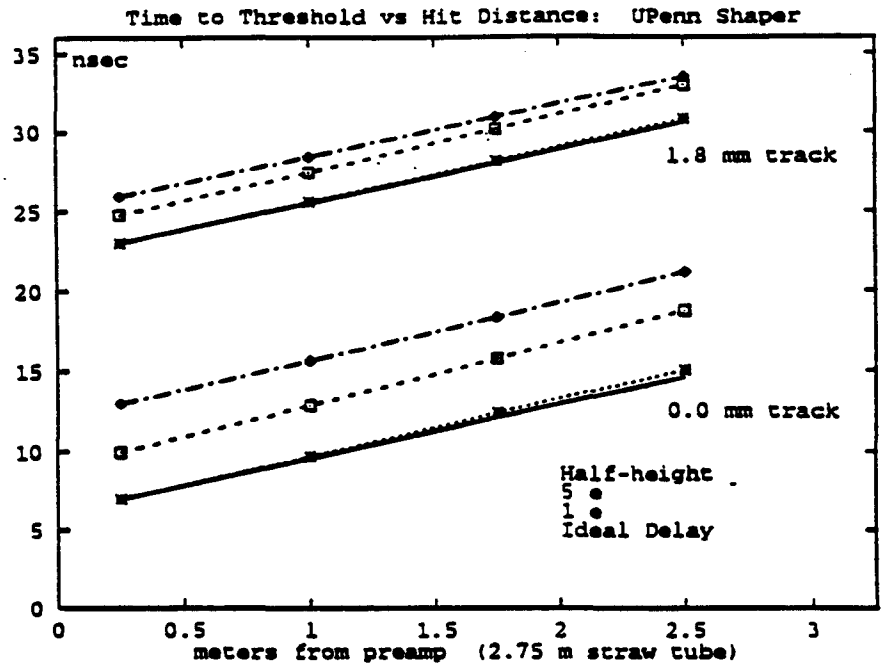

Figure 19: Time-to-Threshold vs Hit Distance: UPenn Shaper

in linearity is observed for the 5 e threshold for 0.0 mm track radius. This is likely a result of the gradual rise of the ionization pulse for this case. As the pulse is attenuated along the straw tube, the threshold voltage moves along the pulse curve.

7 Double-Hit Timing Resolution

The simulation results from Sections 5 and 6 assume that there is only one ionization pulse occurring on the straw tube during the observation period (100 ns). In the actual operation of the SSC the period of particle generation is $\sim$ 16 ns; the probability of only one event occurring in 100 ns is low. The design of the pulse-shaping electronics in the HCTC must account for the possible interaction at the front-end of ionization pulse currents from separate events. Since the ionization pulses will not arrive synchronously at the front-end (due to the variability of hit distance and track radius) the best that can be achieved is to reduce the temporal width of the pulses through the appropriate choice of front-end preamplifier bandwidth and tail cancellation filtering (see Section 4).

If "ideal" tail cancellation can be achieved by front-end signal processing on the ionization pulses, then the double-hit resolution of a straw tube terminated on both ends by the optimum matching impedance (Z_T) will not be impaired if the two hits do not occur within the time range when the initial pulse is rapidly decaying back to the baseline ($\sim$ 30 ns for the NCSU tail cancellation filters). Simulations were performed using the straw tube from Sections 5 and 6 to determine the performance of the NCSU filter. The possible combinations of double-hits that could be observed are endless; for these simulations, two hits of 0.6 mm track radius separated by 32 ns and occurring at the same point along the straw tube are used. The variable of interest is how the time-to-threshold varies between the two hits as they occur along different points on the straw tube. Ideally, the time-to-threshold for the second hit should occur 32 ns after the time-to-threshold for the first hit, however, if the tail of the first pulse has not decayed back to the baseline (or if it has overshot) before the arrival at the front-end of the second pulse then the difference between the two measurements will deviate from 32 ns.

Figure 20 is a plot of a double-hit occurring 1 m from the front-end. The output response of the NCSU filters for 60 MHz and 100 MHz bandwidth is shown. Note that the voltage at the front-end from the inital ionization pulse does not decay back to the baseline before the second pulse arrives. It can be seen for both bandwidths that the NCSU filter dramatically improves the decay time of the initial ionization pulse's tail. By the time the second ionization pulse arrives, each filter's output is very close to the baseline (some overshoot in the filters' response is evident). In comparison, Figure 21 is a plot of the response of the UPenn preamp/shaper to the same double-hit. The lack of tail cancellation for this filter is clearly

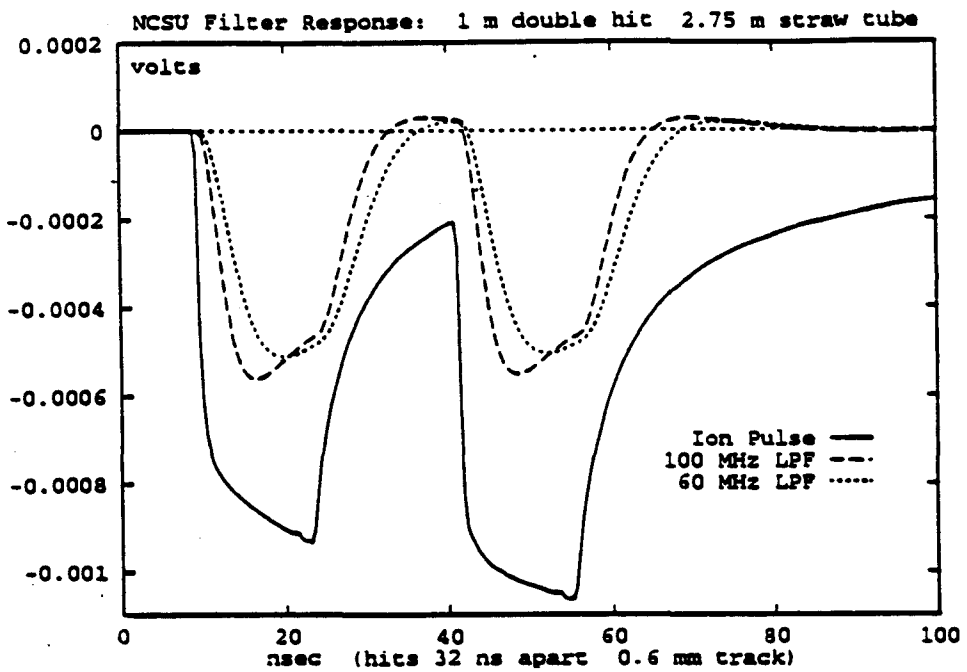

Figure 20: Response of the NCSU filter to a double-hit of ionization pulses of 0.6 mm track radius. The straw tube is 2.75 m long and is terminated by Z_T at both ends. The hits are 32 ns apart and occur 1 m from the front-end.

evident given the fact that the filter's response for the initial ionization pulse does not decay back to the baseline before the arrival of the second ionization pulse.

Figure 22 is a plot of the decrease in time-to-threshold between two hits of 0.6 mm track radius for the NCSU filter for 60 MHz and 100 MHz bandwidth. The values plotted are the decrease in the time to reach each specified threshold for two hits separated by 32 ns. Values are plotted for hit distances of 0.25 m, 1.00 m, 1.75 m, and 2.50 m from the front-end along a 2.75 m straw tube. The thresholds plotted are the 5 e and ideal half-height thresholds from Sections 5 and 6 (the half-height threshold used here varies for the first and second ionization pulses with maximum pulse height). Values for the 1 e threshold are not reported since the tail of the initial ionization pulse does not decay below this threshold before the arrival of the second ionization pulse for all hit distances. A trend can be seen in the results for increasing hit distance; the decrease in time-to-threshold increases. This could possibly be a result of ionization pulse attenuation and smearing in the straw tube. The results for both NCSU filters are nicely packed within an absolute difference of 0.5 ns, and actually go negative for hits near the front-end (due to pulse overshoot). The increase in filter bandwidth to 100 MHz results in a tighter packing of the results.

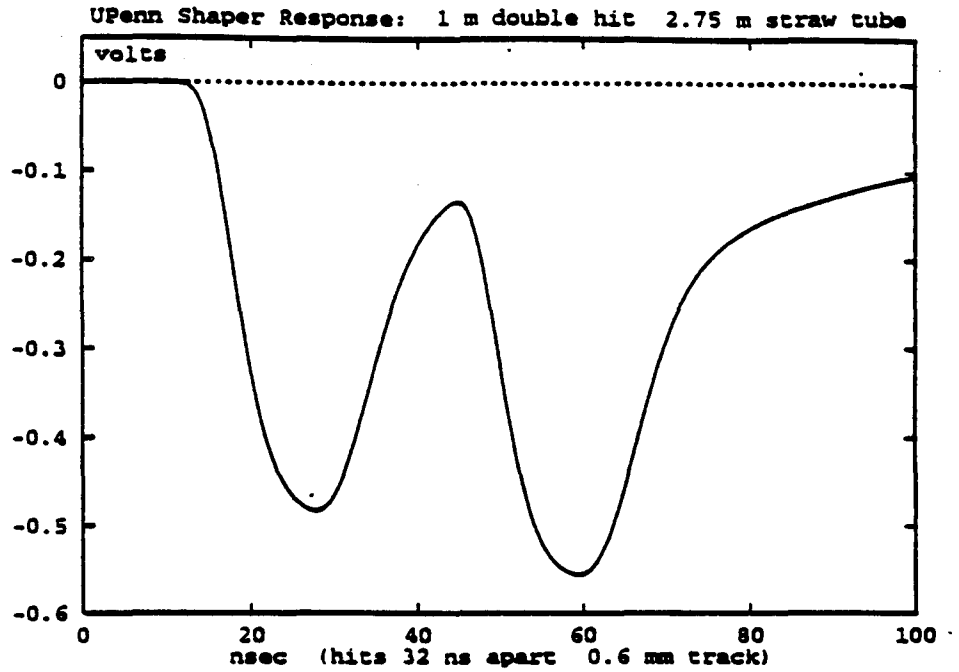

Figure 21: Response of the UPenn shaper to a double-hit of ionization pulses of 0.6 mm track radius. The straw tube is 2.75 m long and is terminated by Z_T at both ends. The hits are 32 ns apart and occur 1 m from the front-end.

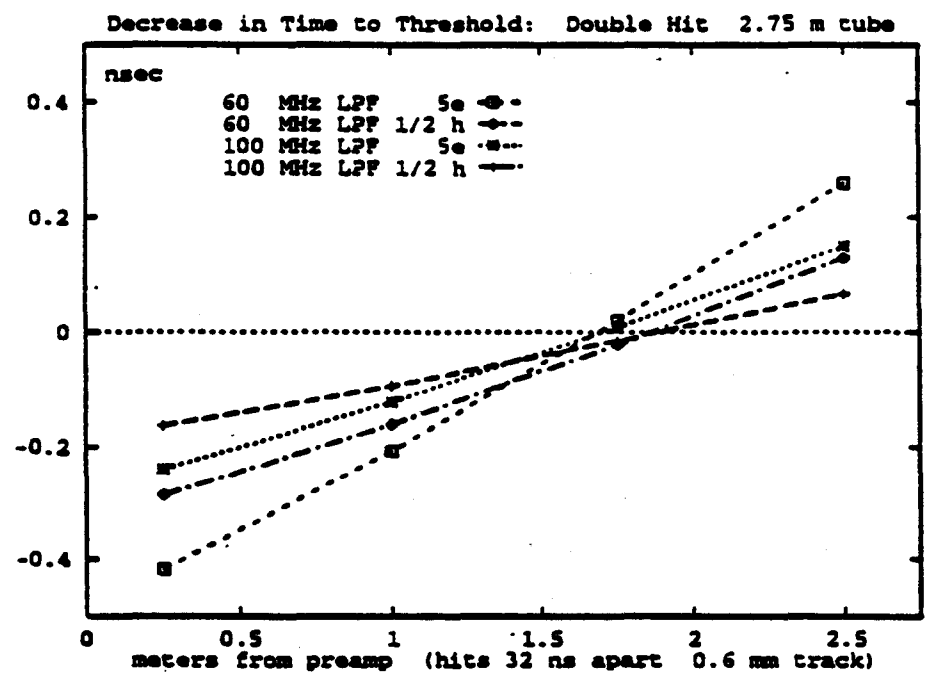

Figure 22: Decrease in time-to-threshold for double-hits for the NCSU filter with 60 MHz and 100 MHz bandlimiting (Z_T termination case).

The possibility of using long straw tubes in the HCTC detector is currently being examined. One proposal is to use 8 m straw tubes, with a break in the middle of the anode wire to reduce total tube occupancy. This break in the wire will cause the two halves of the tube to behave identically to 4 m tubes with an open circuit termination at the far-end (see Figure 5). In Section 2 it was shown how this open circuit termination can lead to severe reflections of an ionization pulse in the straw tube. The impact of these reflections is made worse by the 4 m tube length, since the end-to-end propagation delay exceeds 25 ns. These reflections may have a small impact on time-to-threshold measurements for ionization pulses occurring near the break, since the rising edge of the pulse will be reinforced by the reflection. The reflections should have a severe impact on the decay time of ionization pulses, since the reflection will appear as another incident pulse occurring up to 27 ns later.

Simulations were performed to determine how reflections in the proposed 8 m straw tube design would impact double-hit timing resolution. The straw tube used in the simulation was 4 m long, terminated by the optimal matching impedance Z_T at the front-end and open circuit terminated at the far-end. Simulations were performed at hit distances of 0.5 m, 1.5 m, 2.5 m, and 3.5 m for two hits of 0.6 mm track radius occurring at the same hit distance. The time separation between the hits was 32 ns. Figure 23 is a plot of a double-hit occurring 1.5 m from the front-end. The response of the NCSU filter for 60 MHz and 100 MHz bandwidth is shown. The distinct arrival of reflections can be seen in the plot. The first reflection prevents the tail of the first ionization pulse from returning to the baseline before the arrival of the second pulse. Simulations using the UPenn preamp/shaper indicate that it is infeasible to use an 8 m straw tube without tail cancellation in the front-end preamplifier.

Figure 24 is a plot of the decrease in time-to-threshold between two hits of 0.6 mm track radius for the NCSU filter for 60 MHz and 100 MHz bandwidth. For the 100 MHz bandwidth filter, results for the 5 e and ideal half-height thresholds are plotted. For the 60 MHz bandwidth filter only the half-height threshold results are plotted since results for the 5 e threshold could not be obtained in all cases due to the impact of reflections. The results for the 4 m straw tube are clearly worse than those shown in Figure 22 for the 2.75 m tube with matching termination at both ends. Intuitively, the impact of reflections on the double-hit time-to-threshold measurements should be worse for hits closest to the front-end, since the reflection will then incur an end-to-end propagation delay. Why the double-hit timing errors are less for hits at 0.5 m distance than at 1.5 m distance is not obvious.

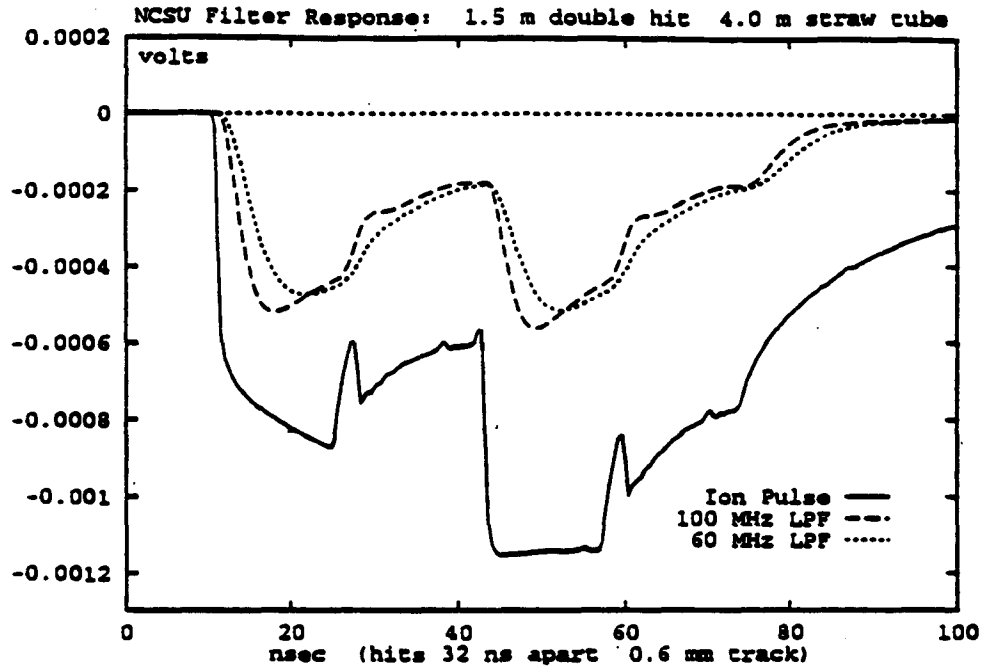

Figure 23: Response of the NCSU filter to a double-hit of ionization pulses of 0.6 mm track radius. The straw tube is 4.0 m long and is terminated by Z_T at the front-end and is open at the far-end. The hits are 32 ns apart and occur 1.5 m from the front-end.

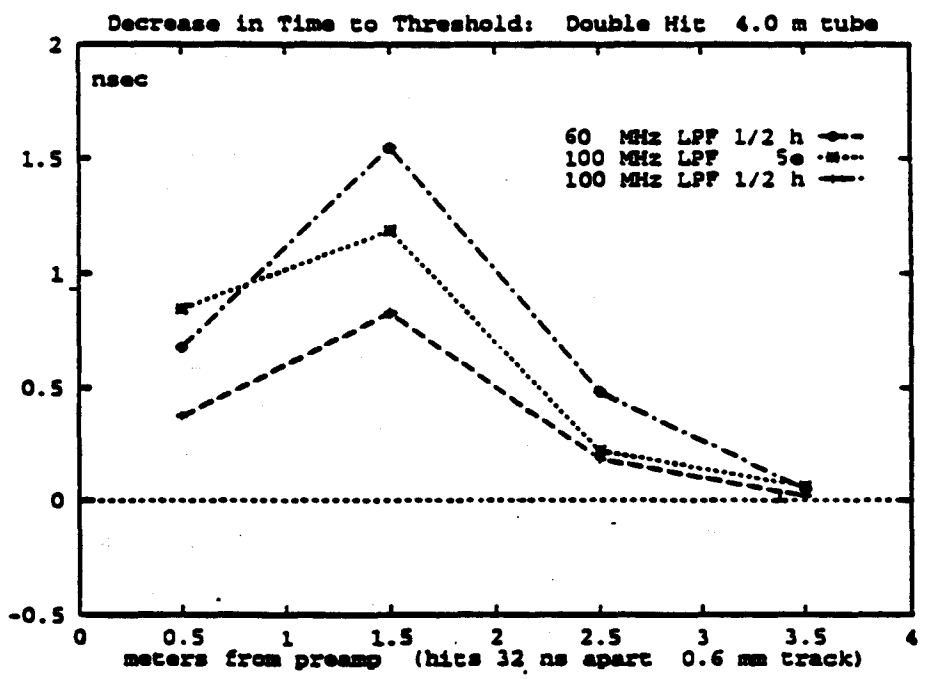

Figure 24: Decrease in time-to-threshold for double-hits for the NCSU filter with 60 MHz and 100 MHz bandlimiting (open circuit termination case).

The maximum deviation in time-to-threshold measurements for the 60 MHz bandwidth filter is ~ 1.5 ns. For the 100 MHz bandwidth filter the maximum deviation is ~ 1.2 ns (for the 5 e threshold), which corresponds to a distance measurement error of ~ 120 μm. The half-height threshold results for the 100 MHz bandwidth filter exhibit even less variance.

In general, the bandwidth increase to 100 MHz appears to improve the double-hit timing resolution. This is likely due to the fact that this higher bandwidth filter better preserves the rise time of ionization pulses. A fast rise time at the filter output decreases the sensitivity of time-to-threshold measurements to the baseline voltage of the filter output when a second ionization pulse arrives; since the filter response reaches any threshold faster, time-to-threshold errors due to the baseline voltage will not exceed the rise time of the pulse. The use of a high-bandwidth front-end preamplifier in conjunction with a tail cancellation filter appears to make the use of an 8 m straw tube detector feasible.

8 Conclusions

It was shown in Section 2 that proper termination of the straw tube at both ends will effectively eliminate any signal reflections. In the proposed 8 m straw tube design, reflections off the anode wire line break will pose a problem. In either event, tail cancellation at the front-end preamplifier must be included to permit adequate double-hit timing resolution. The results from Section 7 seem to indicate that this is feasible.

The results from Sections 5 and 6 seem to indicate that the preamplifier bandwidth will not have a significant effect on timing performance for varying track radii and varying hit distance. However, higher bandwidth does improve timing performance in the presence of double-hits. These results seem to indicate that the front-end preamplifier bandwidth should be greater than 60 MHz. Of course, the trade-off with increased bandwidth is increased noise sensitivity. However, increasing the preamplifier bandwidth reduces the timing detector's sensitivity to noise when a small threshold is not used, since the fast rising edge of ionization pulses is preserved. A threshold greater than 1 e must be used in any event to allow for double-hit detection.

Given the simulation results of Sections 5, 6, and 7, the choice of detector threshold is inconclusive. Overall, the results from the idealized half-height threshold appear to be superior to those of the 5 e threshold. This is due in part to the fact that straw tube attenuation

does not appear to significantly affect the ionization pulse shape. The 5 e threshold results are comparable to the half-height threshold results, except in the case of time-to-threshold versus hit distance measurements where the ionization track radius is small. In this case skew is observed in the 5 e threshold distance predictions. However, for both large thresholds, the prediction of track radius is skewed for small radii ionization pulses due to the lack of a fast edge in the pulse. Accurate timing predictions for tracks with small radii may be impossible. Also, it must be remembered that the results reported for the idealized half-height threshold are probably much better than those that would be observed in a realizable implementation. Given its simplicity of hardware implementation, a large fixed timing threshold $\sim$ 5 e may be the most appropriate choice.

References

[1] T. Ekenberg and M. Newcomer, "Modeling Small Diameter Straw Tubes in Terms of their High Frequency Electrical Characteristics", Univ. of Penn. report #0179E, Nov. 1989.

[2] R. A. Boie, A. T. Hrisoho, and P. Rehak, "Signal Shaping and Tail Cancellation for Gas Proportional Detectors at High Counting Rates", *IEEE Trans. Nuc. Sci.*, pp. 603-609, Feb. 1981.

[3] H. Iwasaki, "A Study on Time Resolution for a Straw Chamber", KEK Preprint #89-158, Nov. 1989.

Hybrid Subsystem Progress Report for FY1991

Studies of Plastic Scintillating Fibers with Avalanche Photodiode Readout

Northeastern University
Physics Department
Boston, MA 02115

G. Alverson
A. Grims
M. Glaubman
I. Leedom
S. Reucroft
T. Yasuda

September 1991

Studies of Plastic Scintillating Fibers with Avalanche Photodiode Readout

The plastic scintillating fiber (PSF) research task associated with the HCTC collaboration includes the following three major subjects: (1) continuing studies of the avalanche photodiode (APD) as a fiber readout device; (2) continuing evaluation of the optical characteristics of individual fiber samples with the aim of selecting the tracker fiber type; (3) investigation of ribbon manufacture alternatives. The progress of these studies are discussed in the following sections.

1.1 APD

We have tested a number of APD's manufactured by EG&G (C30921S) which consist of a 0.5 mm diameter APD and a 0.5 mm diameter light guide in a package. The light guides in our devices have been changed from the standard 0.25 mm diameter ones to improve the optical coupling between fiber and APD. The detection efficiency for ionizing particle of a fiber was measured using a fiber telescope and ^{106}Ru source. The test setup is shown in Fig. 1. We have used APD's in the Geiger mode in this application. Corrections for geometrical effects due to mismatching between the fiber and APD dimensions have been applied to the raw 2-fold and 3-fold coincidence counts. The best result for detection efficiency were obtained with Bicron G2 fibers and are shown in Fig. 2. These results are very encouraging and show that the efficiency is never below 80% over the length of 4 m.

To reduce costs, the diameter of plastic scintillating fibers in the design of the HCTC was increased from 0.5 mm to 0.875 mm last year, and again from 0.875 mm to 1.5 mm this year. This has lead EG&G to fabricate APD's with 1.5 mm ball lenses which provide a better optical coupling for fibers with a diameter greater than 0.5 mm as compared to the standard light guide. A schematic of an APD with a ball lens is shown in Fig. 3. The testing using this device is currently under way.

1.2 Fibers

We have measured the detection efficiencies of several fibers as a function of distance from the photo detector, using the above mentioned setup. We have tested fibers from three manufacturers, Bicron, Kuraray, and Optectron. The test results are shown in Figs. 4-11. Most of the fibers with a 0.5 mm diameter do not give high enough efficiencies, except for the Bicron H fiber. Two Optectron fibers with 1 mm diameter have rather short attenuation lengths. We have obtained promising results from Bicron G2 fiber, and from

Kuraray SCSF 81 and SCSF 3HF fibers. From the tests we have conducted, we are leaning toward choosing Bicron G2 fibers.

1.3 Ribbon Fabrication

We have measured the average center to center spacing of individual fibers and the average width of fiber ribbons manufactured by Kuraray and Bicron. The Bicron ribbon consists of 282 fibers of 1 mm diameter. The average spacing of this ribbon is 1.1025±0.0015 mm over the length of 1 m. The average total width of the ribbon is 310.92±0.30 mm. The Kuraray ribbon consists of 100 fibers of 1 mm diameter. The average center to center spacing of fibers is 1.072±0.20 mm. From these results, we conclude that the manufacturers of plastic scintillating fibers have developed the necessary technique to fabricate fiber ribbons. We propose to purchase the full scale ribbons from these manufacturers and evaluate them in FY1992. A price estimate was obtained for 4-m long ribbons which contain 1024 fibers in two layers, with 50-μm fiber location precision (see Fig. 12).

APD Test Setup

NU

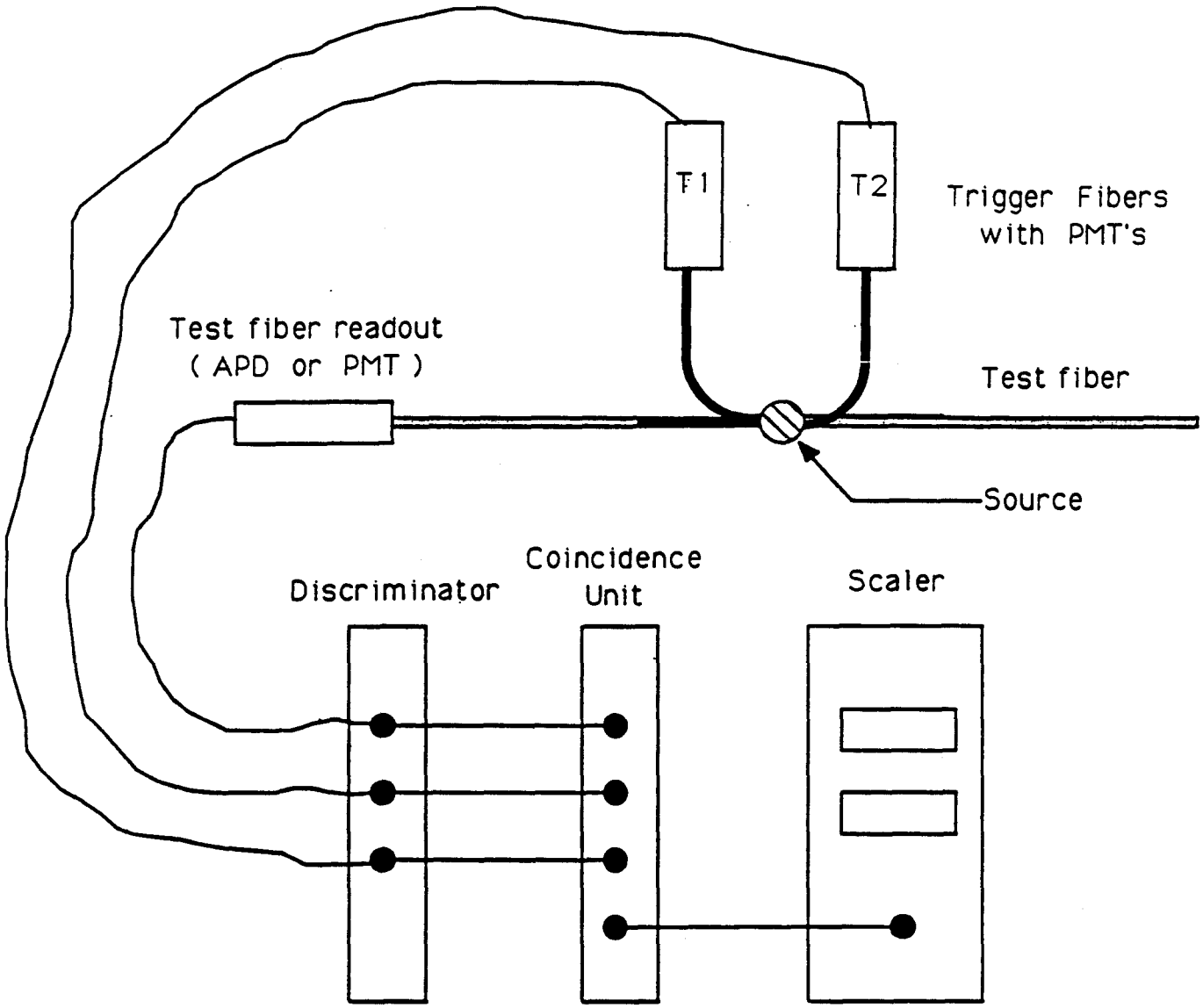

Use a Ru 106, 2mCi source to trigger the system.

Figure 1.

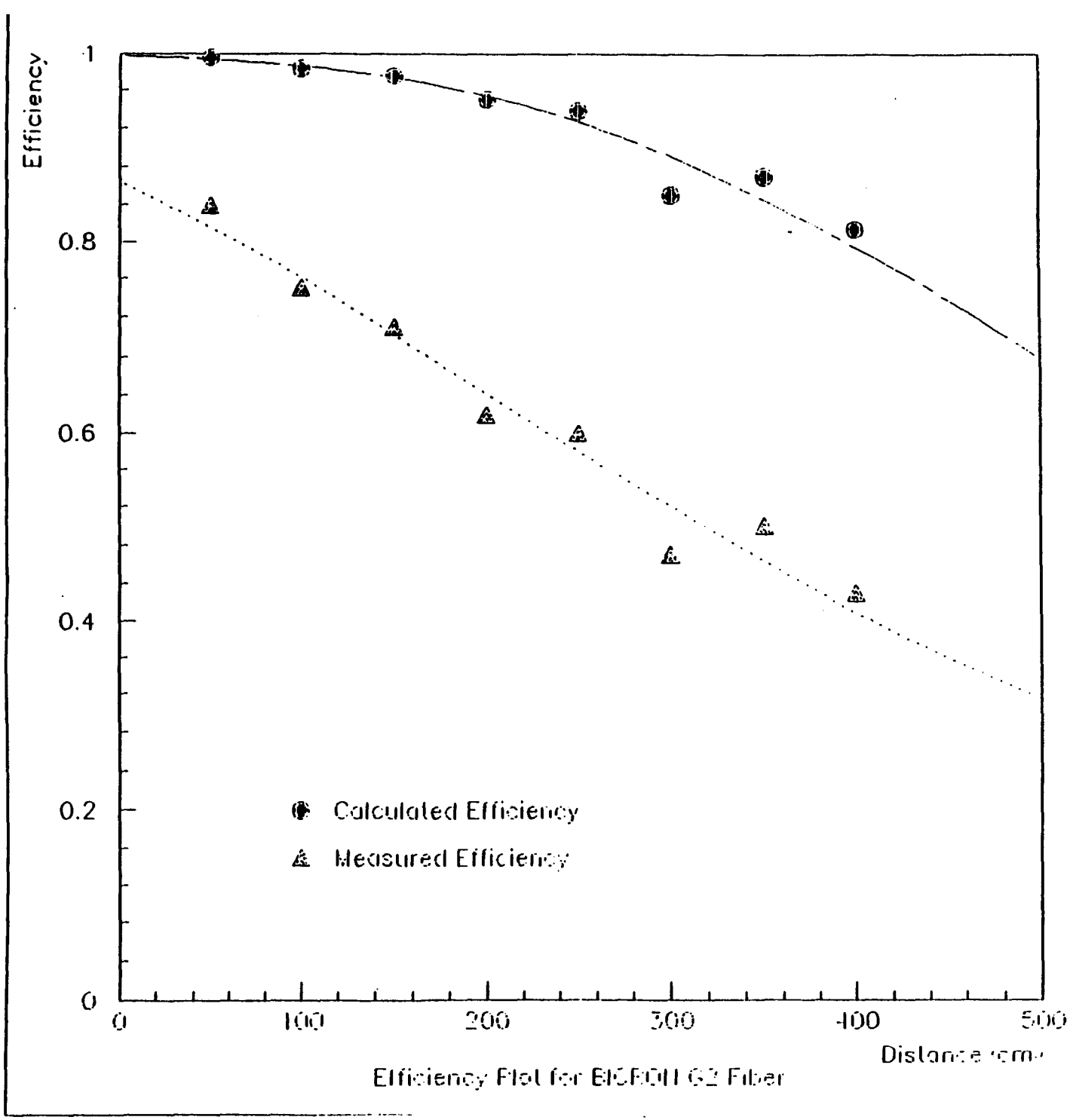
Efficiency
1
0.8
0.6
0.4
0.2
0
0
100
200
300
400
500
Distance (cm)
Calculated Efficiency
Measured Efficiency
Efficiency Plot for BICRON G2 Fiber

Figure 2.

NU

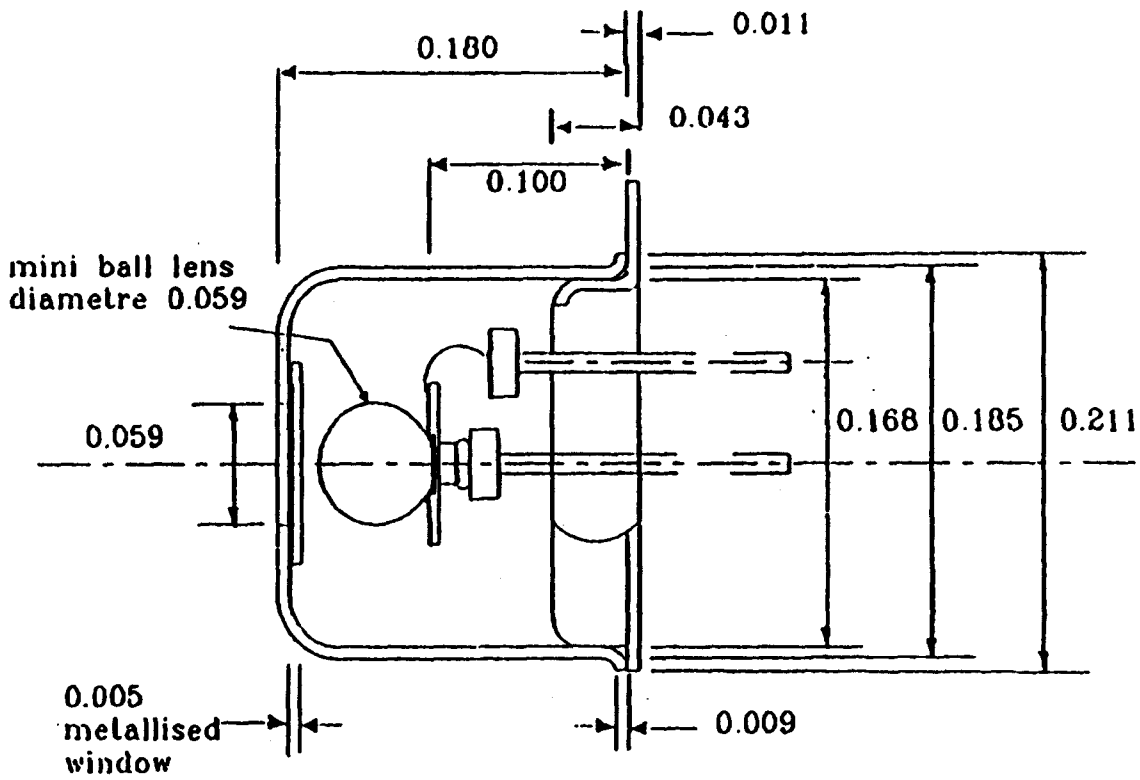

Mini-Ball Lens assembly (TO18 package)
all units in inches, unless specified.

sketch: T 398-1	date: march 5 91

Figure 3.

NU

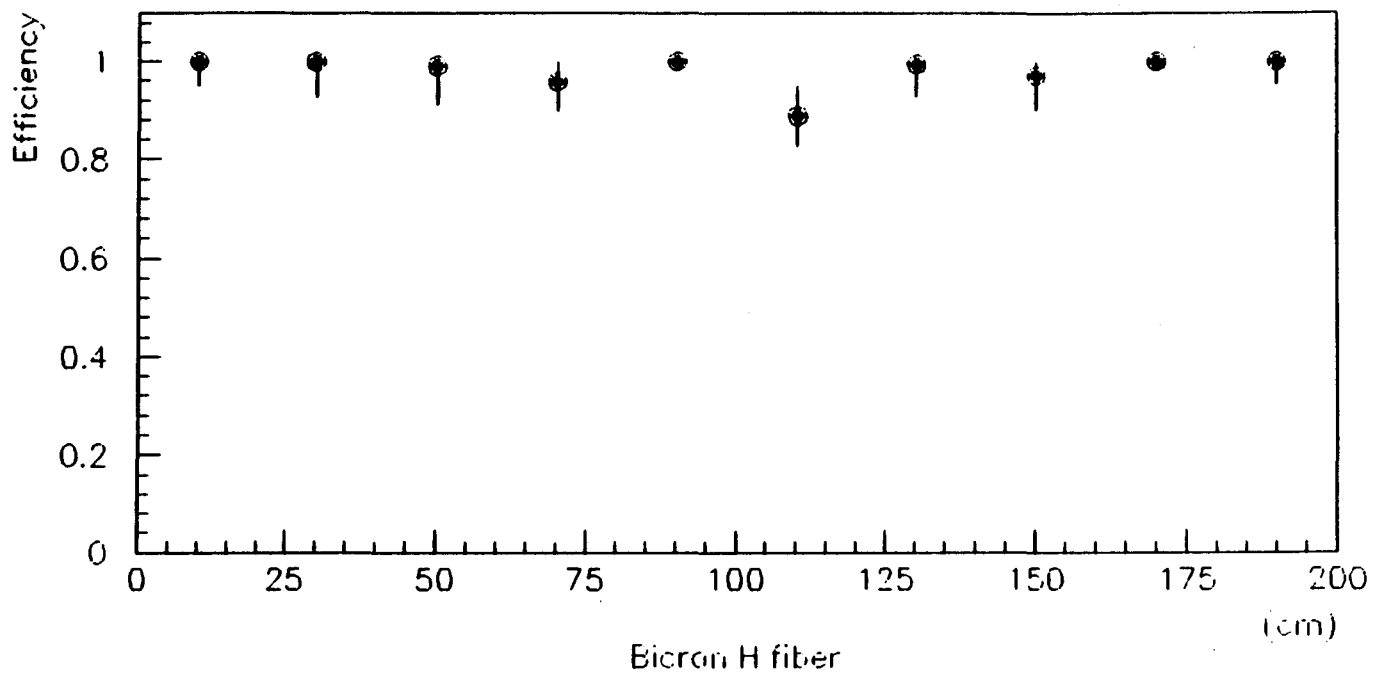
Efficiency
1
0.8
0.6
0.4
0.2
0
0
25
50
75
100
125
150
175
200
(cm)
Bicron H fiber

Figure 4.

NU

Eff. Chart. SCSF 81 1mm

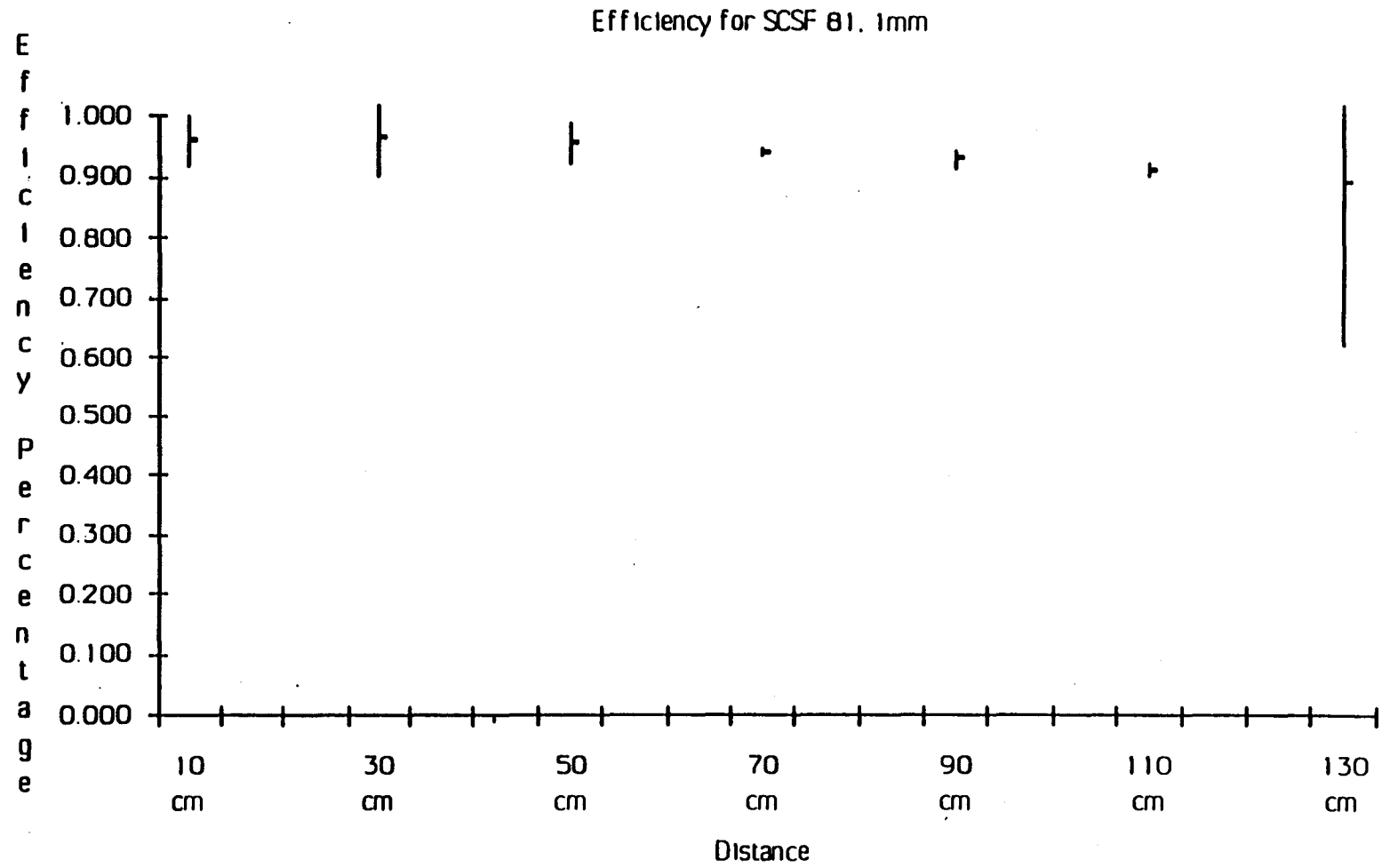

Figure 5.

NU

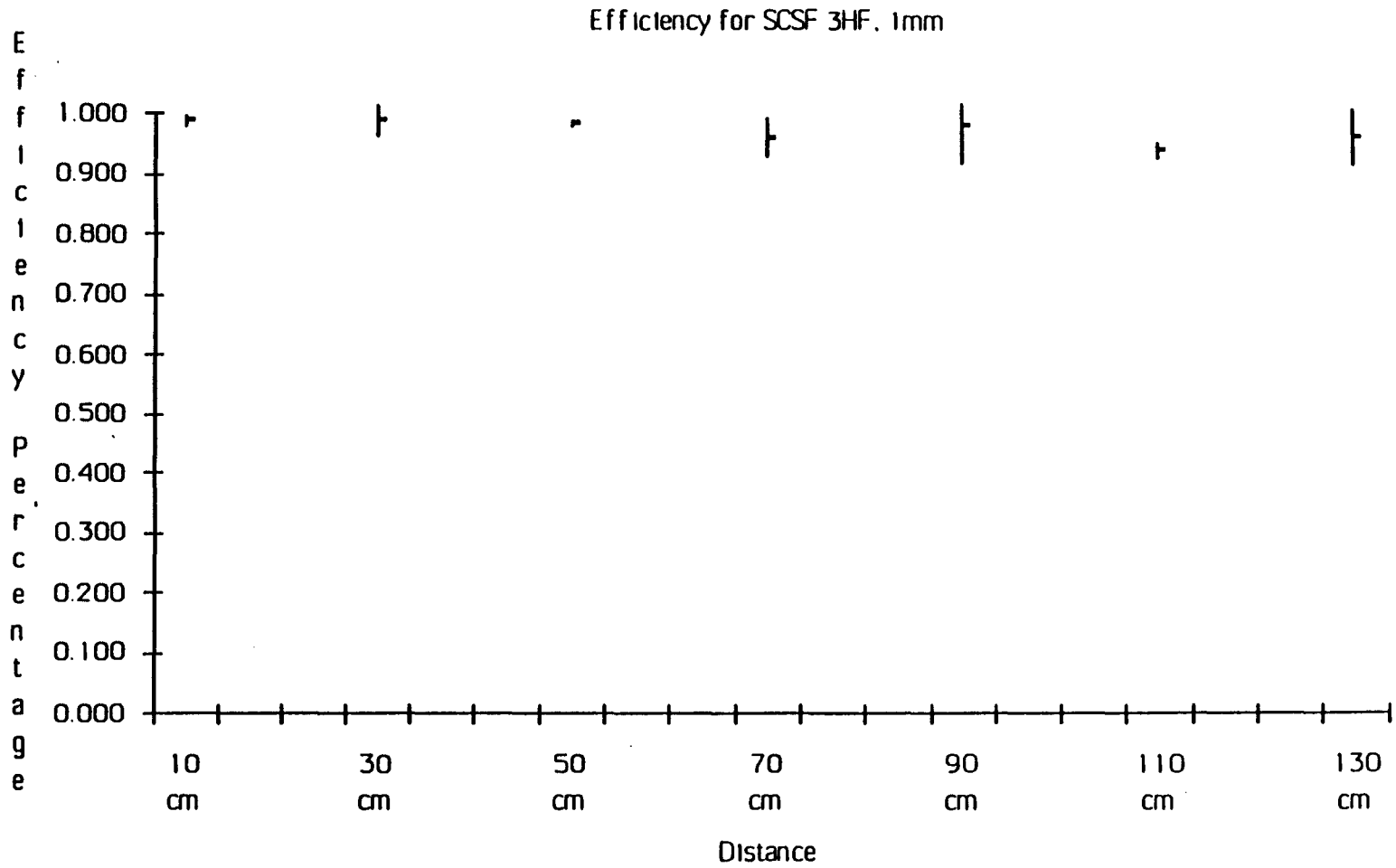
Efficiency for SCSF 3HF, 1mm
Efficiency Percentage
1.000
0.900
0.800
0.700
0.600
0.500
0.400
0.300
0.200
0.100
0.000
10 cm
30 cm
50 cm
70 cm
90 cm
110 cm
130 cm
Distance

Figure 6.

NU

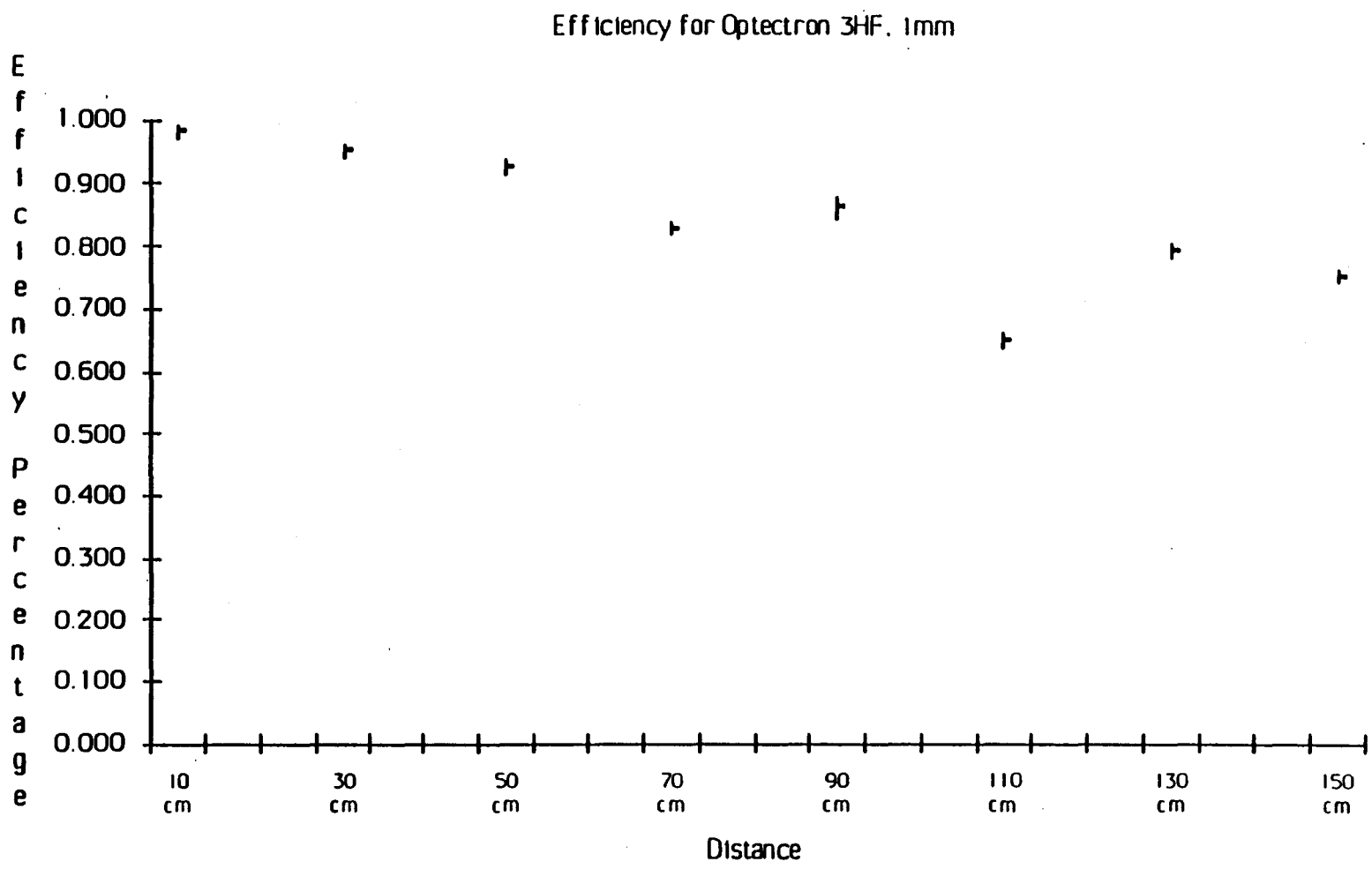
Efficiency for Optectron 3HF. 1mm
Efficiency Percentage
1.000
0.900
0.800
0.700
0.600
0.500
0.400
0.300
0.200
0.100
0.000
10 cm
30 cm
50 cm
70 cm
90 cm
110 cm
130 cm
150 cm
Distance

Figure 7.

NU

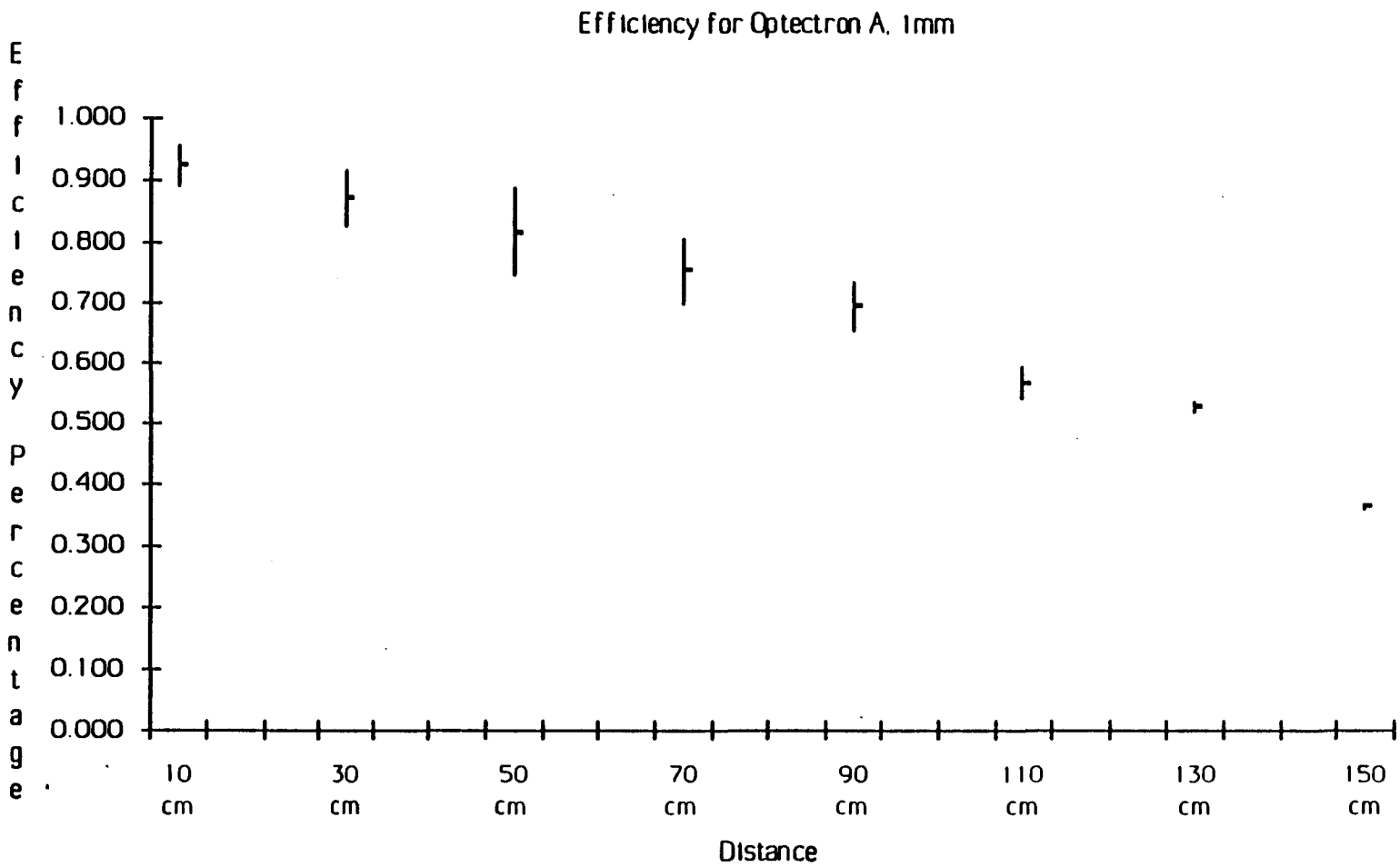
Efficiency for Optectron A, 1mm
Efficiency Percentage
1.000
0.900
0.800
0.700
0.600
0.500
0.400
0.300
0.200
0.100
0.000
10 cm
30 cm
50 cm
70 cm
90 cm
110 cm
130 cm
150 cm
Distance

Figure 8.

NU

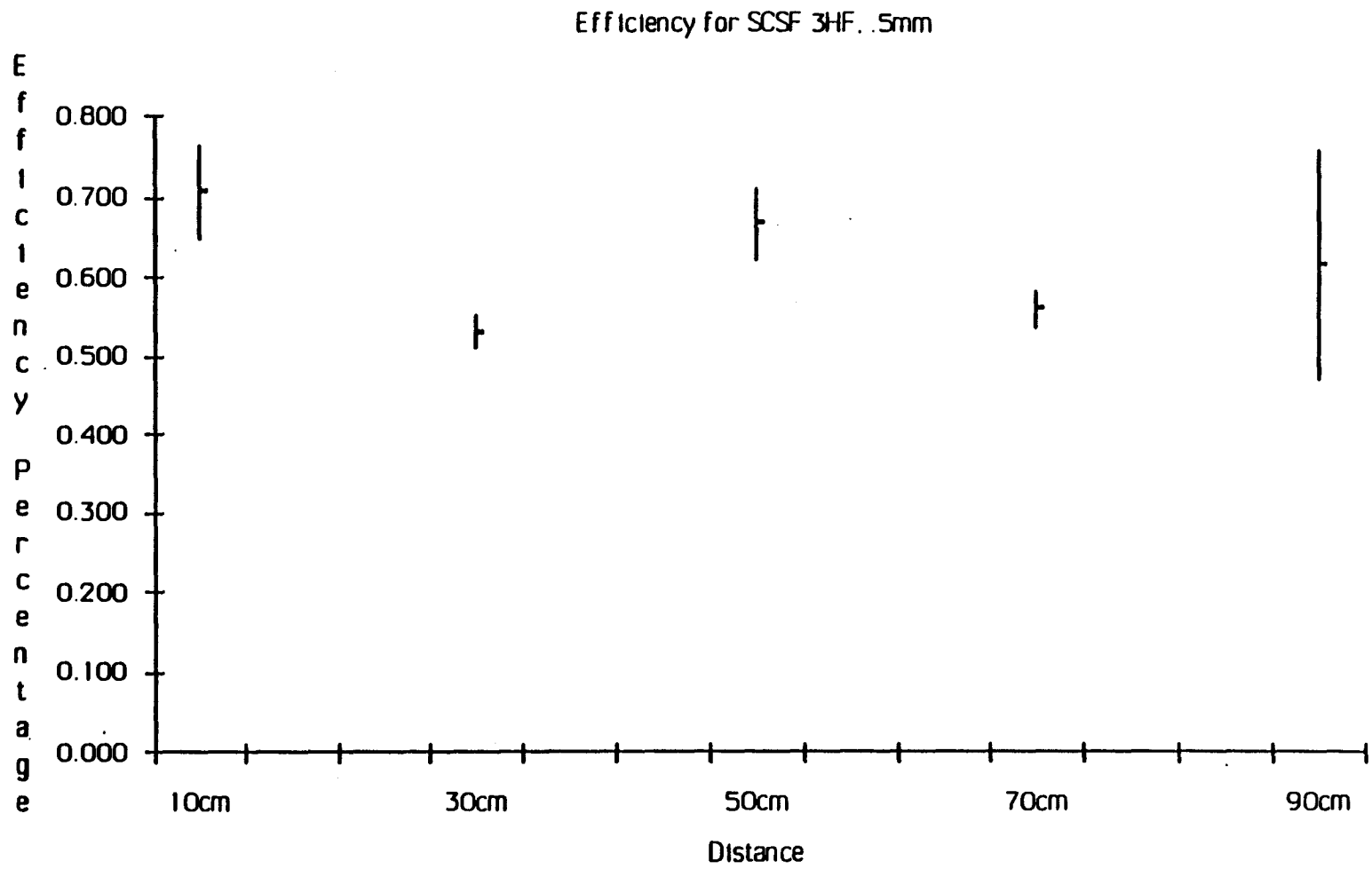
Efficiency for SCSF 3HF..5mm
Efficiency Percentage
0.800
0.700
0.600
0.500
0.400
0.300
0.200
0.100
0.000
10cm
30cm
50cm
70cm
90cm
Distance

Figure 9.

NU

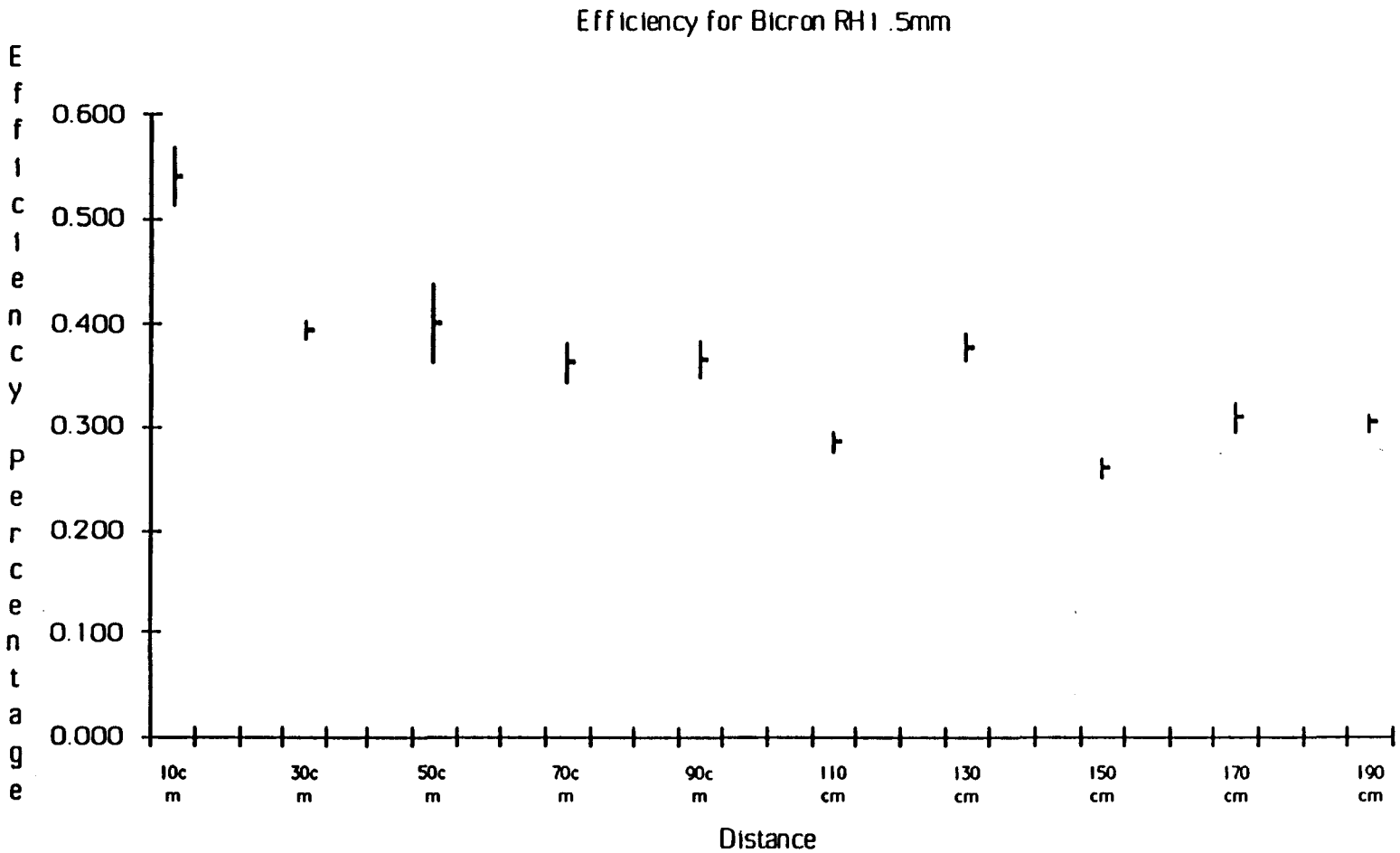
Efficiency for Bicron RH1.5mm
Efficiency Percentage
0.600
0.500
0.400
0.300
0.200
0.100
0.000
10cm
30cm
50cm
70cm
90cm
110 cm
130 cm
150 cm
170 cm
190 cm
Distance

Figure 10.

NU

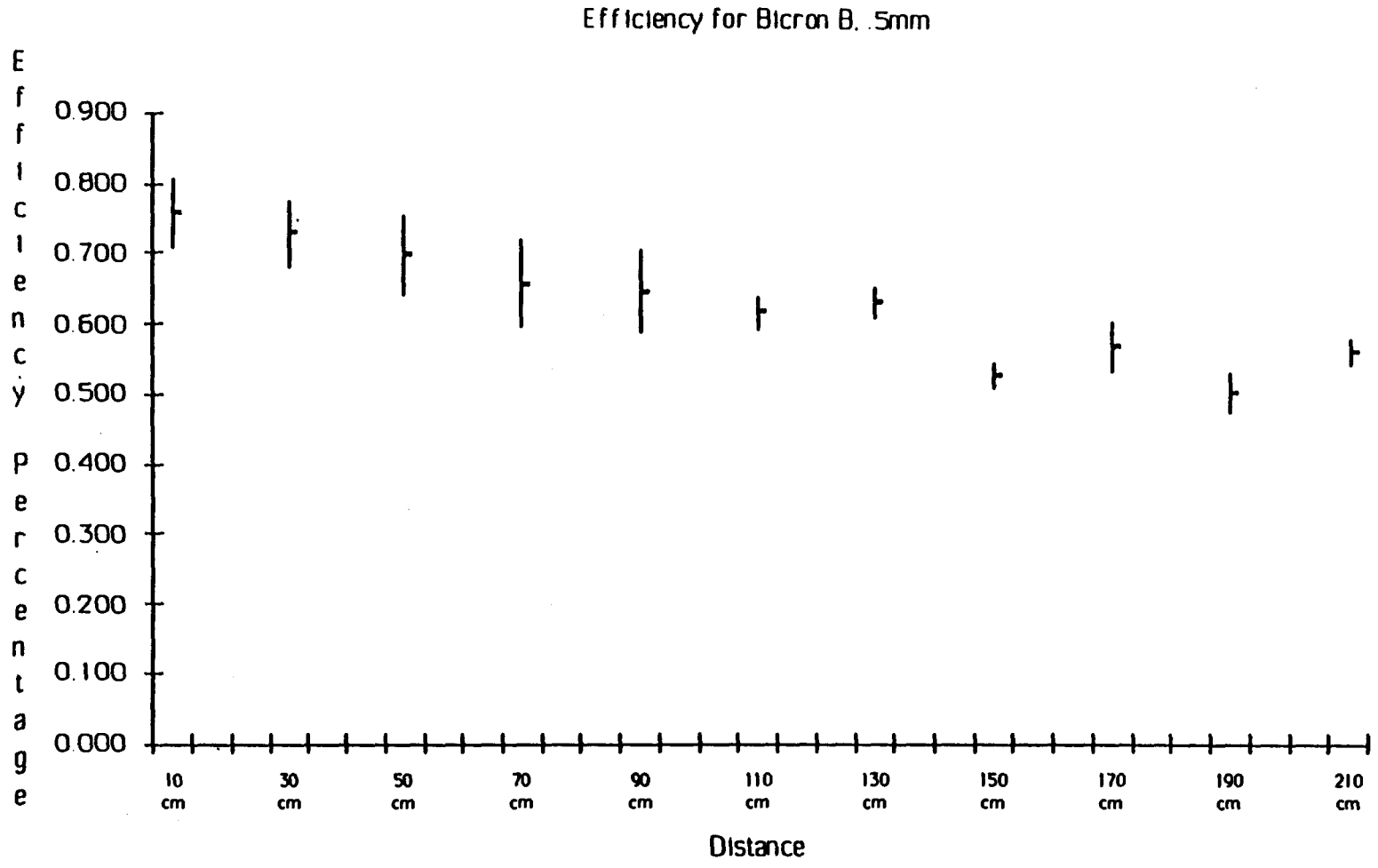
Efficiency for Bicron B. .5mm
Efficiency Percentage
0.900
0.800
0.700
0.600
0.500
0.400
0.300
0.200
0.100
0.000
10 cm
30 cm
50 cm
70 cm
90 cm
110 cm
130 cm
150 cm
170 cm
190 cm
210 cm
Distance

Figure 11.

BICRON FAX

TO: NORTHEASTERN UNIVERSITY, PHYSICS DEPARTMENT
ATTN: DR. S. REUCROFT
FROM: CHUCK HURLBUT
DATED: 29 AUGUST 1991

SUBJECT: FIBER RIBBON BUDGETARY PRICING

Steve,

Confirming our conversation of last evening, here are the budgetary estimates for the fiber ribbons that you requested.

DESCRIPTION:
Precision scintillating fiber ribbons consisting of two nested layers of parallel round fibers of diameters as stated below and four meters long. The fibers would be parallel and uniformly spaced at about 1.02 times the nominal fiber diameter. The second layer would lie in the valleys of the first.

Each ribbon would contain 1024 fibers, 512 per layer.

The fiber type quoted in the examples below is BCF-12 with an emission peak at 434 nm and a principal decay time of 3.4 ns.

Fiber location would be guaranteed to a precision of fifty microns or better referenced to one edge of the ribbon.

The ends of the fibers would be even and diamond milled flat and perpendicular to the fiber axes and ribbon plane to assure good optical coupling to optical waveguides. Both ends would be clamped in precision metal frames providing permanent positioning of the fiber ends and easy attachment and alignment to similar waveguide assemblies. The frames would be curved to match the curvature of the barrel frame over which the ribbons would be wound.

PRICING ESTIMATES:
The following prices apply to quantities of twenty arrays.

A. FIBER DIAMETER: 1.0 MM Unit Price: $5,300

The raw fiber is priced at 36 cents per meter.

B. FIBER DIAMETER: 1.5 MM Unit Price: $6,800

The raw fiber is priced as 69 cents per meter.

Charles R. Hurlbut

Figure 12.

Hybrid Subsystem Progress Report for FY1991

Straw Tube Electronics

Oak Ridge National Laboratory
Oak Ridge, TN
Gary Alley and Mike Emery

September 1991

HCTC Straw Tube Electronics

Support activities for HCTC straw tube electronics during FY91 has been limited due to the absence of SSC funding for most of the year. Therefore, no electronics development was conducted in FY91. We have, however, made an effort to attend most SDC meetings, particularly those related to straw tubes and to maintain contacts with collaborators at Duke, Pennsylvania, Colorado, and Indiana. ORNL overhead funds have been used to underwrite the cost of our travel. Funding (~$70K) finally arrived in the ORNL financial plan in August 1991. Although too late to allow anything to get done in FY91, this funding will help get us started on the work we propose to do for FY92.

Proposed FY92 Support of HCTC

In August of 1990, ORNL developed a printed circuit board assembly that allowed readout of a partial straw tube superlayer (32 straw tubes, 3 meters in length) located at Duke University. This assembly provided physical contact to the anode wires, high voltage distribution to the wires, termination of the straw tubes into their characteristic impedance, and a decoupled signal for the readout electronics. That effort was a successful first order exercise to develop techniques for terminating, biasing, and readout of the thousands of straw tubes that will be required in a full-scale SSC straw tracking system.

For FY92, we propose to extend the work mentioned above, proceeding to the next level of complexity. Although work with the 32 channel array has answered some questions, at least to a first order, some questions can only be answered in experiments using more than 32 channels. Critical issues such as packaging density, crosstalk, power and bias distribution, mechanical alignment, and cooling must be addressed. We believe important information, helpful in the resolution of these issues, can be attained using a straw tube array of ~100 tubes (see Fig. 1). This array, together with appropriate readout electronics, will provide a much needed testbed for addressing the critical questions mentioned above. Duke will be the site for this testbed since they are already involved in building a 100-tube array.

This work will progress in two phases:

a. This first phase will involve designing and fabricating a PC board assembly (endplate) that will provide the necessary physical connection to the straw tubes, high voltage distribution, characteristic impedance termination, and decoupled

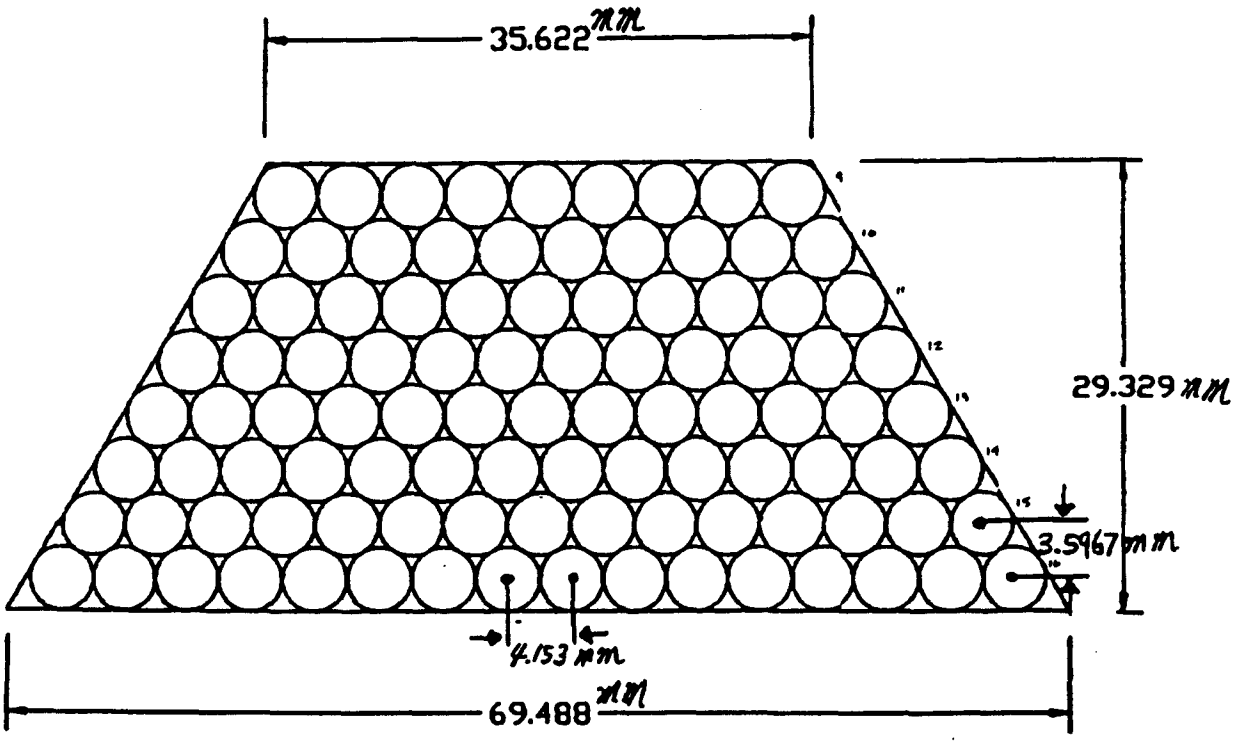

Figure 1. Proposed 100-tube testbed array

signals for readout electronics. Since 7 meter long tubes will be used for this experiment (for the first time ever), it is essential that the tubes themselves be fully characterized and understood. Therefore, initially only a fraction of the tubes (32 channels) will be instrumented for readout. Rather than introducing yet another variable during this important stage of the work, LeCroy 2735DC wire chamber readout electronics (16 channels/card) will be used for the first set of experiments. These electronics are well understood and documented. Furthermore, new techniques for making physical connection to the anode wires will be explored. The "pogo sticks" used in the earlier work on the 32 tube array will not be appropriate for arrays of larger numbers. The alignment of the "pogo sticks" will be come very difficult as the tube count increases. One alternative that will be evaluated is the use of conductive elastomer strips (e.g., zebra strips).

b. This second phase will involve the development of 100 channels of custom readout electronics based on an eight-channel readout chip being designed at Penn. A delivery date for this chip has not been set but is expected in late 1991. Having fully characterized the straw tubes themselves in phase a above, the objective of this phase is to begin the process of addressing issues associated with achieving the density of readout required for an SDC straw tube tracker. Some of these issues include packaging and interconnect techniques, cooling, substrate/materials selection, high/low voltage distribution, and signal routing. Using the testbed and the concept of modular electronics, it will be fairly easy to evaluate different ideas and techniques in all of these areas. In addition to supplying the necessary hardware, we will document the results of all tests and produce a report outlining our findings and recommendations.

During all phases of this work, we plan to continue our attendance at appropriate meetings and maintain a close collaboration with groups at Duke, Pennsylvania, Colorado, and Indiana. The successful completion of this work will be of significant interest to our SDC collaboration because, for the first time, we will have a working demonstration of the packaging, cooling, etc., necessary for a full-scale straw tube tracking system.

Hybrid Subsystem Progress Report for FY1991

Mechanical Engineering and Integration

Oak Ridge National Laboratory
Oak Ridge, TN
Tony Gabriel
Ted Ryan
David Vandegriff

September 1991

1.0 Introduction

Oak Ridge National Laboratory (ORNL) provided engineering design support to the Hybrid Central Tracking Chamber (HCTC) subsystem in FY1991. Mechanical and electrical components of the HCTC were evaluated, and the requirements to integrate the HCTC into the Solenoidal Detector were determined. These requirements include the physical integration as well as costing and scheduling efforts for the tracker. The following sections summarize the support provided to the HCTC by ORNL.

2.0 Mechanical Engineering

The mechanical engineering requirements of the HCTC continue to be refined. In FY1991, the mechanical engineering effort concentrated on developing the model for fabrication and assembly of the hybrid tracker. This model includes such parameters as straw assembly; cylinder fabrication and accuracy requirements; straw tube lay-up procedures; and superlayer arrangement and attachment. Each of these tasks are performed in conjunction with the other members of the collaboration.

The basic model of the Hybrid Central Tracker relies on 4 mm straw tube sense elements for providing radial and phi particle locations and 1.5 mm diameter plastic scintillating fibers for providing stereo locations. The straw sensing elements are individually placed on precision graphite-epoxy composite cylinders. The fibers are combined into ribbons prior to their placement on similar cylinders. The elements are arranged in a manner that maximizes the physics of the tracker while at the same time reducing the structural complexity associated with stereo straws and precision axial fibers.

The two phases of the HCTC tracker, the straw tube and fiber portions, will be built in parallel. Each phase will begin following completion of the stable base cylinders. The cylinders will be fabricated to a tolerance of approximately 0.010" total indicated runout. This will provide the necessary surface for mounting the sense elements without extending the state-of-the-art for this type of cylinder. In parallel with the cylinder fabrication task, the straw tube and fiber ribbons will be assembled.

The straw tubes will be completely assembled and tested prior to placement on cylinders. The straw tube assembly will consist of the tube itself, the sense wire,

intermediate wire supports, a mid tube terminator, end plugs and wire tensioning plugs. These items will be assembled en masse on fabrication jigs. The wires will be tensioned and subjected to operating conditions as an intermediate test. The certified straw tube units will then be packaged and shipped to the final assembly site.

The plastic scintillating fibers and waveguide fibers will be assembled into ribbons consisting of two layers of approximately 512 fibers each at the fiber manufacturers site. The use of the fibers for stereo measurement only reduces the tolerance requirements of the fibers to a level that is currently being met by the fiber manufacturers. The fiber ribbons will then receive end prep treatment and aluminization as required, prior to being packaged and shipped to the final assembly site.

The completed straw and fiber sense element units will arrive at the final assembly facility for placement onto the cylinders, producing the superlayers. The placement procedure is the most critical step in the process of fabricating the tracker. As a result, a significant amount of effort has been placed on the development of a device for placing the sense elements onto the cylinders in a precise and controlled manner. A straw tube placement machine has been developed in a joint effort by ORNL and Duke and is currently being fabricated at Duke University. This device will be used to place straw tubes into a reference surface and measure the accuracy of the overall system. The lessons learned in the development and use of this device will be directly applicable to the final assembly device. The principles shown with the straw tube device will also be applicable to placement of plastic scintillating fibers onto cylinder.

The central tracker will be ready for final assembly upon completion of the superlayers. The superlayers are assembled and aligned within the tolerances specified for the detector. The support structure is the major component in this assembly step. Several designs for this structure were evaluated in FY1991 and are presently being analyzed. The structure will be fabricated from a low-z material such as graphite-epoxy composite tubes. The attachment of the superlayers to the structure will provide the structural integrity necessary to retain the alignment of the assembly, and will allow for relative movements due to thermal and moisture differences. This feature is referred to as kinematic mounting. The details of this mount will evolve as the design reaches maturity. The assembly of the superlayers to the support structure provides a mechanically complete Hybrid Central Tracker.

The HCTC subsystem group has evaluated numerous tracker layouts in FY1991 to determine a design that meets the budgetary constraints associated with the SDC detector. The goal of the HCTC is to optimizer the physics of the detector while providing a cost effective solution. To this end, the model has progressed to its current configuration. As the cost and scheduling effort continues, additional or modified versions of the basic model will surface and be considered for the final HCTC configuration.

3.0 Integration

The integration of the HCTC into the SDC detector was a major focus of the engineering effort at ORNL in FY1991. The requirements of this integration task include both the physical integration and interfacing of the detector components and the integration of the cost and schedule associated with the HCTC into the SDC. Significant progress was made in both arenas. A summary of these efforts is described below, with detailed integration and costing documents available through the SDC.

The physical integration of the HCTC resulted in the production of a document called the Resource Requirements Report (RRR). This document contains detailed dimensional descriptions of the detector. These dimensions provide both enveloped descriptions and interface descriptions necessary for incorporating the HCTC into the SDC detector. Additionally, the RRR contains tables that define the functional interfaces; the electrical requirements, the gas requirements and the cooling requirements. This information was developed through extensive research and analysis into the operation of the tracker. The RRR is a "fluid" document that will change many times over the design life of the detector as changes are made and incorporated.

The final area of interest in FY1991 at ORNL in support of the HCTC is the costing and scheduling effort. This effort began early in FY1991 and is continuing into FY1992 as the overall detector is evaluated and scrutinized. ORNL developed the work breakdown structure (WBS) for the hybrid tracker and has used this as the backbone for both the costing and scheduling. The costing has progressed from a "top-down" approach at estimating the cost per channel of the tracker to a detailed "bottoms-up" estimate. The current estimate assigned costs to each task and item associated with the design, procurement, fabrication, assembly, testing and installation of the HCTC. The scheduling effort has followed a similar path. It has developed into an extensive Gantt chart/network

diagram product complete with interface relationships of the various components as they progress through the fabrication process. Both the cost and the schedule are part of the overall SDC design package.

4.0 Summary

ORNL has supported the HCTC collaboration for two years now. During this time, significant design directions have been established in both the mechanical and electronic readout areas. In FY1991, the focus of the entire collaboration has been on the cost of building the detector and the time required to do so. ORNL has provided concentrated efforts allowing the HCTC to remain a viable option for the central tracker.

Hybrid Subsystem Progress Report for FY1991

Radiation Damage Assessment Activities

Quantum Research Services, Inc.
100 Capitola Drive, Suite 109
Durham, NC 27713-4411
William L. Dunn and Abdelfatah M. Yacout

and

Department of Nuclear Engineering
Box 7909
North Carolina State University
Raleigh, NC 27695-7909
Thomas S. Elleman

September 1991

Hybrid Subsystem Progress Report for FY1991

Radiation Damage Assessment Activities

Quantum Research Services, Inc., and N.C. State University

Section		Page
1.0	Introduction	1
2.0	Irradiation Preparation	2
2.1	Dosimetry Measurements	2
2.2	Neutron Spectrum Calculations	5
2.3	Availability of Cf-252 Fission Sources	7
2.4	Variable-Dose Irradiation Scheme for Long Fibers	7
2.5	Nonuniform Damage Assessment Model	8
3.0	Radiation Damage Testing	12
3.1	Avalanche Photodiode Recovery	12
3.2	Alternative Straws and Glues	14
3.3	Complete Straw Assembly	14
3.4	Mixed Neutron/Photon Fiber Tests	15
3.5	Cf-252 Fiber Tests	17
4.0	Related Activities	18
4.1	SDC Support	18
4.2	SAHEP	18
4.3	CAD Modeling	18
	References	20

1.0 Introduction

This report summarizes progress during FY91 by the team from North Carolina State University (NCSU) and Quantum Research Services, Inc. (Quantum) who are concerned with radiation damage assessment of components that are candidates for use in the central tracking subsystem of the Solenoidal Detector Collaboration (SDC) detector. The NCSU/Quantum team has been concerned principally with neutron and mixed neutron/photon irradiations of both straw-tube and plastic scintillating fiber (PSF) components, including readout electronics, as part of the Hybrid Central Tracking Chamber (HCTS) concept. NCSU operates the PULSTAR research reactor and associated laboratories where the components are irradiated, has performed dosimetry measurements in the irradiation port that is used for the HCTC studies, and assists in the planning and conduct of the irradiations. Quantum is performing analyses to characterize the neutron spectrum in the irradiation port, coordinates the pre- and post-irradiation testing of the components, has developed a procedure for damage assessment of nonuniformly irradiated fibers, and also assists in the planning and conduct of the irradiations.

These studies are being funded primarily through the Hybrid Subsystem, with Duke University providing funds to NCSU to cover irradiation charges and Northeastern University providing funds to Quantum. Some funding also came directly to NCSU, who then subcontracted a portion to Quantum, from the Texas National Research Laboratory Commission (TNRLC).

This progress report is divided into three main sections. The first section describes activities that were necessary to prepare for the irradiations; these include neutron and gamma-ray dosimetry measurements, neutron spectrum calculations, consideration of alternative PSF irradiation schemes, and development of an assessment model for nonuniformly irradiated fibers. The second section describes the tests conducted to date and those that are planned in the immediate future. The third section describes sundry activities by the reporting institutions that are related to the HCTC and SDC, such as related R&D support that has been obtained from TNRLC through the Southern Association for High Energy Physics (SAHEP) and activities involving CAD modeling.

2.0 Irradiation Preparation

The irradiations conducted in the PULSTAR reactor during FY90 for the HCTC collaboration did not require more than a general knowledge of the neutron-to-photon mix or of the specific neutron energy spectrum. For instance, a simple procedure of comparing the responses of avalanche photodiodes (APD's) which had been irradiated with and without cadmium covers was sufficient to demonstrate that APD damage was caused by "fast" neutrons. However, for the more challenging problem of characterizing PSF response to neutron and photon irradiation, a more detailed knowledge of the gamma-ray dose rate and the neutron spectrum in the PULSTAR irradiation port was necessary. Since irradiation in the PULSTAR necessarily exposes the samples to a complex mix of gamma rays and thermal and fast neutrons, schemes were developed to isolate the radiation type and spectrum effects. Also, since the neutron flux varies appreciably over the 5-ft height of the irradiation cannister, thus leading to variable-dose delivery over the length of enclosed fibers, we developed a damage assessment model for variable-dose fiber irradiation. These and other preparatory activities are summarized in this section.

2.1 Dosimetry Measurements

Damage to scintillation fibers and straw tubes that have been irradiated in the PULSTAR nuclear reactor can result from fast neutrons, gamma rays and (to a lesser extent) thermal neutrons. It is necessary to have an understanding of the fluxes and dose rates from all of these radiations in order to establish if neutron effects are qualitatively or quantitatively different from lower LET radiations in their damage to components.

Thermal neutron fluxes along the axis of the radiation capsule were determined at low reactor power using pure indium dosimeter foils. The foils were transmuted through the reaction: $In^{115}(n,\gamma)\ In^{116m}$ and the radioactive In^{116m} was counted in a calibrated scintillation detector to establish the disintegration rate. Similar foils covered with cadmium to absorb thermal neutrons were also irradiated to obtain the epithermal neutron fluxes ($E > 1.5$ eV) which were roughly one order of magnitude below the thermal fluxes in most capsule positions. These results have been reported in an earlier publication.[1]

In subsequent irradiations at higher neutron fluences, pure cobalt or Co-Al wires were used as thermal neutron dosimeters and these values were related linearly to the flux distributions established with In. It is planned to use nickel wires which are activated through the reaction: $Ni^{58}(n,p)\ Co^{58}$ as an additional dosimeter to measure the fast neutron flux. These wires are sensitive to an effective average neutron energy of about 2.5 MeV and will provide a measure of fluxes at higher energy.

The determination of gamma ray dose rates presents some measurement problems in that devices that are sensitive to gamma rays are also sensitive to some extent to neutrons. In addition, the gamma rays coming from fission products in the cold core present a continuous gamma ray background that has to be considered in establishing total gamma-ray dose rates.

A student project was undertaken to estimate the background (cold-core) gamma dose rate and to measure the gamma dose rate after reactor shutdown. The student concluded[2] that the background gamma-ray dose rate was approximately 0.05-0.1 Mrad/hr and that mid-core dose rates of up to 3 Mrad/hr were present a few minutes after reactor shutdown. To supplement and refine the student project, reactor staff placed thermoluminescent dosimeters consisting of Li(6)F and CaF_2 at six inch intervals along the HCTC irradiation capsule axis (see Fig. 1) and exposed them at a reactor power level and time sufficient to minimize exposure from decay fission product gamma rays while still staying below the total dose limits of the dosimeters. Lithium-6 fluoride was selected as it has essentially zero thermal neutron sensitivity while exhibiting sensitivity to gamma rays and fast neutrons while CaF_2 has differing sensitivities to the three radiation fields. In principle, the results from the two dosimeters, along with the thermal and fast neutron results, can be used to calculate the dose contributions from the three radiation sources.

This method of dosimetry was chosen over direct ion chamber measurements since it allows measurements in the actual capsule where specimens are exposed. The measurements have been made and the data appear generally reasonable but the gamma ray dose rates have not yet been calculated. Future work in dosimetry will involve measurements of the flux at higher neutron energies, confirmation of the reproducibility of existing dosimetry results at known reactor power, and comparison with results from neutron spectrum calculations.

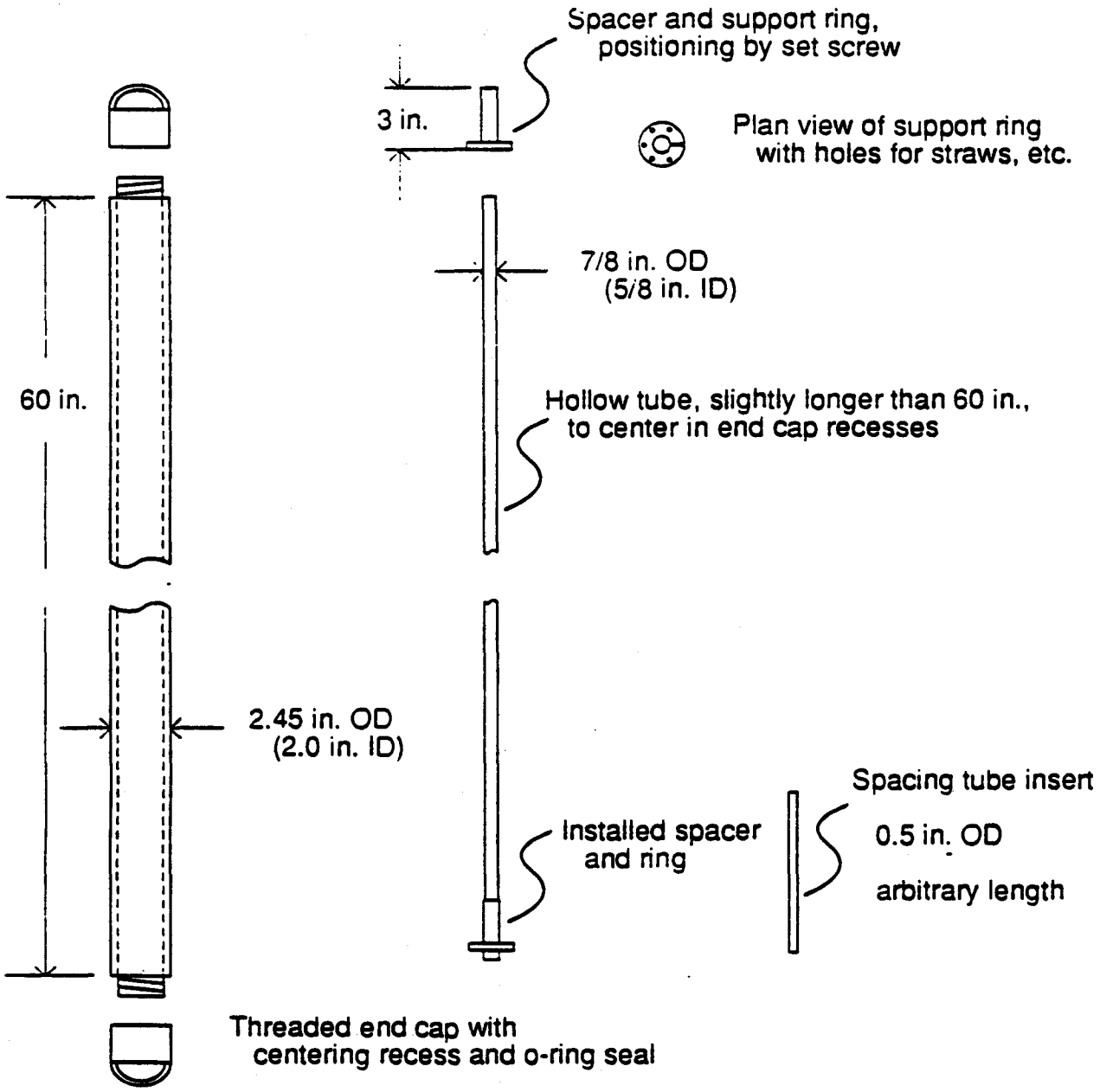

Figure 1. Schematic of the irradiation capsule showing typical dimensions

2.2 Neutron Spectrum Calculations

The PULSTAR core occupies a rectangular parallelepiped volume approximately 15-in. x 16 in. x 24 in. high. As the plan view of the core shown in Fig. 2 indicates, the core is highly heterogeneous with 25 rectangular fuel assemblies arranged in a nonuniform array incorporating four control rods; the entire core is immersed in a water pool and lined on two sides by graphite reflectors. Each assembly structure is made of Zircaloy-2 and consists of 25 individual fuel pins. Several irradiation ports are located near the core; the port marked Y in Fig. 2 was used for the irradiations described in this report. Water is an excellent neutron slowing down medium and hence the fission spectrum is highly moderated at the irradiation ports. Although some fast neutron measurements using foils and wires (see Section 2.1) have been made, the neutron spectrum in port Y is not adequately known. Hence, we undertook a limited theoretical study to calculate the neutron spectrum within port Y.

If the irradiation volume were small with respect to the size of the core, axial dependence could be ignored; however, in our case the irradiation length of 5 ft exceeds the core height by more than a factor of 2. Simple analytical models are out of the question because of the heterogeneity of the core and the tremendous variability of neutron cross sections with energy. In addition, standard core homogenization methods are inadequate, as has been demonstrated by PULSTAR staff in attempts to use the LEOPARD/PDQ codes and by Lee, et al.[3] Thus, we needed a multidimensional analysis procedure and, since the core characteristics change with time due to burnup of the nuclear fuel, we also sought a procedure that could account for burnup. After investigating various approaches for performing the spectral calculations, we eventually elected to use the WIMS reactor lattice cell code package.[4]

The Winfrith improved multi-group scheme (WIMS) code provides a sophisticated scheme of reactor cell calculations for a wide range of reactor types.[5] Rod or plate fuel geometries in either regular arrays or in clusters can be handled by the code. Up to 69 energy groups (14 fast groups, 13 resonance groups and 42 thermal groups) can be used. However, the user is offered the choice of accurate solutions in many groups or rapid calculations in few groups. Solution of the transport equation is provided either by use of the Carlson DSN method or by collision probability

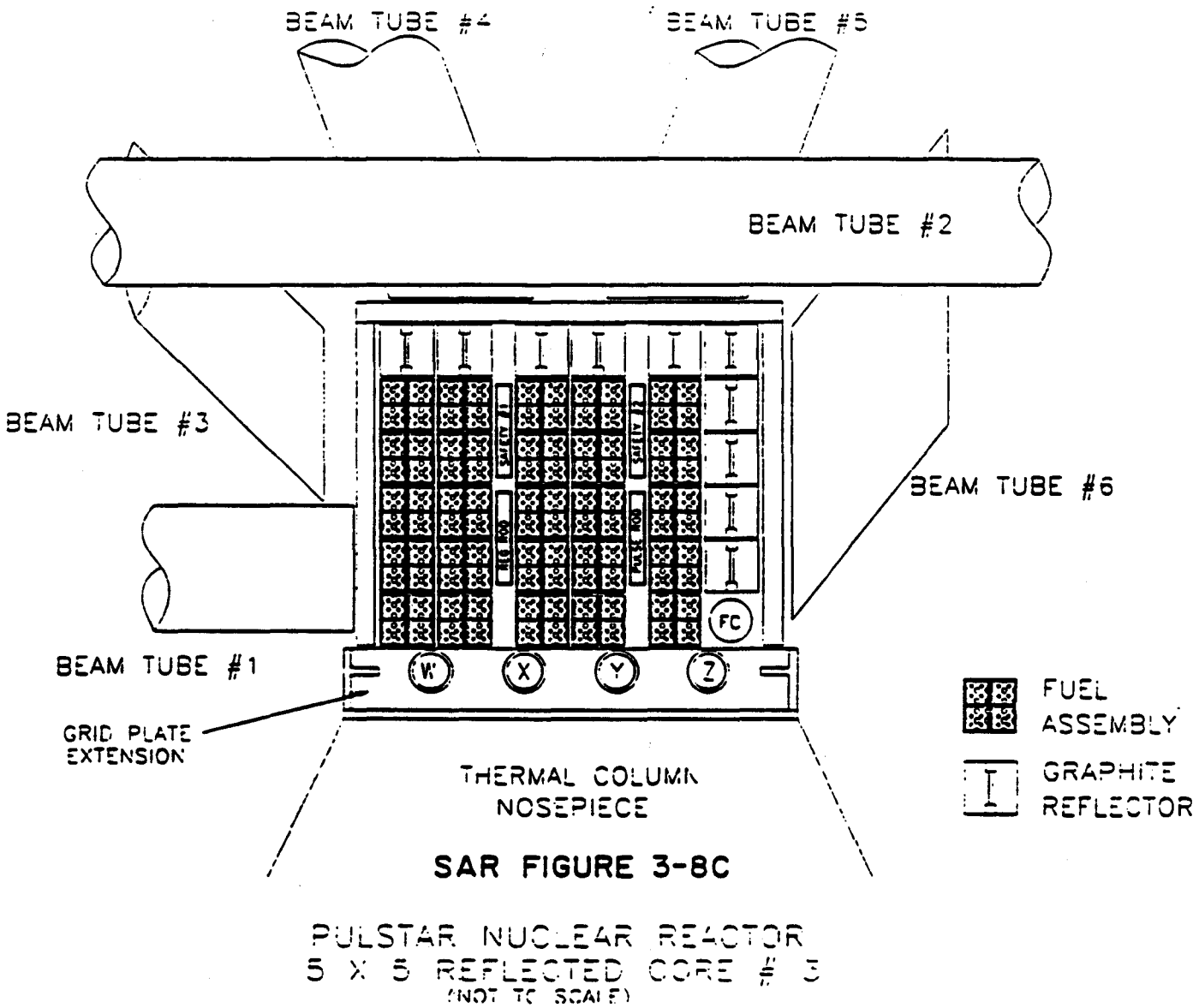

Figure 2. Plan view of PULSTAR reactor core and beam tubes

methods. Leakage calculations including an allowance for streaming asymmetries may be made using either diffusion theory or the more elaborate B_1-method. In addition, the WIMS D/4 code allows multiple cell calculations which will be used in this work for core calculations.

We have had to convert a VAX version of WIMS to run on an IBM machine. This process and the setup and proper characterization of the PULSTAR core within WIMS are nearing completion and neutron spectrum results are expected soon.

2.3 Availability of Cf-252 Fission Sources

Two Californium-252 spontaneous fission sources are available at NCSU to conduct low-dose fast-neutron exposures on scintillation fibers or electronic components. The two sources provide neutron yields of 1.1×10^7 n/sec and 3.2×10^6 n/sec, respectively. It is likely that fluxes on the order of 1×10^5 n/sec-cm^2 could be obtained from the more intense source, which was only recently obtained, for specimens placed in close proximity to the source. This would produce an exposure of 1×10^{10} n/cm^2 per day which should be sufficient to show effects in electronic components and to conduct low-delivery rate tests on scintillating fibers and other samples. The sources produce a fission spectrum of neutron energies with an average value of approximately 1.5 MeV, similar to the average neutron energy expected in detectors at the SSC.

2.4 Variable-Dose Irradiation Scheme for Long Fibers

It is desirable to know if damage to scintillation fibers is a function of total dose only and is essentially independent of the type and LET of the impinging radiation. If this is true, then tests using electron sources or gamma ray sources become the most convenient means for exposing test specimens. Alternatively, if neutrons produce unique damaging effects, then reactor irradiations or exposure to other fast neutron sources become highly desirable.

It is possible to measure the damage in a scintillation fiber as a function of position along the fiber. This fact supports an experiment where the fast-neutron/gamma-ray/thermal-neutron dose rates are varied along the fiber length during a single irradiation to provide information on the effects of different radiation types.

The fibers are exposed at the core face of the PULSTAR reactor where the lower two feet of the fiber are directly opposite the reactor core face and the upper length of the fiber is as much as two feet above the top of the reactor. It is planned to conduct an experiment in which the bottom 8-10 inches of fiber is immersed in water during irradiation to produce a deposited dose which is primarily from gamma rays with lesser contributions from fast neutrons and thermal neutrons. The next length of the fiber would have minimum absorbers between the fiber and reactor core to give the maximum fast neutron exposure while the next fiber segment would have a cadmium cover to give high gamma ray and fast neutron exposures but no thermal neutron dose. The upper regions of the fiber above the core would be essentially exposed only to gamma rays since neutron levels drop appreciably at short distances from the core.

The result would be a fiber that has been divided into four regions where the ratios of dose from gamma rays, fast neutrons and thermal neutrons are different along the fiber length. The observed damage in the four regions would be compared against measured neutron and gamma-ray dosimeter results for the regions to determine what conclusions can be drawn about the effects of different radiation types.

2.5 Nonuniform Damage Assessment Model

Radiation damage to PSF expresses itself in two distinct effects: reduction in light output and increased light attenuation, *i.e.*, reduction in attenuation length. Models of the form

$$I = R_1 e^{-x/\lambda_1} + R_2 e^{-x/\lambda_2} \tag{1}$$

fit attenuation data for fibers of modest length, say $L \leq 3$ m, very well. Here I is a measure of relative light output of the fiber, x is the distance along the fiber at which the fiber is excited by ionizing radiation, R_1 and R_2 are relative magnitudes, and λ_1 and λ_2 are attenuation lengths. The values of R_1, R_2, λ_1, and λ_2 – which depend on fiber diameter and composition, wavelength, radiation dose, and time since irradiation – are obtained by fitting the model of Eq. (1) to measured attenuation data.

Equation (1) fits attenuation curves for both unirradiated and uniformly irradiated fibers. However, if the fiber is subjected to grossly different doses over

different regions, the model of Eq. (1) would not be expected to be adequate. (An example of nonuniform irradiation is the practice of shielding a short length of fiber from exposure during irradiation and using the resulting "hump" in the attenuation curve to infer the intrinsic scintillation loss. In this situation, the hump is ignored when fitting the model to the attenuation data.) If we were to irradiate a fiber as described in Section 2.4 above to four regions of different total doses and fluences, we would expect the model of Eq. (1) to apply approximately over each region but not to the fiber as a whole. We have thus constructed a model for nonuniformly irradiated fibers, as described below.

Let us suppose a fiber is irradiated to different doses over each of J regions, as shown in Fig. 3; we further assume that within each region the dose is approximately constant. We collect attenuation data at $K = k_J$ points along the fiber, giving us K data pairs (x_k, I_k). We assume models of the form of Eq. (1) apply over each region, and so construct a composite model, F, of the form

$$I \equiv F = \sum_{j=1}^{J} [R_{j1}\, e^{-x/\lambda_{j1}} + R_{j2}\, e^{-x/\lambda_{j2}}]\, [H(x-x_{k_{j-1}}) - H(x-x_{k_j})] \ , \tag{2}$$

where H is the unit step function and the x_{k_j} are the endpoints of the regions of different dose.

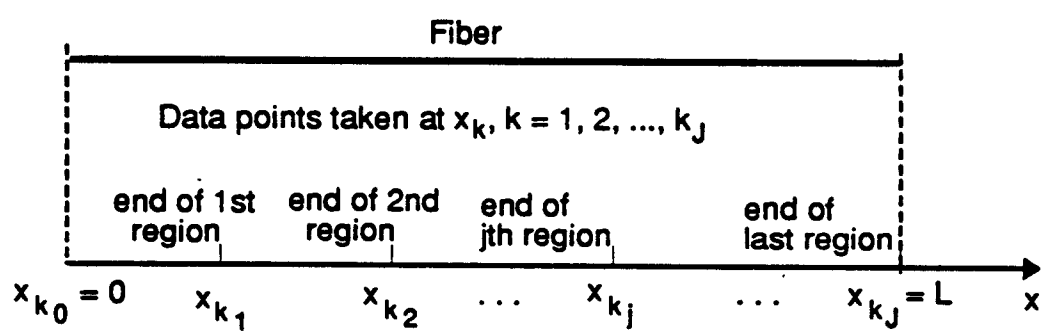

Figure 3. Nomenclature for multiregion fiber irradiation.

We can impose the condition that the model is continuous at the region endpoints x_{k_j}, j=1,2,...,J-1, as of course the data are, to within statistical uncertainties. This constrains the values of J-1 of the magnitude parameters. We form the weighted least-squares function

$$E^2 = \sum_{j=1}^{J} \sum_{k=k_{j-1}}^{k_j} \frac{[I_k - F_j(x_k)]^2}{\sigma^2}, \tag{3}$$

where the F_j are given for j=1,2,...,J as

$$F_j = R_{j1}^* e^{-(x-x_{k_j})/\lambda_{j1}} + R_{j2}^* e^{-(x-x_{k_j})/\lambda_{j2}}, \quad x_{j_{k-1}} \le x \le x_{k_j} \tag{4}$$

and the σ_k^2 are the variances (or other weights) in the measured I_k. In Eq. (4), the R^* are modified magnitude constants from which the R values can be obtained by equating Eqs. (2) and (4) over the appropriate intervals. In our procedure we took the R_{j1}^*, j=2,3,...,J as the constrained parameters. To find the parameters, we take partial derivatives of Eq. (3) with respect to R_{11}^*, the R_{j2}^*, j=1,2,...J, and all the λ_{j1} and λ_{j2}, and set them equal to zero. We supplement the resulting equations with the J-1 constraints which result from requiring continuity at the internal region endpoints. The following system of 4J equations for the 4J parameters is obtained:

$$\frac{\partial E^2}{\partial R_{11}^*} = \sum_{k=1}^{k_1} \frac{2[I_k - F_1(x_k)]}{\sigma_k^2} e^{-(x-x_{k_j})/\lambda_{11}} = 0 \tag{5}$$

$$\frac{\partial E^2}{\partial R_{j2}^*} = \sum_{k=1}^{k_1} \frac{2[I_k - F_j(x_k)]}{\sigma_k^2} e^{-(x-x_{k_j})/\lambda_{j2}} = 0, \; j = 1,2,...J \tag{6}$$

$$\frac{\partial E^2}{\partial \lambda_{j1}} = \sum_{k=1}^{k_1} \frac{2[I_k - F_j(x_k)]}{\sigma_k^2} \frac{R_{j1}^* (x-x_{k_j})}{\lambda_{j1}} e^{-(x-x_{k_j})/\lambda_{j1}} = 0, \; j = 1,2,...J \tag{7}$$

$$\frac{\partial E^2}{\partial \lambda_{j2}} = \sum_{k=1}^{k_1} \frac{2[I_k - F_j(x_k)]}{\sigma_k^2} \frac{R_{j2}^* (x-x_{k_j})}{\lambda_{j2}} e^{-(x-x_{k_j})/\lambda_{j2}} = 0, \; j = 1,2,...J \tag{8}$$

and

$$R_{j1}^* + R_{j2}^* - R_{j+1,1}^* e^{-(x_k - x_{k_{j+1}})/\lambda_{j+1,1}} - R_{j+1,2}^* e^{-(x_k - x_{k_{j+1}})/\lambda_{j+1,2}} = 0, \; j=1,2,...J-1 \; . \tag{9}$$

The final procedure involves inputting the attenuation data and initial estimates for the λ's, finding the R^* values by a matrix inversion of Eqs. (5)-(9), checking parameter constraints (*e.g.*, all $R^* > 0$), calculating the least-squares function value, E^2, incrementing the nonlinear parameters (the λ's) by a modified gradient search algorithm subject to parameter constraints, and calculating a new value of E^2. If the new E^2 is smaller than the first, the nonlinear parameters are updated and the entire process is repeated; if not, the step size is adjusted and a new set of nonlinear parameters is obtained. This establishes an iterative procedure that is terminated when the relative difference between successive E^2 values is less than a specified tolerance or when a specified number of iterations is exceeded. Once the search is completed, a final iteration is carried out, treating all parameters as nonlinear, in order to estimate the uncertainties in the obtained values of the parameters. Finally, the R values are determined from the R^* and λ values.

We note that the model of Eq. (2) is a disjoint collection of models of the form of Eq. (1). However, the cumulative effects of damage along the fiber are inherently accounted for by the fact that we solve for all model parameters simultaneously. We will employ this model in analyzing fibers exposed to different fluence and dose levels over different regions, as described in Section 2.4. We will then attempt to recover information on the relative damage within each region by further analysis.

3.0 Radiation Damage Testing

3.1 Avalanche Photodiode Recovery

In FY90, ten GE Electro Optics modified C30921S APD's were irradiated in the NCSU PULSTAR reactor at low power (1 watt), at preset positions within the irradiation capsule shown in Fig. 1, for various times from 10 to 240 sec. Dark count rate and dark current data were collected before and after irradiation. An ultra-stable power supply and a high-precision voltmeter were used to record the variation inherent in dark count rate as the bias was varied by ±0.5 volts about the nominal voltage. This variation and the statistical count-rate variances were used to estimate the uncertainty in the ratio, R, of dark count rate after irradiation to that before.

We plot in Fig. 4 the dark count ratio, R, as a function of fast fluence for the ten exposures. The results indicate a damage threshold at approximately 2×10^6 cm^{-2}, as evidenced by a rapid increase in R, indicative of higher dark count rates due to radiation damage, above the no-damage value of unity. The dark currents, on the other hand, were unaffected by the neutron exposures. Estimates of gamma-ray dose received during the irradiations are a few rads or less. That the damage is due to fast neutrons was verified by comparison of points A and B in Fig. 4. The APD for point A was covered entirely by cadmium, which filters out thermal neutrons. Since the dark count ratios represent comparable damage (7.9±0.9 for test A and 5.8±0.7 for test B), we conclude that the damage is due to fast neutrons, which is consistent with the fact that the silicon elastic scattering cross section exhibits a significant increase at and above 0.15 MeV. An early version of these results was presented in last year's report.

This year we undertook a study of long-term recovery of the damaged APD's. Quantum personnel tested several of the damaged APD's at various intervals after irradiation. Over the first few months, the damaged APD's all indicated slow recovery, of approximately 10-20% reduction in dark count rate per month. Also, the three APD's that were tested after a little over a year all showed reductions of about 60-70%, indicating that the recovery continues but the rate of recovery eventually declines as the dark count rates approach the pre-irradiation values. We do note, however, that in a test run on February 28, 1991 – about seven months after irradiation – all four diodes tested gave higher dark count rates than in the previous

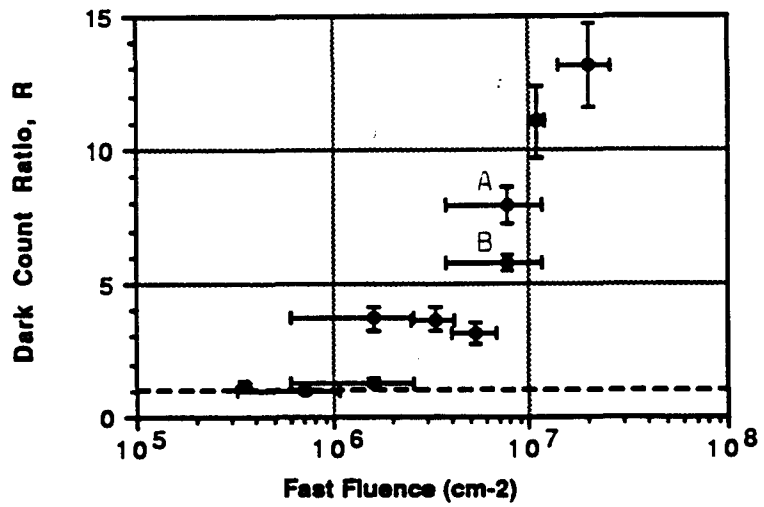

Figure 4. Variation with fast neutron fluence of the ratio of dark count rate after irradiation to that before irradiation

test (some were even higher than the rates just after irradiation). We suspect, although we cannot verify, that in the intervening five months the discriminator setting may have been changed and when reset was put at a slightly lower value than in the other tests, which would pass a greater fraction of the dark count pulses on to the counter. Otherwise, we have no explanation for this one-time anomalous behavior, since all experimental conditions (such as ambient temperature) and procedures were carefully monitored and controlled. We have since verified that the dark count rate is very sensitive to the discriminator setting near the value employed in these tests.

We plot in Fig. 5 the dark count rates as a function of time after irradiation for four of the damaged APD's and the pre-irradiation values (all near 5,000 cps). With the exception of the anomalous results at seven-months, the trend is clearly a gradual recovery toward the pre-irradiation dark count rates. The major conclusion to be drawn is that APD's operated in the geiger mode at room temperature begin to exhibit noticeable radiation damage at fast fluences of approximately 2×10^6 cm^{-2}, and that APD's stored unbiased at room temperature exhibit slow partial recovery. However, the recovery is not complete even after a year, and thus may not be significant for the intermittent irradiation conditions typical of SSC operation.

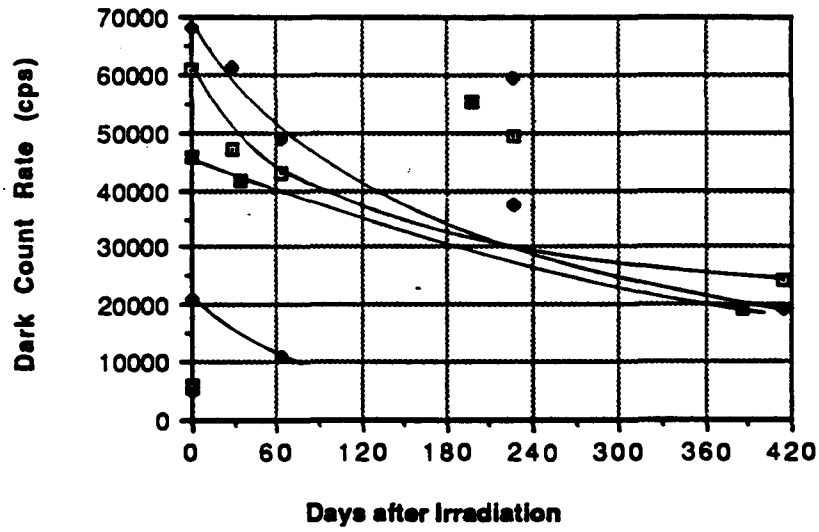

Figure 5. Dark count rate variation with time after irradiation

3.2 Alternative Glues and Straws

In FY90 we had tested mylar straws glued together with a cyanoacrylate glue (super glue) and found that the glue was quite radiation tolerant, showing only a slight (~10%) reduction in the force necessary to cause failure after exposure to neutron fluences of ~10^{15} cm^{-2} and gamma-ray doses of several krad. We also irradiated an array of mylar straws and found no detectable distortion effects after the irradiation. In FY91, we are preparing to irradiate copper-coated mylar straws that have been glued together with two different glues, including a highly-aromatic glue. The straw sections have been obtained and the irradiations are scheduled to take place at the next availability of the PULSTAR reactor in October.

3.3 Complete Straw Assembly

Duke University has constructed and tested several long straw tube drift chambers using copper-coated mylar straws, gold-plated tungsten wires, plastic wire supports, and aluminum end plugs. We have requested a small array of straw tubes with wires, gas, wire supports, and end plugs installed. The array will be tested with a Sr-90 beta source before and after irradiation to a neutron fluence of about 10^{15} cm^{-2} to verify proper operation of the full assembly after mixed neutron/photon exposure.

3.4 Mixed Neutron/Photon Fiber Tests

In a series of three irradiations, five types of fibers were irradiated to fast neutron fluences ranging from about 10^{12} to $5x10^{13}$ cm^{-2}. In the first test, multiple Bicron Type H, RH1, and B fibers were irradiated at a reactor power of 10 kW for 100 sec and the capsule was withdrawn, inverted, and reinserted for another 100 sec. This procedure delivered an approximately uniform exposure of about $2x10^{12}$ cm^{-2} fast fluence and 10^{13} cm^{-2} thermal fluence over the length of the fibers. The gamma-ray dose was not directly measured but can be estimated to be on the order of 3 krads. The irradiated fibers and one unirradiated fiber of each type were shipped using overnight delivery services to Northeastern University. The fibers were tested the day after irradiation and no measurable differences between unirradiated and irradiated fibers were seen.

Based on these results, five types of fibers (H, RH1, B, 3HF, and 81) were irradiated in two batches at twenty times the reactor power of the first tests. The procedure was the same in both cases: a 100-sec exposure at 200 kW followed by capsule inversion and exposure for another 100 sec. These fibers were thus exposed to fast fluences of about $4x10^{13}$ cm^{-2}, thermal fluences of about $2x10^{14}$ cm^{-2}, and measured gamma dose rates of between 6 and 9 krad (depending on position). At these levels, the ink and tape used to identify the fibers became sufficiently activated to delay by several days reshipment of the fibers (without special packaging, etc.) to Northeastern for post-irradiation testing. Also, problems with the fiber scanner further delayed the testing so that two of the fiber types were not tested until 25 days, and the other three fiber types until 29 days, after irradiation. Again, no appreciable difference in light output or light attenuation between the irradiated and unirradiated fibers was detected. Although we cannot distinguish whether the fibers were undamaged by the exposure or simply recovered, we can say that they were either undamaged or that 25 days is sufficient for full recovery. These tests are summarized in Table 1.

Northeastern University is preparing and testing a collection of fibers for another series of irradiations. The fibers will be about 59 inches in length so that they can be hung in the 5-ft irradiation capsule without bending. This year we are using a procedure to strike identifying marks on a plastic plug at one end of the fiber so as to avoid the activation problem encountered last year. A series of irradiations in the PULSTAR reactor is planned beginning soon after the fibers are received from

Northeastern. Some of the fibers will be irradiated so as to receive a nearly uniform exposure by inverting the 5-ft capsule mid-way through the irradiation. Others will be irradiated nonuniformly using the scheme described in Section 2.4. Still others will be exposed to a Cf-252 source. It is hoped that we will be able in this way to differentiate effects due to neutrons from those due to gamma rays or to verify that in fact the effects are the same, within a simple fluence-to-dose conversion factor.

Table 1. Results of Initial PSF PULSTAR Irradiation Tests

Fiber		Fluence (cm^{-2})		Gamma-Ray Dose Rate (krad)	ΔT[1] (days)	Results
Type	Number	Fast	Thermal			
RH1	2	$2x10^{12}$	10^{13}	~3	1	No damage
B	3	$2x10^{12}$	10^{13}	~3	1	No damage
H	3	$2x10^{12}$	10^{13}	~3	1	No damage
RH1	2	$4x10^{13}$	$2x10^{14}$	~6-9	25	No damage
B	2	$4x10^{13}$	$2x10^{14}$	~6-9	25	No damage
H	2	$4x10^{13}$	$2x10^{14}$	~6-9	29	No damage
3HF	3	$4x10^{13}$	$2x10^{14}$	~6-9	29	No damage
81	3	$4x10^{13}$	$2x10^{14}$	~6-9	29	No damage

[1] ΔT is time between irradiation and fiber testing.

3.5 Cf-252 Tests

It is planned to expose components to one or both of the Cf-252 sources to see if effects can be produced from fast neutrons only. In particular, we plan to coil a few fibers into a large circular configuration so that all points of the fibers are equidistant from the source. Irradiation for 10 days would expose the fibers to fast neutron fluences of $\sim 10^{11}$ cm^{-2}, with no gamma contamination. In a few months we expect to have a local fiber scanner (see Section 4.2), and so can test fibers very soon after irradiation. Comparison of results for these strictly neutron exposures with results for the mixed neutron/photon exposures should allow us to isolate effects from the varous radiation types.

4.0 Related Activities

4.1 SDC Support

In early 1991, Quantum applied to join the Solenoidal Detector Collaboration (SDC) as an Industrial Collaborator. Quantum's application was accepted and Quantum is now a collaboration member. Quantum attended the collaboration meeting at ORNL in February and there presented results of its radiation damage assessment activities to that date. Quantum also participated in the sessions held at ORNL and Duke in July and August, respectively, to develop a detailed Work Breakdown Structures (WBS) for a combined straw-tube/scintillating fiber central tracker.

4.2 SAHEP

Both NCSU and Quantum are members of the Southern Association for High Energy Physics (SAHEP). Dr. William Dunn of Quantum serves on the SAHEP Executive Board. SAHEP submitted a solicited proposal to the TNRLC which was funded effective April 1, 1991. Quantum received $20,000 first-year funding to construct a fiber scanner, which will be useful in short-term PSF radiation damage testing, and NCSU received $40,000 (first-year) to construct a special-purpose neutron irradiation facility in the PULSTAR reactor. This facility will allow irradiation of relatively large-volume samples under controlled environmental conditions (e.g., oxygen-free atmosphere, electrical bias applied, etc.). Design of the fiber scanner and the irradiation facility are now underway. Both of these projects will help the Hybrid Subsystem and SDC efforts in future radiation damage assessment activities.

4.3 CAD Modeling

Quantum has an active interest and capability in Monte Carlo simulation and in Computer Aided Design (CAD) modeling. During FY91, Quantum obtained a Small Business Innovation Research (SBIR) Phase I grant from DOE; the purpose of this research was to construct the rudiments of a computer code that would link CAD packages to the GEANT high energy physics simulation code, in order to demonstrate the feasibility of constructing a robust CAD-to-GEANT interface. Quantum constructed and integrated three components of a full CAD-to-GEANT interface: an

extensive Graphical User Interface, which serves as the communication link between the user and the code applications; a Shape Interpreter, which incorporates a procedure for recognizing CAD shapes from Drawing Exchange Format (DXF) CAD output; and a GEANT Input Generator, which writes the appropriate FORTRAN file to input the geometrical and material information into GEANT. The integrated code[6,7] recognizes six basic shapes from either multiple 2-D views or single 3-D CAD representations and produces GEANT input files from DXF CAD files, prepared in accordance with certain rules, for single volumes and systems containing multiple volumes. The Phase I code forms the foundation for the CAD or GEANT Entity Translator (CoGEnT) code, which would be a valuable tool for the simulation community since it would provide direct access between powerful CAD packages and GEANT and would streamline the process of geometry input to GEANT. Quantum is now seeking follow-on funding to develop the CoGENT code.

References

1. Dunn, W.L., T.S. Elleman, A.T. Goshaw, S.H. Oh, W.J. Robertson, A. Grimes, I. Leedom, and S. Reucroft, Radiation Damage Studies of Straw Tube and Scintillating Fiber Elements, *Proc. Symp. Detector Res. Dev. SSC,* Ft. Worth, TX, October 15-18, 1990 (in press).

2. Maldonado, G.I., Experimental Determination of the Post-Shutdown Gamma-Ray Dose Rate from the PULSTAR Nuclear Reactor at North Carolina State University, NE 550/Fall 1990, Laboratory Projects in Nuclear Engineering Report, N.C. State University, Raleigh, NC (13 December 1990, unpublished).

3. Lee, J.T., B.H. Lee, N.Z. Cho, and S.H. Oh, A Homogenization Technique for Strongly Heterogeneous Zones in Research Reactors, *Nuc. Tech.* 94(3):286 (1991).

4. Halsall, M.J., The Use of WIMS D4 and LWRWIMS, READWT and FILSIX, to Generate Two-Group Data for Reactor Calculations, AEEW-M 1785, Energy Systems Analysis Division, AEE, Winfrith, Dorchester, Dorest, England (July 1980).

5. Askew, J.R., F.J. Fayers, and P.B. Kemshell, A General Description of the Lattice Code WIMS, *J. Brit. Nucl. Energy Soc.* 5(4):564 (Oct. 1966).

6. Yacout, A.M., J.D. Simpkins, W.L. Dunn, S. Youssef, and W.J. Womersley, Development of a Robust CAD-to-GEANT Interface, *Proc. Symp. Detector Res. Dev. SSC,* Ft. Worth, TX, October 15-18, 1990 (in press).

7. Womersley, J., P. Dragovitsch, S. Youssef, W.L. Dunn, J.D. Simpkins, and A.M. Yacout, Absorbing CAD System Geometries into GEANT, *Proc. Workshop Detector Event Sim. HEP,* (MC91) Amsterdam, April 8-12, 1991 (in press).

Hybrid Subsystem Progress Report for FY1991

Central Tracking Chamber Simulation

Supercomputer Computations Research Institute
Florida State University
Tallahassee, FL 32306

M.J. Corden
M.E. Mermikides
D. Xiao

September 1991

Just as FY91 has seen the integration of the HCTC into an overall tracking detector design for the Solenoidal Detector Collaboration (SDC), it has also seen the incorporation of the HCTC simulation software into the SDC software environment ("Shell"). In the Shell, the HCTC simulation, as described in the HCTC FY90 progress report, coexists alongside simulations of other SDC detector subsystems, such as the silicon strip inner tracker.

The SCRI group has led the development of a common tracking data structure for all the tracking subdetectors being considered for SDC. This has enabled the HCTC reconstruction software to be extended to perform track finding and fitting in the combined inner (silicon) and outer (hybrid) tracking detector in a single step. This is important, since budgetary pressures within SDC make it impossible to design a single tracking subdetector with adequate stand-alone performance. It is essential to simulate the combined system in order to optimize the overall cost and performance.

The HCTC detector has been descoped several times from the design of the FY90 progress report, which had 8 axial superlayers of 8 straws each, and 3 stereo scintillating fiber superlayers. Intermediate designs have had 7 and later 5 straw superlayers of 8 and later 6 straws per layer, with two stereo fiber superlayers. The later design also had an inner axial fiber superlayer for improved two track resolution at high luminosity. All of these designs were simulated.

Figure 1a shows the isolated single track momentum resolution for 200 GeV/c muons for a system with 5 straw, 1 fiber and 8 silicon axial superlayers. Figure 1b shows the same for a system with one less straw superlayer, corresponding to a reduction in the magnet radius from 170 to 150 cm. The momentum resolution is degraded by over 30%. SDC has subsequently decided to retain a coil radius of 170 cm.

Figures 1c and 1d show examples of the resolution in the tangent of the dip angle, obtained from stereo silicon and scintillating fiber measurements. The dip resolution, typically about 2 mrad, will contribute less to the uncertainty on the Z^0 mass than will the momentum resolution.

Figures 2a-d show fitted track residuals in projection for the vertex, silicon(pairs), fiber, and straw tube superlayers. The nominal

resolution for a single layer of 1mm fibers is just under 300 microns. Figure 2c confirms that adding a second layer offset by half a fiber width improves the position resolution for near-radial tracks by a factor of 2 (and not simply the square root of two).

The study of Higgs decays via Z^0 pairs into four muons is continuing. Figure 3 shows an example of such an event having three muons within the acceptance of the central barrel tracker. All three muons have been found and reconstructed, with momenta close to the generated values. The central tracker geometry in this figure is 5 straw, 1 figer and 8 silicon axial layers. The fiber layer and the 2nd and 3rd straw superlayers have nearby stereo fiber superlayers (1mm fibers, 5 degree stereo).

The current (further descoped) HCTC design has 4 axial straw superlayers, and a single outer stereo fiber superlayer. The performance of this chamber, in conjunction with an inner silicon system of either 8 or 4 layers, is being investigated. Figure 4 shows the momentum resolution for single 200 GeV/c muons superposed on a minimum bias background corresponding to luminosities of 0, 1 or 2 x 10^{33} $cm^{-2}s^{-1}$, for both inner tracking options. Here a beam constraint of +/- 10 microns in both transverse directions is assumed. The track finding efficiency and momentum resolution are approximately 99% and 2%, falling only slightly from figure 4a to 4e. The deterioration is more noticeable for the more sparse detector at the higher luminosity in figure 4f, where the efficiency and resolution become 92% and 3% respectively.

Detailed simulation of the complete SDC tracking system is very cpu-intensive and is limited by available computing resources. Work on adapting the simulation to parallel processing on high performance, networked workstations is being pursued. This will be exploited to push the studies of figure 4 to higher luminosities.

Figure 5 shows a detailed simulation of pulse formation in a single straw tube. This takes into account the formation of primary ionization clusters, electron trajectories through the electric and magnetic fields, and avalanche fluctuations, amplification and signal formation at the wire. This is of value in predicting drift time-distance relationships (Figure 6), pulse shapes and dependence of measured time on pulse height.

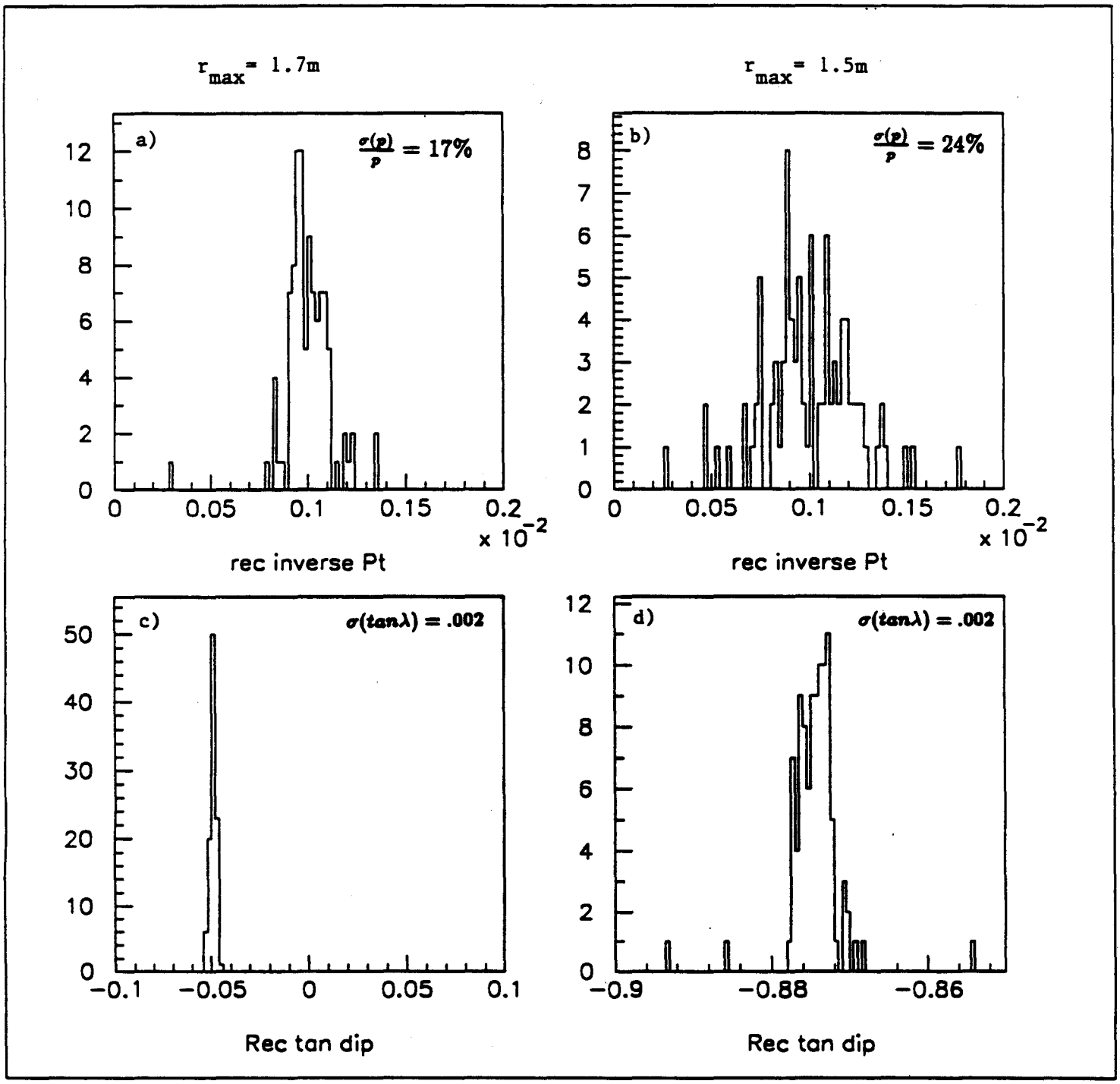
r max = 1.7m
r max = 1.5m
a)
σ(p)/p = 17%
b)
σ(p)/p = 24%
x 10^-2
rec inverse Pt
c)
σ(tanλ) = .002
d)
σ(tanλ) = .002
Rec tan dip

FIGURE 1

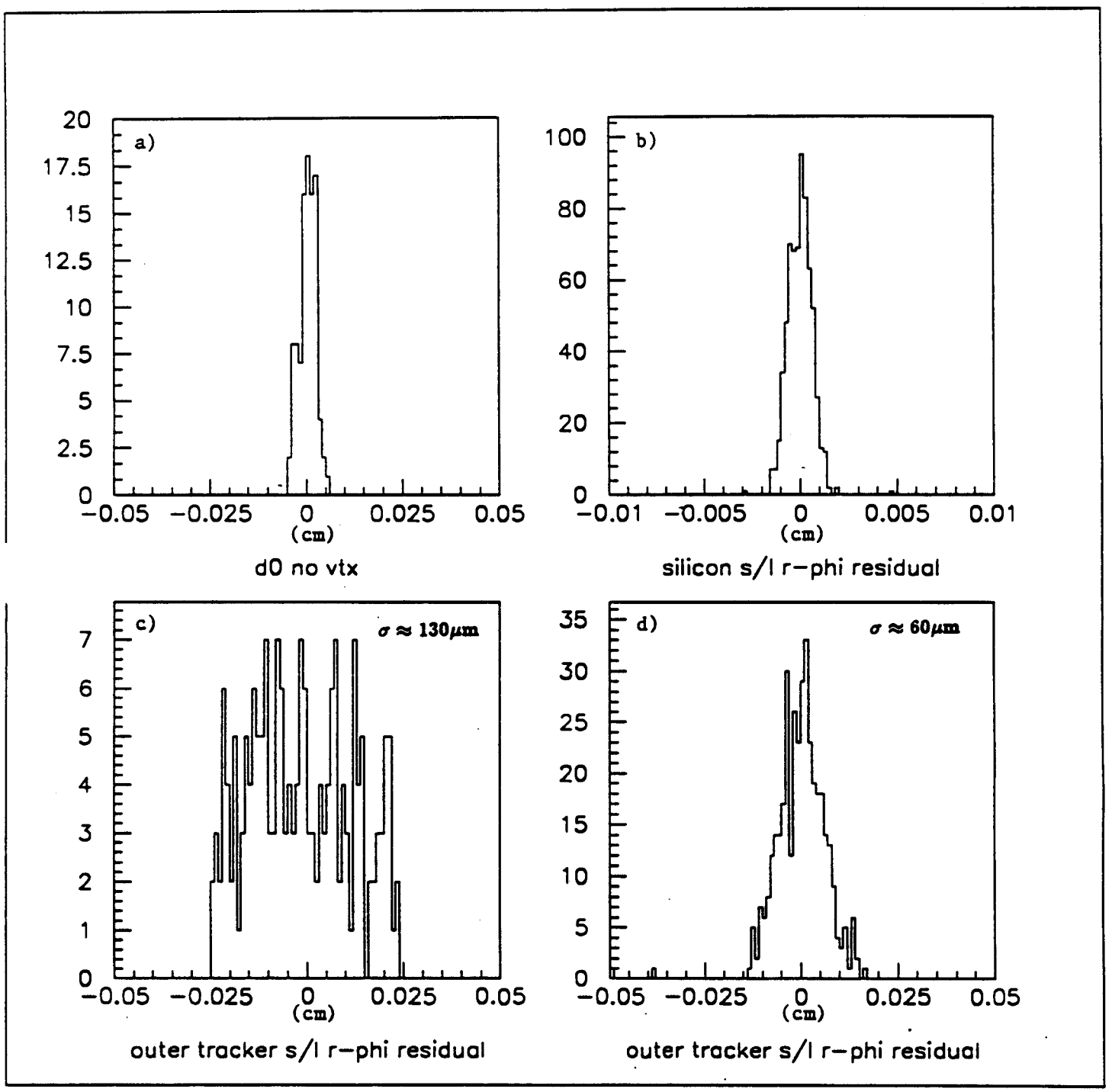

Scintillating Fiber **Straw Tube**

FIGURE 2

FIGURE 3

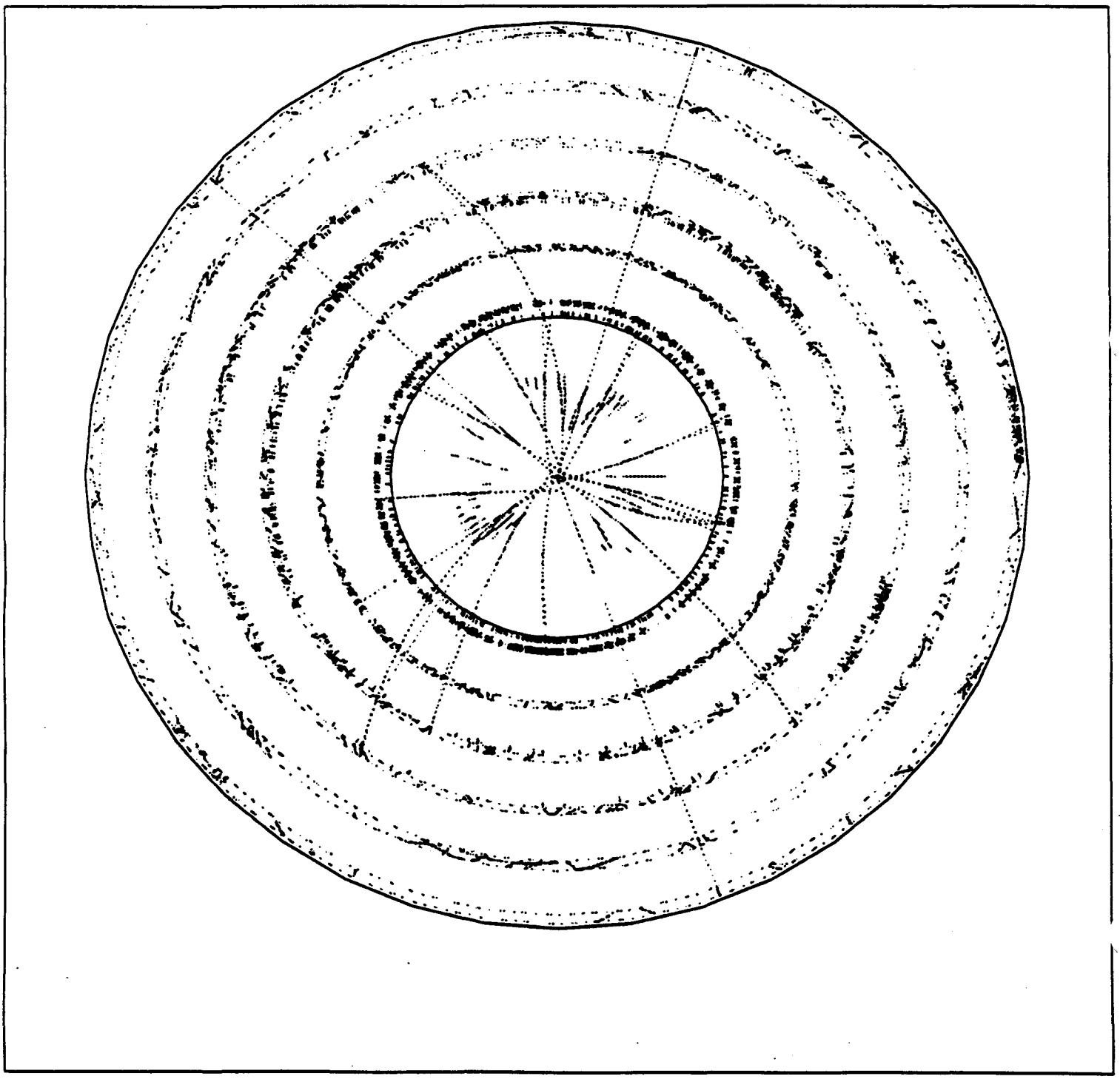

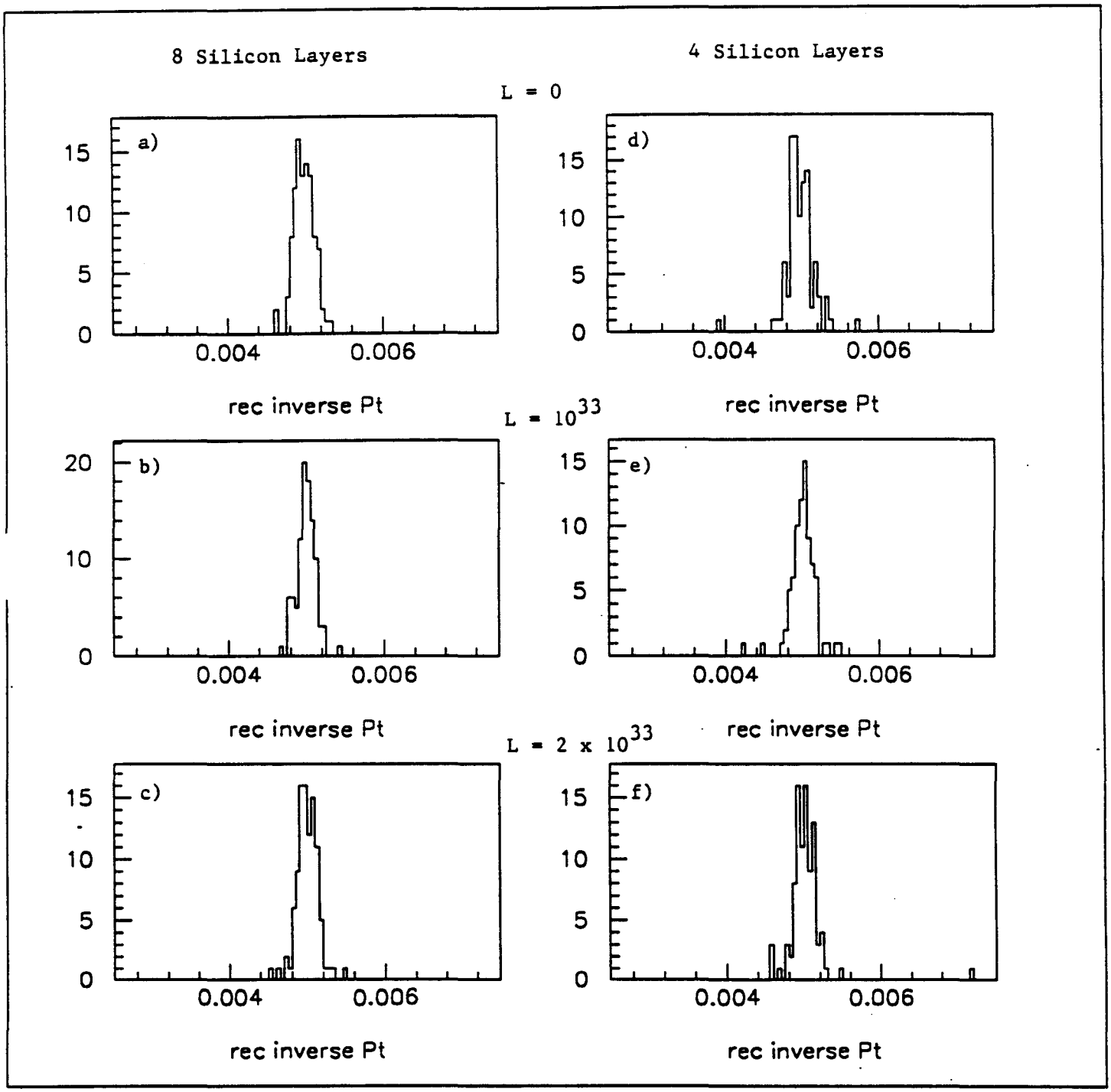
8 Silicon Layers
4 Silicon Layers
L = 0
L = 10^33
L = 2 x 10^33
a)
b)
c)
d)
e)
f)
rec inverse Pt
0.004
0.006
0
5
10
15
20

FIGURE 4

FIGURE 5

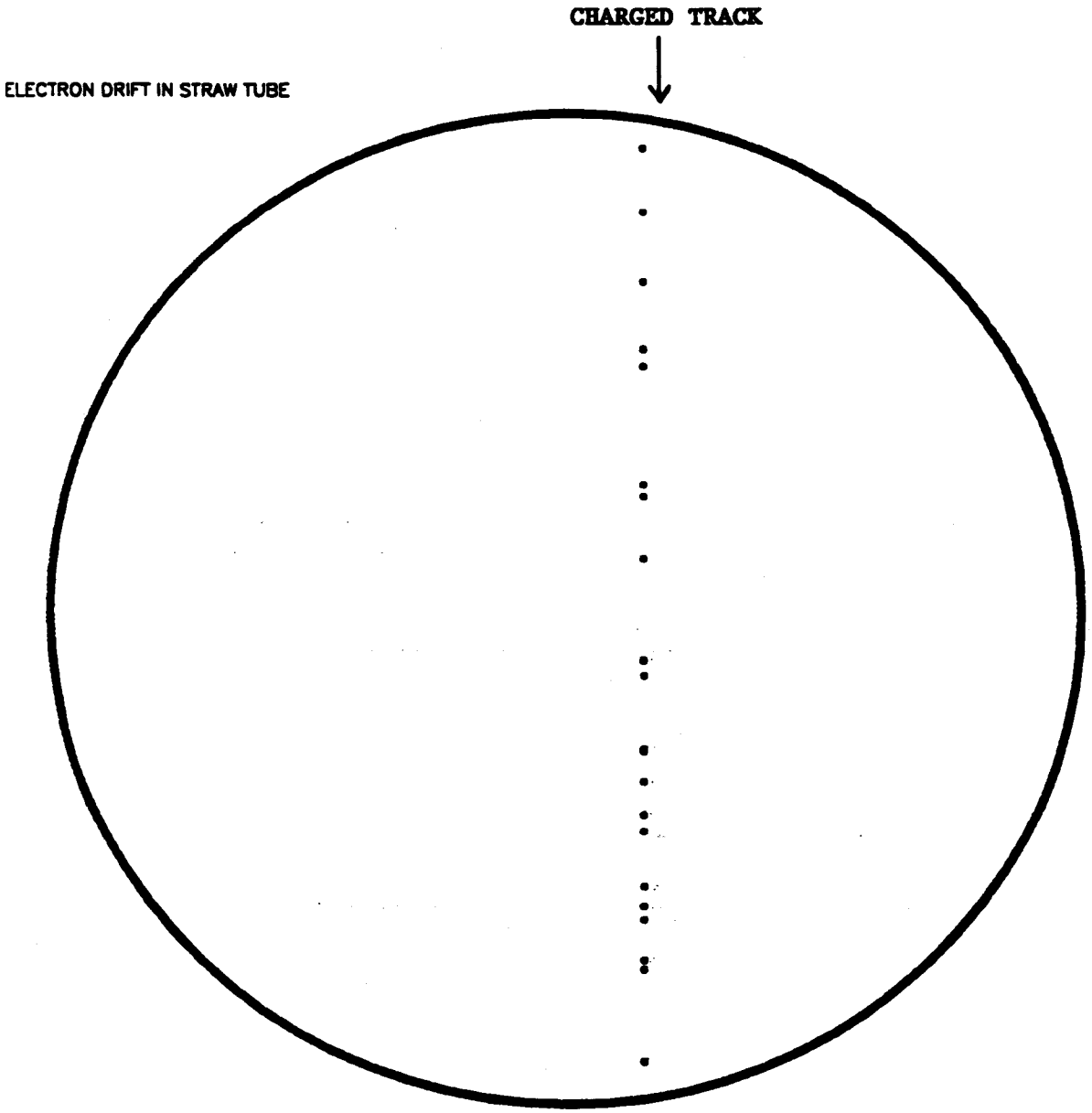

SCRI

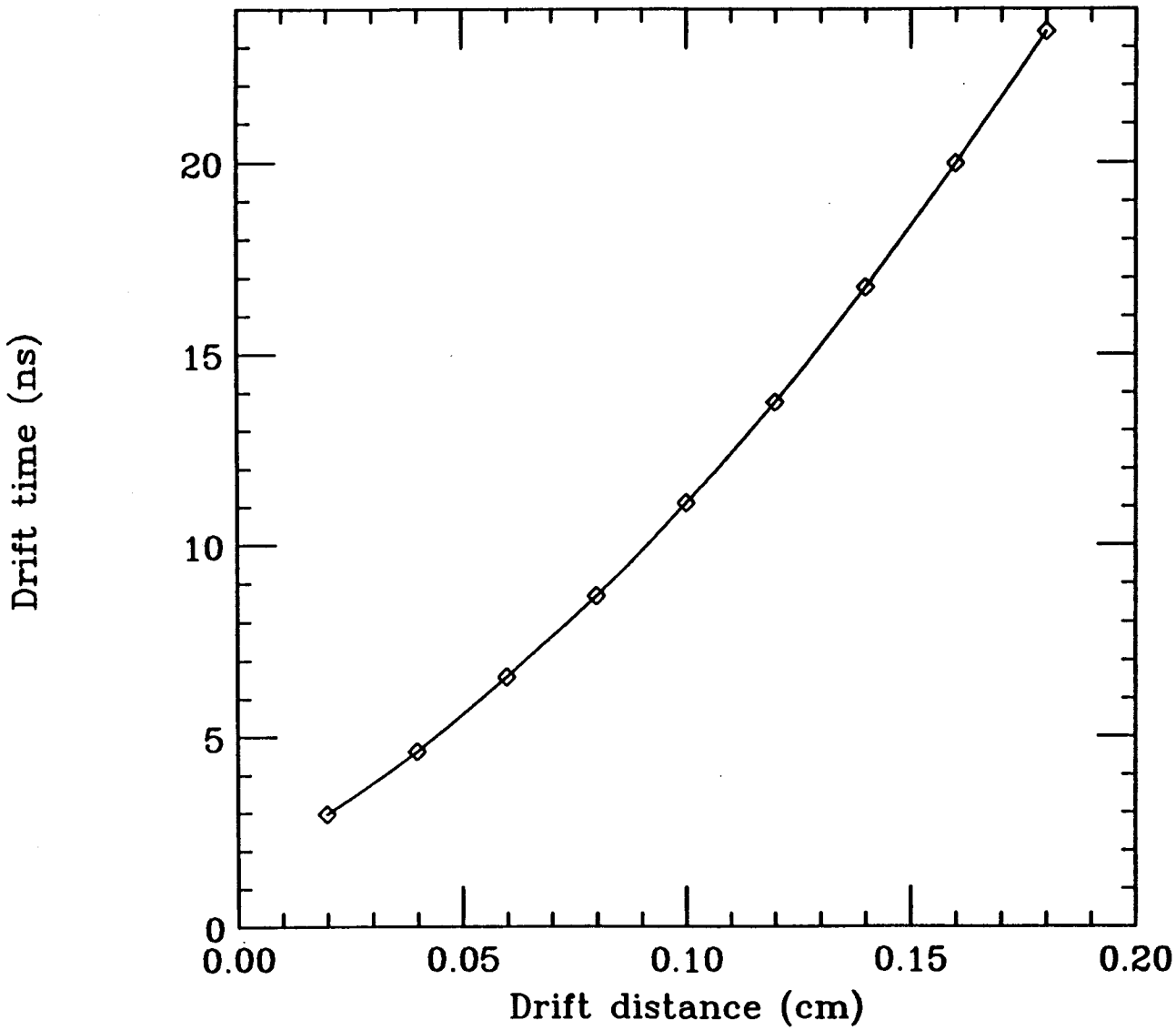

FIGURE 6

Hybrid Subsystem Progress Report for FY1991

Straw Tube Radiation Damage Studies

TRIUMF
Vancouver, Canada

Q. Fraszer
R. Henderson
R. Openshaw
M. Salomon

September 1991

Straw Tube Radiation Damage Studies

In the last year we continued our work of radiation damage of gaseous detectors and straw tubes in particular with the aim of selecting the best combination of gases, cathode material and other operating conditions for use in the central tracking volume of the SDC. We have identified problems with the aluminum cathodes due to non-uniformities in the straw surface. These were policarbonate straws of very poor construction. The imperfections were the source of sparking and eventual damage of the straws. They had to be rejected.

New straws made of Kapton with Cu cathodes were much better, and the tests with them and CF4+Isobutane (80,20) have just started. We are also studying other cathode materials. This is a very important problem because we have observed in the past that when using the radiation resistant CF4+Isobutane combination there was a slow but persistent erosion of the aluminum cathodes. The solution to this problem is either to use a thicker cathode or to find other conducting layers less susceptible to the ion bombardment. We have tried carbon, copper and nickel with several thicknesses and each of these alternatives have advantages and disadvantages, and some are easier to fabricate than others. We are still in the process of evaluation.

The selection of cathode material is also related to another line of activity we are presently starting. This is to construct our own straws. The reason for this effort is the fact that the straws we have received so far from manufacturers has variable quality and in general are not thin enough to insure total low mass for the tracker. This work is still in its infancy and we have nothing to report yet.

Several stringing methods are presently investigated, and the mechanical support for anode wires and their tensioning are being tested.

It is clear that the gas will have to be recirculated if the cost of operation is to be reasonable. A very important problem in the recirculation of CF4 gas is the type of filters required. This problem is also addressed now and long term effects are investigated. The main objective of the filters is to remove oxygen and water vapor from the gas. These impurities are incorporated to the original gas mixtures when circulating through the detector and need to be removed for proper operation. The recirculation rate is related to the flow rate one wants to achieve. This in turn is related to radiation damage as well as cooling of the straws. We are studying these variables now. For a realistic tracking

detector, most of the functions and controls in the recirculation system will be automated. This will require a system of sensors and controls that will be rather complicated. We are studying now how to do it, and towards that end we have built a smaller and simpler system for a transition radiation detector for HERA which is being tested now at CERN. This device recirculates Krypton gas and has some of the problems that will exist in the SDC straw tube tracker.

Hybrid Subsystem Progress Report for FY1991

Straw Electronics

University of Pennsylvania
Philadelphia, PA

Rick van Berg

September 1991

Straw Electronics

Exhaustive technical details of the progress during the past year of straw electronics research and development effort are contained in the report of the Front End Electronics Subsystem collaboration (1 September 1991), but highlights from that effort are listed here and some discussion of integration and system issues is attempted.

During the past year we have:

- Fabricated, tested, packaged, and distributed the low noise, fast shaping time (5 ns) single channel preamplifier and shaper in large size (>600) sample lots. This preamplifier/shaper is:
  - Constructed using the AT&T complementary bipolar process.
  - Designed with fully differential inputs to allow pickup cancellation.
  - Packaged in small outline 16 pin package suitable for surface mounting.
  - Available with yields before packaging of ~95% and after packaging of ~90%.
  - Radiation hard to doses in excess of 1 MRad-Signal/Noise and offset voltage variations after 1 MRad of Co^{60} are nearly unmeasurable.
- Designed, fabricated, tested, and distributed a small multilayer printed circuit test board to house four of the AT&T single channel amplifiers.
- Finished the design and nearly finished the layout of an eight channel preamplifier, shaper, tail cancellation, and discriminator circuit. This circuit is:
  - Designed using the Tektronix SH-Pi high speed bipolar process which as lower parasitic capacitances than the AT&T process, but lacks the fully complementary (PNP as well as NPN) transistors of the AT&T process.
  - Layed out using *Quick Tiles* as a compromise between the very high densities possible with a full custom design and the predictability and high yield of a fully characterized fixed array. We should note that even with the compromise density we are apparently limited by the number of pins rather than the actual silicon area needed for devices and connections.
  - Likely to be capable of triggering reliably on about one femto-coulomb of charge generated by a single avalanche – the noise floor is set largely by the 300Ω resistance needed to properly terminate long straw tubes.
- Designed using a process that is also radiation hard (at least in terms of gain and offset voltage variations – noise figures have not been measured yet) to better than 1 MRad.
- Finished the complete redesign of the TVC/AMU.

- All cells have been examined and, where necessary, redesigned and relayed out and resimulated to operate properly at above the design rate.
- The most complex parts of the logic (the *transfer* block) have been fabricated in a 2 μm non rad hard process and have been tested and shown to work properly at speed.
- Blocks which were inefficient in terms of area or power have been redesigned to make better use of the silicon – most notably the Delay Logic which is sensitive to changes in the length of the Level 1 Trigger Time.
- The complete, single channel, TVC/AMU up through L1 logic and including eight L1 and four L2 memory units has been tied together for simulations at both the schematic and layout level.
- Extensive measurements have been undertaken on the UTMC 1.2 μm CMOS process to characterize DC and noise behavior before and after radiation. These measurements indicate that this process is likely to be capable of producing TVC/AMUs and other analog objects capable of operating successfully well past the 1 MRad region.
- Layout and fabrication of test structures in the IBM 1.0 and 0.5 μm CMOS processes has begun with the expectation of having parts to measure this fall.

The tasks remaining include:

- Fabrication and test of the eight channel preamp/shaper/discriminator.
- Fabrication and test of the single channel TVC/AMU.
- Layout of the full (L2 logic) TVC/AMU.
- Layout of four or eight channel TVE/AMUs.
- Transfer of the TVC/AMU design to a radiation hard process.

But, probably most importantly, the difficult issues will center around packaging of a complete system and interactions between the detectors, front end signal processing, and back end trigger and DAQ signals. The test chips and the test modules that are just beginning to be available are vital to a beginning understanding of the complex set of interactions that will occur in the full scale detector, but the present single channel devices fall far short of the densities actually necessary in the final detector. As multi-channel preamps become available in the fall or winter, it will be possible to begin making nearly full density mock-ups of electronics packaged directly onto the straw ends as is presently envisaged (see the Preliminary Conceptual Design Report for SDC Straw Electronics). This will require closer coordination of mechanical and electronic efforts over the coming year.

Nuclear Instruments and Methods in Physics Research A303 (1991) 277–284
North-Holland

Design and performance of a straw tube drift chamber

S.H. Oh, D.K. Wesson, J. Cooke, A.T. Goshaw, W.J. Robertson and W.D. Walker
Department of Physics, Duke University, Durham, NC 27706, USA

Received 19 November 1990

The design and performance of the straw drift chambers used in E735 is reported. The chambers are constructed from 2.5 cm radius aluminized mylar straw tubes with wall thickness less than 0.2 mm. Also, presented are the results of tests with 2 mm radius straw tubes. The small tube has a direct detector application at the Superconducting Super Collider.

1. Introduction

Drift chambers are now used in almost every high energy physics experiment. There are many different designs of drift chambers and one of them uses straw tubes as detector elements [1]. In this article, we report the design, construction, and performance of large straw tube drift chambers used in the spectrometer arm of E735 at the Fermilab collider. E735 is an experiment to study low transverse momentum particles to search for a phase transition of hadron gas to quark–gluon plasma from the highest center of mass energy $\bar{p}p$ interactions [2]. We also present preliminary results of a study done with 2 mm radius tubes which have a direct detector application at the Superconducting Super Collider (SSC).

Using straw tubes has several advantages. First, since the cells are isolated from one another, cross talk is minimized. If a sense wire is broken, then the channel can be easily removed without turning off all channels. Second, straw tubes can be pressurized for better resolution, and for mechanical rigidity. Third, the resolution of tracks is independent of a particle's incident angle, so one does not have to incorporate angular correction factors when the drift distance is calculated from the drift time, as with typical drift chambers. This was the main reason we chose straw drift chambers since tracks in the spectrometer arm have large slopes.

This article is organized as follows. In section 2, we discuss the design and construction of chambers, and in section 3, testing and performance of the chambers are discussed. In section 4 we describe a method to measure the drift velocity and resolution. Section 5 includes the track reconstruction in the chambers, and section 6 contains a study done with 2 mm radius tubes, which may have a detector application for the Superconducting Super Collider.

2. Design and construction of chambers

The basic ingredient of the chamber is a 2.5 cm radius tube made of aluminized mylar. The wall of the tube consists of 0.018 mm of aluminum, 0.075 mm of paper and 0.075 mm of mylar, a thickness of about 0.04% of a radiation length. The tubes were wound by Stone Industrial [3] with length of about 110 cm. The tubes are strong enough to support about 10 kg of weight placed on one end, and an internal pressure of at least 3 atm.

The tubes are positioned between two aluminum plates as shown in fig. 1. Two aluminum plates on both the top and the bottom provide protection for the tube ends, feed-throughs and electronics. The size of the holes and the distance between holes were milled to be better than 0.1 mm. There are about 60 to 100 holes in each chamber. The holes in each chamber are in two staggered rows. After the holes were made, the center of each hole was measured with respect to a survey point to determine the exact position of the sense wire.

As shown in fig. 2, each tube is connected to the plates by means of aluminum end-pieces. A hose clamp is used to ensure the mechanical and electrical connection between the aluminum end-piece and the tube. Each aluminum piece is grounded to the frame by a ground cable. An end-piece made of delrin and a feed-through are inserted into the aluminum end-piece. 100 μm diameter gold plated Cu–Be wire is strung between feed-throughs under 250 g of tension. The elastic limit of the wire is about 1000 g. Cu–Be wire is used because its thermal expansion coefficient is close to that of the aluminum frame. A larger diameter wire is chosen to provide a higher electric field near the outer wall of the tube. The drift velocity saturates if the electric field is high enough.

Gas leakage, especially around the ends of the tubes,

0168-9002/91/$03.50 © 1991 – Elsevier Science Publishers B.V. (North-Holland)

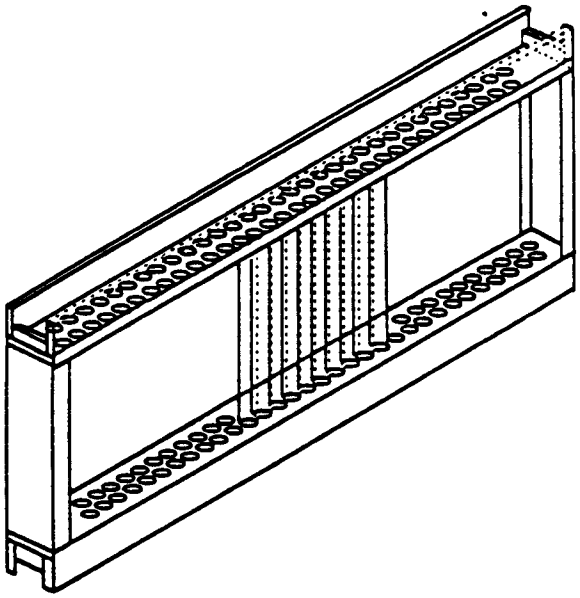

Fig. 1. The aluminum frame structure of a straw drift tube chamber for E735. A few tubes between the two aluminum plates are also shown.

was a major problem during construction. The gas seal is accomplished by pouring low viscosity RTV-615 around the tubes. RTV-112 is used to provide the gas seal around the feed-throughs and around the gas tubing.

Gas is provided by 0.6 cm diameter plastic tubing at the top of the aluminum end-piece. 16 tubes are connected in series and an independent gas line is provided for each group of 16. This is to minimize contamination to other tubes in a chamber in case a tube develops a leak. When data is being taken, each chamber receives gas at a rate of about 1 ft^3/h.

The output from the sense wire is connected to an amplifier-discriminator through a 0.001 μF capacitor. The amplifier-discriminators are mounted on the top part of the frames of the chambers near the ends of the tubes. The amplifier-discriminator is designed using MC10116 and its performance is quite comparable with LeCroy 2735DC whose minimum threshold is 2 μA. 130 ft of twisted pair ribbon cables connect the output of the amplifier-discriminator to LeCroy TDCs. We have used 4299B with 1 ns time resolution.

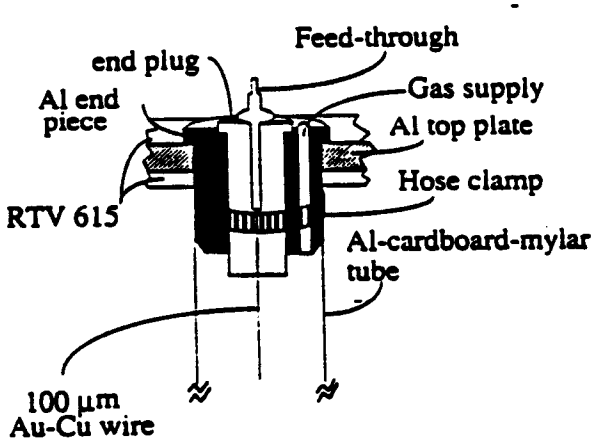

Fig. 2. A detailed view of a tube end including end pieces.

There are seven chambers with two planes of tubes in each chamber. The size varies from 75 cm (height) × 220 cm (length) to 110 cm × 340 cm. Four out of seven chambers have tubes positioned vertically to measure the horizontal position of tracks. The strong component of the magnetic field is along the vertical direction. The tubes in the other three chambers are slanted by 4° for stereo reconstruction. When in place, chambers with slanted tubes alternate between chambers with vertical tubes. There are about 700 channels in the detector.

3. Testing and performance of chambers

In order to find the operating voltage for the chambers, the singles rate as a function of voltage was studied. Fig. 3 shows a typical plateau taken with cosmic rays, and ^{137}Cs source with Ar–ethane (50%–50% mixture). The operating voltage is selected at the end of the plateau curve as shown in the figure.

After chambers were constructed, we measured the resolution by using cosmic rays. A chamber is sandwiched between two scintillators. A trigger is generated from the coincidence signal from the two scintillators and used to start the TDC. The measured time is converted to distance from the sense wire. For the

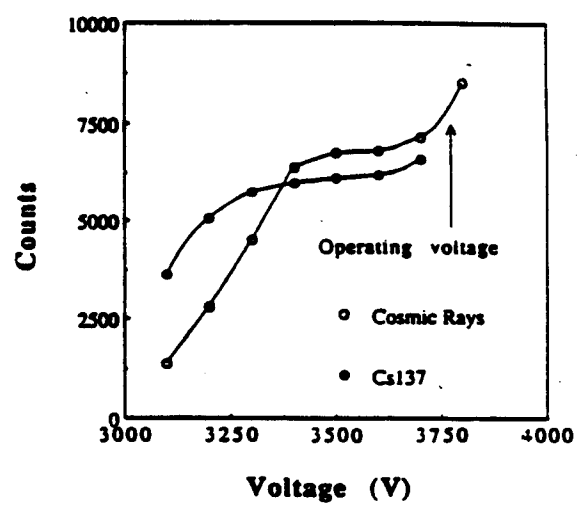

Fig. 3. Two plateau curves obtained using cosmic rays and ^{137}Cs. The gas used is Ar–ethane (50%–50% mixture).

conversion, the drift time as a function of distance is measured (section 4) and plotted. This curve was fitted with a polynomial and used to convert the measured time to distance. Sometimes it was necessary to divide the data into two regions to get a good overall fit. After the conversion of time to distance, tracks were reconstructed (section 5) and the residual was calculated.

We have tried two different gas mixtures, Ar–ethane (50%–50%) and P10 (Ar–methane, 90%–10%). The Ar–ethane mixture produced slightly better resolution than Ar–methane mixture. Fig. 4 shows the residuals for the two gases, and the σ is less than 200 μm. The residual is calculated from tracks with more than 6 hits.

An earlier study [4] showed that the radiation level from the accelerator at the chamber position was expected to be high. Therefore a radiation test was performed on a prototype consisting of a single tube. The tube was exposed to an intense source (^{90}Sr) such that the sense wire drew about 1 μA/cm. This corresponds to about 0.09 C cm^{-1} d^{-1}. We used the Ar–ethane (50%–50%) mixture for the test because of the higher hydrocarbon content. Hydrocarbon is a known aging agent. The exposure lasted for four months with periodic checks made of the current draw, single count and the shape of plateau. The results of the current draw and the single count as a function of integrated charge/cm on the sense wire is shown in fig. 5. They remained constant during the period. After the test, the tube was opened and examined for radiation damage. No signs of whisker growth or other deterioration were found. It was reported that some chambers using the same gas became inoperative after much less dosage [5]. We believe that this is due to the lower electric field at the cathode and a much larger cathode area.

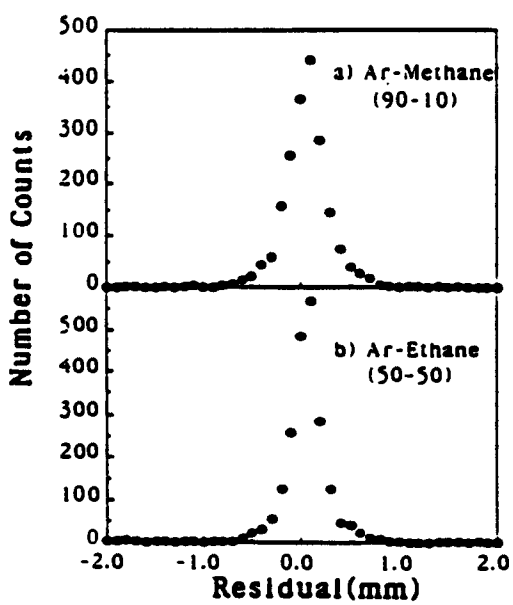

Fig. 4. The residual obtained using cosmic rays for two different gases. The sigma is less than 200 μm for both gases.

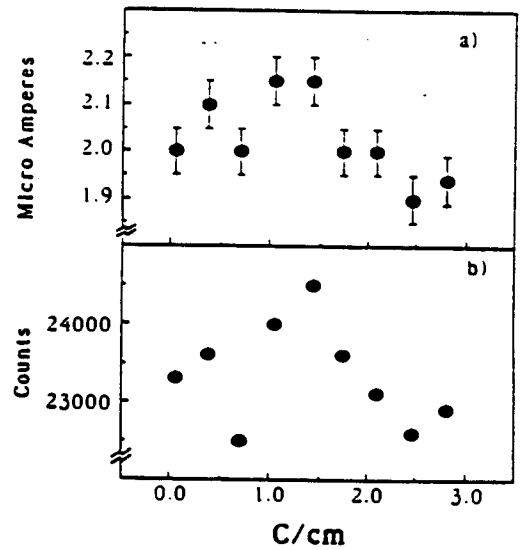

Fig. 5. Results of an aging test using ^{90}Sr source. (a) Shows the current draw by the sense wire as a function of total charge deposited on the sense wire. (b) Shows the single count as a function of total deposited charge.

4. Drift velocity measurement

We have used a simple method to measure the relationship between the drift time and the distance from the sense wire. A 1 mCi ^{90}Sr source is placed in front of a slit followed by a chamber and another slit as shown in fig. 6. The two slits (1 mm wide and 1 cm in height) determine the beam position. A scintillator is placed behind the second slit and used to start a TDC and the signal from the tube is used to stop the TDC. Since the energy of electrons from the ^{90}Sr source is low, we did not use the coincidence of two scintillators. We used one small scintillator large enough to cover the slit to reduce the random background start. This method provides a fast way to measure the drift velocity and resolution of different gases under operating conditions as shown below.

The time distribution for a given slit position is plotted and fitted with a Gaussian to determine the mean time and σ. The mean time and σ are plotted as a function of the slit position. In fig. 7 the mean time is plotted as a function of distance for methane. The position of the sense wire is the intersection point between two curves which fit the data points in the left and right side of the sense wire. By differentiating the fitted curve, the drift velocity can be calculated as a

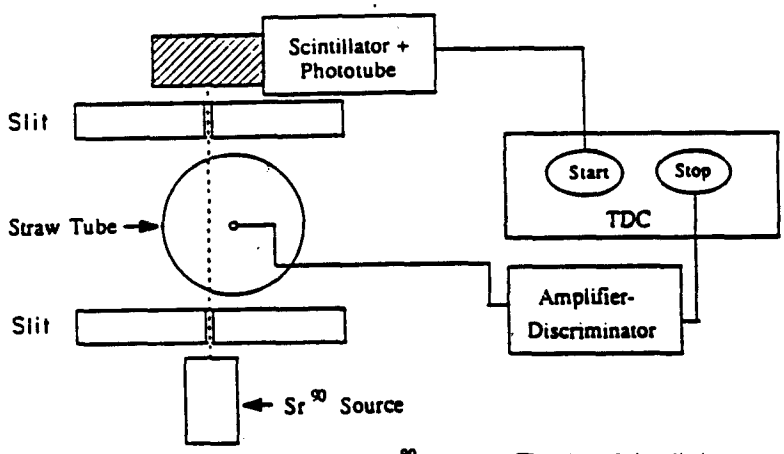

Fig. 6. Schematic to measure drift velocity and dispersion using a ^{90}Sr source. The size of the slit is 1 mm (width) by 1 cm (height). See text for details.

function of the distance from the sense wire or the electric field since the electric field is easily calculable for the cylindrical geometry. In fig. 8, the measured drift velocity as a function of electric field is plotted for several gases. Fig. 8a shows the electron drift velocity for Ar–ethane (50%–50%) and P10 (90% Ar–10% methane). Fig. 8b shows the same for pure methane and methane with 5% ethyl-alcohol. This mixture is tried because mixing alcohols increases the lifetime of chambers. Mixing alcohol changes the characteristics of the drift velocity as a function of the electric field.

In fig. 9, the drift velocity using mixtures of CF_4 and CH_4 is presented. The mixtures are tested because of a possible application to an SSC detector. For an SSC drift chamber, gas with fast electron drift velocity (larger than 100 μm/ns) is desirable since the time between bunches is 16 ns (see section 4). As seen from the figure, pure CF_4 as well as the mixtures of CF_4 and CH_4 have drift velocities larger than 100 μm/ns. Although not plotted, some of our data points are compared with the existing data [6] and they are in fair agreement.

The σ of the time distribution is related to the resolution as a function of drift distance. We convert the σ, measured in time to distance using the time to distance conversion plot, i.e., $t \pm \sigma_t$, in time to $d \pm \sigma_d$ in distance. We point out that the σ_d does not measure the absolute resolution directly because of the slit size and the multiple Coulomb scattering of electrons. However σ_d provides a good way to compare the relative resolution as a function of the drift distance between different gases.

In fig. 10a the σ_d (dispersion) is plotted as a function of drift distance. For P10 and Ar–ethane, the dispersion is fairly constant as a function of distance. In fig. 10b, the same is plotted for methane and methane with 5% ethanol. It is interesting that the dispersion rises steeply

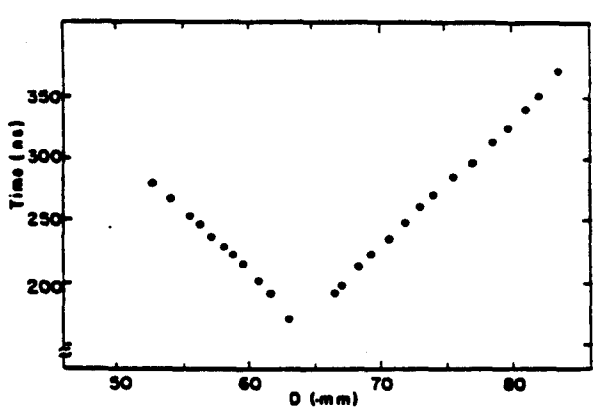

Fig. 7. A typical mean drift time plotted as a function of distance. The sense wire is at the symmetry axis. The data is obtained with CH_4.

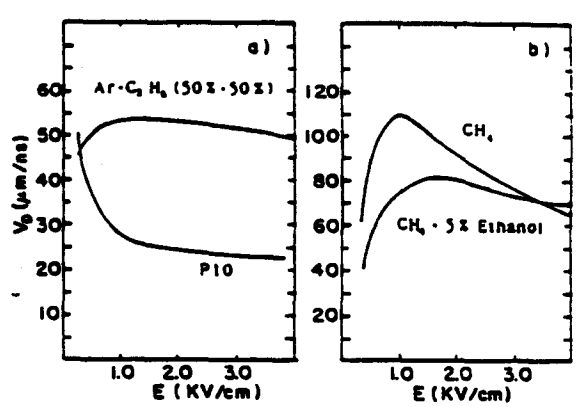

Fig. 8. Drift velocity as a function of electric field as measured using the setup in fig. 6 for P10, Ar–ethane (50%–50%), CH_4, and CH_4 + 5% ethanol.

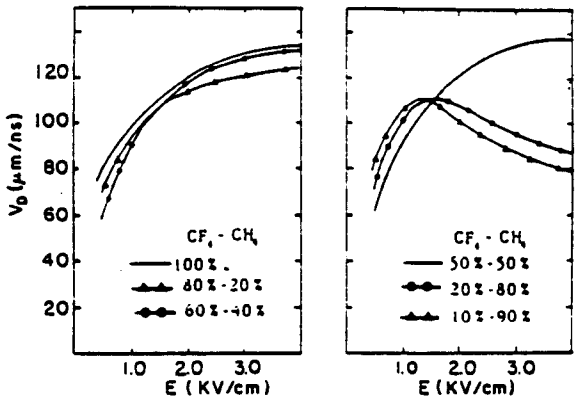

Fig. 9. Same as fig. 8, but with different mixtures of CF_4 and CH_4.

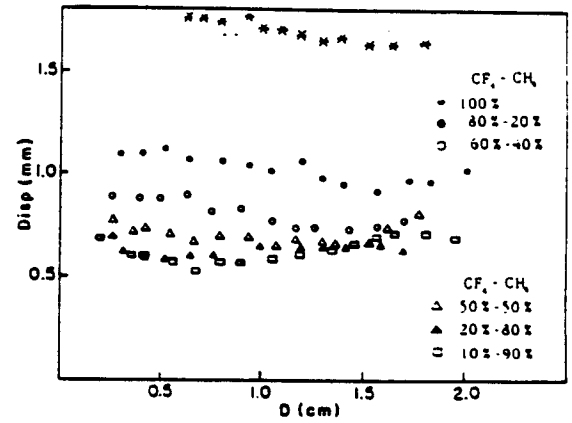

Fig. 11. Dispersion as a function of drift distance for different mixtures of CF_4 and CH_4.

at a certain distance from the sense wire when the alcohol is mixed. This may be due to the electron attachment to alcohol molecules. We have tried several mixtures of different gases with different kind of alcohols, and we found that mixing alcohol always increases the dispersion at a large distance (~ 1 cm from the sense wire).

In fig. 11, the dispersion is plotted for the mixtures of CF_4 and CH_4 as a function of distance. It was shown earlier that these mixtures produced fast electron drift velocity as required for an SSC detector application. Fig. 11 shows that CF_4 alone is not a suitable gas for a drift chamber due to a large dispersion. As will be shown later, pure CF_4 not only results in a large dispersion, but also produces a long tail in the time distribution. The dispersion is reduced when CH_4 is mixed. The reduction increases as the fraction of CH_4 increases.

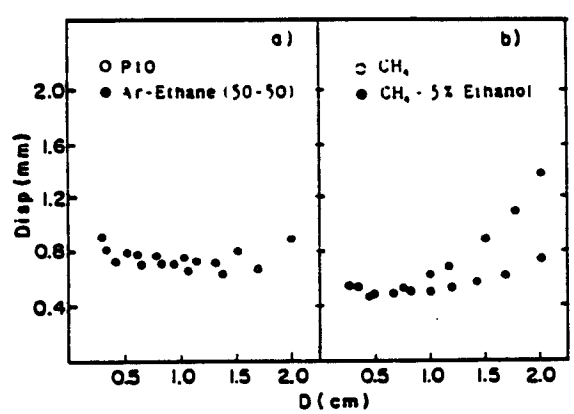

Fig. 10. Dispersion as a function of drift distance from the sense wire for several different gases: P10, Ar–ethane (50%–50%), CH_4 and CH_4 + 5% ethanol.

Mixing other hydrocarbon gases, such as ethane produces the same effect. It seems to us that a mixture with more than 50% of CH_4 may be acceptable in terms of dispersion.

In fig. 12, the converted time distribution (to distance) is plotted when the slit is about 2 mm away from the sense wire for different mixtures of CF_4 and CH_4. As pointed out earlier, pure CF_4 produced a long tail.

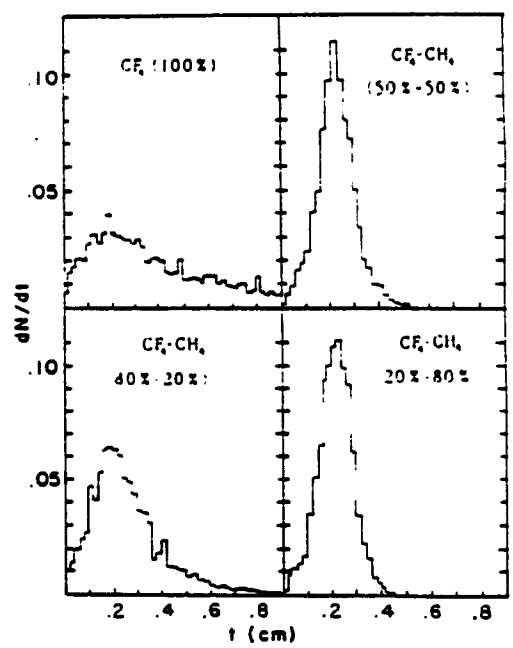

Fig. 12. Converted time (to distance) distribution when the slit is about 2 mm away from the sense wire for different mixtures of CF_4 and CH_4. The width of the slit is 1 mm.

The dispersion and the tail get smaller as the CH_4 content increases.

5. Track reconstruction

Fig. 13 shows some tracks passing through the chambers. Since a drift time represents the distance from the sense wire, a hit is represented by a circle around the sense wire. Tracks are reconstructed in the chambers with vertical tubes and then the chambers with slanted tubes are used for the stereo reconstruction.

The first step to reconstruct a track is to calculate the four possible tangential lines between two circles as shown in fig. 14. The two circles are chosen in the furthest chamber from the interaction region to avoid any field from the analysis magnet. The magnetic field strength is a Gaussian with maximum strength of 3 kG. The field strength drops to about 700 G at the first chamber (20 cm from the center) and to about 10 G at the last chamber location (100 cm from the center of the magnet).

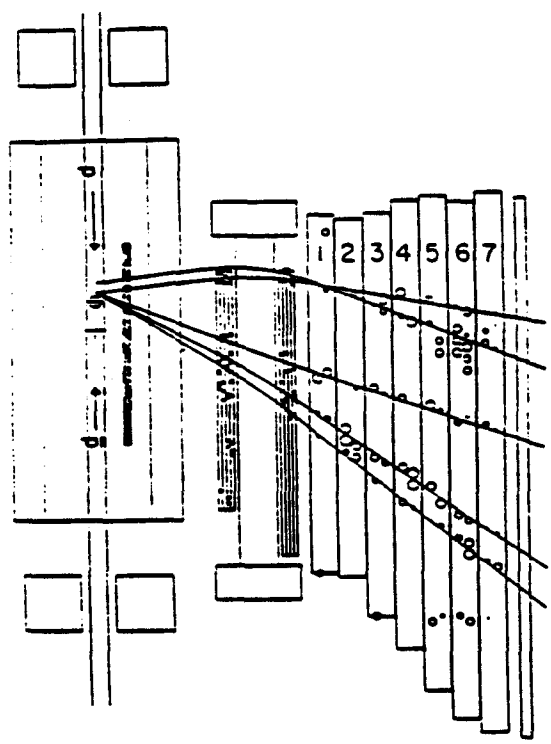

Fig. 13. Tracks passing through the E735 spectrometer arm. E735 is one of the collider experiments at Fermilab. Hits in the straw chambers are represented by a circle with a radius corresponding the converted drift time to distance from the sense wire. The tubes in the chambers with even numbers are tilted by 4°. The directions of protons and antiprotons are also shown.

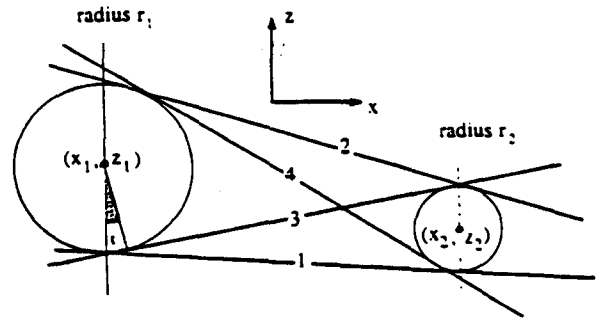

Fig. 14. Tracks which are tangential to two circles (hits). The number 1, 2, 3 and 4 and symbols correspond to the same in eq. (1)

The lines satisfy the following equations (see fig. 14 for the definition of variables):

$$\sin(t)(x_2 - x_1) - \cos(t)(z_2 - z_1) + (r_2 - r_1) = 0. \quad (1)$$

$$\sin(t)(x_2 - x_1) - \cos(t)(z_2 - z_1) - (r_2 - r_1) = 0. \quad (2)$$

$$\sin(t)(x_2 - x_1) - \cos(t)(z_2 - z_1) - (r_2 + r_1) = 0. \quad (3)$$

$$\sin(t)(x_2 - x_1) - \cos(t)(z_2 - z_1) + (r_2 + r_1) = 0. \quad (4)$$

After t is found from each equation, the slope ($\tan(t)$) and intercept are calculated for each line. Once the equation of a line is found, the line is projected to the next chamber (toward the interaction region) and the predicted position is compared with the measured position. If the difference is within a given limit, the hit is tagged to belonging to the line. A hit can be tagged by more than one line. The search continues until there are five good points or the search reaches chambers with appreciable magnetic field (first chamber). When the search is over, those tracks with more than four points are fitted with a straight line. If only one track is reconstructed and its χ^2/df is less than 2, then the track is accepted for further processing. If more than two tracks with χ^2/df less than 2 resulted from the four tangential lines, the track with the most points is selected. If the number of points is the same, then the line with best χ^2/df is chosen. Those hits belonging to good tracks are deleted from the data bank and not used further. This process is continued until all hits are tried.

Using the slope and intercept of the selected track, the approximate momentum of the track is calculated using the interaction vertex and the integrated magnetic field. Using this momentum, the track is swum through the magnetic field to the remaining chambers and the nearest hits within a given limit are selected. After all hits belonging to a track are found, the track is finally fitted with a second order polynomial.

After the horizontal position of a track is found, the hits in the slanted tubes along the track are collected. From the hits and known horizontal positions of the track, the corresponding vertical position of each hit in the slanted tubes is calculated. A linear fit is performed with the hits and the track with most hits (with good χ^2/df) is chosen. We found this procedure reconstructs tracks correctly with better than 95% efficiency.

6. Application for the Superconducting Super Collider

The concept of using straw tubes can be easily extended to a detector for the Superconducting Super Collider. As discussed earlier, there are several advantages of using tubes for a drift chamber. The chamber could be either a cylindrical central chamber or just a rectangular type tracking chamber [7].

The upper limit of the tube radius is set by the bunch spacing of the SSC. Since electrons produced from tracks of an interaction should have reached the sense wire before the next bunch arrives, the radius of the tubes should be about 1.5 mm if a fast gas with electron drift velocity 100 μm/ns is used. As shown previously, there are gases with drift velocity higher than 100 μm/ns within the small tubes under an operating voltage.

In this section we present some tests performed using 2 mm radius tubes. The tube wall is made of 0.025 mm thick mylar coated with 200–300 Å thick aluminum [8]. Several single straw tube prototype chambers were constructed with 25 μm diameter gold plated tungsten wire under 50 g tension. We were able to pressurize the chamber to 3 atm for a month without any problem. Pressurizing tubes not only keeps them round and stiff but also could result in a better resolution.

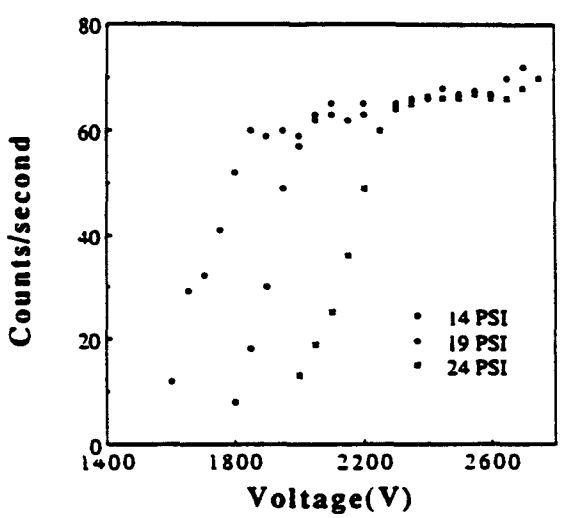

Fig. 15. Plateau curves obtained using small straw tubes (2 mm radius) filled with CH_4 under different pressures.

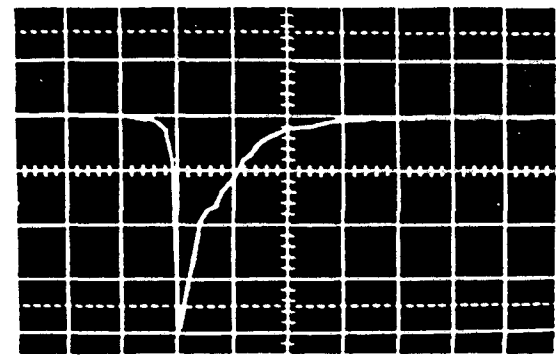

Fig. 16. The shape of the averaged signal using ^{90}Sr into a 50 Ω resistor. 1000 signals are averaged. HV = 2200 V. gas = methane. The vertical scale is 0.5 mV/div and the horizontal scale is 20 ns/div.

In fig. 15, plateau curves obtained with a ^{90}Sr source at several different pressures with pure methane are plotted. We observe a very nice plateau for all pressures. It is interesting that the knee of the plateau changes as a function of pressure. Fig. 16 shows an averaged signal using ^{90}Sr source. The gas mixture is pure methane at 1 atm and the high voltage is set at 2200 V. The peak is about 2 mV into a 50 Ω resistor. The signal rises to the maximum within 3 ns and falls to about 10% of the peak after 30 ns.

Using 4 mm diameter straw tubes, we have constructed a 60 channel, 2.7 m long prototype. It has eight layers of tubes. Some preliminary results are already reported [9]. The detailed construction and performance test will be reported in the near future.

References

[1] C. Broll et al., Nucl. Instr. and Meth. 206 (1983) 385;
P. Baringer et al., Nucl. Instr. and Meth. A254 (1987)542.
[2] T. Alexopoulos et al., Phys. Rev. Lett. 60 (1988) 1622;
S. Banerjee et al., Phys. Rev. Lett. 62 (1989) 12;
T. Alexopoulos et al., Phys. Rev. Lett. 64 (1990) 991.
[3] Stone Industrial Division, College Park 20704, MD, USA.
[4] C. Lindsey et al., Nucl. Instr. and Meth. A254 (1987) 212.
[5] M. Turala and J.C. Vermeulen, Nucl. Instr. and Meth. 205 (1983) 141.
[6] F. Sauli, CERN preprint 77-09;
B. Jean-Marie et al., Nucl. Instr. and Meth. 159 (1979) 213;
L. Christophorous et al., Nucl. Instr. and Meth. 163 (1979) 141;

T. Yamashita et al., KEK preprint 88–133;
there are some disagreements between published drift velocity measurements, for example, in CH_4.

[7] SSC subsystem proposals, submitted to SSC Lab. 1989, PC-024 (G. Hanson et al.), PC-035 (A.T. Goshaw et al.).

[8] The small radius tubes were wound by Precision Tubing, Wheeling, IL, USA.

[9] S.H. Oh et al., Proc. Int. Workshop on Solenoidal Detectors for the SSC, KEK, Japan, eds. F. Abe and R. Hasegawa (1990) p. 279.

Nuclear Instruments and Methods in Physics Research A (1991) 000–000
North-Holland

& METHODS
IN PHYSICS
RESEARCH
Section A

Construction and performance of a 2.7 m long straw drift tube prototype chamber for the SSC

S.H. Oh, A.T. Goshaw and W.J. Robertson
Department of Physics, Duke University, Durham, NC 27706, USA

Received 4 April 1991

We report the construction and testing of a 2.7 m long straw tube drift chamber consisting of 60 channels. The straw tubes with 2 mm radius are stacked in a pyramid shape up to eight tube layers. There are two wire supports inside each tube for electrostatic stability. 28 tubes out of 60 are instrumented for measurement of resolution, gas gain, and attenuation length. Resolution of close to 110 μm and attenuation length of 500 cm are obtained.

1. Introduction

The design of the central tracking chamber in a solenoidal detector [1] for the Superconducting Super Collider (SSC) calls for a cylindrical tracking chamber ≥ 6 m long. Using straw tubes with small radii is one of the options [2] for the tracking chamber. Due to the bunch spacing and the occupancy rate, the tube radius should not be greater than 2 mm. The central tracking chamber will likely consist of several cylindrical superlayers, with each superlayer typically made up of about eight layers of tubes. In order to cover a large tracking volume, superlayers are separated by about 10–15 cm from each other. In this chamber, track segments are found in each superlayer first and then the segments from different superlayers are linked to form a complete track.

For a feasibility study, we have constructed a 2.7 m long superlayer on a flat surface. In the prototype, 60 straw tubes with 2 mm radius are stacked in a pyramid shape up to eight tube layers. The tubes used in the prototype have a wall thickness of 50 μm of mylar on a 8 or 12 μm thick aluminum cathode. Because of the length of each cell, sense wires have to be supported and our study shows that the support is needed about every meter. Two wire supports are placed inside each tube in the prototype.

By successfully constructing and operating the prototype, we have verified that the basic design concept is sound and can be extended to a full size cylindrical central chamber. Specifically we have demonstrated the following: First, we showed that layers of tubes can be placed straight with an accuracy better than 100 μm over several meters once a flat base surface is provided. Second, a double-wall endplate designed by our group provides a simple way to supply gas, tension the sense wire and mount electronics. Third, the wires can be supported inside tubes at 1 m intervals to make a long working straw cell. Fourth, a large number of channels can be made operational simultaneously without difficulty. This is important since the expected number of channels for the final tracking chamber is about 200 000. Finally, we showed that spatial resolution of close to 110 μm can be achieved and the attenuation length is long enough that signals from the end of the detector farthest from the readout electronics are not significantly degraded.

Although using a tube for a drift cell is not new [3], and there have been efforts to use small radius straw tubes [4], our prototype is the first of its kind in terms of length, tube radius and number of channels.

This article is organized as follows. In section 2, we present results of an electrostatic stability study. We measured the position of the sense wire inside a 2 mm radius tube as a function of high voltage with different tension in the wire and different initial displacement. In section 3, we discuss a design of a wire support. Section 4 contains details of the design and construction of the 2.7 m prototype. In section 5, we present the results of tests to measure the gain, attenuation length and resolution of the prototype. We present our conclusions in section 6.

2. Electrostatic stability

The design for the central tracking chamber in a solenoidal detector at the SSC uses 2 mm radius straw tube detector elements. The sense wire would be oper-

0168-9002/91/$03.50 © 1991 – Elsevier Science Publishers B.V. All rights reserved

ated at around 2000 V to achieve gas gains which give suitable signal pulses. The ideal case in which the sense wire is exactly centered within a perfectly cylindrical cathode is electrostatically stable. Practically, however, the sense wire will not be exactly centered due to positioning error and gravitational sag and the straw tube cathode will be neither perfectly cylindrical nor perfectly straight. Therefore it is important to determine the conditions under which an operational straw tube detector element will perform satisfactorily. The electrostatic force per unit length due to offset of the sense wire in the straw tube is given by (mks unit)

$$F_e = \frac{2\pi\epsilon_0 V^2 \delta}{R^2(\ln(R/r))^2},$$

where V is the sense wire potential, δ is the offset of the sense wire from the center of the straw tube, R is the radius of the straw tube cathode and r is the radius of the sense wire.

We have constructed a straw tube model using a stainless steel tube which is held in alignment by a 2 cm square steel "backbone" and machined mounting brackets. The tubing has an inner radius of 1.95 mm. The steel tube is placed in a horizontal orientation. A manifold on one end allows gas flow to purge air. We have used CH_4, CO_2 and CF_4 as stable gases.

We find that the longest cell that is stable above 2.5 kV with a 25 μm sense wire centered in the tube under 50 g tension is about 1 m. The tensile strength of 25 μm diameter gold plated tungsten wire is 150–200 g so the applied tension to the wire should be kept below 100 g. Keeping the wire tension to a minimum will also reduce the mechanical load on the detector assembly.

Using a 1 m long tube, we have conducted a series of tests to determine the effect of the wire offset in the tube on the maximum voltage the cell can sustain before breakdown. A sense wire is positioned in the tube so as to be centered vertically. The horizontal position of the sense wire with respect to the center of the tube is adjustable. The distance from the center of the tube to the position of the sense wire is measured by means of a travelling microscope to an accuracy of better than 20 μm. The wire position was adjusted relative to the center of the tube and the potential on the wire was then increased until breakdown occurred in the cell.

Fig. 1 shows the maximum stable operating voltage that a 1 m long cell filled with CH_4 can sustain as a function of the sense wire displacement from the center of the cathode for wire tensions of 50 and 100 g. Two other gases mentioned earlier give slightly different results. The test shows that the wire offset of up to a few hundred micrometers will not compromise cell operation.

One can study the displacement of the sense wire

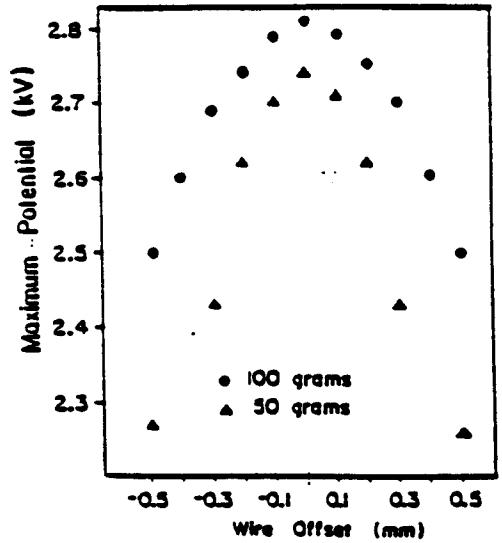

Fig. 1. Maximum stable operating voltage for two different wire tensions of 50 and 100 g as a function of initial wire offset.

under increasing electric potential. This has been done by drilling a hole in the middle of the steel tube to observe the position of the sense wire with a travelling microscope as the wire potential is raised.

In our setup, the sense wire was positioned off center by a known amount (δ) horizontally, and then the sense wire potential was increased. The deflection of the midpoint of the wire (d) from its initial position was measured for several different potentials. This deflection is related to the potential on the wire of length L to good approximation by the expression

$$d = L^2 F_e / 8T.$$

This problem is similar to the wire sag calculation due to gravity. For a 50 g tension, the sag due to gravity at the middle for a 1 m long wire is about 25 μm thus we ignore the gravity effect in this analysis. Using the F_e previously defined, then d can be written as

$$d = \frac{2\pi\epsilon_0 V^2 L^2(\delta + d/2)}{R^2(\ln(R/r))^2}.$$

$d/2$ is added to δ in order to take into account the additional force (approximately) due to the wire deflection d. For 1 m long wire, the displacement is given by

$$d = \frac{\delta(V/V_0)^2}{1 - \frac{1}{2}(V/V_0)^2},$$

where $V_0 = 2700\sqrt{T/50}$, with T the wire tension in grams and V the applied potential in volts.

Fig. 2 shows measurements of the wire deflection versus sense wire potential for tensions of 50 and 100 g. The lower set of data in each case is with an initial

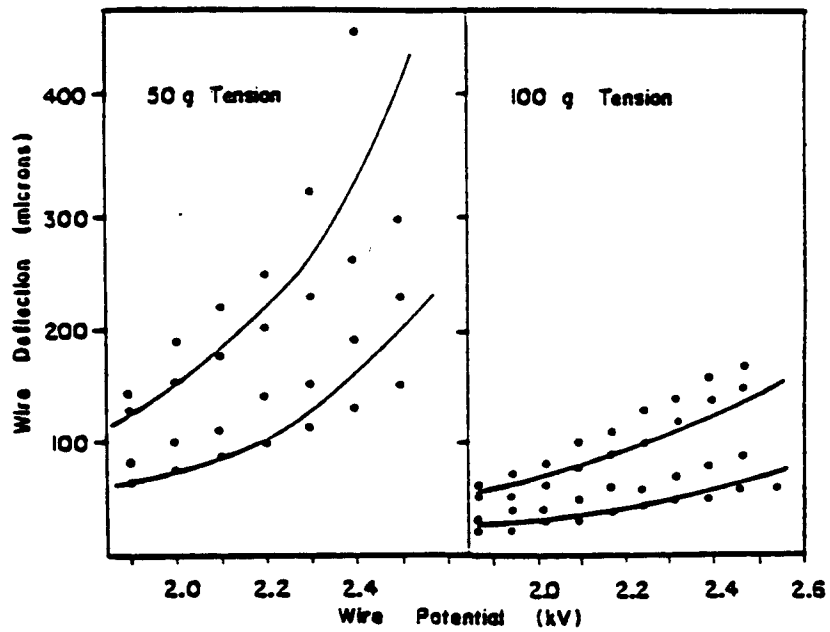

Fig. 2. Wire deflection as a function of voltage for two different initial displacements, 100 (lower set) and 200 (upper set) μm. The left panel is for 50 g tension, and the right panel for 100 g tension. The solid curves are the prediction from the formula in text. The open circle data points are for initial offset in one direction while the closed data points are for initial offset in the opposite direction.

offset of 100 μm and the upper set of data is for an initial offset of 200 μm. The solid curves are predictions from the formula for the wire deflection. The open circle data points are for initial offset in one direction while the closed circle data points are for initial offset in the opposite direction. The discrepancies between the data are indicative of some nonlinearity of the tube. The measurements agree quite well with the predictions of the above calculations.

With 50 g wire tension the amount of deflection of the wire from its initial position is about 80 μm for the initial displacement of 100 μm at potentials at which the straw tubes are expected to be operated. In order to optimize spatial measurement resolution such wire deflection must be minimized. 50 g of tension is probably acceptable with wire supports at distance intervals of 1 m if the initial wire displacement is less than 50 μm.

3. Sense wire support

To achieve adequate geometric acceptance for charged tracks the SSC central tracking chamber will have to be 6 m long at an outer radius of 1.7 m. Some designs consist of two 3 m long chambers. In this case there is a gap in the middle of the chamber. In either case it will be necessary to provide centering support for the sense wires in the straw tubes at about 1 m intervals to ensure electrostatic stability, and minimize the wire deflection.

The wire supports must center the wire in the straw tube while at the same time not restricting gas flow through the tube. Our design for the wire support consists of a plastic cylinder with a helical groove which is a cylinder radius deep and makes at least one complete revolution around the cylinder in a length of

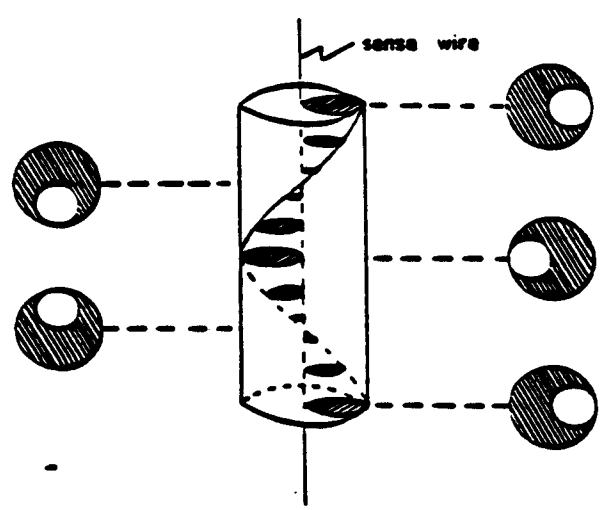

Fig. 3. Duke wire support design. A helical hole is made inside a plastic cylinder.

less than 1 cm. Such a device will provide gravitational support regardless of the orientation of the tube. A schematic drawing of the wire support design with cross section views is shown in fig. 3. We have produced a few samples using two methods, injection molding and using a milling machine to make the groove. In the latter case the plastic cylinder translates as well as rotates while being cut. The cutting method seems to produce better pieces with lesser cost.

The wire supports will be attached to the straw tube. The wire will then be threaded through the tube. This has the advantage that if a wire should break during installation in a straw tube it will be easy to remove the broken wire and re-string the tube.

4. The construction of the prototype

We have successfully constructed a 2.7 m long prototype chamber with eight layers of tubes. In this section, we present the construction of the prototype. The geometry of the tubes in the prototype is shown in fig. 4. The 60 tubes are arranged in a pyramid shape with eleven tubes at the bottom and four tubes at the top. The radius of each tube is 2 mm.

The construction of the prototype starts with a sturdy base. The base could be an optical table or a rail. It is important that the base has a flat surface that tubes can be placed on. Our base looks like the bottom third of a disk. It is 3.3 m long with a 7 cm wide machined face. The surface was scanned with a survey telescope and found to be flat to better than 25 μm over the entire surface. Present design concept for our final tracking chamber for SSC requires a cylindrical surface for each superlayer, which is constructed out of carbon fiber. Preliminary study [5] shows that a 6 m long cylindrical surface constructed with carbon fiber thickness of less than 0.3% of radiation length has a

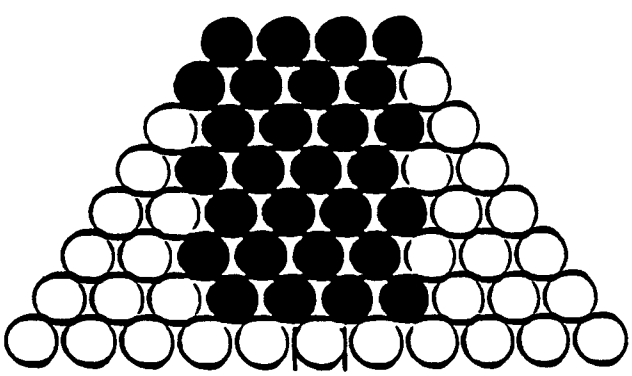

Fig. 4. Cross section of the straw tube superlayer in the prototype. The shaded tubes were instrumented.

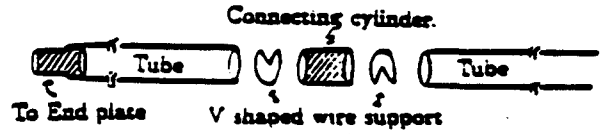

Tube assembly.

Fig. 5. Tube assembly with tube connector and wire support.

maximum deflection of less than 25 μm at the center when the ends are fitted with endplates.

On the top of the base, four aluminum plates with machined grooves are placed. The grooves on the plates are to guide the tubes. The plates are aligned among themselves using the survey instrument. The plate simulates the cylindrical base to be used in the final tracking chamber.

Straw tubes were assembled prior to placing them on the aluminum plate. The tubes used in the prototype have a wall thickness of 50 μm and were made of mylar strips wound on top of 8 or 12 μm thick aluminum foil (cathode) strips [6]. Although we have chosen the aluminum cathode for convenience, it is not clear whether that was the best choice. It has been known that a cell with aluminum cathode will draw a large continuous current when it is exposed to a high radiation. The speculation is that the aluminum cathode becomes oxidized and results in the buildup of positive ions on the oxide layer. Eventually the potential across the oxide layer becomes large enough to extract electrons from the cathode, which causes the continuous current draw. This effect is known as the Malter effect [7]. We are investigating different cathode materials such as a several hundred ångströms thick copper.

Three tubes of 90 cm length were joined. Before the tubes were connected together using thin aluminum sleeves, wire supports were inserted inside tubes as shown in fig. 5. Because we were not able to obtain the wire support described above in time for use in the prototype, we instead used two V-shaped disks back to back. Although the disks were machined carefully, measurements using a microscope showed that they were about 75 μm in tolerance. As we have discovered, joining tubes was not the best approach since the tube joints introduced alignment errors along the vertical direction at the joint. In the next prototype different techniques will be tried, for example, the wire supports will be inserted from the ends of continuous straws.

Once enough tubes are assembled for a layer, they are inserted to the endplates (fig. 6) and placed on the grooves of the aluminum plate. The endplate design is very important since straw tubes, electronics, gas and high voltage connections and cooling are done through endplates. Our endplate consists of two plates with

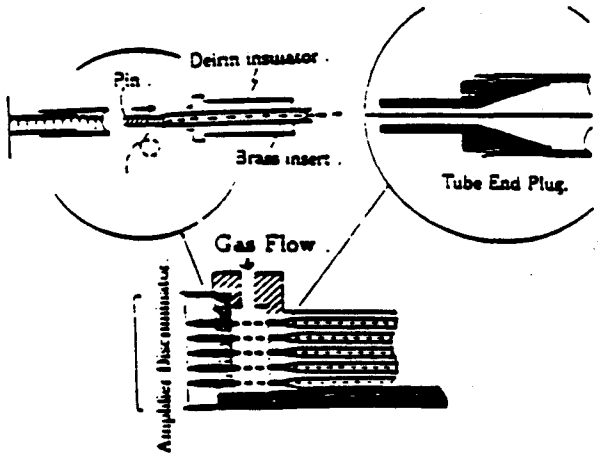

Fig. 6. The endplate used in the prototype. The details of the tube end plug and feedthrough are shown.

space between them. Tubes are fitted to the inner plate, and feedthroughs are inserted from the outer plate for sense wire, high voltage and amplifier connection. The space between the plates serves as a plenum to provide gas flow to the straw tubes. The gas may be cooled to reduce ohmic heating inside the tubes. In order to attach the tubes to endplates, the tubes were bowed slightly.

After all tubes for a layer are placed, the tubes are glued to the layer below (or on the aluminum base plate for the first layer). To obtain better placement accuracy, the tubes are pressed slightly using finger-shaped jigs from the top. After the tubes are properly placed, a small amount of fast drying glue (cyanoacrylate) is used to glue the tubes. The gluing has two purposes. First, the fixed tubes act like the grooves on the aluminum plates, so that the next layer of tubes can be aligned accurately. Second, it straightens the tubes. The tubes from the factory are not only very flexible but also are slightly bent. Tubes are glued about every 10–20 cm depending on the quality of tubes.

As we assembled each layer, the vertical and horizontal position of the tubes was measured. Fig. 7 shows the horizontal position of the tubes in the third layer at three different locations along the tube length. The plotted points are the difference between the expected tube position and measured tube position with respect to the first tube. The figure shows that tubes can be positioned to an accuracy of bettern than 100 μm. Fig. 8 shows the vertical position of the top layer (eigth layer) measured along the tube length from one end. As we mentioned earlier, the tube joint at 90 cm is out of place by about 100 μm.

After all tubes were placed and glued, sense wires were strung. To accomplish this, high pressure air (we used 20 psi air from a tube with 1.5 mm radius) was

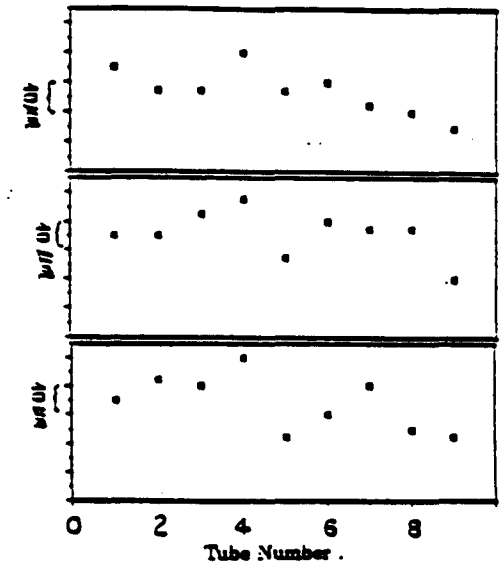

Fig. 7. Horizontal position of straw tubes in the third layer as a function of straw tube number. The plotted points are the difference between the measured position and the expected position with respect to the first tube. Each plot is taken at a different distance from one end along the length of tubes. The measurement error in each point is about 25 μm.

blown from one end of a tube to string a guide wire with 100 μm diameter. A gold plated tungsten sense wire with 25 μm diameter was attached to the guide wire and pulled through. (The procedure can be done without the guide wire.) The sense wire was passed through a feedthrough and then tensioned to 50 g, pinned, and soldered. The feedthrough design shown in fig. 6 consists of three pieces: a cylindrical insulator made of delrin, a brass insert which fits inside the insulator and a pin. At the end of the brass insert there is a 60 μm diameter opening which positions the sense wire accurately.

Each cell was tested for high voltage. Out of 60 tubes, we instrumented 28 of them (shaded tubes in fig. 4). Of these, we found that only one tube does not hold an operating voltage (1800 V). For the rest of the tubes, we were able to raise the high voltage to at least

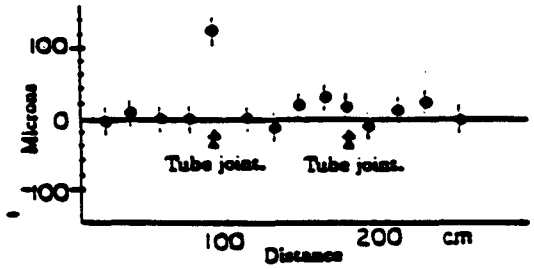

Fig. 8. The vertical position of straw tubes on the top layer as a function of distance from one end.

2500 V. It is not clear why one cell is bad, but we think that the wire support inside the cell may not be positioned properly or was moved by high pressure air. In this one tube, we strung another wire with 100 g tension, and were able to raise the voltage to 1900 V.

5. Performance of the prototype

In this section, the tests performed with the prototype chamber are described. We studied the attenuation length, gas gain and resolution. to eliminate signal reflection, one end of the sense wire was terminated. Since the impedance of a 2 mm radius tube with 25 μm sense wire is about 300 Ω, one end of the sense wire is terminated to ground through a 150 pF capacitor and 300 Ω resistor in series. By comparing the time difference between the reflected signal and unreflected signal, we obtain $(2.9 \pm 0.1) \times 10^6$ m/s for the propagation velocity.

Fig. 9 show the averaged signal using ^{90}Sr. 1000 signals are averaged in the plot. The gas used for the plot was a mixture of CF_4–Ar–ethane (33–33–33) and the high voltage was set at 1800 V. Although different gas mixtures show slightly different decay time, the typical signals (using ^{90}Sr) into 50 Ω from the chamber have a rise time of about 2–3 ns. About 30 ns later, the signal is reduced to about 15% of its maximum.

Fig. 10 shows plateau curves obtained using a Lecroy 2735DC amplifier–discriminator with a 3 μA threshold. A ^{90}Sr radiation source is used. One curve is taken with the source near the readout end and the other with the source 250 cm from the readout end. The gas used is CF_4–Ar–ethane (33–33–33) mixture. As expected, the knee of the plateau curve measured at the far end location moves compared to the other curve. The shape of the signal from the near end compared to the far end (with respect to the readout end) is very similar although the height is down by about half (i.e. the dispersion is small).

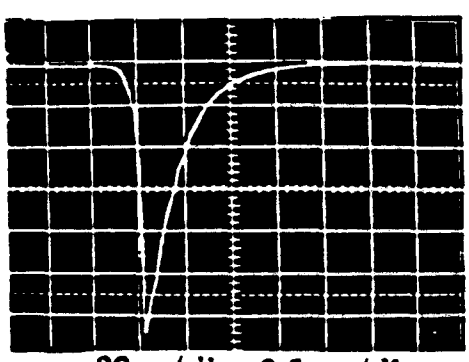

Fig. 9. The averaged signal using ^{90}Sr source. The gas mixture [illegible]-ethane (33–33–33) and high voltage is 1800 V.

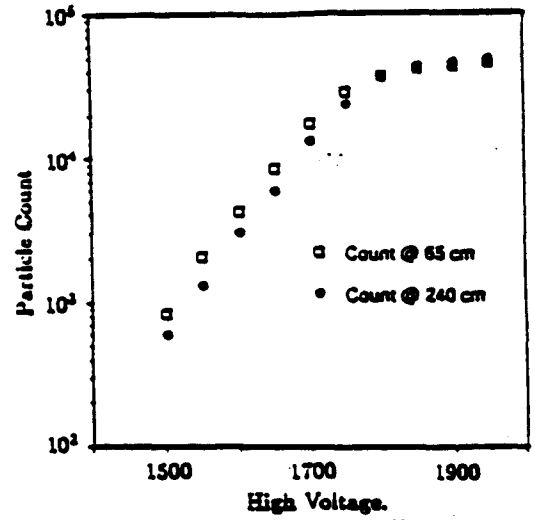

Fig. 10. Plateau curves obtained using ^{90}Sr source at two different positions from the end of tubes. The gas mixture is CF_4–Ar–ethane (33–33–33).

The attenuation length (λ) is measured using a ^{55}Fe source. Because of the variation of gas gain near the straw tube joints, the peak of the signal is measured from both ends of the chamber. From the ratio of the two peaks as a function of distance from one end, the attenuation length is calculated. Fig. 11 shows the

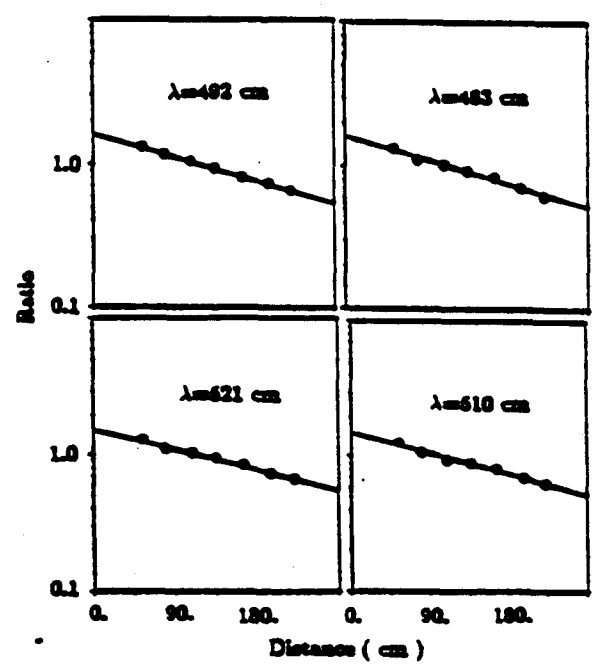

Fig. 11. The ratio of amplitude from one end to the other end using ^{55}Fe source. The attenuation length is obtained from the slope. See text for detail.

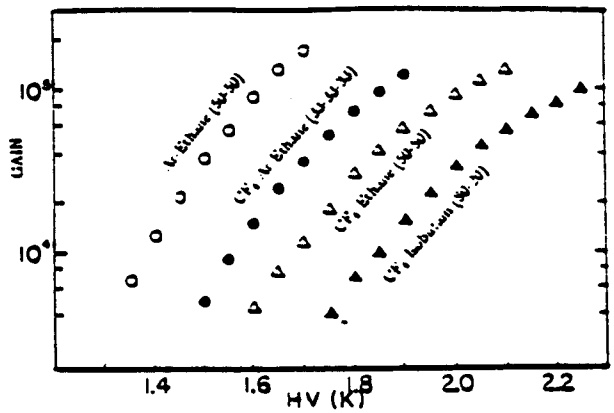

Fig. 12. The gain as a function of high voltage for several gas mixtures.

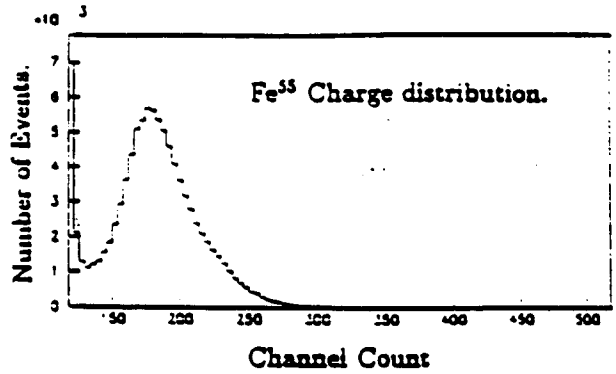

Fig. 13. Typical ^{55}Fe spectrum measured from a cell using a multichannel analyzer.

plotted ratio for several channels. The overlapped curves are fits using an exponential function. Although there is some variation between tubes, an average attenuation length of 500 cm is obtained. (The attenuation length calculated this way is one half of the true attenuation length. The 500 cm and the numbers in fig. 11 are already multiplied by a factor of 2.) The signal attenuation is likely due to the resistance in the sense wire. The resistance of the sense wire is about 100 Ω/m which is much larger than the resistance of the cathode, which is less than 1 Ω/m. Our value is somewhat higher than a previously reported value of 450 cm [4]. The difference may be due to the different cathode thickness.

Fig. 12 shows the gas gain as a function of high voltage for several different gases using a ^{55}Fe source. The output from a cell is connected to a charge amplifier and then to a multichannel analyzer. Fig. 13 shows the typical charge spectrum from the multichannel analyzer. The rms width of the peak is about 35%. The absolute calibration is accomplished by inserting a known amount of charges into the amplifier. However, due to the uncertainty in the calibration, we expect about 10–20% systematic error in the absolute gain values. We have tried several different mixtures in an attempt to find a mixture with high electron drift velocity and high gas gain. It is desirable to lower the sense wire voltage as much as possible since the earlier electrostatic stability study showed that the wire deflection increases as a function of V^2.

The 28 channels were instrumented with electronics for the resolution study using a cosmic ray trigger. The outputs from the chamber were connected to the Lecroy 2735DC amplifier–discriminator with 5 μA threshold. The discriminated outputs were connected to Lecroy TDCs (2229). Fig. 14 shows the raw time distribution for several different gases: Ar–Ethane (50–50) mixture with the operating voltage = 1700 V, CF_4–ethane (50–50) mixture with the operating voltage = 2100 V, and CF_4–Isobutane (80–20) mixture with the operating voltage = 2200 V. The average electron velocity inside tubes for the gases are 51, 89, and 110 μm/ns, respectively. Because the bunch crossing of

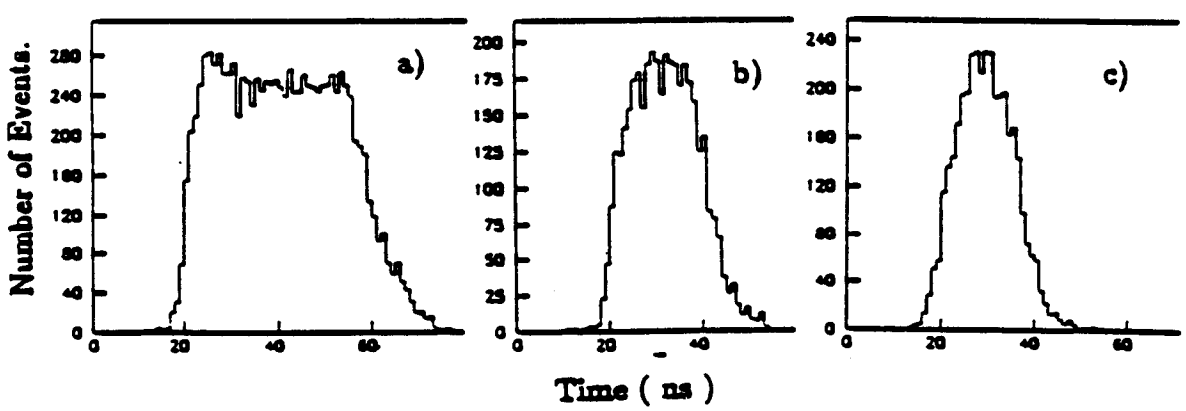

Fig. 14. Raw time distributions measured using different gas mixtures: (a) Ar–Ethane (50–50), (b) CF_4–ethane (50–50), (c) CF_4–isobutane (80–20).

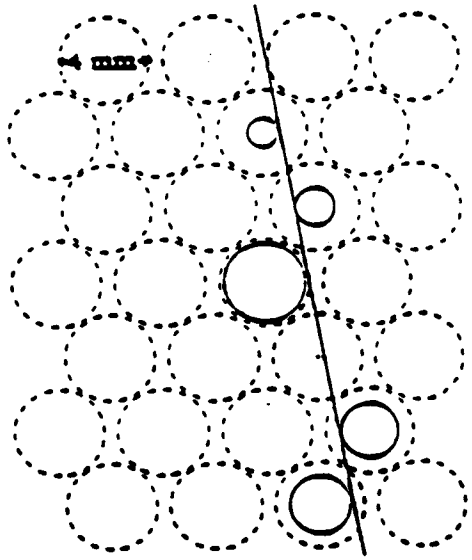

Fig. 15. A triggered cosmic ray track traversing the superlayer.

the SSC is 16 ns, and the average number of interactions is 1.5 per crossing at the design luminosity of 10^{33} cm^{-2} s^{-1}, the fast electron drift velocity is necessary in order to reduce the occupancy rate.

Fig. 15 shows a triggered cosmic ray track traversing the straw tube array. Using the tracks, the sense wires are aligned among themselves before residuals are calculated. The amount of correction to align sense wires is consistent with the deviation of the tube positions shown in fig. 7. Using the fitted tracks, the residuals are calculated and plotted in fig. 16 for the gas mixture of Ar–ethane (50–50) with operating voltage of 1700 V. The residuals are calculated using tracks with six or more hits. A sigma of 110 μm is obtained by fitting the distribution with a Gaussian curve. Several different gas mixtures are tried for comparison. For CF_4–ethane (50–50 mixture, operating voltage = 2100 V) a sigma of 120 μm, and for CF_4–isobutane (80–20 mixture, operating voltage = 2200 V) a sigma of 125 μm is obtained.

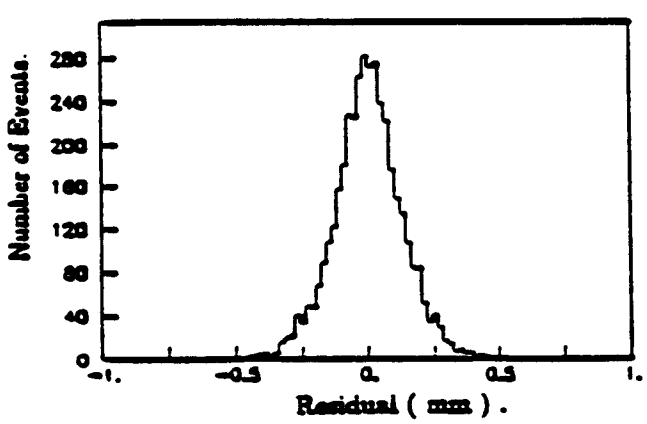

Fig. 16. Residual in mm obtained using cosmic ray tracks. Only tracks with six or more hits are used. Sigma of 110 μm obtained from a Gaussian fit to the curve.

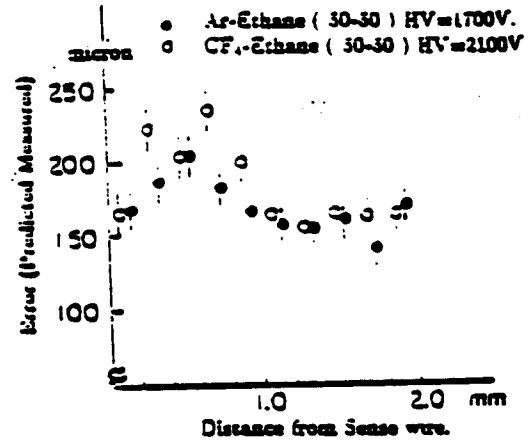

Fig. 17. The error as a function of distance from the sense wire. See the text for the definition of the error.

The resolution is also measured as a function of distance from the sense wire. Fig. 17 shows the error plotted for two gas mixtures. The error is calculated like the residual calculation except the hit from the cell of interest is not used in the track fit. In order to increase statistics, any tracks with more than four hits are used. As seen in the figure, the resolution is worse near the wire.

Presently we are studying long term aging effects. The expected radiation level at 50 cm distance from the interaction region causes about 0.05 C/(cm yr) charge deposit on a sense wire at the design luminosity with the gas gain of 5×10^4. It is essential to find a proper gas mixtures which results in a good resolution, high gain, fast electron drift velocity and a long chamber lifetime. Results of these tests will be reported when available.

6. Conclusion

For a feasibility study of using small radius tubes for a central tracking chamber for a SSC experiment, we have constructed and operated a 2.7 m long prototype straw tube drift chamber. The prototype consists of eight layers of tubes with a total of 60 channels. 28 channels were instrumented with readout electronics. By doing so we have demonstrated the following: First, we showed that layers of tubes can be placed straight with an accuracy better than 100 μm over several meters once a flat base surface is provided. Second, an endplate designed using two plates provide an easy way to mount tubes, supply gas, string wire and mount

electronics. Third, the wires can be supported inside tubes with proper wire supports to make a long working straw cell. Fourth, a large number of channels can be made operational simultaneously without difficulty. Using the prototype, we obtain about 500 cm for the attenuation length and about 110 μm for the resolution. We believe that the design and construction concept can be extended to a full size cylindrical central tracking chamber.

References

[1] SDC Collaboration, EOI, submitted to SSC Lab. (1990); L* Collaboration, EOI, submitted to SSC Lab. (1990).

[2] SSC subsystem proposal, Submitted to SSC Lab. (1989); G. Hanson et al., PC-024, A.T. Goshaw et al., PC-035.

[3] C. Broll et al., Nucl. Instr. and Meth. 206 (1983) 385; P. Baringer et al., Nucl. Instr. and Meth. A254 (1987) 542; S. Bhadra et al., Nucl. Instr. and Meth. A268 (1988) 92; S.H. Oh et al., to be published in Nucl. Instr. and Meth. A.

[4] S.H. Oh et al., Proc Int. Workshop on Solenodial Detectors for the SSC., KEK, Japan, 1990, eds. F. Abe and K. Hasegawa, p. 279; H. Ogren, ibid. p. 302.

[5] D. Vandergriff, ORNL, Oak Ridge, TN, private communication.

[6] The tubes were wound by Stone Industrial Division, College Park, MD 20704, USA.

[7] L. Malter, Phys. Rev. 50 (1936) 48.